Synthesis and characterization of magnetron-sputtered Ta N thin films for the photoelectrolysis of water

Martin Rudolph

To cite this version:

Martin Rudolph. Synthesis and characterization of magnetron-sputtered Ta N thin films for the photoelectrolysis of water. Plasma Physics [physics.plasm-ph]. Université Paris Saclay (COmUE), 2017. English. NNT : 2017SACLS094 . tel-01784063

HAL Id: tel-01784063
https://theses.hal.science/tel-01784063

Submitted on 3 May 2018

NNT : 2017SACLS094

THESE DE DOCTORAT
DE
L'UNIVERSITÉ PARIS-SACLAY
PRÉPARÉE À
L'UNIVERSITÉ PARIS-SUD

ECOLE DOCTORALE N°572
Ondes et Matière

Spécialité de doctorat : Physique des plasmas

Par

M. Martin Rudolph

Synthesis and characterization of magnetron-sputtered Ta_3N_5 thin films for the photoelectrolysis of water

Thèse présentée et soutenue à Orsay, le 2 Mai 2017 :

Composition du Jury :

M. Ian Vickridge	Directeur de la recherche, Université Pierre et Marie Curie, Paris	Président
M. Jón Tómas Guðmundsson	Professeur Háskóli Íslands, Reykjavik et Kungliga Tekniska Högskolan, Stockholm	Rapporteur
Mme. Angélique Bousquet	Maitre de conférences, Université Blaise Pascal, Clermont-Ferrand	Rapporteur
M. Philippe Lecoeur	Professeur, Université Paris-Sud, Orsay	Examinateur
Mme. Marie-Christine Hugon	Maitre de conférences, Université Paris-Sud	Directrice de thèse
Mme. Brigitte Bouchet-Fabre	Chargée de la recherche, CEA Saclay	Co-directrice de thèse

Yes, my friends, I believe that water will one day be employed as fuel, that hydrogen and oxygen which constitute it, used singly or together, will furnish an inexhaustible source of heat and light, of an intensity of which coal is not capable.

Jules Verne, The Mysterious Island

To my parents, my family and my friends.

Acknowledgments

First of all, I would to like to express my sincerest gratitude to my advisor Marie-Christine Hugon who has shared with me her immense knowledge on various measurement techniques in materials science. I have appreciated all the scientific and technical discussions we had in the last three years out of which new ideas continuously emerged. And I am particularly grateful for having put me in contact with so many researchers from diverse fields to discuss my questions. I strongly believe that this has been a key to the success of such an interdisciplinary study.

Furthermore, I am very grateful to Tiberiu Minea for having accommodated me in the group “Théorie et Modélisation des Plasmas - Décharges et Surface” at the Laboratoire de Physique des gaz et des plasmas (LPGP) and for the many discussions we had around the physics of discharges. Despite his responsibilities as the head of the laboratory later on, it has always been possible to discuss recent results and his advice for simulations and plasma measurements has been very supportive.

Thanks as well to my co-advisor Brigitte Bouchet-Fabre. Her enthusiasm for materials and renewable energies has been a steady source of motivation for me.

I would also like to thank the jury members Ian Vickridge, Jón Tómas Guðmundsson, Angélique Bousquet and Philippe Lecoeur, for having read carefully through my manuscript and for their advice in polishing up the final version. I have very much appreciated their questions and comments during my defense.

I would like to thank the French team of the SNON project: José Alvarez, Sofia Gaiaschi and Jean-Paul Kleider from the GeePS laboratory of Central Supélec in particular for the electronic and AFM measurements; and to Dana Stanescu and Hélène Magnan of the CEA Saclay in particular for the photoelectrochemical measurements. I thank all of them, including Nathalie Herlin-Boime from the CEA Saclay, for the discussions on so many different facets of the study.

I am also very grateful to the Romanian team of the project in particular to Lucel Sirghi for inviting me for a stay at his laboratory at the Alexandru Ioan Cuza University. I enjoyed working with his colleagues, Vasile Tiron, Alexandra Demeter, Ilarion Mihaila and Claudiu Costin, particularly on the mass spectrometry, but I have similarly appreciated the discussions on the physics and chemistry of surfaces.

The measurements at the accelerators at the University of Namur, at the CEA Saclay and the Institut des NanoSciences de Paris at the Université Pierre et Marie Curie have certainly been the most captivating experiments. I am grateful to Jean-Jacques Ganem, Emrick Briand, Hicham Kodja and Tijani Tabarrant for their support with the measurements and the analysis, for sharing their knowledge on nuclear reactions and for the continuous effort to get the most out of the accelerators.

With a special mention to Eddy Foy from the CEA Saclay, for having introduced me to the fascinating field of X-ray diffraction and in particular for the countless diffractograms we recorded. I have not forgotten the day we saw the Ta_3N_5 phase for the first time.

I am very grateful to Martine Wery for the effort she made to accommodate meetings into her tight schedule to share her vast knowledge on electrochemistry with me.

I am also grateful to Séverine Le Moal from the Institut des Sciences Moléculaires d’Orsay, Diana Dragoe from the Institut de Chimie Moléculare et des Matériaux d’Orsay and Jocelyne Leroy from the CEA Saclay for the XPS measurements and the assistance with fitting and interpreting the spectra. I have learnt a lot from them. Thanks as well to Patrick Bonnaillie from the CEA Saclay for his incredible skills in taking SEM images.

During my thesis, I have asked many little favors to many people at the LPGP. I am grateful to Joel Baudet for having put my unskilled technical drawings into reality. Thanks to Gérard Bauville for having pushed the limits of his laser cutter further and further. Thanks to João Santos Sousa for his assistance with the pH measurements and for having let me work in his chemistry lab. Thanks to Stéphane Maingot for always having had the right tools at hand. Furthermore, I would like to thank Michel Fleury, Marc Bisson and Michel Pascanu for their their help with electronics and software. Thanks as well to Olivier Antonin, for having shared with me all the tricks to get the sputter system running reliably and finally, thanks to Charles Ballage for helping me find and repair the leak in the deposition chamber.

The administration of the LPGP has always been very supportive. A big thanks to Nicolas Dessaint and the current and former members of his team, Thierry Devillers, Sophie Granon, Ophélie Molle, Bérénice Saidi and Nathalie Rico-Perez.

I have in particular appreciated the working atmosphere at the LPGP. Thanks to all the PhD students, postdocs and researchers that have contributed to this, Jean-Sébastien, Frédéric, Adrien, Lise, Alexis, Patrick, Thomas, Steven, Benjamin, TJ, Felipe, Daniel, Alexandra, Sébastien and Mathieu.

Finally, I would like to thank my parents and grandparents for their support throughout my studies, my siblings for their encouraging words, and all my friends who have supported me in one way or another in the last years.

Content

1 Context, objectives and outline of this thesis

The vision of a clean energy supply has challenged scientists and engineers for the last two decades. Its attraction springs from the image of tapping virtually infinite resources of energy with little side effects. But it is also based on more rational grounds. Global warming urges us to substitute our fossil energy sources to limit the greenhouse effect. Moreover, emission of particulate matter from coal-fired power plants, risks of nuclear technologies and the reliance on oil-producing, possibly politically unstable countries, to mention only some points, render renewable energies very attractive.

Possible sources of renewable energies available on our planet are manifold and so are the technologies to convert their energy into a useable form: reactors ferment biomass to methane, the tidal range drives electricity generators and solar collectors heat up water for domestic use. The exploitation of various sources is wanted and contributes to a stable and reliable supply. However, in view of the world demand, only a few sources have the potential to contribute a significant share to the world energy supply: biomass, the wind and the sun. Each of the latter two even supplies sufficient power to cover the world demand (Fig. 1). An energy transition is thus to rely on these sources.

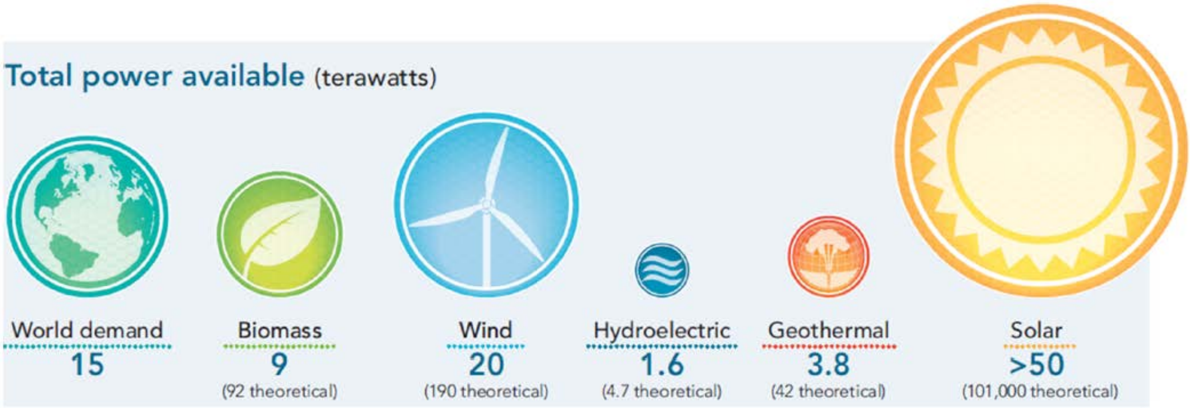

Fig. 1: World power demand and total power available by renewable sources [1].

To approach the objective of having an energy supply from entirely clean sources, the European Union set a target. 20% of the total gross energy consumption should come from renewable energy sources by 2020 [2]. And indeed, renewable energies have gained a significant percentage, which rose from 8.7% in 2005 to 15.2% in 2014 [2]. This growth was mainly carried by the installation of wind turbines and photovoltaic panels (Fig. 2) as these technologies reached maturity and became cheaper over the years [3]. There is no doubt that they will continue to play a key role in pushing the share of renewable energies towards the 20% target in the near future.

In the long term, solutions for two major challenges need to be found, in order to reach even more ambitous goals. Firstly, the production of renewable electricity from the sun and the wind is highly fluctuating on various time-scales due to weather and seasonal changes. This, in combination with the unavailability of storage capacity for large amounts of electricity, has already today let to the absurd phenomena of negative wholesale electricity prices [4], which could impair future investments in wind turbines and photovoltaics. The development of storage capacity is thus a prerequisite for further exploiting the wind and the sun for the production of electricity [5].

Secondly, the high contribution of renewable energies to the total energy consumption is shadowing the fact that the three energy sectors, electricity, heating & cooling and transport differ greatly in their contribution to this single figure. While the share of renewables in the electricity sector was at 25.2% in 2014, the transport sector lagged largely behind with only 5.2% of all consumed fuels coming from renewable sources [2]. Cars, vessels and planes still today rely heavily on fossil fuels and this is likely not to change any time soon, as clean transport technologies are still under development [6]. Investing in today's mature technologies like wind turbines and photovoltaic panels alone, is thus insufficient for reaching the long-term goal of having all energy come from renewable sources.

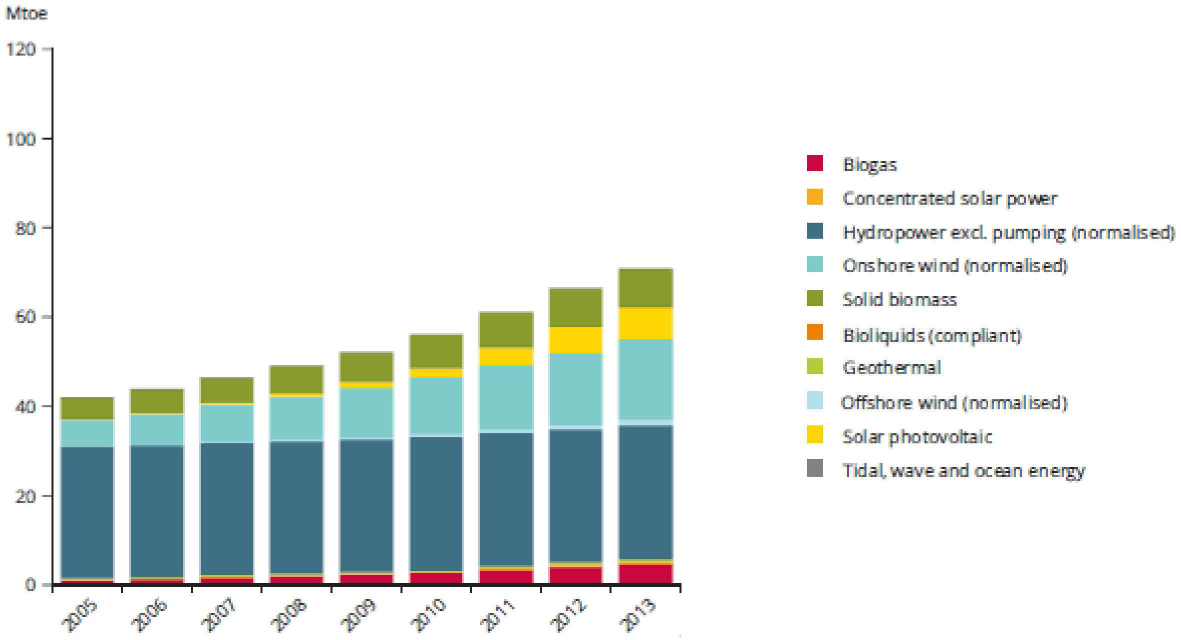

Fig. 2: Million ton of oil equivalent (Mtoe) of renewable energies decomposed by their source from 2005 to 2013. From [2].

Therefore, development efforts are focussed on the renewable production of chemical fuels and the storage of energy [7]. One possibility to approach both targets at the same time is to convert renewable electricity into chemical fuels by electrolysis. The advantage is that chemical fuels are more practical when it comes to storage. Hydrogen, for example, has still an unprecedented specific energy density of 141MJ/kg compared to commercially available batteries ranging between 0.09MJ/kg and 2.3MJ/kg [8]. Furthermore, its transport by pipelines or in liquid form on trucks or ships is principally possible [9] [10]. But not only could hydrogen serve as an energy storage alone. It can partially replace natural gas used for heating [11]. It is also considered suitable as a fuel in transport. Already today, hydrogen-fueled vehicles are just entering the market [12] [13].

Today, the clean production of hydrogen is possible by using renewable electricity to electrolyze water into oxygen and hydrogen. This is an energy-consuming process as efficiencies of 50% are reached at tops for electrolyzers [10]. In conjunction with a commercially available photovoltaic generator efficiency of 20%, a system like this results in a solar-to-hydrogen efficiency of 10%.

This rather low efficiency presents opportunities to alternative technologies that are still at the beginning of their development and thus lag behind in technology readiness level.

One alternative is the photoelectrolysis of water which is the direct use of photon energy for the splitting of water molecules to produce hydrogen and oxygen. It was discovered by Akira Fujishima and Kinichi Honda in 1971 [14]. Their setup consisted of a semiconducting TiO_2 electrode connected to a platinum cathode both immersed into a water-based electrolyte. When illuminating the setup with ultraviolet light, they observed the evolution of oxygen and hydrogen on the anode and cathode respectively. This groundbreaking experiment triggered a number of developments in the years to follow but still today, the efficiencies remain low.

The principal challenge is to find and synthesize suitable materials. In particular, the requirements on the position of the valence and conduction band edges, combined with the need for a small band gap, are rarely found. In order to overcome this issue, tandem cells have been developed with multiple layers, that have reached quite high efficiencies of up to 14% [15]. From an application point of view, simple systems would be preferred, though, mainly for cost reasons. Those systems, consisting of a photoactive material and possibly a co-catalyst, however, have only reached efficiencies of around 1% in the past [16] [17].

This thesis focusses on the synthesis of Ta_3N_5, one of the most promising semiconductors for the photoelectrolysis of water. It has a band gap of 2.1eV and suitable band positions [18] [19]. For its synthesis, magnetron sputtering is chosen. It is technique widely used in industry that offers a large parameter space for tuning film properties. However, until today, the synthesis of this material by magnetron sputtering is little studied. Only three groups of authors have published results on the sputter-deposition of this material [20] [21] [22]. The possibilities offered by this technique thus still lack a systematic investigation.

This thesis identifies the relevant physical mechanism for the successful deposition of Ta_3N_5. Moreover, using that knowledge, the deposition process is optimized to obtain high-quality thin films of Ta_3N_5. The focus here lies on the bulk properties, i.e. the deposition process is optimized to obtain highly crystalline films with large grains.

The thesis is structured in the following way:
After the general overview of the subject in this chapter, the second chapter presents a more detailed compendium of the three fields relevant for this thesis. It starts with an introduction to the photoelectrolysis of water. This is followed by a summary of Ta_3N_5 properties and a presentation of its synthesis by conventional ammonolysis. The chapter closes with an introduction to magnetron sputtering covering the effects that are important to understand the results of this thesis.

The third chapter is dedicated to the experimental and computational techniques employed throughout this thesis. It covers a description of the sputter deposition system used, introduces X-ray diffraction, ion beam analysis including Rutherford backscattering and nuclear reaction analysis. This is followed by a subsection on transmission and reflection spectroscopy including the presentation of a code, developed during this thesis to fit the experimental spectra to optical models. Finally, the four remaining subsections are dedicated to techniques that played a minor importance during the course of this thesis. They are X-ray photoelectron spectroscopy, optical emission spectroscopy, mass spectrometry and photoelectrochemical measurements.

The fourth chapter is dedicated to the first results obtained from the deposition of δ-TaN films. This phase serves as a model system to identify relevant mechanisms in sputtering from a Ta cathode. Particular focus is placed here on the size of the grains in these films, as this is the parameter to be optimized in Ta_3N_5 films. For that, direct current and high-power impulse magnetron sputtering modes are investigated. The observations are correlated with measurements of the ion flux onto the substrate and an analysis of the backscattered ion energy distribution. This leads to the recommendation to use the direct current sputtering mode for the deposition of Ta_3N_5-crystalline films.

The fifth chapter analyses the influence of oxygen incorporated into magnetron-sputtered Ta_3N_5 thin films. After giving a recipe for the deposition of Ta_3N_5-crystalline films, the material properties as a function of oxygen incorporation are measured. These measurements comprise X-ray diffraction, the determination of the complex dielectric function from which the band gap is determined and electrical measurements, notably the conductivity and the efficiency-mobility-lifetime product. X-ray photoelectron spectroscopy is done before and after the photoelectrochemical measurements, to observe chemical changes to the surface induced by the photoelectrolysis. The films deposited in this chapter are shown to work as photoanodes, but their crystallinity remains small.

The sixth chapter presents the implementation of a technique to increase the ion flux onto the growing film. This is shown to increase in particular the flux of N_2^+ onto the growing film, which effectively increases the degree of crystallinity as observed on the surface of these films by atomic force microscopy. This allows to determine the elemental composition of Ta-O-N magnetron-sputtered films. The correlate of this with the appearance of the Ta_3N_5 phase then yields a stability range with respect to the incorporation of oxygen into the structure. Photoelectrochemical measurements reveal the advantages of having a high incorporation of oxygen into the lattice.

The last chapter concludes the important findings for the sputter-deposition of Ta_3N_5 and its properties. Open questions arising from this thesis are summarized in a section on the perspectives.

2 Introduction and literature review

This chapter gives a general introduction to this study. To understand the motivation behind the thesis, this chapter starts with a basic introduction to the photoelectrolysis of water (Section 2.1). This is followed by a subsection on the Ta_3N_5 phase comprising a description of its place within the Ta-O-N ternary system as well as experimentally and theoretically derived physical and electrochemical properties. Its conventional synthesis is shortly discussed at the end to compare it with the synthesis by magnetron sputtering (Section 2.2). The last subsection is dedicated to a general introduction into the magnetron sputtering technique (Section 2.3). A conclusion terminates the chapter (Section 2.4).

2.1 The photoelectrolysis of water

The photoelectrolysis of water is the splitting of water molecules into hydrogen and oxygen by using directly the energy of incident photons.

$$2H_20 \ + h\nu \ \rightarrow 2\mathrm{H}_2 + O_2 \qquad \textit{Eq. 1}$$

The photon in this process provides the energy for the uphill reaction. Its Gibbs free energy change is ΔG = 238 kJ/mol which, broken down to the production of a single H atom equals 1.23eV.

As water is transparent to visible light, it cannot directly absorb the incident energy. In the photoelectrolysis of water, a semiconducting electrode is therefore utilized which is in direct contact with a water-based electrolyte. It absorbs incident photons which create electron-hole pairs that are separated in an internal electric field. For n-type semiconductors, holes migrate towards the electrolyte where they recombine with electrons from HO^- in the electrolyte under formation of oxygen. Electrons migrate in the opposite direction towards a metallic counter-electrode from where they can transfer onto H_2O molecules under the formation of hydrogen molecules. The electric field and the associated band bending that ensure the charge separation is provided by the space charges at the semiconductor/electrolyte interface.

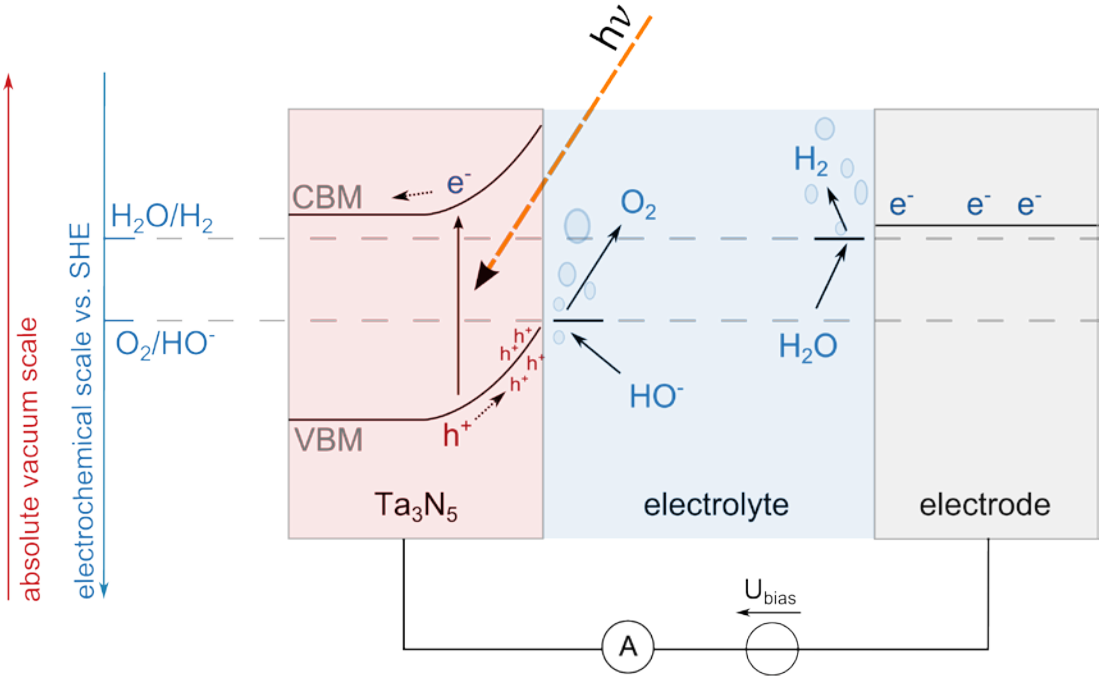

Fig. 3: Schematics of the photoelectrolysis of water using a Ta_3N_5 semiconductor (red) and a counter electrode (grey).

Before entering a more detailed discussion on the physics and chemistry of the photoelectrolysis, the basic concepts used to describe the behavior of electrons in solids, i.e. metals and semiconductors, and aqueous electrolytes are introduced. This is followed by a more detailed discussion on the individual processes at the semiconductor-solution and the metal-solution interface.

2.1.1 The solid state: metals and semiconductors

Contrary to free electrons, electrons in a crystalline solid material are bound in an electrostatic well with a periodic potential formed by the atomic nuclei and their core electrons. In this potential, electrons occupy energy levels that can be grouped into bands, whereas each band has a dispersion relation linking an energy state to a wave vector of the electron wave function. Each of these states, by reason of the symmetry of the crystal, can be occupied by two electrons with opposite wave vectors. A fully occupied band thus cannot contribute to electrical conduction, as an electron propagating into one direction has a counterpart propagating into the opposite direction. Partially filled bands, on the other hand, render a material conductive, and its electrical properties depend exclusively on these partially filled bands [23].

The distribution of electrons among possible energy states follows the Fermi-Dirac statistics which is a function of the temperature. In the ground state, i.e. at a temperature of 0K, only the lowest lying levels are occupied up to the Fermi energy. At higher temperatures, the distribution extends beyond the Fermi energy as some electrons have sufficient energy to occupy higher-lying energy states. This occupancy of states is described by the Fermi-Dirac distribution [24]:

$$f(E) = \frac{1}{1 + \exp(\frac{E - E_F}{k_B T})}, \qquad \textit{Eq. 2}$$

where E_F is the Fermi level, that according to above equation is the level at which an energy state has the probability of 1/2 to be occupied. It is typically measured against the energy of a free electron in vacuum and takes values of a few eV.

Metals

In a metal, the Fermi level lies within a band, which is naturally only partially occupied. Therefore metals are conductive and the electrons can be approximately described as a free electron gas [25]. The depth of the potential well, in which electrons are located is termed the work function, which is the energy required to remove an electron from the Fermi level to the field-free vacuum. The energy required for that is the sum of $|E_F|$ and a contribution from a dipole barrier at the surface from to lattice relaxation [26] and contaminants [27]. In addition, surface treatments can alter the work function of a material drastically. While polycrystalline gold has a work function of 4.4eV to 4.7eV under ambient atmosphere, sputter cleaning the same material gives it a work function of between 5.3eV and 5.4eV [28]. The work function is thus only a rough approximation for $|E_F|$.

Semiconductors

In intrinsic semiconductors, the Fermi level lies within a band gap, a gap in energy space without any electronic states. At the absolute zero, all bands below E_F (valence bands) are fully occupied, while those above E_F (conduction bands) are empty. As a consequence, electronic conduction is not possible and the material remains an insulator. As an example, Fig. 4 shows the band structure of the metallic δ-TaN phase and the semiconducting Ta_3N_5 phase. The Fermi level E_F in these cases is indicated as a vertical line at 0eV.

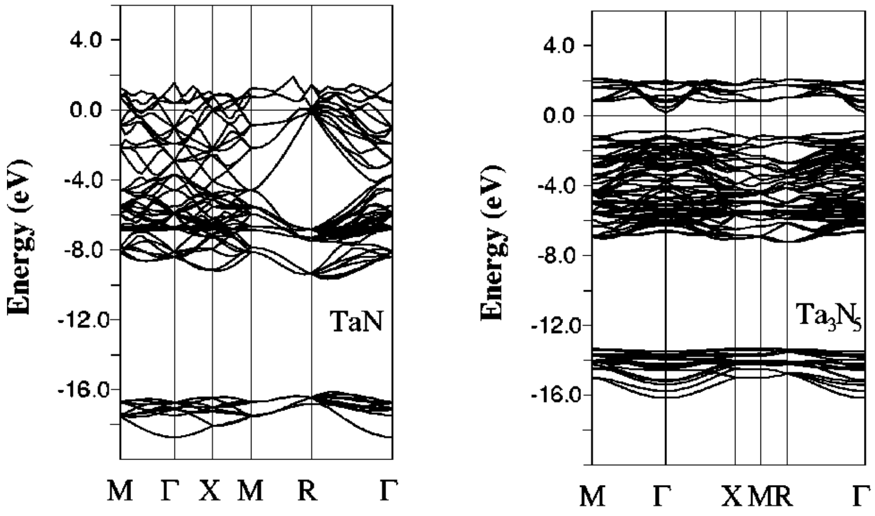

Fig. 4 : Band structure as calculated by density functional theory (DFT) for the metallic δ-TaN (left) and the semiconducting Ta_3N_5 *phase (right). The Fermi level* E_F *is indicated by a horizontal line at 0.0eV. M, Γ, X, R indicate crystallographic directions. From [29].*

For higher temperatures, the Fermi distribution (Eq. 2) extends to higher energies which allows some electrons to occupy the conduction band. This creates a conduction band that is partially occupied by electrons and a valence band that is partially occupied by holes, a hole being the lack of an electron. These two bands can thus contribute to a current and the material conductivity increases the more electron-hole pairs are created. The number density of each of the charge carries, electrons n and holes p, can be determined by an integral over the distribution function (Eq. 2) multiplied by the density of states for the conduction $g_c(E)$ and the valence band $g_v(E)$, respectively [23]:

$$n = \int_{E_c}^{E_{top}} g_c(E) f(E) dE \qquad \textit{Eq. 3}$$

$$p = \int_{E_{bottom}}^{E_v} g_v\,(E)[1 - f(E)] dE \qquad \textit{Eq. 4}$$

For an intrinsic semiconductor, the number density of holes is always equal to the number density of electrons. Taking the density of states derived for an electron in a simplified infinite square well potential, the position of the Fermi level can be calculated [23]:

$$E_F = \frac{E_c + E_v}{2} + \frac{3k_B T}{4} \ln\left(\frac{m_p^*}{m_n^*}\right), \qquad \textit{Eq. 5}$$

where m_n^* and m_p^* are the effective masses of holes and electrons respectively. The Fermi level is thus positioned approximately half-way between the conduction and the valence band, provided the effective masses are similar and the semiconductor is at room temperature (300° C).

An additional mechanism for creating charge carriers exists for extrinsic semiconductors. They can be produced by doping which is the addition of small quantities of atoms having a different valency compared to the intrinsic semiconductor. Some materials are inherently extrinsic, among which is the Ta_3N_5 phase [30].

An extrinsic semiconductor has occupied (empty) energy states within its band gap that can donate (accept) electrons to (from) the conduction (valence) band. As these levels usually lie close to the conduction (valence) band, electrons are injected (accepted) already at room temperature, increasing the charge carrier density and rendering the material more conductive compared to the intrinsic semiconductor. As this mechanism either creates only electrons or holes, one of these charge carriers now becomes dominant and is said to be the majority carrier. The material is then called n-type if electrons dominate, or p-type if holes dominate the electric conduction [23]. Ta_3N_5 is an n-type semiconductor [30].

At ambient temperature, the extrinsic mechanism dominates over the intrinsic one. The resulting dominance of one charge carrier to the other directly affects E_F, which now becomes [23]:

$$E_F = k_B T ln(N_{A,D}/n_i) \pm E_{F,i} \qquad Eq.\ 6$$

where $E_{F,i}$ is the Fermi level for the intrinsic semiconductor, $N_{D,A}$ the donor or acceptor density and n_i the intrinsic charge carrier density. The plus applies to the case of an n-type material, the minus to the case of a p-type material. One can see, that the Fermi energy is shifted up or down from its mid-band position depending on the type of doping. This is illustrated in Fig. 5.

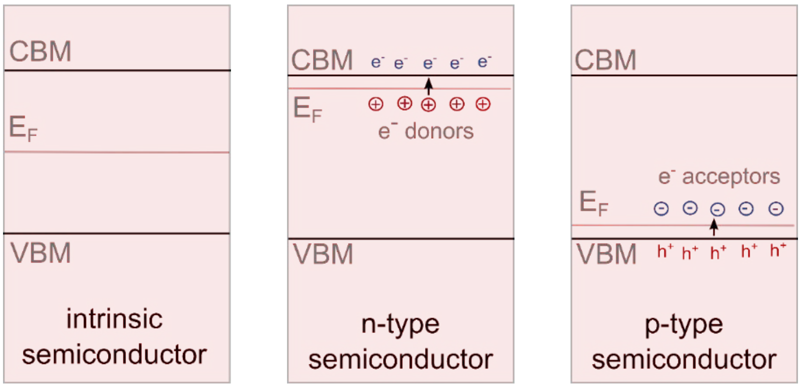

Fig. 5: Schematic illustration of the Fermi level in intrinsic semiconductors, n-type and p-type semiconductors.

2.1.2 Electrolytes

While the conductivity of a metal or semiconductor is provided by electrons, the conductivity of an electrolyte is provided by ions. A water-based electrolyte is made by adding either an acid or base into water. To limit corrosion of electrodes, alkaline solutions are normally preferred in electrolysis [31] and KOH is a typical base used for electrolysis due to its high conductivity in an aqueous solution [32]. It dissolves in water according to Eq. 7 under the formation of K^+ and HO^- ions:

$$KOH_{aq} \leftrightharpoons K^+ + HO^- \qquad Eq.\ 7$$

Some of the HO^- react with H_3O^+ present in the solution from the autoionization of water which increases the pH value of the electrolyte [32]:

$$pH = -\log\frac{c_{H_3O^+}}{c^0} = 13.9965 - \log\frac{c^0}{c_{OH^-}} \qquad Eq.\ 8$$

In such an alkaline solution, the two redox reactions shown in Eq. 9 and Eq. 10 can principally occur at metallic electrodes held at a certain minimum potential difference of 1.23V. The equations indicate, that hydrogen gas is formed in the forward reaction of Eq. 9 while the backward reaction of Eq. 10 yields oxygen. The former is called the reduction of water, while latter is the oxidation of HO^-. The corresponding electrochemical couples are H_2O/H_2 and O_2/HO^-, respectively. To prevent the built-up of charges, the reduction and oxidation have to occur simultaneously and the overall reaction is given by Eq. 1.

$$2H_2O + 2e^- \rightleftharpoons H_2 + 2HO^-, E^0 = -0.83V\ vs. SHE \qquad \textit{Eq. 9}$$

$$O_2 + 2H_2O + 4e^- \rightleftharpoons 4HO^-, E^0 = +0.40V\ vs. SHE \qquad \textit{Eq. 10}$$

E^0 is the standard potential of the corresponding half-cell reaction, which corresponds to the reversible potential at standard conditions, i.e. an electrode immersed into a solution of $1M$ at $25°C$ [32]. It is measured against the standard hydrogen electrode (SHE), which is a reference electrode to standardize the measurement of electrode potentials of half-cell reactions [32]. Accordingly, the standard potential of the SHE is defined to be at 0.0V [32]. The sum of the two standard potentials from Eq. 9 and Eq. 10 yield the energy required to split water, which is 1.23eV per H atom.

The standard potential of a redox couple reflects the electron energy level in an electrolyte. This is termed Fermi level of the redox couple $E_{F,redox}$. Its position with respect to E_F of a solid electrode is important as it determines the direction and rate of a charge transfer. For comparing both, the electrochemical scale, measuring a potential against an arbitrarily chosen reference electrode, needs to be converted to the absolute vacuum energy scale that is commonly used in solid state physics. This can be done by knowing that the standard potential of the SHE measured against the potential of an electron in field-free vacuum E_{abs}^0 is estimated to lie at (4,44±0.02)V at 25°C according to a IUPAC definition [33] [34]. This translates to a Fermi level $\mathrm{E}_{\mathrm{F,redox}}^0$ of the SHE of (-4,44±0.02)eV.

Any deviation from the standard state causes $E_{F,redox}$ to shift. Taking a reaction of type red ↔ ox + e^-, where *ox* stands for the species on the oxidized side of the equation and *red* for those on the reduced side of the equation. Then, the variation of $E_{F,redox}$ with the concentration of the oxidized species c_{ox} and that of the reduced species c_{red} is given by the Nernst equation [35]:

$$E_{F,redox} = E_{F,redox}^0 - k_B T \ln\left(\frac{c_{ox}}{c_{red}}\right), \qquad \textit{Eq. 11}$$

$E_{F,redox}$ thus changes in particular with the concentration of the HO^- ions, which is related to the pH value and Eq. 11 can be expressed as follows [36]:

$$E_{F,redox} \propto -59\mathrm{mV/pH} \qquad \textit{Eq. 12}$$

It is important to note, that due to chemical processes at the surface, a similar shift of the band positions of a semiconductor can be measured, if the HO^- are the potential determining ions [37]. This applies in particular to all semiconductor oxides and is confirmed also for Ta_3N_5 [19]. This means, that the important difference between the band positions on the surface and $E_{F,redox}$ remains constant with changes of the pH value.

2.1.3 Interfaces

The photoelectrolysis of water is an interface phenomenon, so that the individual components of a photoelectrochemical cell cannot be regarded separately. Their interaction at the interfaces is important for an understanding of the physics and chemistry of solar water-splitting.

Metal-electrolyte interface

An inert metallic electrode put into contact with an electrolyte has, initially, a Fermi level different from the level of the Fermi level of the electrolyte. This is an unstable situation that triggers the transfer of electrons from the higher to the lower level, accumulating a space charge at either side of the interface. As a consequence, E_F of the metal and $E_{F,redox}$ of the electrolyte move towards each other until they are aligned [36].

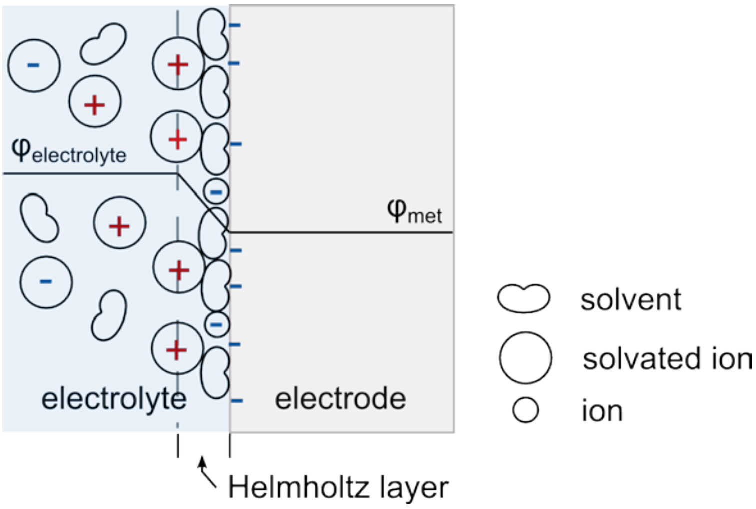

Fig. 6: Simplified schematics of the Helmholtz layer at the surface of a metallic electrode that is formed by adsorbed ions on the surface. Drawn after [36].

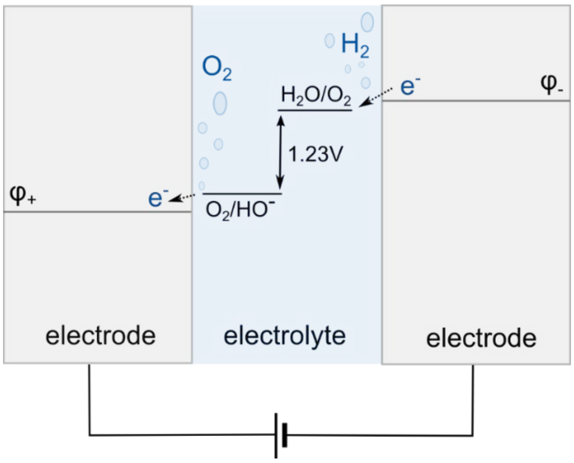

Fig. 7: The production of hydrogen and oxygen by two metal electrodes held at a minimum potential difference of 1.23V.

A simplified view on the accumulated charges in steady state is depicted in Fig. 6. On the electrode, the space charges are located on the surface as the high conductivity of the metal does not sustain electric fields. The electrolyte forms a more extended space charge region of around 0.1nm that is termed Helmholtz layer [37]. It is made up of solvated ions, specifically absorbed ions and oriented solvent molecules.

In order to produce oxygen and hydrogen from an electrolyte, two electrodes are necessary with a minimum differential potential of 1.23eV (Fig. 7). In this way, electrons can transfer from the negatively biased electrode onto the solution while the other electrode accepts electrons from the electrolyte. In general, the thermodynamically necessary energy of 1.23eV is not sufficient as energy must be provided to compensate resistive losses. In addition, for an appreciable kinetics of the process, a higher potential difference must be envisaged and for the photoelectrolysis, an overpotential of 0.8V is estimated to be necessary [38]. This translates into a band gap of $\gtrsim$2.03eV.

Semiconductor-solution interface

Under equilibrium conditions, the physics at the semiconductor/electrolyte interface is similar to that at the metal/electrolyte interface. In contact, the semiconductor Fermi level aligns with the Fermi level of the electrolyte by the transfer of charges. These, again, results in a charge accumulation of opposite polarity on each side of the interface (Fig. 8). Due to the typically much lower charge carrier density in a semiconductor compared to a metal, though, the charges on the semiconductor side extend deeply into the material. With width w_{sc} of this space charge layer typically ranges from 10nm to 1000nm depending on the charge carrier concentration [35].

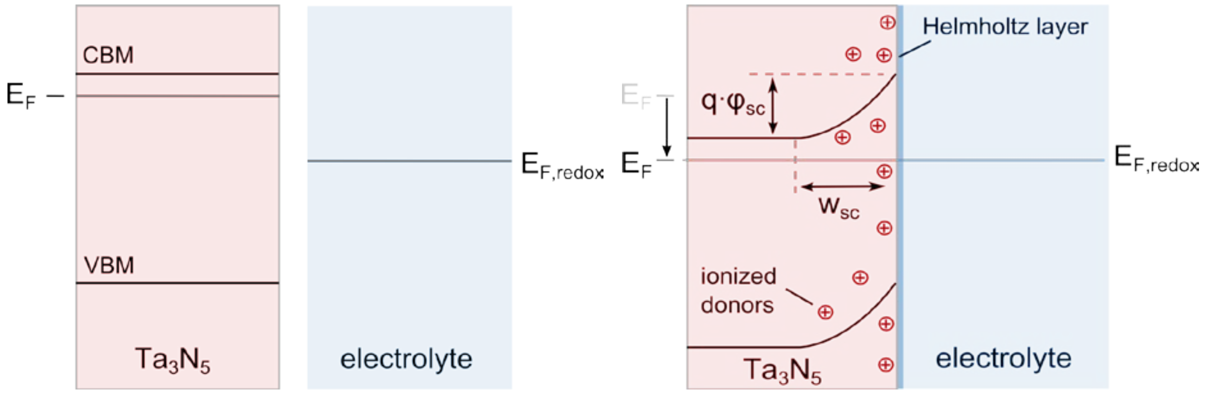

Fig. 8: Left: Ta_3N_5 semiconductor and an electrolyte not in contact. CBM and VBM are the conduction band minimum and the valence band maximum, respectively. Right: Ta_3N_5 and the electrolyte are in contact and in equilibrium.

For an n-type semiconductor such as Ta_3N_5, the Fermi level E_F of the bulk of an unbiased semiconductor not in contact with the solution normally lies above the electrochemical potential of the electrolyte $E_{F,redox}$. The alignment thus forces the built-up of a negative space charge in the Helmholtz layer and a positive space charge on the semiconductor. The resulting electric field, directed from the semiconductor to the electrolyte, bends the valence and conduction bands upwards, creating a Schottky-like barrier. This separates any electron-hole pairs created in that region. Electrons are pushed towards the bulk and holes are attracted towards the interface.

Biasing the semiconductor via an ohmic rear contact, shifts the Fermi level of the semiconductor (Fig. 9). In an ideal case, the band positions at the surface, however, remain fixed [36], so that the band bending is more shallow for a cathodic or forward bias, or steeper for an anodic or reverse bias [35]. The potential at which the bands do not show any bending is termed flat-band potential V_{fb}.

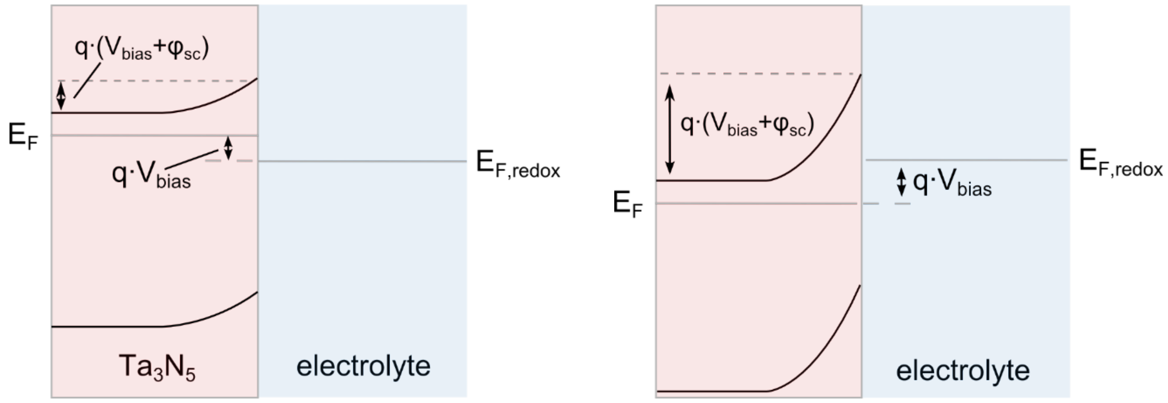

Fig. 9: Left: Cathodic (forward) bias achieved by a applying a negative voltage to the semiconductor. Right: Anodic (reverse) bias from a positive voltage applied to the semiconductor.

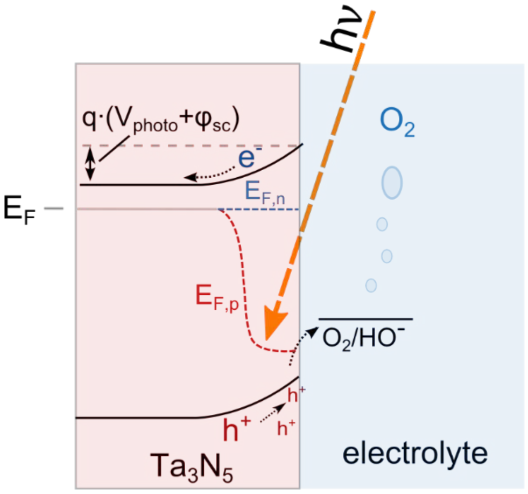

Fig. 10: N-type semiconductor in contact with an electrolyte under illumination.

Illuminating the semiconductor disturbs the equilibrium between holes and electrons and their formerly common Fermi level E_F splits up into separate quasi-Fermi levels for electrons $E_{F,n}$ and holes $E_{F,p}$ (Fig. 10). The charge separation gives rise to a photovoltage V_{photo} that has a similar effect as the forward bias in Fig. 9. Under illumination $E_{F,n}$ moves upwards above the hydrogen evolution potential, so that the transfer of electrons from the counter-electrode onto the electrolyte is thermodynamically favorable [35].

On the other hand, $E_{F,p}$ shifts downwards. The significant shift is due to the drastic relative increase in the number density of holes Δp compared to the number density under dark conditions ($\Delta p >> p_0$). Under illumination therefore, $E_{F,p}$ lies close to the valence band [35] and below the oxygen evolution potential. Holes can then transfer onto the electrolyte to produce oxygen on the semiconductor surface [39]. Under these conditions, water can be electrolyzed according to Fig. 3.

2.1.4 Prerequisites on semiconductors for photoanodes

As can be understood from the discussion above, not all semiconductors can be used as photoanodes. The material requirements are harsh and are listed in the following [39]:

1) Valence and conduction band position

The main prerequisite for a semiconductor electrode to work as a photoanode is that its quasi Fermi levels under illumination straddle the oxygen and hydrogen evolution potentials. In this way the transfer of holes and electrons onto HO^- or H_2O are energetically favored. This implies that the band gap is larger than the minimum energy required to split water, i.e. 1.23eV. In practice, as discussed above, overpotentials are necessary that can amount to up to 0.8V so that a minimum band gap of $\gtrsim$2.03eV is necessary [38].

The straddling condition can be relaxed when using an external bias that allows to lift electrons from the semiconductor to the counter-electrode above the water reduction potential. In this case, at least the quasi-Fermi level of the holes must be below the oxidation potential of HO^-.

While above requirements are critical for the pure functioning of the photoanode, other requirements impact the efficiency of the water splitting [39]:

2) Absorption and band gap
For an efficient charge carrier creation mechanism, the absorption coefficient should be high from the UV range to the band gap. At the same time the band gap should be as small as possible to absorb a large part of the solar spectrum.

3) Charge carrier transport
The efficient transport of charge carriers to the conducting substrate and the semiconductor interface, is necessary to reduce recombination losses. The parameter describing this is the minority carrier diffusion length L_D or the μτ-product. This parameter is affected by both, the quality of the semiconductor and the inherent charge carrier properties of the material.

4) Charge carrier injection
Created charge carriers need to transfer across the semiconductor/electrolyte interface sufficiently fast to avoid their accumulation and recombination on the semiconductor. The oxygen evolution reaction on an n-type semiconductor is usually rate-determining as four charges need to be transferred for the production of one O_2 molecule [36]. Enhancing the charge transfer kinetics can be done by using a co-catalyst such as Co [40], IrO_2 [21] [16], Co-phosphite (Co-Pi) [41] or RuO_2 [42].

5) *Stability*
Finally, the semiconductor needs to be stable in an aqueous solution at elevated pH values. This is typical investigated using XPS [21] to observe changes in the chemical order on the surface of the photoanode. Long-term performance tests, however are rarely found in literature and the studies found are still far away from the 5000h stability tests recommended by leading experts in this field [43].

2.1.5 Semiconductors for photoelectrolysis

Some possible semiconducting materials that fulfill at least the first requirement have been identified in the past. The most promising and most researched being hematite (Fe_2O_3) [44], $BiVO_4$ [45] and WO_3 [46], Cu_2O [47], TaON [48] and Ta_3N_5 [49]. The pace for identifying new materials is taken to a new level by the use of computational screening studies, of which two are published to date.

Castelli et al. [50] screened binary oxides of the perovskites type (ABO_3) and their derivatives such as oxinitrides (ABO_2N), single and bimetal nitrides (A_xN_y) and ($A_xB_yN_z$) and single metal oxinitrides ($A_xO_yN_z$) [50]. A material was selected when it fulfilled each of three selection criteria: a band gap from 1.5 to 3.0eV, a negative formation energy and a straddling of the oxygen and the hydrogen evolution potentials at least for the direct band gap. The yield, however remained poor. From the 5400 materials tested, only 15 fulfilled the requirements from which 6 where already known.

The study of Wu et al. [51] was somewhat less restrictive, as the crystal structure was not limited to perovskites. They tested single metal nitrides (A_xN_y), single metal oxi-nitrides ($A_xO_yN_z$) and bimetal oxinitrides ($A_xB_yO_{z1}N_{z2}$) based on d^0 (Ti^{4+}, Zr^{4+}, Hf^{4+}, V^{5+}, Nb^{5+}, Ta^{5+}, Cr^{6+}, Mo^{6+}, Sc^{3+}, Y^{3+}) and d^{10} (Ga^{3+}, In^{3+}, Ge^{4+}, Sn^{4+}, Sb^{5+}, Bi^{5+}) cations [52]. These atoms where artificially assembled by taking known structures from the Inorganic crystal structure database (ICSD). Similar to the study by Castelli et al [50], materials were selected based on a band gap with a slighly larger range between 1.3eV and 3.6eV. Their phase stability was determined by measuring the difference in formation energy to a known stable phase. And finally, an empirical law was applied to determine the band positions with respect to the oxygen and hydrogen evolution potential. Similar to the study above, the yield was poor. From the 68 binary nitrides, the 1503 ternary oxinitrides and the 1377 quarterny oxinitrides, in total 27 candidates were identified, 11 of them were already known and among them was Ta_3N_5.

It becomes clear, that the requirements for a material to work as a photoanode are harsh and eliminate most semiconductors known to date. This becomes even more pronounced when considering the rather loose criteria applied to select materials with large ranges of allowed parameter values such as the band gap. As all parameters retrieved for those unknown phases are based on simple (semi-)empirical models, the ranges need to allow for uncertainties, though. It is thus clear that the already small yield from those studies may become even smaller when measurements on experimentally prepared materials are known.

2.1.6 Efficiencies and benchmarks

Different definitions to benchmark the solar water-splitting efficiency are used to compare device performances. The most general form is the solar-to-hydrogen efficiency which is simply the ratio between the energy of the hydrogen gas that is produced per time ($j_{photo}V_{redox}$) and the incoming solar power P_{light}. The first still needs to be corrected by the supplementary power input from a potential bias voltage with respect to the reversible hydrogen electrode RHE ($j_{photo}V_{bias,\ RHE}$).

$$\eta_{STH} = \frac{j_{photo}\left(V_{redox} - V_{bias,RHE}\right)}{P_{light}} \qquad \textit{Eq. 13}$$

where j_{photo} is the photocurrent, V_{redox} is the minimum redox potential to split water, V_{bias} is the bias voltage applied between the reference and the semiconducting electrode. V_{redox} can be taken as 1.23eV, corresponding to the Gibbs free energy change of 238kJ/mol. From Eq. 13, theoretical limits for solar-water-splitting as a function of the band gap of a material can be calculated (Fig. 11). Taking the Ta_3N_5 semiconductor with a band gap of 2.1eV, i.e. providing for an overpotential of roughly 0.8V, results in a theoretical maximum solar-to-hydrogen efficiency of 15.9% [53].

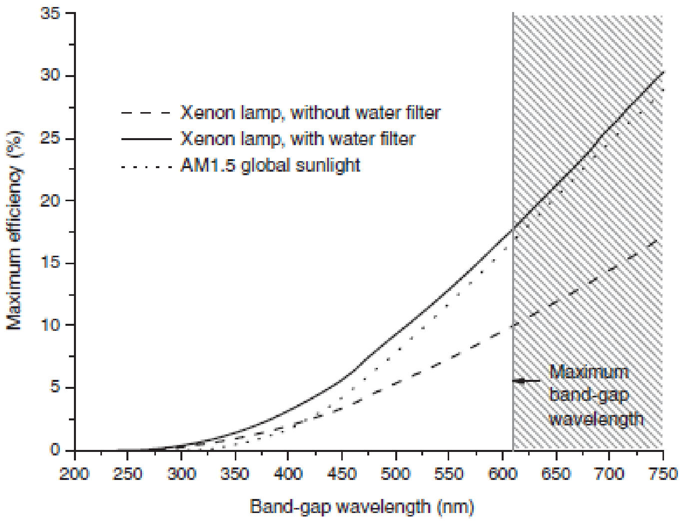

Fig. 11: Theoretical limits for solar water splitting as a function of the band gap. The optimum band gap is determined to be around 2eV. From [38].

To take the band gap dependency on the efficiency out of the equation, the incident-photon-to-current efficiency is used. It gives the efficiency of a photon to create a charge carrier that contributes to the photocurrent, i.e. recombined charge carriers are not take into account:

$$IPCE(\lambda) = \frac{hc}{\lambda q}\frac{j_{photo}(\lambda)}{P_{light}(\lambda)}, \quad \text{Eq. 14}$$

where h is Planck’s constant, c is the speed of light, λ is the wavelength and q the elementary charge.

Some benchmarks are published and listed in Table 4 for Ta_3N_5 photoanodes. In general, the overall efficiency still remains small with a solar-to-hydrogen efficiency barely exceeding 1%. Using different configurations than the single semiconductor photoanode described above, higher efficiencies can be reached. However, this comes at the cost of added complexity. One example is the use of a heterojunction tandem absorber combined with a Rh-functionalized, $Al_xIn_{1-x}P$ passivated surface and an RuO_2 counter-electrode that holds the current record in STH efficiency for a bias-free photoelectrolysis of 14% [15].

Table 1: Published benchmarks for Ta_3N_5-based photoanodes.

Photoanode	η_{STH}, %	**Ref.**
Ta_3N_5 nanorods with IrO_2 co-catalyst	0.5%	[16] [17]
Ba-doped Ta_3N_5 nanorods with Co-Pi co-catalyst	1.56% @ 0.87V vs. RHE	[17]
Ba-doped Ta_3N_5 nanorods without cocatalyst	0.89% @ 0.93V vs. RHE	[17]
Ta_3N_5 theoretical limit	15.9%	[53]

2.2 The Ta_3N_5 crystalline phase

2.2.1 Crystalline phases of the Ta-O-N ternary system

Tantalum belongs to the transition metals, which are known for their variety of oxidation states [54] and the stability of their compounds over large non-stoichiometric ratios [55]. Of interest for this thesis are in particular its compounds formed with nitrogen (Chapter 2.2.1.1). But as Ta_3N_5 is only synthesized so far by incorporating oxygen into the lattice, some important oxygen-containing phases are discussed as well (Chapter 2.2.1.10). Finally, formation enthalpies of some phases are discussed as they offer valuable clues on the stability of certain phases (Chapter 2.2.1.3).

2.2.1.1 The Ta-N binary system

The Ta-N system knows 9 crystalline phases from the pure tantalum phase and the solid solution Ta(N) up to the strongly nitrided Ta_3N_5 phase (Table 2). Most of them are metallic phases without interest for this thesis. It is however, instructive to follow the changes in chemistry, structure and the optical and electronic properties when successively adding nitrogen to an initially pure Ta crystal. Also, it is important to define the phases, as names can change between publications. The δ-TaN phase in [56], for example, is a hexagonal phase with lattice parameters a=0.293nm and c=0.289nm and of WC-type, while in another publication, the δ-TaN phase has a rocksalt structure with lattice parameter a=0.43nm [57]. The definition of phases used in this thesis is based on the PhD thesis by Ganin from 2005 [58] and is complemented by the Ta_2N_3 phase [59].

Pure Ta crystallizes in the body-centered cubic (bcc) structure and can accomodate interstitial N up to a 4at.% to form the solid solution Ta(N) [60]. At higher nitrogen at.%, the Ta atoms arrange in a closed-packed hexagonal structure to accommodate N in every second octahedral hole [56]. This is a typical phase transition that can be observed in many transition metal nitrides and also carbides [56]. In the Ta-N system, the homogeneity region of this phase is centered around 30at.% (Fig. 12) and is termed β-Ta_2N.

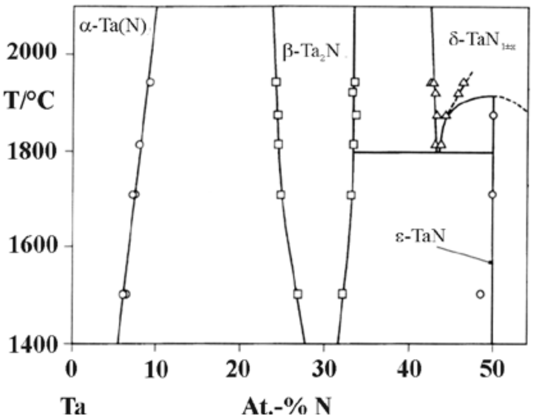

Fig. 12: Ta-N phase diagram (from [58] [61]).

The TaN phase exists in three polymorphs, the rocksalt δ-TaN, the hexagonal ε-TaN (CoSn-type) and the hexagonal θ-TaN (WC-type). Latter is the most stable structure, followed by δ-TaN and ε-TaN being the least stable structure judging from DFT calculations [62].

δ-TaN is a high-pressure, high-temperature phase that can accommodate excess nitrogen far beyond its stoichiometry. TaN_x phases were prepared with x going up to 1.66 [63] which exceeds even the N at.% of Ta_3N_5. The nonstoichiometry in δ-TaN is accompanied by Ta vacancies, that, with increasing concentration, reduce the electronic density of states (DOS) around the Fermi level [29].

Table 2: Summary of known stoichiometric phases of the binary system Ta-N. Phases and reference were taken from [58] *and complemented. For some phases, alternative structures exist, that are not mentioned in this table. The bct-TaN phase is not listed in the Inorganic crystal structure database (ICDS), but was found by magnetron sputtering by two different groups* [55] [64] *and was later identified as* Ta_2N_3 [58].

phase	chemical formula	crystal structure and lattice constants (nm)	space group	ref.
Ta	Ta	bcc (W-type)	$Im\bar{3}m$	[56]
		a = 0.3311		
α-Ta(N)	$TaN_{0.0}$ -$TaN_{0.04}$	bcc, solid solution	$Im\bar{3}m$	[60]
		a = 0.3315		
β -Ta(N)	$TaN_{0.05}$	bcc, α phase with 3x3x3 superstructure	$Im\bar{3}m$	[56]
		a = 10.11 (3x3.369)		
β-Ta_2N		hexagonal	$P\bar{3}m1$	
(γ-TaN)	$TaN_{0.41}$	a = 0.3041; c = 0.4907		[56]
	$TaN_{0.5}$	a = 0.3048; c = 0.4919		[60]
δ-TaN		fcc (NaCl type)	$Fm\bar{3}m$	
	$TaN_{0.91}$	a = 0.4337		[57]
	$TaN_{0.99}$	a = 0.4336		[65]
	TaN_x	a = 0.498 to 5.047		[55]
ε-TaN		hex. (CoSn-type)	$P6/mmm$	
	$TaN_{1.00}$	a = 0.5185; c = 0.2908		[56]
	$TaN_{1.00}$	a = 0.5191, c = 0.2911		[60]
	$TaN_{1.00}$	a = 0.5188; c = 0.2903		[66]
θ-TaN		hex. (WC-type)	$P6m2$	
	$TaN_{1.00}$	a = 0.2936; c = 0.2885		[67]
	$TaN_{1.08}$	a = 0.2938; c = 0.2868		[57]
Ta_2N_3,	Ta_2N_3	cubic (La_2O_3-type)	$Ia\bar{3}$	[59]
(bct-TaN)		a = 0.98		[55]
				[64]
Ta_5N_6	Ta_5N_6	hexagonal	$P6_3mcm$	
		a = 0.5175; c = 1.0307		[55]
Ta_4N_5	Ta_4N_5	tetragonal (defective NaCl type)	$I4/m$	
		a = 0.6835; c = 0.4272		
				[66]
Ta_3N_5	Ta_3N_5	orthorhombic (Fe_2TiO_5-type)	$CmCm$	
		a = 0.38862		
		b = 1.02118		[68]
		c = 1.02624		

This can be observed experimentally by an increase of resistivity with increasing the N at.% [69]. A clear border for this metal-to-insulator transition is given in [29], which states that films of $Ta_{1.12}N$ up to $Ta_{0.74}N$ are metallic and barely metallic respectively while $Ta_{0.66}N$ is an insulator. Electron counting for a $Ta_{0.6}N$ structure confirms this: In total, 40 valence electrons from the atoms (5 valence electron from 3 Ta atoms plus 5 valence electrons from 5 N atoms) need to be distributed over the bands of the $Ta_{0.6}N$ structure. Its valence bands are formed by the s- and p-orbitals of the nitrogen atoms and can thus accommodate 40electrons (2 electrons per s-orbital plus 6 per p-orbital for each of the 5 N atoms). Hence, all valence electrons of the atoms can be accommodated in the valence band of the structure. The conduction band therefore remains empty and the material is an insulator [69].

Four higher ordered nitrides of the Ta-N exists, that are, in order of increasing nitrogen at.%, the hexagonal Ta_5N_6, tetragonal Ta_4N_5 and the orthorhombic Ta_3N_5 phase. Despite their elevated content of nitrogen, only the highest nitride, Ta_3N_5 is a semiconductor, all other phases being metallic [62]. As Ta_3N_5 and $Ta_{0.6}N$ (see above) contain the same at.% of N, the same electron counting example from above applies here. The electronic, optical and electrochemical properties of Ta_3N_5 are discussed in more detail below.

2.2.1.2 Important phases of the ternary Ta-O-N system

Ta_3N_5 has only been synthesized so far by the incorporation of oxygen into the lattice, the reason for which will be discussed later (Section 5.1). Therefore, some important phases containing oxygen are introduced here in addition to those of the Ta-N system summarized in Table 2.

Of importance here is the highly stable orthorhombic Ta_2O_5 phase (Table 3). It has a large band-gap of 3.9eV which is responsible for its transparent appearance [19].

Another important phase is the TaON phase. Initially, this chemical formula was believed to have two polymorphs termed α-TaON and β-TaON (Table 3). Recent investigations suggest, however, that the α-TaON phase does not exist and is recommended to be removed from crystallographic databases [70].

TaON belongs to the large group of transition metal oxynitrides. Of particular interest for this class of material is their band gap that can be tuned by changing the O/N ratio. In these materials the conduction band minimum is formed by the empty metal d orbitals while the valence band maximum is formed by the 2p oxygen or nitrogen orbitals. As the nitrogen orbitals are shallower than the oxygen ones, a substitution of oxygen by nitrogen can decrease the band gap, thus changing the color of the material [52]. The same reasoning applies for explaining the much smaller band gap of Ta_3N_5 compared to that of Ta_2O_5. Fig. 13 schematically illustrates the formation of valence and conduction bands around the band gap.

Table 3: Summary of important phases from the Ta-O-N ternary system.

phase	chemical formula	crystal structure, lattice constants (nm)	space group	ref.
~~α-TaON~~	~~TaON~~	likely an erroneous entry in literature, see [71]		
β-TaON	TaON	Monoclinic (baddeleyite) a = 0.494941 b = 0.501662 c = 0.516430	$P2_1/C_4$	[72]
Ta_2O_5	Ta_2O_5	Orthorombic a=0.6198 b=4.290 c=0.3888	Pccm	[73]

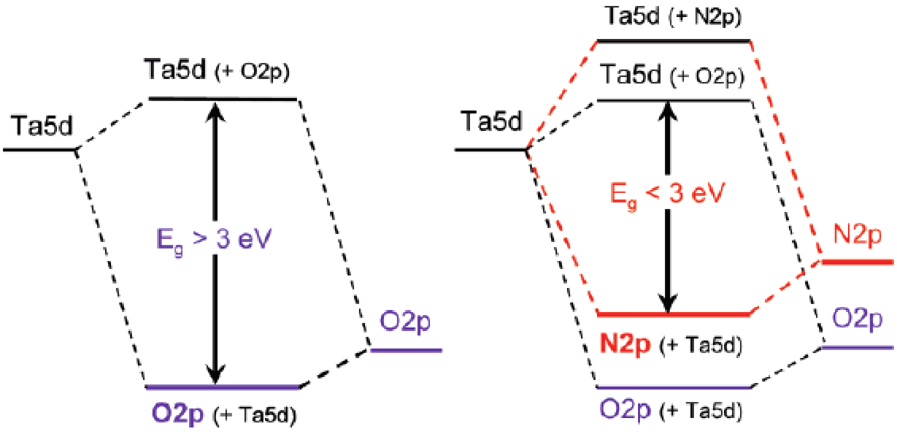

Fig. 13: The formation of band structures by bonding of a transition metal to oxygen and nitrogen. The top of the valence band are formed by O 2p orbitals while the bottom of the conduction band is formed by empty transition metal 5d orbitals. The schematics illustrate this at the example of the pure oxide $NaTaO_3$ (left) and the oxynitride $BaTaO_2N$. From [52].

2.2.1.3 Formation enthalpies of some selected phases from the Ta-O-N ternary system

The knowledge of the stability of a phase is important for its synthesis, as stable materials are usually easier to synthesize than metastable materials. The energetics of the binary Ta-N system is shown by help of a convex hull plot in Fig. 14. It is a scatter plot of formation enthalpy vs. anion molar fraction and by connecting the structures having the lowest (most negative) formation enthalpies the stable phases can be distinguished from the metastable ones [74]. It can be seen from this plot, that the structures Ta_2N and Ta_5N_6 and Ta_3N_5 are stable, while the phases Ta_4N_5, ε-TaN and δ-TaN are metastable. This result was confirmed independently by a different group [75].

An interesting feature on the convex hull plot in Fig. 14 is the evolution of formation enthalpy for the non-stoichiometric δ-TaN phase (TaN cubic, $TaN_{1.13}$, $TaN_{1.33}$). As the stoichiometry approaches the Ta_3N_5 stoichiometry, the formation enthalpy of the δ-TaN_x phase diminishes. The data point at which the two phases have an identical stoichiometry (δ-$TaN_{1.67}$ vs. Ta_3N_5) is not shown in this study. The question which of the two phases has the lower formation enthalpy at this point, can therefore not be answered.

Values of experimentally measured formation enthalpy for some phases of the ternary Ta-O-N system are summarized in Table 4. It can be seen that, Ta_3N_5 has, as in Fig. 14, a very low formation enthalpy of -850 kJ/mol. Calculations show in addition, that the substitution of N by O can lower the formation enthalpy even more [76] [77] [78].

Table 4: Experimentally measured formation enthalpies of selected phases from the Ta-O-N system measured under standard conditions 298.15 K, 0.1MPa [79].

phase	**formation enthalpie ΔH (kJ/mol)**	**ref.**
Ta	0.0 (by definition)	
Ta_3N_5	-849.7 ± 11.7	[80]
TaON	-635.51 ± 4.27	[76]
Ta_2O_5	-2045.98 ± 4.18	[81]

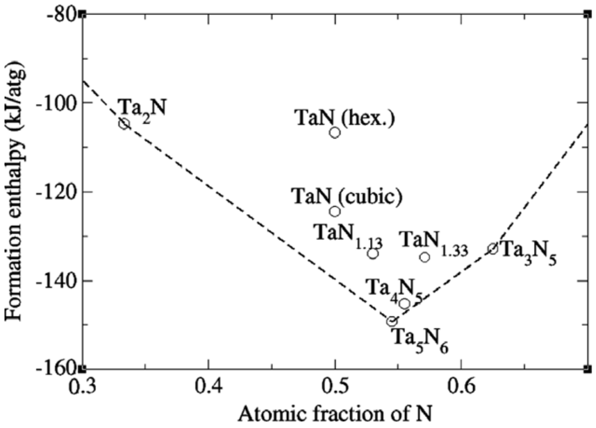

Fig. 14: Formation enthalpies as calculated by DFT for some phases of the Ta-N system. The hexagonal TaN phase is the ε-TaN phase in Table 2 and the nonstoichiometric phases $TaN_{1.13}$ *and* $TaN_{1.33}$ *are all derived from the δ-TaN phase (from [82]).*

2.2.2 The crystalline Ta_3N_5 phase

This subchapter serves to summarize known properties of the Ta_3N_5 phase that are relevant for the water splitting process: structure, optical properties (band gap, dielectric function), electrical properties (carrier mobility) and electrochemical properties (band position, stability).

2.2.2.1 Ta_3N_5 structure

Ta_3N_5 crystallizes in an orthorhombic structure with the space group $CmCm$ (Fig. 15). In this crystal, Ta is 6-fold coordinated by N and the TaN_6 octahedra are irregularly oriented. Each N is three or four-fold Ta coordinated and this structure allows an increased accommodation of N compared to rocksalt δ-TaN that has oriented TaN_6 octahedra, with each N being 6-fold Ta coordinated (Fig. 15) [18].

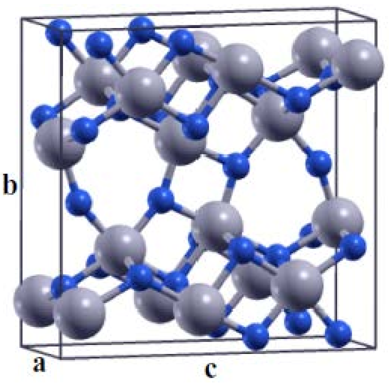

Fig. 15: Ta_3N_5 *crystal: unit cell. The grey spheres indicate the position of the Ta atoms, the blue ones the positions of the N atoms. From [18].*

There is still some confusion in the literature, whether the structure is orthorhombic as stated in [83] or monoclinic as proposed in [66] (cf. e.g. [18] [20] for references to the orthorhombic structure and e.g. [84] [40] for reference to the monoclinic structure). In both references, the lattice constants are determined to be a = c = 1.0264nm compared to b ≈ c ≈ 1.03nm and b = 0.3893nm compared to a = 0.37nm for the orthorhombic structure and the monoclinic one, respectively. The determining parameter is thus the angle which is stated to be β=90° in the case of the orthorhombic interpretation and β≈90° in the case of the monoclinic interpretation. The proposed structures are thus at least very close to each other. The latest experimental results on the structure of Ta_3N_5 is obtained by Brese et al. [68], using neutron diffraction. They come to the conclusion that both structures are too close to each other to discern by their experiemnt, but decide that the orthorhombic structure is likely the correct one. In this thesis, the structure refined by Brese et al., referenced under the powder diffraction file (PDF) 01-079-1533, is thus used.

2.2.2.2 Ta_3N_5 band gap and dielectric function

Ta_3N_5 is an indirect semiconductor as can be seen from the band structure in Fig. 16. Its direct band gap is often stated to lie around 2.1eV with an indirect band gap below that value [18], possible around 1.9eV [85]. The optical properties that result from such a band structure can be calculated from the complex dielectric function. Two measurements exits to date using ellipsometry.

The first one was published by Langereis et al. [86]. They deposited a thin film of around 50nm of Ta_3N_5 by atomic layer deposition (ALD) and measured the dielectric constant by ellipsometry in-situ. The second study, published by Morbec et al. [18], was a computational study that was validated using experiments. The sample was prepared by depositing 29nm of Ta by electron beam evaporation. The film was then oxidized at 700°C under a flow of O_2 for 1h and subsequently nitride at 850°C in NH_3 for 8h. The results from both studies are plotted in Fig. 16.

A comparison reveals that both results do not match very well. Some difference can be explained by the different preparation methods as well as that the measurement of Langereis et al. was done in-situ [86]. As the dielectric function in the measurement of Morbec et al. reveals more features, it likely is more accurate while the features in Langereis et al. can be imagined to be smeared out.

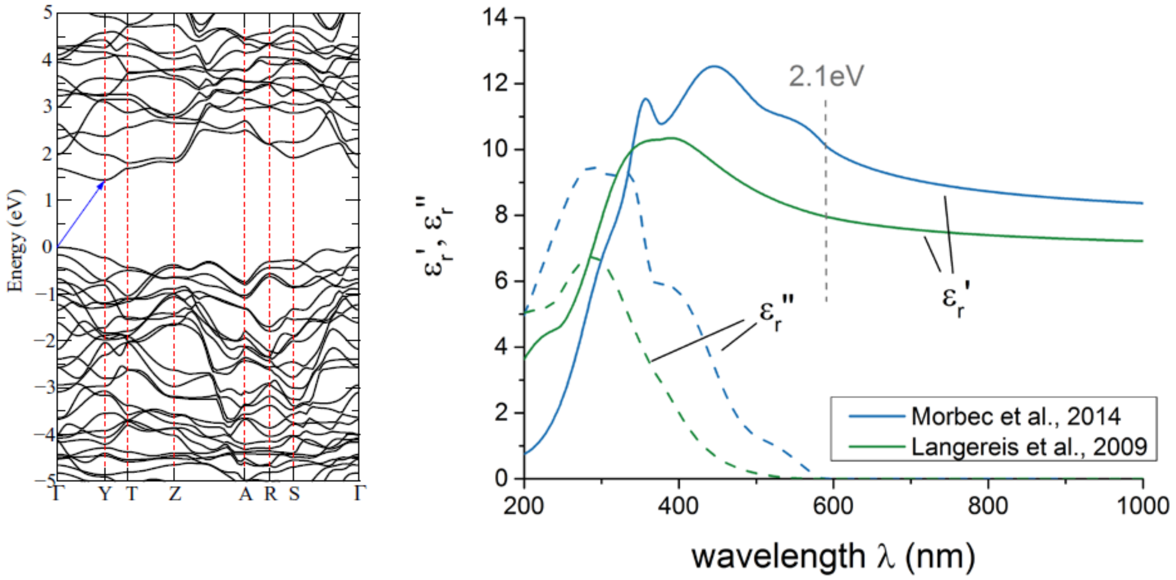

Fig. 16: Left: Band diagram of Ta_3N_5 calculated by DFT. The blue arrow indicates the indirect band gap. It is smaller than the usually stated 2.1eV which is an intrinsic shortcoming of conventional DFT calculations. From [18]. Right: Complex dielectric function measured by Langereis et al. [86] and Morbec et al. [18]. The two vertical line at 2.1eV indicates the position of the direct band gap.

Using some simple conversions between the dielectric function and the refractive index N = n + jk (cf. Section 3.4), the absorption coefficient $\alpha = 4\pi k(\lambda)/\lambda$ can be calculated. Its inverse is the absorption length, which is the thickness of an absorbing medium that decreases the initial intensity I_0 of an incident beam to $1/3 \approx 37\%$. Both, the absorption coefficient and its absorption length are plotted in Fig. 17. The figures show that despite the band gap of 2.1eV, a considerable absorption for thin films of around 100nm only occurs for photons having energies greater than around 2.7eV. Below that, the film needs to considerably thicker by a factor of 10 to increase absorption between 2.7eV and 2.2eV.

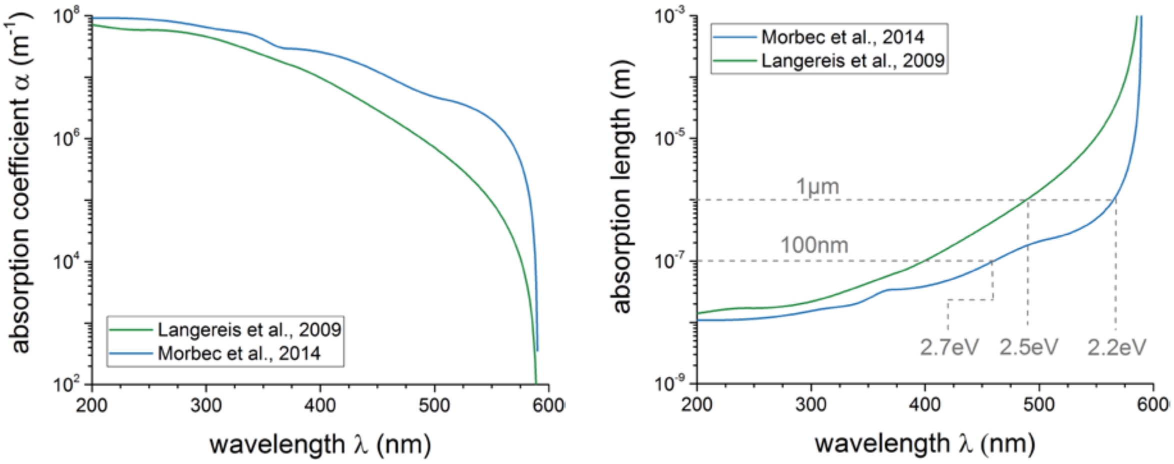

Fig. 17 : Absorption coefficient α and absorption length for the measured dielectric function by Morbec et al. [18] and Langereis et al. [86].

2.2.2.3 Ta_3N_5 charge carrier mobility

The absorption is naturally in competition with the electronic properties as the first demands a film as thick as possible and the latter demands it to be as thin as possible to avoid recombination of excited charge carriers. The parameter to describe the charge carrier dynamics is the mobility-lifetime $\mu\tau$ product that describes, how fast a particle propagates and on what timescales it recombines. Using the $\mu\tau$-product of the minority carriers, the minority carrier diffusion length L_D can be calculated [87].

$$L_D = \sqrt{\frac{k_B T}{q}(\mu\tau)_{minority}}, \qquad \textit{Eq. 15}$$

where k_B is the Boltzmann constant, T the temperature and q the elementary charge.

Theoretical studies by Morbec et al. [18] and Nurlaela et al. [88] both predict strong anisotropies in Ta_3N_5 with some directions having large effective masses for holes and electrons (Table 5). They suggest this poor bulk charge transport properties to be the reason for the low photocurrents observed on Ta_3N_5. More recent experimental measurements, show however, while the mobility is low, the carrier lifetime is comparable to that of Si (~ ms) which results in a long diffusion length [47].

Table 5: Hole and electron effective masses for Ta3N5 in comparison with those of monocrystalline Si.

phase	type of study	holes m_h^*/m_0	electrons m_e^*/m_0	ref.
Ta_3N_5	DFT	0.27-3.56	0.23-2.70	[18]
Ta_3N_5	DFT	0.85-3.38	0.60-1.94	[88]
		for comparison:		
monocrystalline Si	n/a	0.81	1.182	[23]

2.2.2.4 Ta_3N_5 band positions

The band positions of the Ta_3N_5 semiconductor have been measured by an electrochemical (EC) method and by ultraviolet photoelectron spectroscopy (UPS) for a sample prepared by ammonolysis by Chun et al. [19].

Both measurements, conducted by the same authors, result in the same band position. The valence band was found to be at -6.0eV and the conduction band at -4.0eV measured on the absolute vacuum scale at a pH value of 0 [19]. As the oxygen and hydrogen evolution potentials are at -4,5eV and -5,73eV at pH = 0, the measurements confirm that the bands actually straddle the oxygen and hydrogen evolution potential. In the same paper, it is furthermore confirmed, that the band positions change with pH at the same rate as that of the electrolyte (60mV/pH), so that the relative positioning of the bands with respect to the oxygen and hydrogen evolution potential remains constant at all pH values.

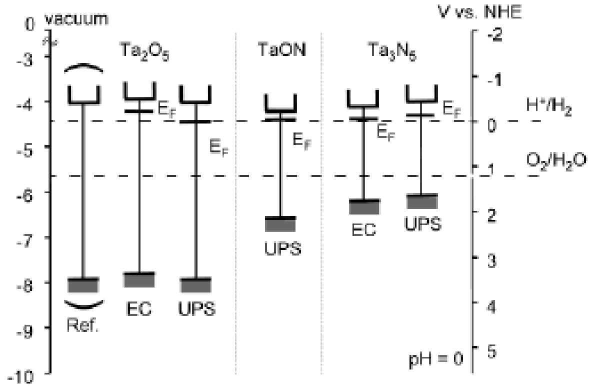

Fig. 18: Band positions of Ta_2O_5, TaON and Ta_3N_5 as measured by ultraviolet photoelectron spectroscopy (UPS) and electrochemically (EC). From [19].

As these are experimental measurements, the prepared Ta_3N_5 photoanode likely contains defects and impurities. It is actually those deviations from the ideal structure that places the bands into the right position as shown by DFT calculations by Harb et al. [78] [89]. They show that the bands of an ideal Ta_3N_5 structure lie much higher than depicted in Fig. 18 so that the valence band lies above the oxygen evolution potential. Only by oxygen incorporation into the lattice ($Ta_{2.83}N_{4.16}O_{0.83}$), the bands shift sufficiently downwards so that they bracket the hydrogen *and* oxygen evolution potential [78]. A different paper by the same author shows that the same downward shift of bands can also be induced by Ta and/or N vacancies [89].

2.2.2.5 Ta_3N_5 stability in solar water splitting experiments

The stability of Ta_3N_5 in photoelectrolysis experiments and its degradation mechanisms have not been systematically investigated yet. The studies mentioned in literature resort to the observation of the photocurrent at a fixed bias voltage or the change of N/O surface atomic ratios by XPS measured before and after the photoelectrolysis experiments (Table 6). All authors agree that the photocurrent diminishes over a certain period of time and that at the same time the N/O ratio decreases. Yokohama et al. [21] attribute this to a decomposition of the photoanode, while Hara et al. attribute this to the attachment of hydroxyl groups that function as a protective layer against surface oxidation [90]. The use of a co-catalyst (IrO_2 [21], Co [40]) seems to at least prolong the lifetime of a photoanode in photoelectrochemical experiments.

As the stability of the films is likely influenced by the preparation method, the crystallinity of the films, the film composition, the electrolyte, the pH and the bias voltage, a conclusive statement on the stability of Ta_3N_5 in photoelectrolytic experiments is not possible. The answer to this question requires long-term tests over weeks, months and years. Leading experts in the field of photoelectrolysis recommend long-term stability tests of 5000h [43].

Table 6: Selected studies for testing the stability of Ta_3N_5 films in photoelectrochemical measurements.

photoanode and preparation method	**test**	**interpretation**	**ref.**
(IrO_2/)Ta_3N_5 by sputtering with post-annealing in NH_3	Photoelectrolysis at 0.5V vs. Ag/AgCl for 60 min yield a strong reduction of photocurrent. The use of IrO_2 as a co-catalyst increases the photocurrent by a factor of 30 but a decrease over 60min is still observable. XPS confirms these measurements as the N/O ratio is reduced in both cases.	Decomposition of the photoanode due to self-oxidation. The use of a co-catalyst did not prevent the degradation.	[21]
Ta_3N_5 by ammonolysis	Storage for 10 days in air resulted in no reduction of the surface atomic ratio N/O measured by XPS. Storage for 20 days in distilled water reduced the surface atomic ratio N/O from 5.0 to 0.9.	Essentially stable in distilled water due to the formation of a protective layer of hydroxyl groups.	[90]
(Co/)Ta_3N_5	Constant current density on a Co/Ta_3N_5 photoanode at 1.23V vs. RHE over 20min while the naked Ta_3N_5 showed a reducing current density already over 6min.	Increase in stability by coating the surface of the photoanode by 10nm of Co.	[40]
(Co-Pi)//Ta_3N_5 nanorods	Constant current density for 20min at 1.0V vs. RHE for Co-Phosphite (Co-Pi) co-catalyst while rapid decrease in current density for bare Ta_3N_5 nanorods.	Stable photoanode by using Co-Pi co-catalyst.	[16]

2.2.2.6 Surface morphology

The increase in surface area by nanostructuring is an important measure to increase the performance of photoanodes. One example is to grow nanorods of Ta_3N_5 as published by Li et al. [16]. They have a diameter of 60nm and an increase in IPCE efficiency is clearly visible (Fig. 19). The choice of preparation method for this thesis, namely magnetron sputtering, naturally limits the possibilities of nanostructuring the surface, however, modifications of surface morphologies within boundaries are still possible (see Section 2.3.2.2).

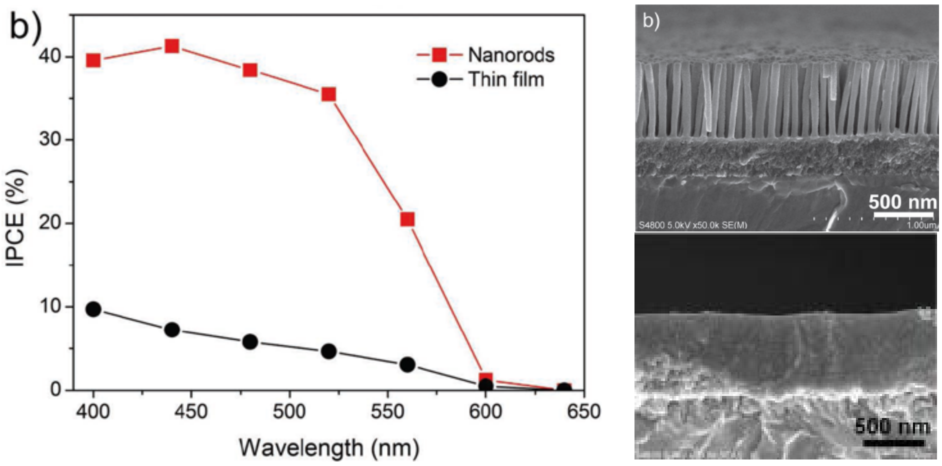

Fig. 19: The increase in performance due to an increase in surface morphology by using nanorods instead of thin films. From [16].

2.2.3 Conventional synthesis of Ta_3N_5

Ta_3N_5 is mostly prepared in a two-step process, and while many variations exist for each of the two steps, the basic principle remains the same. Some of the preparation methods are summarized in Table 7. The first step is to prepare Ta-O by the oxidation of metallic Ta either in the form of a powder or a thin film. Subsequent annealing at high temperature in a nitrogen-containing gas then yields the Ta_3N_5 phase. Tries to prepare Ta_3N_5 directly by ammonolysis of pure Ta, i.e. without preparing the intermediate step of oxidizing the Ta first, seems not to be possible [30] [91] (see also Chapter 5.1).

Table 7: Conventional synthesis of Ta_3N_5.

preparation method	ref.
oxidation of Ta powder, then nitridation in NH_3 at 850°C for 15h	[90]
Ta film prepared by sputtering, then oxidation at 550°C in air and nitridation in NH_3 at 900°C	[91]
oxidation of a Ta foil at 550°C in air, then nitridation in NH_3 at 850°C for 4h	[30]

This conventional preparation method comes with certain disadvantages. The strong oxidation and nitridation at high temperatures result in a strong expansion and contraction of the sample during the process due to the large differences in density. While Ta has a density of 16.65g/cm^3 [92], Ta_2O_5 has a density of 8.2g/cm^3 [93] and Ta_3N_5 a density of 9.85 g/cm^3 [94]. This is reported to result in cracks and delamination [21] [30]. Thus, already on a macroscopic scale, the films have defects.

Furthermore, despite the ammonolysis for long times at elevated temperatures (Table 7), the films are known to contain oxygen [17] and tries to reduce the oxygen content by increasing the ammonolysis time resulted in nitrogen vacancies [95] [96]. Thus, it is difficult to control the oxygen content in the films.

An important parameter for photoanodes is the thickness because a good compromise between absorption and charge carrier recombination is necessary [97]. However, it is difficult to control the thickness of the Ta_3N_5 layer by this preparation method. Some publications mention that the nitrided Ta_3N_5 forms only in the oxidized surface of the Ta foil, so that the time of oxidation determines the final Ta_3N_5 thickness [30] [91]. However, a smooth transition in oxygen and/or nitrogen at.% can be expected rather than a sharp interface between the photoactive Ta_3N_5 film and the electron-collecting metal Ta foil. This can cause resistive losses as Ta suboxides and -nitrides have a lower conductance than pure Ta.

2.3 Magnetron sputtering

Magnetron sputtering is a physical vapor deposition (PVD) technique to coat thin films onto substrates. It is used in academic laboratories, but is also widely used in industry due to its comparably high deposition rates. In the following, its physical and technical basics are discussed to the point which is needed to understand the results of this thesis. A broader discussion on magnetron sputtering can be found in literature [98] [99]. The specific deposition system used for this thesis is detailed in Section 3.1. More details on discharge physics can be found in Chapman [98] and Lieberman and Lichtenberg [99], where most of the examples from this section are taken from.

2.3.1 Electrical gas discharges

In the following, the different discharge regimes are discussed in order to define and characterize a glow discharge.

2.3.1.1 Discharge regimes

A magnetron discharge is derived from a classical glow discharge that is distinct from other discharges, historically by its appearance, but today, more quantitatively by its current-voltage characteristics.

Two flat electrodes in a gas-filled tube at low pressure are electrically insulated even when low potentials are applied to the electrodes. In this regime (A to B in Fig. 20), cosmic rays can cause some ionization of the gas that allows a small current to pass. With increasing potential, the current-voltage characteristic flattens until the breakdown voltage V_b is reached where the discharge enters into the Townsend regime (region B-D). In this regime electrons gain sufficient energy before a collision, that a colliding atom can be ionized according to Eq. 16. This increases the number of electrons with each collision step, creating an ionization cascade, which is the characteristic phenomena in a Townsend discharge.

$$A + e^{-}\left(E_{kin} > E_{ion,A}\right) \rightarrow A^{+} + 2e^{-} \qquad \textit{Eq. 16}$$

The minimum voltage V_B under which this cascade can occur is given by Paschen’s law that describes the interplay between the two most fundamental processes in this regime: the kinetic energy gain of electrons in between collisions and the production of electrons using this energy, to sustain the discharge. The first is a function of the electric field and directly correlates to the mean free path λ_{mfp} while latter is proportional to $1/\lambda_{mfp}$. An optimum for V_B thus exist that is, in Paschen’s law given as a function of the macroscopic parameter pressure p, that correlates with the mean free path, and the inter-electrode distance d, that changes the electric field at a constant [100].

$$V_b = \frac{BPd}{\ln(Apd) + \ln(ln\left[\frac{1}{\gamma} + 1\right])}, \qquad \textit{Eq. 17}$$

where A and B are constants depending on the gas and γ is the secondary electron emission yield.

By increasing the current, the discharge drifts into the glow discharge regime. Here, secondary electrons are emitted from the cathode by impinging ions. They are then accelerated in the sheath in front of the cathode (see below). This presents a supplementary source of electrons that are injected into the plasma at a high energy. As a consequence, the plasma becomes more conductive compared to the Townsend regime, as evidenced by the falling I-V characteristic between the two regimes. The valley that is ultimately reached at the minimum (region E to F) is the normal glow discharge regime in which magnetrons work.

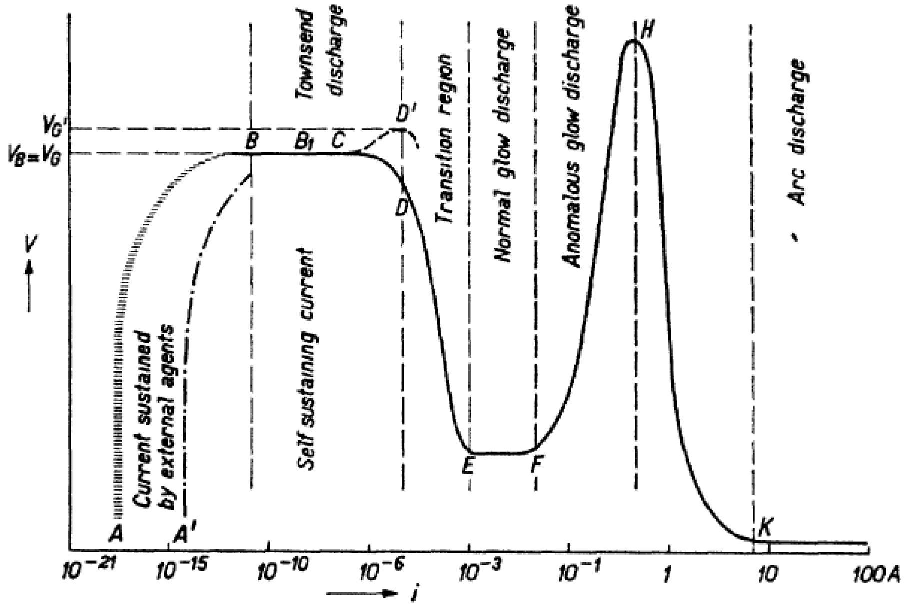

Fig. 20: Nomenclature of different discharges regimes on the voltage-current plane [101].

2.3.1.2 The glow discharge tube

A typical discharge tube consists of an anode and a cathode with a gas-filled space in between at typical pressures between 1.3Pa and 13kPa [98]. For igniting the discharge, the breakdown voltage V_B must be applied which results in an ionization cascade like in the Townsend discharge. By allowing the current to increase, the discharge drifts into a glow discharge at which the applied voltage can be reduced to keep the operation point in the glow discharge valley (region E-F in Fig. 20).

A plasma is a partially ionized gas that contains equal numbers of electrons and ions (quasi-neutrality principle) [98]. As such, plasmas in general do not support the existence of electric fields as any electric field results in the displacement of charges to cancel this electric field. So while before igniting the discharge, a constant electric field is present throughout the inter-electrode space, it is strongly reduced in most parts of the discharge and has a complex shape in the presence of a plasma. Linked to the electric field distribution is the typical appearance of a glow discharge with its distinct zones that are shortly discussed in the following:

Cathode dark space or cathode sheath

One of the few exceptions in plasmas, in which electric fields exist and quasi-neutrality does not hold, is the sheath region in front of the cathode where most of the potential applied between the electrodes falls off. It is a direct consequence of the strong negative potential applied at the cathode that repulses the electrons and attracts ions.

But ions alone are not able to carry the current through the cathode sheath which can be shown by considering current continuity between the different discharge regions [99]. The effect, that then becomes important, is the emission of secondary electrons upon the impact of energetic ions onto the cathode. As they are injected into the sheath from the cathode surface, they can gain an energy equivalent to the sheath voltage, before entering the negative glow where their energy is dissipated in ionizing and exciting collisions.

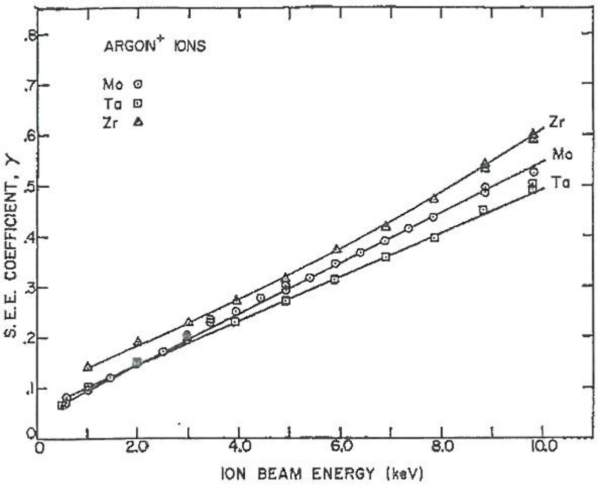

Fig. 21 : Measurements of the secondary electron emission (S.E.E) coefficient for Mo, Ta and Zr from impact of Ar^+ at varying energies. From *[102].*

An effect, unwanted in glow discharges, but important for the operation of magnetrons is sputtering. This effect is spared here and is explained in detail in Section 2.3.2.

Negative glow and Faraday dark space

The negative glow is a strongly luminous region which is characterized by a high number of excitations and ionizing collisions. This is because it is bombarded by highly energetic secondary electrons emitted at the cathode and accelerated in the sheath. In the negative glow, collision by collision, they dissipate their kinetic energy to the surrounding gas atoms.

Positive column and anode zone

The positive column connects the negative glow with the anode and thus serves to transport the particles. It is the part of the discharge that is extended or compressed when the inter-electrode distance is increased or shrunk and it can even completely disappear [98]. It resembles the transport zone in magnetron discharges. It is followed by an anode zone in front of the anode, which is irrelevant in magnetron discharges and not discussed here.

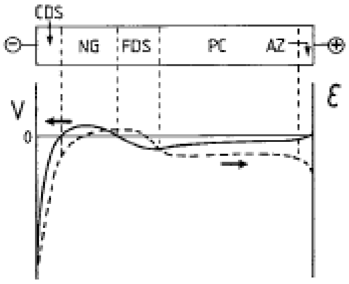

Fig. 22 : Glow discharge regions shown with the potential variation in between the anode and the cathode. CDS stands for cathode dark space, NG for negative flow, FDS for Faraday dark space, PC for positive column and AZ for anode zone. From [103].

2.3.2 Magnetron discharge

2.3.2.1 Magnetron cathode and substrate

While sputtering and material deposition are unwanted side effects in a glow discharge tube, they become the main objective in a magnetron discharge. In order to enhance sputtering, i.e. the ejection of single atoms from the cathode into the discharge, a magnetic field is added to the vicinity of the cathode (Fig. 23). As a consequence, the electrons are forced into a gyration motion which confines them close to the target. This enhances the number of ionizing collisions with the working gas, the flux of ions onto the target and finally the number of sputtered particles [98].

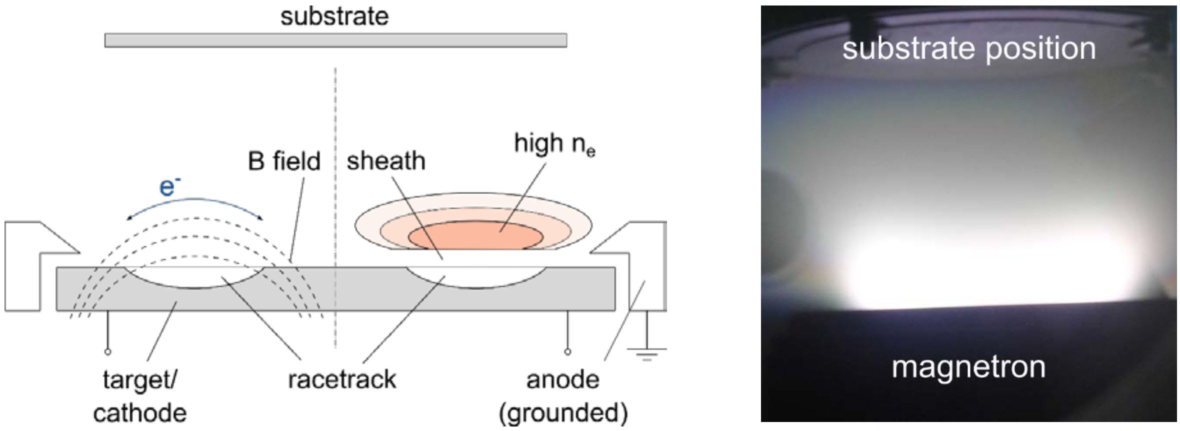

Fig. 23 : Left: Sectional view of a planar magnetron. On the left side, the B field and the e^- *effective motion is shown. The other side shows the ionization region at which the electron density is highest. Right: Photograph of a magnetron used for this study in operation.*

Taking a typical magnetic flux density in the target vicinity of a magnetron of B = 50mT just above the racetrack of a planar magnetron, the gyration radius of an electron $r_{g,e}$ injected into the ionization region at 300eV equals

$$r_g = \frac{u_{e,\perp} m_e}{eB} \approx 1.2\mu m, \qquad \textit{Eq. 18}$$

where $u_{e,\perp}$ is the electron velocity perpendicular to the direction of B, m_e is the electron mass, e is the electron charge and B is the magnetic flux density. For ions, the same rule applies but due their heavy mass that is at least a factor of 1000 greater compared to the mass of electrons, ions are usually not confined by the magnetic field. However, due to the confinement of the electrons, ions are retained by the electric field that would appear if they left the region. Techniques like high power impulse magnetron sputtering (HiPIMS) [104] or unbalanced magnetrons [105] are developed to overcome this issue and increase the ion-to-neutral flux onto the substrate.

A second effect of the magnetic field important for magnetrons is, that the pressure can be lower, thus increasing the deposition rate and at the same time allowing to deposit energetic species that would be decelerated at higher pressures. The lower pressure is a direct effect of the more efficient use of electrons that are kept close to the target instead of being lost to the walls [98].

The substrate is mounted typically at a distance of around 10cm from the cathode surface. It can be electrically grounded, can have a potential applied to it, or left electrically floating. For insulating substrates, the surface is always floating irrespective of the electrical connection. In this case, a sheath forms between the discharge and the substrate and the substrate charges negatively due to the much higher mobility of electrons compared to that of ions. In the case of a thermalized plasma, the floating potential V_f is given by [106]:

$$V_f = \frac{k_B T_e}{q} \frac{1}{2} \ln\left(\frac{2\pi m_e}{M}\right), \qquad \textit{Eq. 19}$$

where q is the elementary charge, k_B is the Boltzmann constant, T_e is the electron temperature, m_e is the electron mass and M is the ion mass.

The floating potential can be an important source of energy for ions as they are accelerated from the plasma potential V_p and gain an energy of $q(V_p-V_f)$ before they hit the surface of the growing film.

2.3.2.2 Magnetron deposition

The deposition process can be subdivided into four phases which are, in chronological order, ionization, sputtering, transport and deposition and growth of a thin film.

Ionization

The region just above the target is the negative glow region with a sheath acting as a transition between the solid surface of the target and the plasma. The negative glow extends from the target surface to up to a few cm above and can be observed by a bright illuminated donut-shaped plasma (Fig. 23). This region feels the strong influence of the magnetic field originating the magnets positioned just under the target.

The negative glow serves principally to ionize the noble gas that is necessary for sputtering (Eq. 20). Metal atoms sputtered from the target, however, also need to pass this region and there is a probability of ionization. This is an important effect in particular for high electron densities that can be achieved in the high-power impulse magnetron sputtering mode (see Section 2.3.3).

$$Ionization: \qquad X + e^- \rightarrow X^+ + e^- \qquad \textit{Eq. 20}$$

The phenomenon responsible for this region to glow is due to excitation of bound electrons to a higher energy level within an atom. From there, they fall back to some lower level while sending out a photon (Eq. 21, Eq. 22). While this process is of secondary importance for running a magnetron discharge, it is of high value for diagnosing the plasma optically by emission spectroscopy.

$$Excitation: \qquad X + e^- \rightarrow X^* + e^- \qquad \textit{Eq. 21}$$

$$Deexcitation: \qquad X^* \rightarrow X + h\nu \qquad \textit{Eq. 22}$$

Reactive gases like N_2 or O_2 come as molecules and the impact of electrons can break their bond. This is important in particular for N_2 that is an almost inert gas due to its triple bond that requires a high energy of 9.7eV [107] to break. A magnetron discharge can thus dissociate the molecules forming radicals that are, unlike N_2, very reactive.

$$Dissociation: \qquad X_2 + e^- \rightarrow X + X^* + e^- \qquad \textit{Eq. 23}$$

Sputtering and backscattering

Sputtering describes the knock-out of individual atoms by the impact of energetic atoms (projectiles) onto a target. For magnetrons, the projectiles are atoms in the gas phase that are ionized by the discharge and subsequently accelerated towards the target by its sheath. They thus can acquire an energy up to the maximum target voltage. Lower energies are possible depending on the point of ionization inside the sheath.

Upon impact of an ion, energy is absorbed by the bulk atoms either directly or via a collision cascade. In this process, a target atom can acquire an energy exceeding the surface binding energy, which allows it to leave the target. Typically these atoms are in the ground state and leave the target at a few eV [108]. The parameter describing this process is the sputter yield. It gives the average number of atoms sputtered per incoming projectile ion and is typically given a as function of impinging ion energy (Fig. 24).

$$Y(E_{inc}) = \frac{number\ of\ sputtered\ atoms}{number\ of\ impinging\ ions} \qquad \textit{Eq. 24}$$

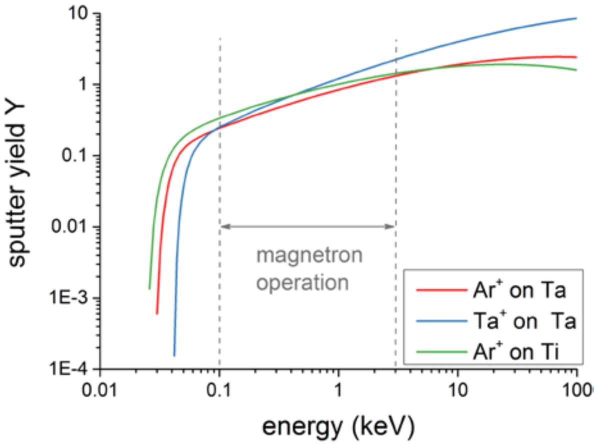

Fig. 24: Sputter yield as a function of energy for selected projectile and target atoms. The curves are fits to experimental data taken from [108].

A simple semi-empirical model is the one of Sigmund [109] [110] that illustrates all principle dependencies on the sputter yield (see Eq. 25). It is valid in the linear cascade region, which coincides with the operational range of a magnetron between a few 100 to 2000V (Fig. 24). The three variables that determine the sputter yield are the incident ion energy E_{inc}, the surface binding energy U_s and the energy transfer factor γ which is a function of the projectile and target mass ($\gamma = \frac{4m_1m_2}{(m_1+m_2)^2}$).

$$Y(E_{inc}) = \frac{3}{4\pi^2}\alpha\frac{\gamma E_{inc}}{U_s} \qquad \textit{Eq. 25}$$

The energy distribution of sputtered atoms is given by the Thompson distribution [111] (Fig. 25). It typically shows a maximum at half the surface binding energy of the target metal. Plots are shown in Fig. 25 for the cases of Ar at 300eV and at 1000eV impacting on a Ta target and, for comparison, Ar at 300eV impacting on a Ti cathode. As can be seen, due to the higher surface binding energy of Ta, its energy distribution maximum is slightly shifted to the right compared to Ti.

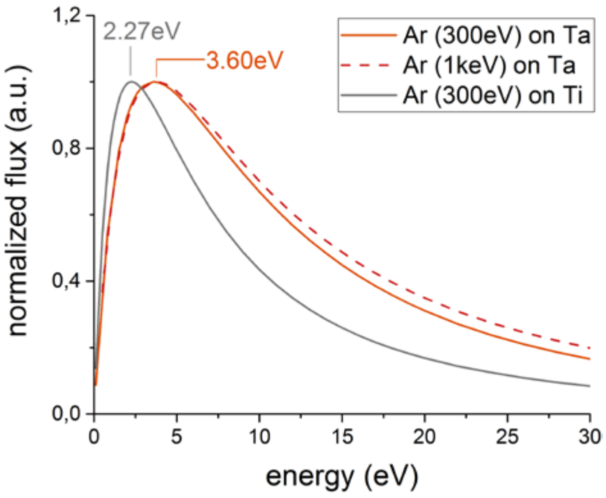

Fig. 25: Thompson energy distribution of Ta at various incident energies and Ti for comparison.

The backscattering of neutrals is an effect that accompanies the impact of ions onto a cathode surface. The phenomenon is illustrated in Fig. 26. An ion (here: Ar^+) is accelerated towards the cathode. Close to the cathode, it acquires a negative charge and transforms into a neutral. By interaction with the target atoms, in can be redirected towards the surface where it can escape as a backscattered neutral.

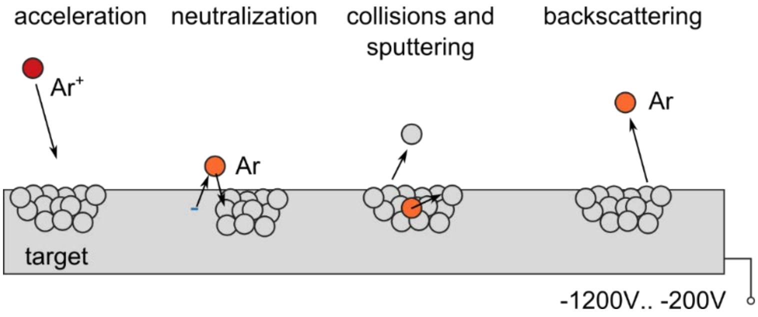

Fig. 26: Illustration of the different steps leading to backscattering.

The energies of these backscattered neutrals can be quite significant in particular for large target-to-ion mass ratios. A simple result from the binary collision theory allows to estimate the maximum energy of these neutrals [112].

$$E_{backscattered,max} = \left(\frac{m_{target} - m_{ion}}{m_{target} + m_{ion}}\right)^2 E_{ion} \qquad \text{Eq. 26}$$

Assuming, that the rare gas ions are accelerated to an energy equivalent to the cathode potential of 1100V, then the highest energy backscattered neutrals can be expected around 450eV, an energy large enough to cause damage in a growing thin film (see section on Nucleation and film growth).

More precise calculations undertaking in Section 4.3 actually show that the maximum energy is even higher.

This effect has been identified to be of a problem for preparing high critical transition temperature superconductors Nb_3Ge and Nb_3Sn films, for which the sputtering pressure needed to be very high (≈ 26Pa) in order to thermalize backscattered ions (see Section 4.3) [113] [114].

Reactive sputtering
Injecting a reactive gas into the deposition chamber changes the sputter yield in two ways. As a reactive gas can be ionized just like a noble gas, it can be accelerated towards the cathode and contribute to the sputtering of the target. However, reactive gases such as O_2 or N_2 are lighter than Ar, so they are typically less efficient in sputtering N_2. As a consequence, the sputter yield drops.

The second way they can influence the sputter yield is by forming a compound layer that is not only limited to the surface but exceeds below the surface due to the implantation of energetic ions [110]. This usually increases the bonding of surface atoms, further decreasing the sputter yield [110].

This latter effect gives sometimes rise to a hysteresis of the deposition rate which can be measured indirectly by monitoring the reactive gas partial pressure, the reactive gas emission intensity or the discharge potential and current [63]. The effect appears when increasing the reactive gas flowrate above the limit that can immediately be gettered by the target and the sputtered metals. At this point, the deposition rate drops due to the effects mentioned above. This increases the partial pressure of the reactive gas, further decreasing the deposition rate. This is a positive feedback loop that leads to a quasi-discontinuous change in the deposition rate. The target is then said to have gone from an elemental to a reactive mode.

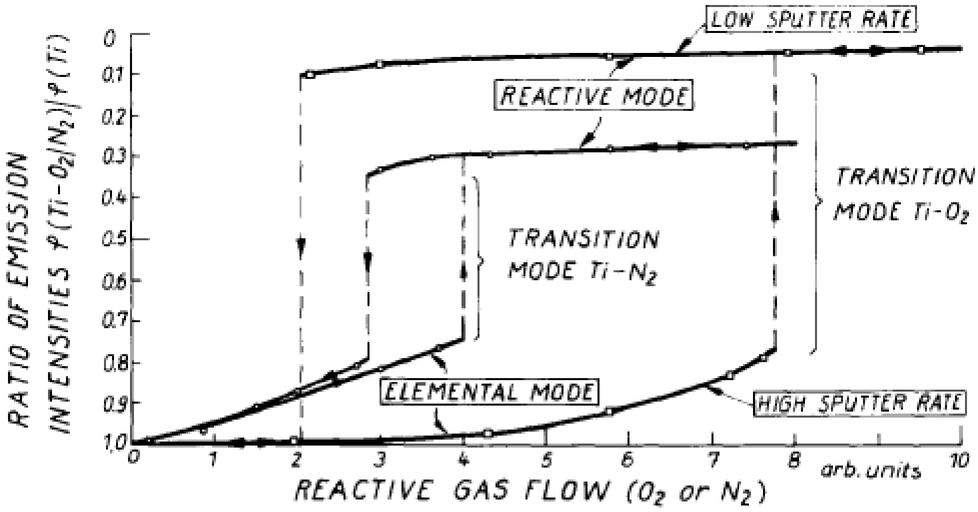

Fig. 27: The hysteresis effect as observed on optical emissions spectra from sputtered metal and reactive gases [115].

In reactive mode, the cathode provides an additional source of reactive gas. So when decreasing the reactive flowrate, the transition from the reactive to the elemental mode does not take place at the same point as the initial transition from the elemental to reactive mode. The flowrate sometimes needs to be decreased below that initial transition point, in order to reach the elemental mode. Plotting the metal emission lines upon increasing and decreasing the flowrate, yields a typical hysteresis curve (Fig. 27).

For the case of nitrogen, the hysteresis effect is reduced, and in some cases even absent [63] [116]. This could be reasoned by a reduced sticking coefficient of nitrogen compared to oxygen [115]. As a result, the reactive gas accumulates in the gas phase rather than on the target, making the transition between an elemental mode and a fully nitrided target smoother.

Transport

On their way from the cathode to the substrate, atoms and molecules are subject to collisions in which they transfer a part of their energy to the background gas. In general, it is beneficial not to decelerate atoms as their energy can promote film density and crystallinity. On the other hand, high energetic backscattered atoms can have energies >100eV which is several times the bulk displacement energy, so that a deceleration of particles may be required [113].

The thermalization of energetic neutrals is dominated by elastic collisions between the energetic atoms leaving the ionization region and the background gas atoms (i.e. Ar gas with the possible addition of a reactive component) [117]. The collisional dynamics can be described by the classical kinetic gas theory. Assuming the background particles at rest is normally a good approximation as they are estimated to have temperatures of below 1000K.

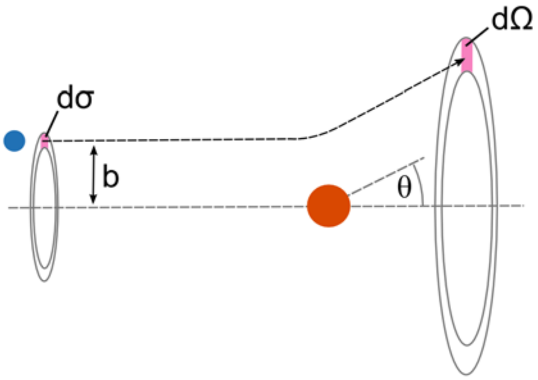

Fig. 28: Dynamics of a collision between a propagating atom (blue sphere) and an atom at rest (red sphere).

The energy transferred in a binary collision is a function of the impact parameter *b* which is the distance between the center of gravity of each particle measured perpendicular to the direction of flight (Fig. 28).The impact parameter corresponds to a scattering angle θ, that, by using the energy and momentum conservation principles, can be related to a fractional energy loss δE/E of the propagating particle [114] :

$$\frac{\delta E}{E} = \frac{\gamma \sin^2 \theta}{2}, \qquad \text{Eq. 27}$$

where γ is the energy transfer factor $\gamma = \frac{4m_1m_2}{(m_1+m_2)^2}$.

The degree of thermalization is then determined by how many collisions take place between the target and the substrate which is determined by the average distance travelled between two collisions, termed the mean free path λ_{mfp} [118]:

$$\lambda_{mfp} = \frac{k_B T}{p\sigma\sqrt{1 + \frac{m_1}{m_2}}} \qquad \textit{Eq. 28}$$

It is a function of the momentum transfer cross-section σ which again is a function of the kinetic energy of the collision and the impact parameter b. This cross-section is known for the Ar-Ar momentum transfer reaction and illustrated in Fig. 29. It shows a decreasing cross-section with growing incident energy and growing scattering angle. The largest cross-section can thus be found for impacts of particles that undergo only small deviations in the process.

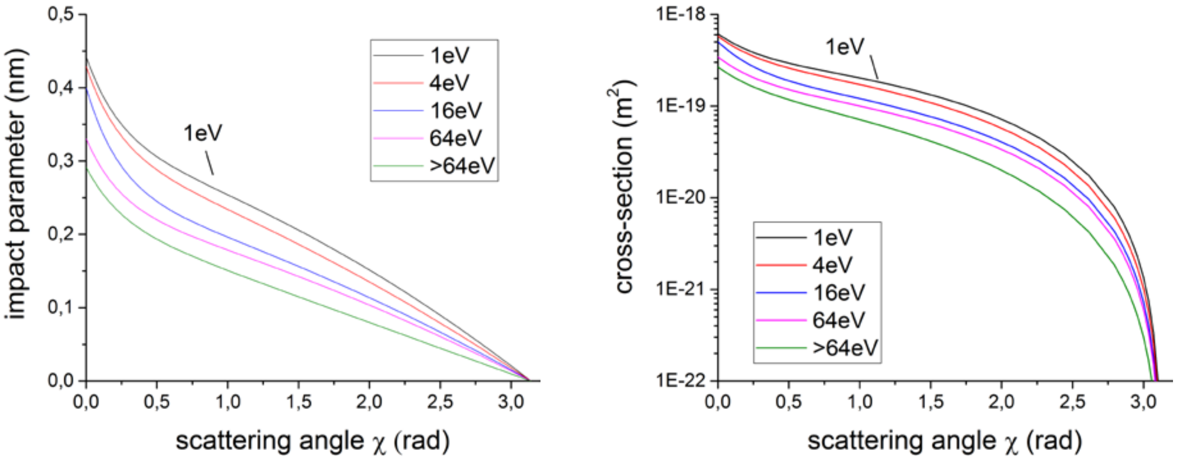

Fig. 29 : Near-linear relation between impact parameter and scattering angle for Ar-Ar collisions (left) and the corresponding cross-section. The data was taken from [119].

Taking an average value for the Ar-Ar momentum transfer cross-section of of $5\cdot10^{-20}$ m^2 and a temperature of 700K [120], results in $\lambda_{mfp} \approx 27$cm for a pressure of 0.5Pa and a $\lambda_{mfp} \approx 2.7$cm at a pressure of 5.0Pa. As a result, it can be seen, that for low pressures, the backscattered Ar population is not thermalized, while for the high pressure case, several collisions between the target and the substrate result in a lower average kinetic energy of Ar species arriving at the target. Whether or not the population is thermalized can only be answered by computer simulation (see Section 4.3).

Some insights may still be retrieved from the distribution of mean free paths that follows a Poisson law. The probability of a collision at a distance x of the last collision is given by [117].

$$P(x) = \exp\left(-\frac{x}{\lambda_{mfp}}\right) \qquad \textit{Eq. 29}$$

An example can be given taking again the high pressure case from above (5.0Pa) with an Ar-Ar momentum transfer cross-section of $5\cdot10^{-20}$ m^2 corresponding to a deflection of the incident particle by 90°. As calculated above, this configuration can be expected on average every λ_{mfp} = 2.7cm. Considering a substrate target distance of x = 10cm, the probability of a particle passing without collision is 2.5% and the probability of only one collision lies at 10%. This means, that even at high pressure, the arrival of energetic backscattered neutrals at the substrate position is to be expected.

It should be emphasized, though, that these calculations are susceptible to some uncertainty. In particular, the temperature of 700K is an estimate that is subject to changes depending on the discharge power [114] and pressure [117]. Taking instead a value slightly higher than room temperatures, i.e. 400K [117] almost halves the mean free path. On the other hand, the cross-section in Fig. 29 is seen to decrease with energy. This makes it increasingly difficult to decelerate backscattered neutrals the higher their energy.

With increasing pressure, not only neutrals, but also ions are decelerated. Cross-sections involving ions are typically greater than the neutral-neutral momentum transfer cross section. For Ar, this difference is roughly a factor of 35 at 10eV when summing the charge transfer (CT) and the momentum transfer (MT) cross-section. For N_2, this is still a factor of 12 at 10eV (Fig. 30). Therefore, as a result of increasing the pressure in order to slow down and scatter out backscattered ions towards the wall, one can expect that ions are slowed down and scattered out first. As ions typically supply the growing film with energy and momentum, scattering them out is unwanted.

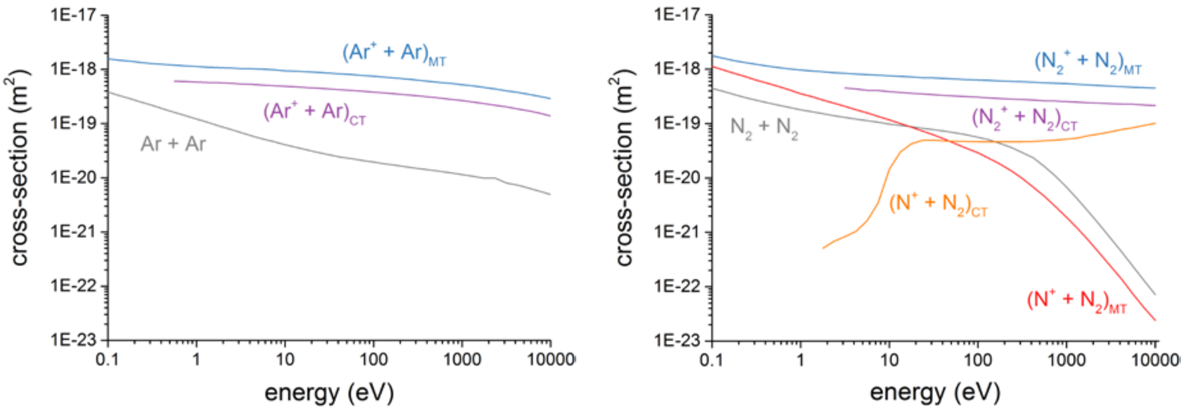

Fig. 30: Cross-sections for neutrals and ions in Ar (left) and N_2 (right). MT stands for momentum transfer, CT for charge transfer. The grey curves show the momentum transfer cross-section of neutrals. Data from [121].

Nucleation and film growth

A simple model for nucleation is described in the following that is based on thermodynamics and can be found in many text books (see e.g. [122]). It describes the shape of a hemispherical cluster formed on an idealized flat substrate surface. Forces appear at the interfaces due to the unlike bonding on each side of the interface. A surface atom of a cluster is thus pulled into the bulk or repulsed from the bulk and this results in a stress perpendicular to the surface, called the surface tension. The profile of such a deposited cluster is shaped by the equilibration of surface tensions at the three interfaces vacuum/substrate, substrate/film and film/vacuum.

$$\gamma_{sub/vac} = \gamma_{sub/film} + \gamma_{film/vac} cos\phi, \qquad \text{Eq. 30}$$

where ϕ is the contact angle between the substrate and the surface of the drop. If the surface tension between the substrate and the vacuum dominates ($\gamma_{sub/vac} > \gamma_{sub/film} + \gamma_{film/vac}$), ϕ must be nonzero for the equality to hold and the film is said to grow in island mode. On the other hand, for increasing values of $\gamma_{sub/vac}$, ϕ approaches 180° and the film is said to grow in layer mode.

It is to be noted that this model is simplistic and has merely phenomenological value. One of the main critics often stated is the use of terminology from continuum mechanics such as surfaces to describe the interaction of single or at most few atoms [122].

At a later stage, once the first crystal seeds are formed, the substrate becomes less determining for the growth as it is successively covered by the growing film. In this situation, the crystal orientation becomes important as the mobility of adatoms depends on the atomic termination of the surface. Crystal facets on which the mobility is enhanced grow faster, as the residence time of adatoms is longer on facets with a lower mobility. The probability of permanently attaching to one of the low mobility facets is thus larger which grows the high mobility facets [117].

Structure zone models (in this thesis they are referred to as morphology zone models as structure refers to the crystallographic structure) are developed to describe the general morphology. The first model to be developed by Movchan and Demchishiin introduced the term ‘homologous temperature’ T_h which is the ratio between the substrate temperature and the melting temperature of the bulk metal [123].

$$T_h = \frac{T_{substrate}}{T_{melting}} \qquad \textit{Eq. 31}$$

On cold substrates, the adatoms have limited mobility, which leads to a columnar and porous growth of the film. As the substrate temperatures rises, adatoms have sufficient energy to diffuse into gaps, filling them up and resulting in a denser film. Increasing the substrate temperature even more, allows the recrystallization of grains, increasing considerably the grain size [110].

The model was later complemented by Thornton [124] who added the effect of energetic condensation. This term describes an additional source of energy provided by the atoms arriving onto the substrate themselves. This energy can be of kinetic or potential nature, i.e. by fast atoms or ions, respectively. Fig. 31 depicts the concept. The energy of the arriving species is plotted on the lower axis while the temperature is plotted on the upper axis. The different zones are color-coded and range from a porous zone (in dark blue) to a highly crystalline morphology (in yellow). As the temperature increases, it suggests, that for a similar mrophology, a reduced temperature is necessary [125].

At high kinetic energies, i.e. 20eV ≤ E ≤ 50eV [110] [126], atoms carry sufficient momentum to displace already bonded atoms rendering them mobile again [110]. This leads to favorable conditions found in the center of the morphology zone model in Fig. 31. It claims that there is a “region of possible low-temperature low energy ion-assisted epitaxial growth”, i.e. a dense film with large grains can be expected around that region. Above the upper limit of ~50eV, bulk displacement can occur, possibly inducing defects into the crystal. This limit, however is not fixed and depends on the material system, notably on the arriving and target species [127]. This leads in the extreme case of very high energies ($\geq 400eV$) to the etching of the material indicated by the red zone in Fig. 31 [126]. It is important to note that all ions including rare gas ion contribute to the momentum transfer to the film [128]

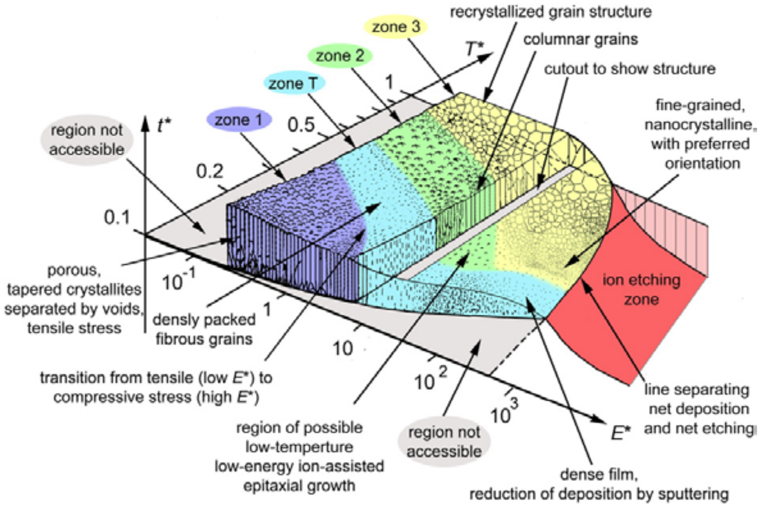

Fig. 31: Morphology zone model for plasma-based deposition [126].

One system abundantly addressed in literature to study effects of temperature and energetic condensation is that of the transition between the TiN [111] preferred orientation to the TiN [200] preferred orientation [117]. When the adatom mobility is low, a film forms with the TiN [111] plane parallel to the substrate as this plane has a lower adatom mobility. The plane therefore has a higher perpendicular growth rate. Increasing the energy during deposition, a transition of the preferred orientation to the TiN [200] plane can be observed as this plane has the lowest surface energy. Interestingly, this transition can be achieved by heating the substrate, by increasing the energy of arriving species or by increasing the ion-to-neutral ratio [117].

The difference between temperature-induced effects and those of energetic condensation, is that latter carries the risk of inducing damage to the film, notably by lattice point defects [129]. Defects believed to cause renucleation, resulting in smaller grain sizes [129]. The energies necessary for damaging thin films in magnetron sputtering can easily be reached so that care must be taken in tuning the species energy. Some examples of optimum energies between the surface displacement and the bulk displacement are shown in Table 8. The examples show that a large ion-to-neutral ratio is always beneficial for large grain sizes and a dense film. For the ion energy, on the other hand, an optimum value exists and depends on the material system [127]. For TiN, optimum values lie <100eV. As Ta has a higher atomic number and has thus s larger interaction radii, a Ta-containing film stops incident ions closer to the surface [127] which possibly allows even higher ion energies compared to Ti-based films.

Table 8: Examples of optimum energies of arriving species onto a growing film.

system/ phase	**type of investigation**	**observations**	**ref.**
TiN	Review of experimental and computational studies	100eV onset for change of (111) towards (200) preferred orientation	[117]
TiN	Experimental study on energetic condensation at low ion flux ($J_i/J_{neutral} \leq 1$) and varying ion energy E_i	E_i = 80eV: dense columns with open voids, onset energy for pronounced increase in defect density between 80eV and 120eV E_i = 120eV: further densification but appearance of intragranular residual damage, compressive stress and incorporation of working gas E_i > 160eV similar to above case but with renucleation on defect sites which refine grains.	[129]
δ-TaN	low energy ($E_i \leq 20$eV), varying ion flux $J_i/J_{neutral}$	Ion energies remain below the displacement energy required for bulk atoms. Texture change from (111) to (002) with increasing ion flux similar $J_i/J_{neutral} < 6.3$: Films show a strong (111) texture with an underdense zone T morphology. $J_i/J_{neutral} \geq 7.4$: Films show strong (002) texture and are fully dens than those at lower ion fluxes.	[130]
TiN	Epitaxial growth of TiN on MgO(100) with N_2^+ ions as a function of substrate bias V_s between 100 and 500eV at an ion-to-neutral ratio of 1.3 and a substrate temperature of 650° C	Defect density (dislocation loops) has a minimum at T_s = 300V and grows for lower or higher T_s.	[131]
TiN	Calculation	Optimum energies for surface displacement is 18eV - 110eV for (111) surfaces and 16eV - 80eV for (200)	[132]
Ta_2O_5	Experimental, growth as a function of bias voltage	Substrate bias between -50 to -200V yields Ta_2O_5 compared to an amorphous phase for no bias.	[133]

Besides the material, also the substrate temperature has an effect on the allowable ion energy as ion-induced damage can, to some degree be repaired by heating the substrate. Fig. 32 illustrates this by showing the substrate bias for which the defect density in the growth of epitaxial TiN thin films as a function of substrate temperature. Apparently, the films can tolerate a higher energy of incident ions at a higher substrate temperature [131].

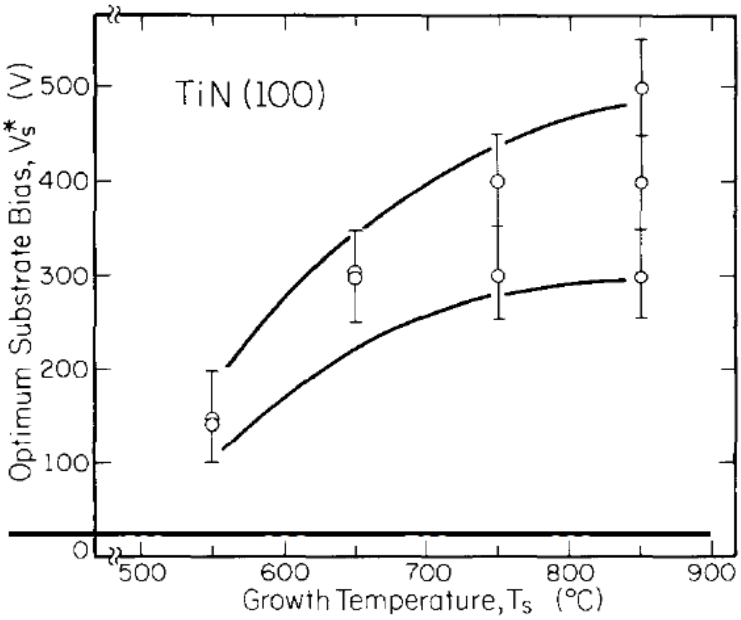

Fig. 32 : Optimum substrate bias to obtain a minimum defect density in growth of epitaxial TiN as a function of substrate temperature. From [131].

2.3.3 Modes of magnetron operation

Direct current (DC) magnetron sputtering

Modes of magnetron operation refer to the type of bias applied to the target. In the simplest case, a continuous voltage is applied that can be controlled to give a constant current or a constant power. In reactive sputtering, this mode is rarely used due to the formation of an insulating compound layer on the surface of the target. This can lead to electrical breakdown of the compound surface layer accompanied by arcs, fusing of the material and the formation of droplets. These can degrade the film quality [134]. As all but one phase of the Ta-N binary phase diagram are metallic, arcing is not expected for the experiments done for this thesis, though. The only phase being non-metallic from this phase diagram is Ta_3N_5, but its formation is only observed at high temperature ($T \geq 600°C$). As the target is water-cooled from the back, this temperature range is not expected to be reached.

High-power impulse magnetron sputtering (HiPIMS)

High power impulse magnetron sputtering is a technique in which pulses of high voltages (up to around -1000V) are applied to the target. These yield electron densities of up to $10^{19}m^{-3}$ (see Fig. 33) that are responsible for a high degree of ionization of the metal vapor of between 40% to 70% [135] [136] [137]. Fig. 33 shows the optical spectra from the negative glow of a DC and HiPIMS discharge with a much stronger emission intensity from Ta^+ in the HiPIMS case. A comprehensive review of the HiPIMS mode is written by Guðmundsson et al. [138].

The energetic condensation of this vapor onto the growing film can have positive effects such as film densification [139], improved film adhesion [135], a decreased necessary substrate temperature [140] [141] or the possibility to deposit on complex-shaped substrates [142]. All these effects are explained by the high ion-to-neutral flux onto the substrate and the associated energy and momentum transfer of condensing species.

The property for which HiPIMS films have not shown a clear trend compared to DC-sputtered films is the grain size of films. This is, however, a key parameter for semiconductors, as electron-hole recombination at grain boundaries should be avoided. Smaller grains in HiPIMS compared to DC sputtered films were shown for the case of TiN by Magnus et al. [143]. A similar result was published for CrN, in which a peak broadening is evidenced on diffractograms with increasing the HiPIMS peak current [144]. However, the opposite effect can also be found. Jouan et al. report a larger grain size for a HiPIMS film of AlN compared to one prepared by DC sputtering [145]. A possible reason for the observation of grain shrinkage in CrN and TiN could be that both, Cr and Ti are heavier than Al. This increases the energy range of backscattered neutrals from the cathode (cf. Section 4.3).

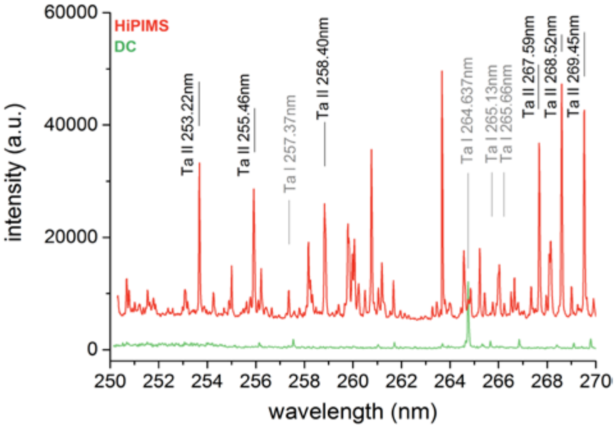

Fig. 33: Optical emission spectroscopy of the negative glow of a magnetron discharge on a Ta cathode in Ar. (Discharge parameters: 80W power (DC), a cathode bias of -1100V, a pulse width of 10µs and 80W average power (HiPIMS).

2.3.4 Magnetron sputtering of the Ta-O-N system

Many publications exists on magnetron-sputtered films of Ta(-O)-N. Most of them are on the δ-TaN phase that has, several industrial applications. In the following, some important studies are summarized:

Shin et al., University of Illinois

One of the earliest and most comprehensive studies on the Ta-N binary system is the PhD thesis by Chan Soo Shin [146]. He obtained a phase map as a function of substrate temperature and nitrogen fraction in the injected gas mixture (Fig. 34). Increasing the nitrogen fraction at lower temperatures (< 670° C), i.e. going from left to right on the phase map, the following phases appear in the following order: α-Ta and β-Ta, $TaN_{0.1}$ and Ta_4N, γ-Ta_2N, δ-TaN and finally at sputtering in pure N_2, the bct-TaN phase appears. At higher temperatures, the δ-TaN phase co-exists with the ε-TaN phase.

The lines on the phase map contour approximately the spaces in which a specific type of phase grows. For the phases appearing at a low nitrogen fraction (<0.1), these are vertical lines that are slightly inclined towards higher nitrogen fractions at higher temperatures indicating less nitrogen incorporation at higher temperatures [64].

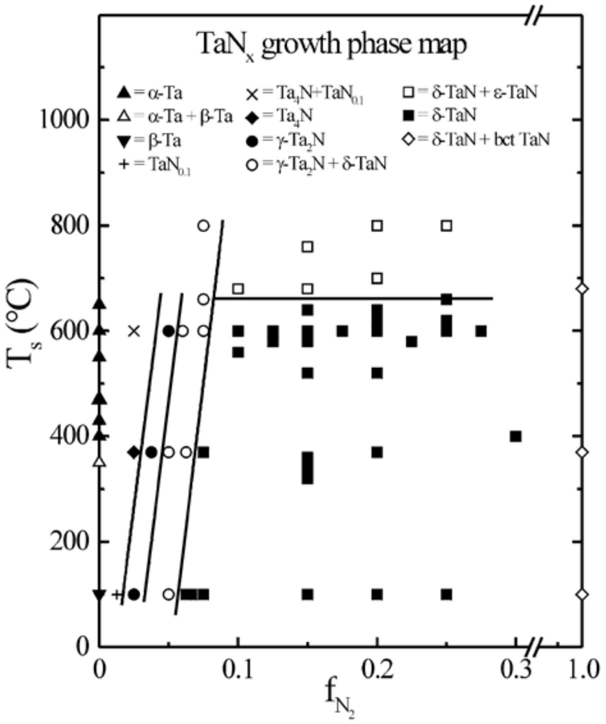

Fig. 34 : Phase map of the Ta-N system. From [64].

Sun et al., California Institute of Technology
A similar comprehensive study was undertaken by Sun et al. [147]. They employed radio-frequency sputtering and left the substrates thermally floating. The study confirms the appearances of phases with increasing nitrogen concentration in the film, from bcc-Ta, Ta_2N, an amorphous region, TaN (δ-TaN) and Ta_5N_6. Usually the phases appear not purely but in mixtures of several phases.

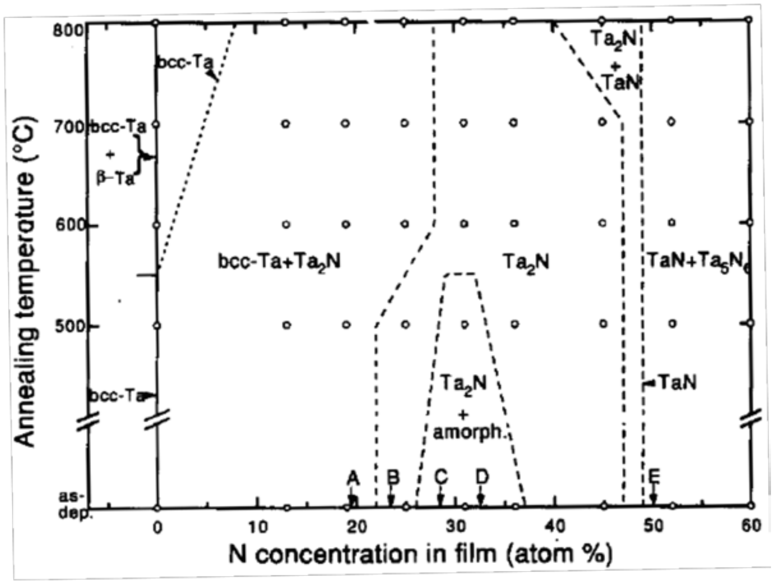

Fig. 35 : Effect of annealing of sputter-deposited films of Ta-N. From [147].

The sputtered films where then annealed for 65min in vacuum at temperatures between 600°C and 800°C which had only little effect as only a few samples change their crystal structure (Fig. 35). Upon annealing, the films loose little nitrogen which is different for other nitride as e.g. WN which is explained by the high negative heat of formation for the δ-TaN phase of ≈ -250kJ/mol [29] [79].

Stavrev et al., Dresden University of Technology

Stravrev et al. were the first to publish results on sputtering Ta in an Ar/N_2/O_2 gas mixture which shows an amorphous sample [148]. For Ta-O-N, these are characterized by two broad peaks at $2\Theta_{Cu} = 37°$ (wavevector $q = 26nm^{-1}$) and at 67° ($q = 45nm^{-1}$) (Fig. 36). At least the first one is found similarly by Bousquet et al. [149] for amorphous films of Ta-O-N by RF sputtering.

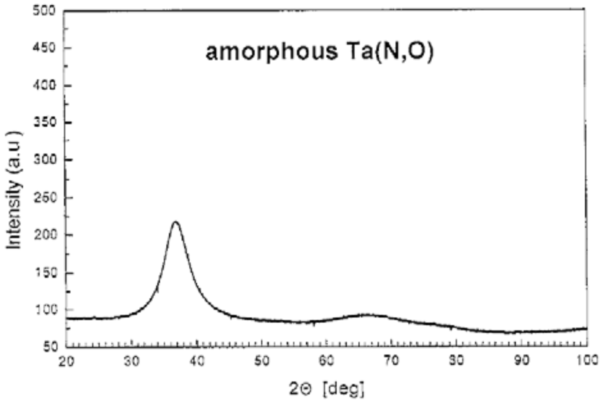

Fig. 36 : Diffractgram of a radio-frequency sputtered Ta-N-O sample from *[148]*.

Bousquet et al., Université Blaise Pascal, Clermont-Ferrand

The study by Bousquet et al. [63] focusses, among others, on the state of the Ta target when sputtering in an Ar/O_2, Ar/N_2 or Ar/N_2/O_2 atmosphere in RF mode. The differences between the first two are striking, as a hysteresis is observed for the oxygen case (Ar/O_2, Fig. 37, left hand-side) while for the nitrogen case, the hysteresis is strongly reduced and almost absent (Ar/N_2, Fig. 37, right hand-side). This could be due to the different sticking coefficients of oxygen and nitrogen as explained in Section 2.3.2.2.

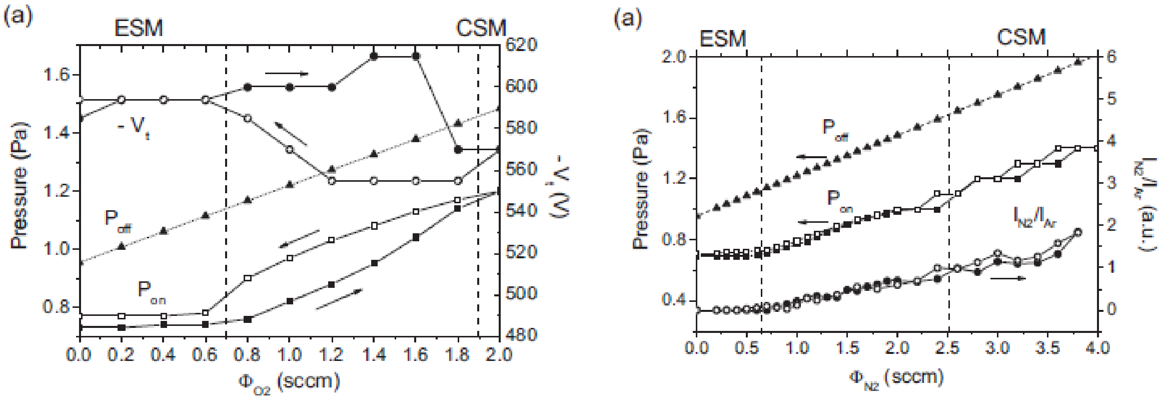

Fig. 37: Comparison of hysterisis measurements of Ta sputtered in O_2 (left) and in N_2 (right). ESM and CSM stand for elemental sputtering mode and compound sputtering mode. Both are termed elemental mode and reactive mode, respectively, in this thesis. From [63].

A second study by Bousquet et al. [149] discusses the structural composition of films as a function of the oxygen-to-nitrogen flowrate. Similar to the study by Stavrev et al. [148], all films deposited in $Ar/N_2/O_2$ are amorphous. One film, deposited without any oxygen injected into the reactor, shows the signature of the δ-TaN phase (Fig. 38). At higher values of R_F, this signature disappears and an amorphous halo appears around $2\theta_{Cu} \approx 35°$ (wavevector $q = 25nm^{-1}$). The position of this halo has almost identical positions to that observed by Stavrev et al. [148]. There is thus some short-range ordering in amorphous films of Ta-O-N that shows up as at least one broad halo.

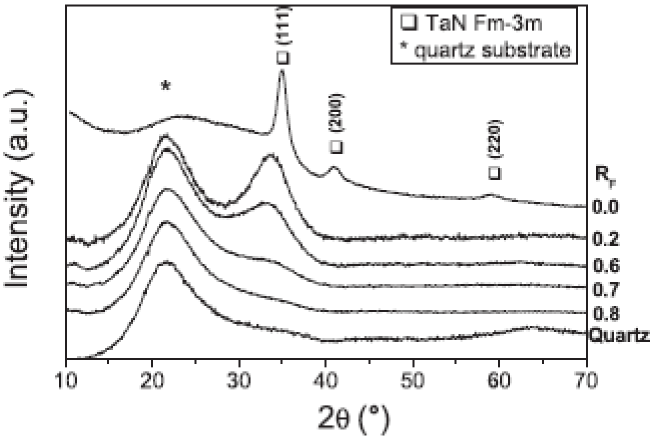

Fig. 38: X-ray diffractograms of Ta-O-N films deposited by RF sputtering at varying $R_F = \phi_{O2}/\phi_{O2} + \phi_{N2})$, where ϕ is the flowrate of oxygen or nitrogen. The Ar flowrate and the total flowrate of reactive gases are fixed to 5sccm and 1.25sccm, respectively. From [149].

2.3.5 Magnetron sputtering of Ta_3N_5

Three studies were published, that have shown that thin films of Ta_3N_5 can be prepared by magnetron sputtering (Table 9). The first published results was that of Ishihara et al., who deposited Ta_3N_5 thin films by RF magnetron sputtering in an $Ar/N_2/O_2$ gas mixture as a function of temperature (Fig. 39). They deposit films between 50nm and 100nm and obtain a Ta_3N_5 phase for substrate temperatures ≥ 600°C. A second study was conducted by Yokohama et al. [21] that similarly employed RF magnetron sputtering and studied the appearance of crystalline phases as a function of temperature and N_2/O_2 flow rate and temperature. Latter resulted in the conclusion that films are amorphous without the addition of oxygen, while an excess of oxygen resulted in the Ta_2O_5 phase. In between, they achieved a Ta_3N_5/TaON phase mixture that became richer in TaON by increasing the temperature from 624°C to 840°C (Fig. 39).

Table 9: Publications on magnetron-sputtered thin films of Ta_3N_5.

author	**mode**	**gas mixture**	**post-deposition treatment**	**phase**	**ref.**
Ishihara et al. 2008	RF	$Ar/N_2/O_2$	None	Ta_3N_5	[20]
Yokohama et al., 2011	RF	$Ar/N_2/O_2$	Annealing in NH_3 to increase crystallinity	Ta_3N_5/TaON phase mixture	[21]
Lin et al., 2016	DC	Ar/N2/O_2	None	Ta_4N_5/Ta_3N_5 phase mixture	[22]

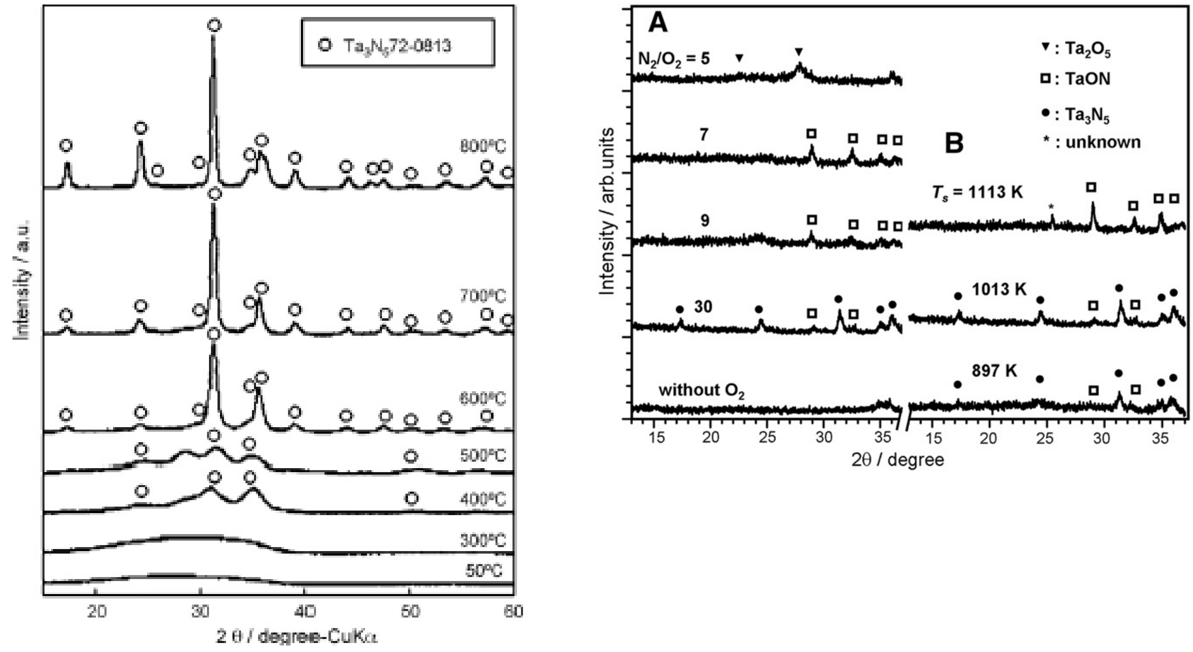

Fig. 39: Diffractograms of Ta3N5 thin films deposited by RF magnetron sputtering. Left: As a function of temperature by Ishihara et al. [20]. Right: As a function of N_2/O_2 ratio and temperature by Yokohama et al. [21].

2.3.6 Summary of magnetron-sputtered films from the ternary Ta-O-N system

Some of the works on magnetron sputtering of phases from the ternary Ta-O-N system are presented above and many others are published up to today. They cannot all be discussed in the frame of this thesis but the relevant ones are summarized in Table 10 classified according to the injected gases used.

Two main conclusions can be drawn from this for the synthesis of Ta_3N_5 crystalline thin films:

1) To obtain the Ta_3N_5 phase, oxygen must be incorporated into the lattice similar to the synthesis of the Ta_3N_5 phase by ammonolysis (see Section 2.2.3). This can best be seen by the fact that Shin et al [64], although covering a comprehensive parameter space with substrate temperatures going up to 600°C, did not obtain the Ta_3N_5 phase. In addition, the oxygen incorporation must be precisely tuned to avoid the appearance of by-phases such as TaON as seen by Yokohama et al. [21].

2) Secondly, the synthesis may only take place at elevated temperatures (≥600°C) as sputtering in an $Ar/N_2/O_2$ atmosphere at low temperatures resulted in amorphous films in three independent studies [148] [150] [149].

Table 10 : Selection of publications on sputtering thin films of Ta-O-N. P, d_{target}, p_{base}, p_{dep}, temp stand for the power supplied to the target, the target diameter, the base pressure, the pressure during deposition and the substrate temperature, respectively.

author(s)	sputter mode	P (W)	d_{target} (mm)	p_{base} (Pa)	p_{dep} (Pa)	temp. (°C)	phases obtained	ref.
Sputter deposition in Ar/N_2								
Sun et al., 1993	RF	300	75	10^{-5}	1.3	not controlled	bcc-Ta, Ta_2N, δ-TaN, Ta_5N_6	[147]
Shin et al., 2002	DC	150	75	10^{-6}	2.67	100-800	α-Ta, β-Ta, $TaN_{0.1}$, Ta_4N, γ-Ta_2N, δ-TaN, ε-TaN, bct-TaN	[64]
Stavrev et al., 1997	RF	1000	332	10^{-6}	0.22-0.3	Not controlled	Ta, Ta(N), δ-TaN	[148]
Sputter deposition in Ar/O_2								
Chandra et al., 2009	DC		75	10^{-4}	0.1	30	amorphous, Ta_2O_5	[133]
Sputter deposition in Ar/O_2/N_2								
Stavrev et al. , 1997	RF	1000	332	10^{-6}	0.22-0.3	not controlled	amorphous	[148]
Dréo et al., 2006	DC	n/a	100	10^{-4}	1.1-1.7	not controlled	amorphous	[150]
Bousquet et al., 2013/14	RF	250W	100	10^{-4}	1.0	not controlled	amorphous	[63] [149]
Yokohama et al., 2011	RF	150	n/a	$<10^{-3}$	0.57	629-874	Ta_3N_5, TaON	[21]
Ishihara et al., 2008	RF	150	n/a	10^{-4}	0.48	600-800	Ta_3N_5	[20]
Lin et al., 2016	DC	450	n/a	n/a	4	600	Ta_4N_5, Ta_3N_5	[22]

2.4 Conclusion

Ta_3N_5 is a promising candidate for efficient solar water splitting. Essential for this conclusion is its small band gap and its band positions that straddle the oxygen and hydrogen evolution potential in an aqueous solution. Two major issues related to its possible performance, however, are still open. One question raised above is whether its charge carrier mobility is sufficiently high. This is a matter of importance as its low absorbance above the direct band gap at 2.1eV demand a rather thick photoanode. A second issue not tackled at all, is its stability in the long term. The question of importance here is whether the observed initial fast decline in performance over the first minutes of operation yields to a saturation value or if it drops to zero.

In terms of performance, the solar-to-hydrogen efficiencies achieved by Ta_3N_5 in various forms remain far from the theoretically possible. The record for single junction materials lies around 1% and is only possible by applying an external bias. The reasons for the low efficiencies can only be speculated about but one possibility could be the preparation process that is almost entirely limited to the ammonolysis of oxidized Ta foils.

Indeed, this process has some drawbacks: 1) limited control over the oxygen incorporation, 2) limited control over sample thickness and 3) lack of a sharp interface between the photoactive Ta_3N_5 surface and the metal Ta foil due to the high necessary process temperatures.

Magnetron sputtering is a promising technique for the synthesis of Ta_3N_5 as it overcomes the three shortcomings of ammonolysis mentioned in the paragraph above. In magnetron sputtering, the oxygen incorporation can be precisely controlled as sputtering is a one-step process compared to the oxidation and nitridation of Ta foil. Similarly, the thickness can be precisely controlled by adjusting the time of the sputtering process. And finally, as the incorporation of reactive gases is by surface diffusion rather than by bulk diffusion, the growth temperatures are lower, so that a sharper interface between the substrate and the film can be expected.

Magnetron sputtering has been rarely investigated to synthesize Ta_3N_5. Three studies have shown the feasibility of sputtering the Ta_3N_5 while only the one by Ishihara et al. [20] and Lin et al. [22] did not require post-annealing of the samples. Thus, a systematic investigation of the mechanisms leading to Ta_3N_5 films with a high degree of crystallinity and large grains is not available and will thus be pursued in this thesis.

3 Experimental techniques

In this chapter, the main techniques and instruments used in this study are introduced. It starts with a description of the magnetron sputtering system, in which all films were prepared and is followed by introducing grazing incidence X-ray diffraction and ion beam analysis (IBA). These are two principle techniques used in this study to identify the film elemental and phase composition. Optical properties, in particular the band gap, are derived from total transmission and reflection spectrometry (TTRS) using a routine developed within this thesis to invert models of dielectric functions to fit the data. Finally, the principle of X-ray photoelectron spectroscopy (XPS) is outlined, a technique to obtain information on the chemical bonding of atoms at the surface of a sample. Following the film characterization techniques, two plasma characterization techniques are outlined. These are optical emission spectroscopy (OES) and mass spectrometry (MS) that were used at two points during this thesis. Finally, to proof the water splitting capability of the samples, photoelectrochemical measurements are conducted, for which the experimental setup is explained in the last subsection.

3.1 Magnetron sputtering system

3.1.1 Sputtering chamber

All thin film samples are prepared in an Alliance Concept magnetron sputtering system schematically shown in Fig. 40. It consist of a vacuum chamber with a diameter of around 60cm with a pumping system combining a multi-stage roots pump and a turbomolecular pump. The base pressure is $< 5 \cdot 10^{-4}$ Pa. Samples are inserted via a load lock with a separate pumping system similar to the one used for the deposition chamber. Ta_3N_5 samples, that require a substrate temperature of 600° C, need to be introduced directly into the chamber, which required a pumping time of 24h to reach the base pressure again.

Samples are clamped onto a Cu substrate holder. During the deposition process, it is suspended from the chamber ceiling. For samples requiring a substrate temperature of 600°C, a ceramic heating element is installed between the sample and the substrate holder. An electrical connection to the substrate holder allows to apply a radio-frequency (RF) bias. Finally, the substrate can be rotated around the chamber axis. This allows to get a homogeneous film and at the same time to keep the substrate temperatures low.

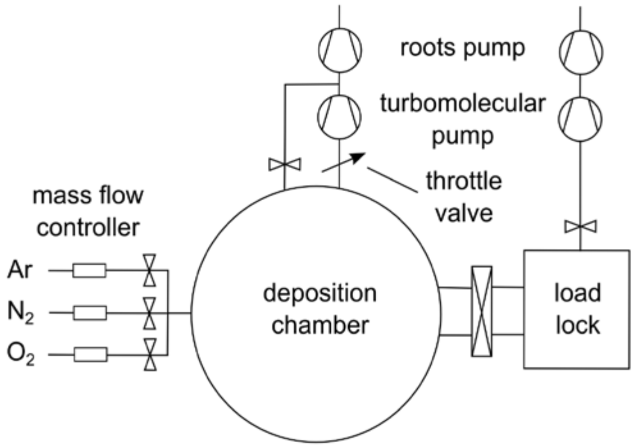

Fig. 40 : Conceptual drawing of the sputtering reactor used in this study.

3.1.2 Magnetron

The system described above is equipped with two equivalent planar circular magnetron sources each with a diameter of 10cm. The magnetrons are facing upwards and can be closed by a shutter. The cathodes can operate in direct current (DC), radio-frequency (RF) or high power impulse magnetron sputtering (HiPIMS) mode.

The magnetrons are balanced which is achieved by using magnetic ribbons that are rolled-up below the cathode surface (Fig. 41). This configuration exhibits a strong gradient of the magnetic flux density above the target, which is in particular true for the region above the racetrack (Fig. 42).

This has consequences on the stability of the electrical discharge conditions over the lifetime of a cathode. As the racetrack is eroded with time and the cathode surface in the racetrack region lowers, the magnetic field on the surface of the cathode effectively strengthens. This promotes electron confinement and lowers the impedance between the cathode and the plasma. Taking the derivative of the two values of magnetic flux density at the cathode surface (Fig. 42), gives a gradient of

19.2mT/3mm = 6.4mT/mm (cf. Fig. 42), meaning that the magnetic field strengthens by 10% when eroding a fresh target by 1mm.

Fig. 41: Left: Assembled magnetron. Right: Opened-up magnetron showing the rolled-up magnetic ribbon.

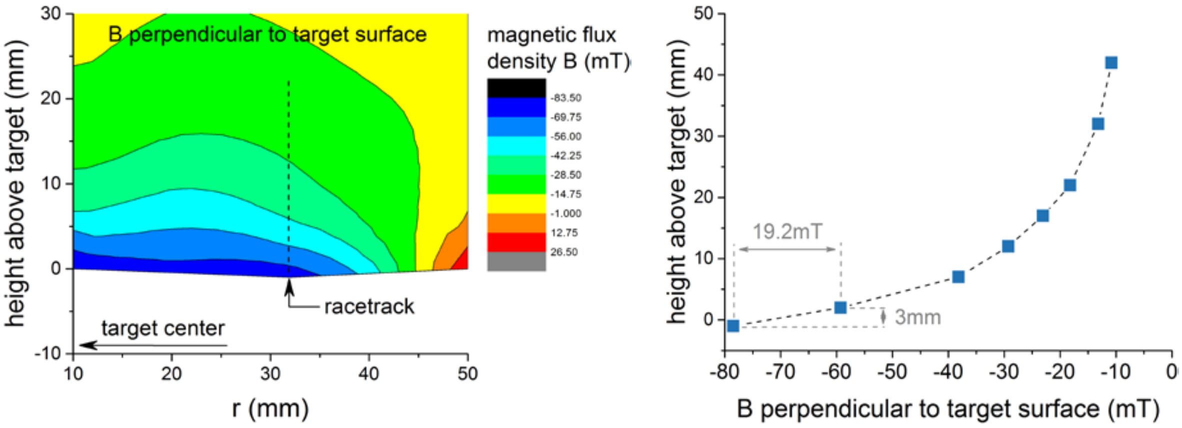

Fig. 42: Left: Magnetic flux density measurements B parallel to the target surface. Right: Variation of magnetic flux density B above the racetrack as a function of height.

As a consequence of this, the discharge reacts with a higher current at a constant average power. Fig. 43 shows the evolution of a HiPIMS pulse over the time of 128h45min during which a HiPIMS discharge in pure Ar at 0.5Pa, at a cathode potential of -1100V and an average power of 80W is run. During the time of 128h 45min, half of the nominally 3mm thick target is consumed (Fig. 43, right hand side).

This is in particularly an issue for the HiPIMS mode as the current peak reached during the pulse doubles between the initial and the final pulse width. In Comparison to that, Fig. 44 shows the potential and current evolution during the same time period. Here, a drop in potential of only 15% and a current rise by a similar percentage is observed.

This means that films deposited with a new target may differ from those deposited with a partially eroded target. Samples to be compared to each other are therefore always deposited in a batch using a target with the same degree of erosion.

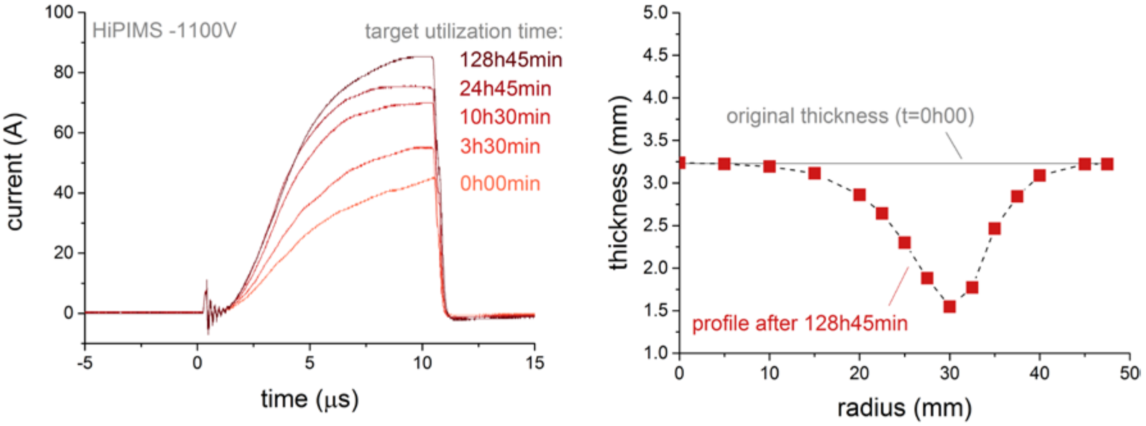

Fig. 43: Left: Variation of the current shape during a HiPIMS pulse at a cathode bias of -1100V. Right: Radial target profile of a nominally 3mm thick target after 128h45min utilization running a HiPIMS discharge of 80W average power.

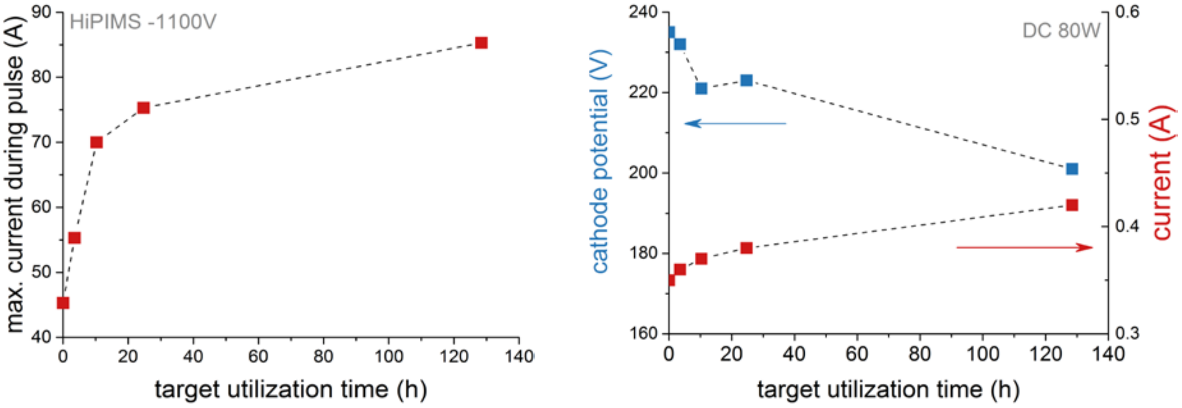

Fig. 44: Left: Maximal current during pulse of a HiPIMS discharge at a cathode bias of -1100V. Right: Evolution of cathode potential and current for an 80W average power DCMS discharge as a function of target utilization.

3.2 X-ray diffraction

X-ray diffraction is a measurement technique to determine the crystalline structure of thin films. It is based on the fact that X-rays have wavelengths comparable to the distance between crystallographic planes so that photons scattered off two adjacent planes, can interfere [151]. This interference pattern can be recorded and is characteristic for a certain crystal.

In the simplest way, just considering parallel planes with a distance d in between the crystallographic planes, the condition for constructive interference of a beam scattered off two distinct planes is given by the Bragg relation [151]:

$$n\lambda = 2asin\theta, \qquad \textit{Eq. 32}$$

where n is the diffraction order, λ the wavelength of the X-ray, a is the lattice parameter, and θ is the angle of incidence (see Fig. 45, left).

If the surface normal of a crystal is moved out of the drawing plane by an angle ψ (Fig. 45, right hand side), the incident beam is also diffracted out of the drawing plane. A film with randomly oriented crystallites, forms thus a circular diffraction pattern.

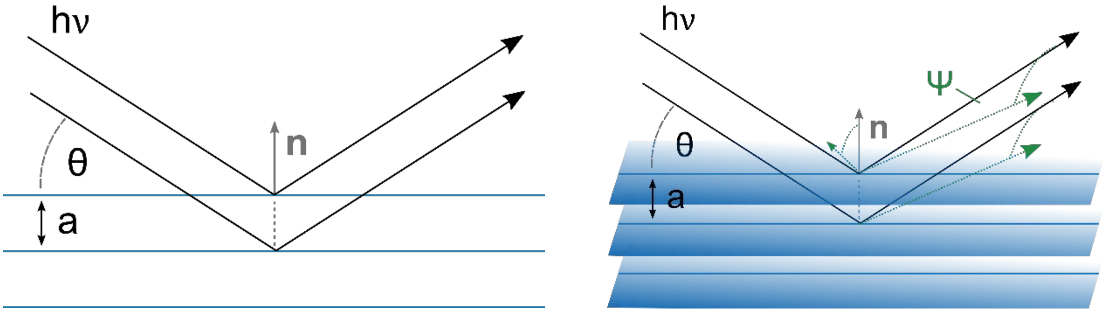

Fig. 45 : Schematics of the X-ray diffraction principle. Blue lines indicate the crystallographic planes.

The films prepared during the thesis are typically in the order of 50 to 500nm which is thin for conventional diffractometers. To increase the interaction of the beam with the sample, three measures are taken compared to conventional X-ray diffractometers. Firstly, the penetration depth of the beam into the films is increased using a Mo anode emitting at 0.071nm which more than doubles the beam energy compared to a conventional Cu anode (Table 11). Secondly, the diffractometer is setup in grazing incidence configuration (Fig. 46), i.e. the beam strikes the sample at an angle of 0.5° with respect to the surface plane. From this point of view, the sample is effectively thicker for the X-ray beam compared to the thickness, measured orthogonally to the surface plane. And finally, the diffracted beams are recorded using an X-ray sensitive plate covering the solid angle of diffracted beams. In this way the whole pattern is recorded simultaneously. The typical exposition time for a sample was 1h.

The grazing incidence configuration comes with a drawback that is indicated in Fig. 46 by the red and the green line. As the projection of the incident beam onto the sample is rather long, the beam leaving the sample has a certain width which broadens the peaks on the screen. To minimize this broadening, the beam diameter has to be tiny and in the case of this thesis a beam size of 30µm is actually used. This results in a spot size of the incident X-ray beam on the sample of 3.4mm. This broadening is believed to limit the resolution of the instrument to ~0.3nm^{-1}.

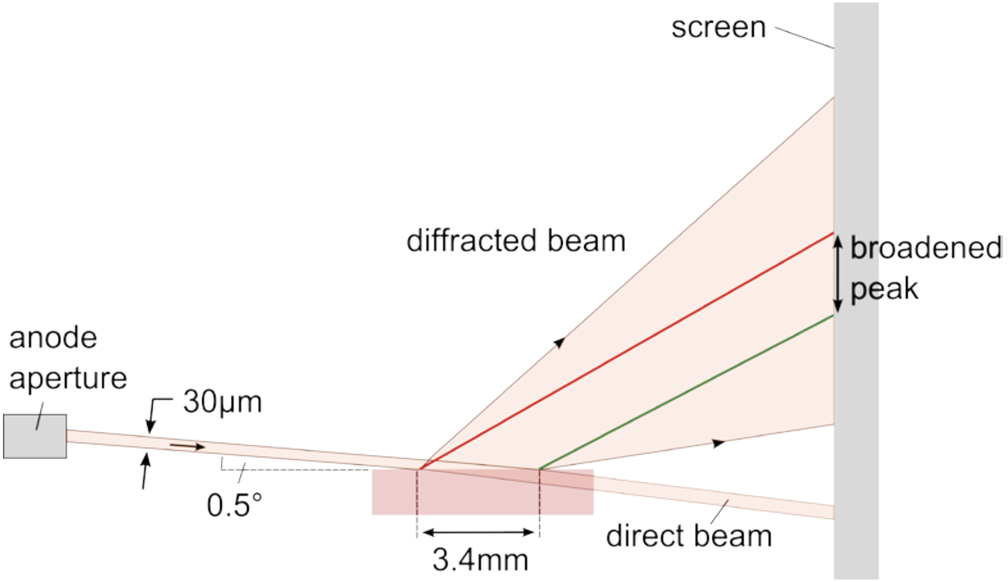

Fig. 46 : Setup of the grazing incidence X-ray diffraction experiment. The red and the green line leave the sample under the same angle but, due to their lateral displacement, do not coincide at the screen any more, which leads to peak broadening. Drawn schematically and not to scale.

Table 11: Wavelengths and energies of the K_α and K_β lines of Cu and Mo.

anode material	wavelength / nm		energy, keV
Cu	$K_{\alpha 1}$	0.154060	8.048
(conventionally used)	$K_{\alpha 2}$	0.154443	8.028
	K_β	0.139217 (filtered by Ni)	
Mo	$K_{\alpha 1}$	0.070962	17.472
(used in this thesis)	$K_{\alpha 2}$	0.071354	17.376
	K_β	0.063225 (filtered by Nb)	

The screens to record the diffraction pattern are read out using a scanner. An example of such a scan is presented in Fig. 47. It shows the circular diffraction pattern together with the direct beam spot and some reflections that are artifacts and as such are ignored for further data processing. The remaining image is radially integrated using the software fit2d [152] which results in a diffractogram such as that presented on the right hand side of Fig. 47. Calibration of the peak positions is done by passing a thin film of gold onto an amorphous substrate.

The use of a different beam energy compared to the usual Cu K_α wavelength can lead to confusion because the peak positions on the 2θ scale varies as a function of wavelength used (Eq. 32). Using the wavevector q instead, renders the scale independent of the wavelength used, which is why this scale is used in this thesis. The conversion to 2θ is as follows:

$$q = \frac{4\pi \sin(0.5 \cdot 2\theta)}{\lambda} \qquad \textit{Eq. 33}$$

$$2\theta = 2 \cdot \operatorname{asin}(\frac{q\lambda}{4\pi}) \qquad \textit{Eq. 34}$$

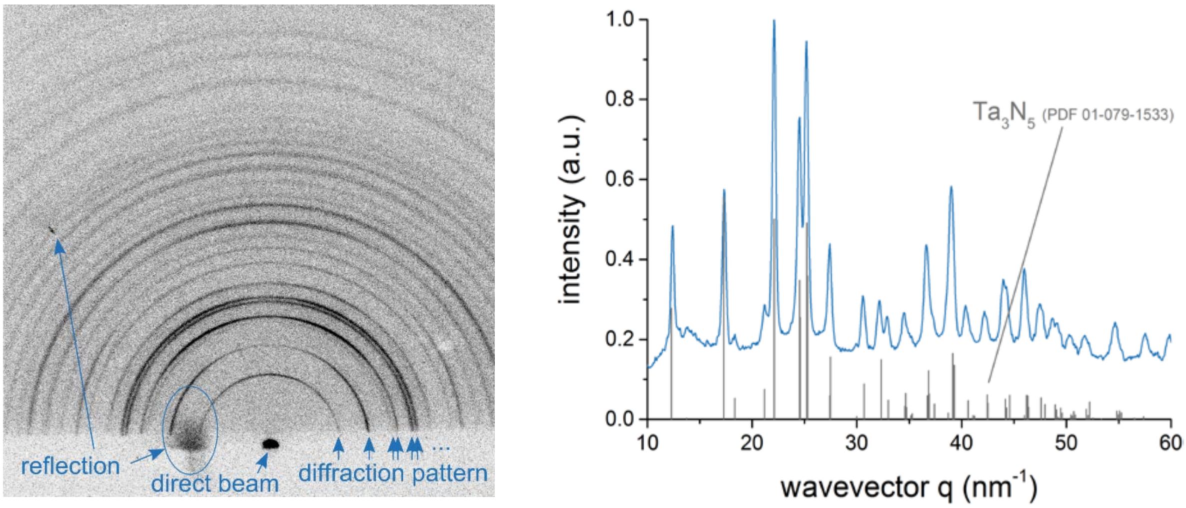

Fig. 47: Typical circular diffraction patterns observed on a sample deposited (left) and the resulting integrated diffractogram (right).

3.3 Ion beam analysis

Ion beam analysis (IBA) exploits the particle signature from collisions between sample atoms and a beam of energetic ions, to reveal the elemental composition of a film. In general, two variants can be distinguished that are classified according to the type of collisional process. In Rutherford backscattering spectrometry, the projectile collides with the nucleus of the target and is backscattered while in nuclear reaction analysis (NRA) the impacting particle is colliding with the nucleus triggering a nuclear reaction which can be detected by its products (Fig. 48).

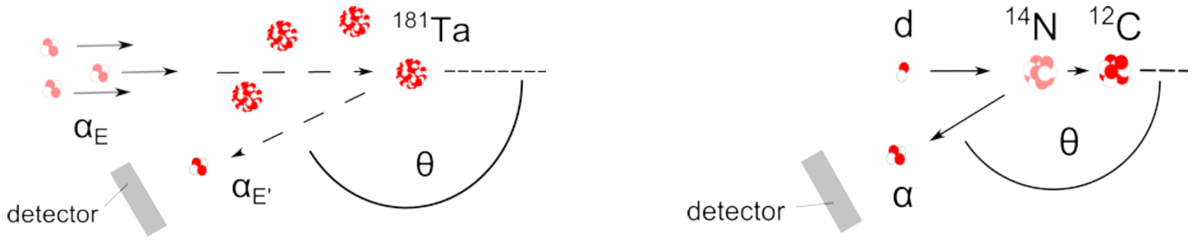

Fig. 48: Working principle of RBS (left) and NRA (right). θ indicates the scattering angle.

3.3.1 Rutherford backscattering spectrometry (RBS)

In RBS, energetic alpha particles (α, He^+) are shot onto a sample where they traverse the film until they collide with an atom from which they are backscattered. From momentum and energy conservation, the mass of the target atom can be calculated from the energy of the backscattered α, $E_{\alpha,backscattered}$ [151] :

$$E_{\alpha,backscattered} = \frac{\sqrt{M^2 - M_\alpha^2 \sin^2\theta} + M_\alpha cos\theta}{M_\alpha + M} E_\alpha \qquad \textit{Eq. 35}$$

where θ is the scattering angle according to Fig. 48, M_α is the mass of the α, M denotes the mass of the target atom and E_α is the energy of the projectiles.

A typical spectrum is shown in Fig. 49 where the heavy metal Ta peak appears at high energy in accordance with Eq. 35. Its shape depends on the sample. As a material grows thicker, the peak also broadens as the beam loses energy while penetrating through the film and reversing to the surface after a collision. Its height is proportional to the number of backscattering events and thus to the local number density of atoms. For different atomic species, it also depends on the scattering cross-section. The result of a classical treatment of the scattering process yields the differential Rutherford cross-section [153] which has a dependency on the square of the atomic number of the target atom.

$$\frac{d\sigma}{d\Omega} = \left(\frac{Z_1 Z_2 q^2}{4E_\alpha}\right)^2 \frac{1}{\sin^4\left(\frac{\theta}{2}\right)}, \qquad \textit{Eq. 36}$$

where Z_1 is the atomic number of the projectile ($Z_1 = 2$ for α), Z_2 is the atomic number of the target, E_α is the energy of the projectile atom and θ is the scattering angle from Fig. 48.

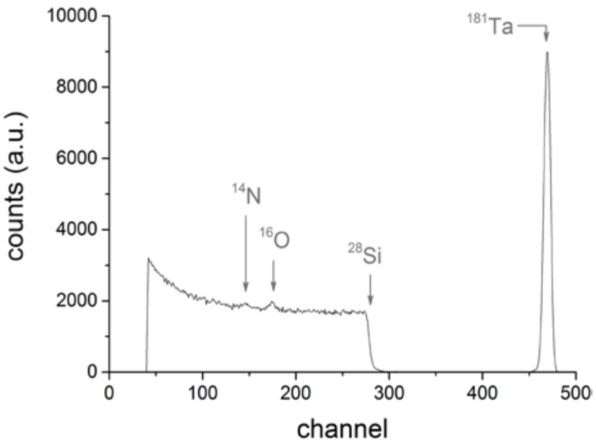

Fig. 49: RBS spectrum of a Ta-O-N thin film on a Si substrate. (Deposition parameters: 80W DCMS, 5.0Pa working pressure, Ar/N_2 atmosphere with flowrates of 40sccm and 10sccm, respectively.)

Using the relation between the cross sections of two different atoms, the absolute areal density of Ta (AD_{Ta}) can be retrieved from a reference of another element with a known AD. The experiments in this thesis are all calibrated on a bismuth (Bi) reference with $AD_{Bi} = 5.65 \cdot 10^{15} cm^{-2}$. AD_{Ta} can then be retrieved using:

$$AD_{Ta} = \frac{Z_{Bi}^2 \cdot counts_{Ta} \cdot Q_{Ta}}{Z_{Ta}^2 \cdot counts_{Bi} \cdot Q_{Bi}} AD_{Bi}, \qquad \text{Eq. 37}$$

where Q_{Ta} and Q_{Bi} are the total charges received by the sample and the reference respectively during the measurement.

In Fig. 49, the Ta peak is well separated from any other peak and can, after having subtracted the background, readily be integrated to yield the $counts_{Ta}$ and to determine AD_{Ta} from Eq. 37. At lower energies a broad plateau appears from the underlying Si substrate with a thickness of 500µm. On top of it, the backscatter signals from the light elements ^{16}O and ^{14}N appear. These peaks are typically weak, due to the low Z and the corresponding low cross-section. To determine precisely the content of these elements, NRA is used instead.

3.3.2 RBS profiling

As the beam of α-particles traverses the film, it loses energy by the interaction with the electrons of the target. Thus, it makes a difference whether an α is colliding with a surface atom or a bulk atom as in the latter case its nominal energy is reduced at the point of collision. This can be exploited to sample the areal density at a certain depth within a sample by using resonances in the cross-sections.

In the profiling experiment presented in this thesis, the oxygen density profile with depth is determined. For this, the resonance of the $^{16}O(\alpha,\alpha)^{16}O$ reaction cross-section around 3.0MeV is used (Fig. 50). It has a pronounced peak that is a factor of 25 above the Rutherford cross section while at the same time being narrow (FWHM 10keV for the SigmaCalc cross section at θ=165° [154]). However, the peak of the resonance has an uncertainty of around 7keV judging from the different experimentally determined cross sections. Those of Jarjis [155], Demarche et al. [156], and Leavitt et al. [157] peak around 3.032MeV, while those of Feng et al. [158] and Cheng et al. [159] peak at 3.037MeV. These correspond approximately to the peaks of the SigmaCalc cross sections at 3.037MeV (θ=165°) and 3.038MeV (θ=170°) but fall short of representing the height of the cross section.

The disagreement in cross-sections cannot be resolved in the frame of this thesis. For the fittings done for the oxygen profiling in this thesis, the SigmaCalc cross section is taken for several reasons

1) It is based partially on quantum mechanical calculations, thus avoiding the introduction of uncertainties from by the accelerator or the detector.
2) The experimental cross-sections are broader, which may be due to experimental limitations such as the sample thickness.
3) The simulation program used (SIMNRA [160]) interpolates linearly between two data points. If a point is offset from the general trend, the value for the cross-section at that energy changes rapidly. This is avoided by taking the smoothly varying SigmaCalc cross-section.

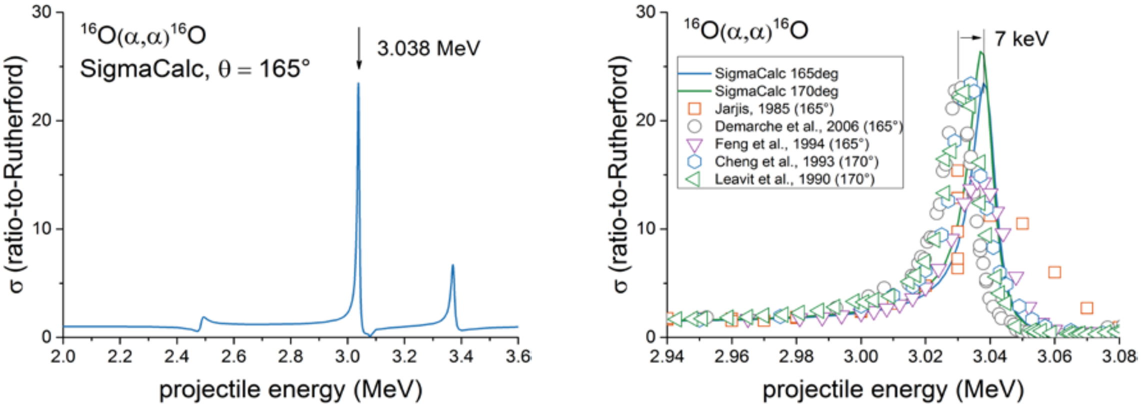

Fig. 50: Cross-section resonance for the ^{16}O(α,α) ^{16}O reaction around 3.0MeV. The SigmaCalc cross-sections are based on semi-empirical models [154]. The experimental data is taken from [155], [156], [158] (Feng et al., see comment in [161]), [159] and [157].

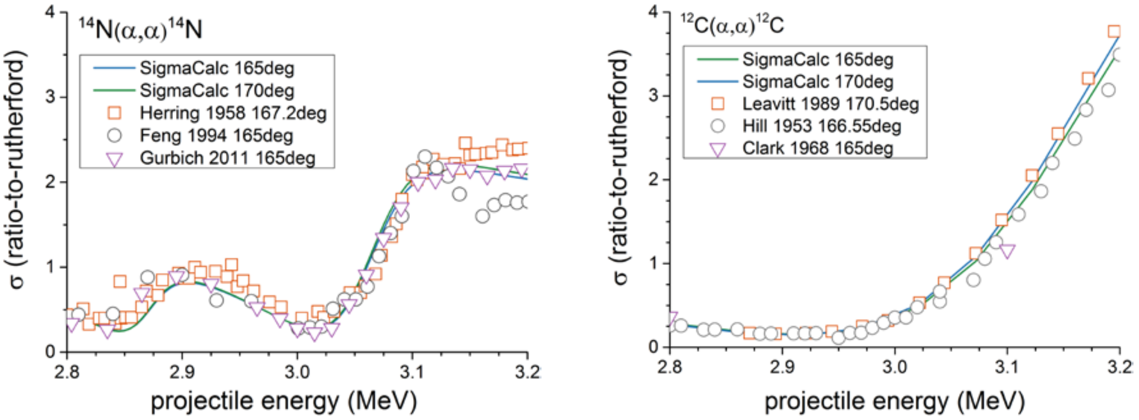

Fig. 51: Rutherford backscattering cross sections for nitrogen and carbon in the range of the oxygen resonance around 3.0MeV.

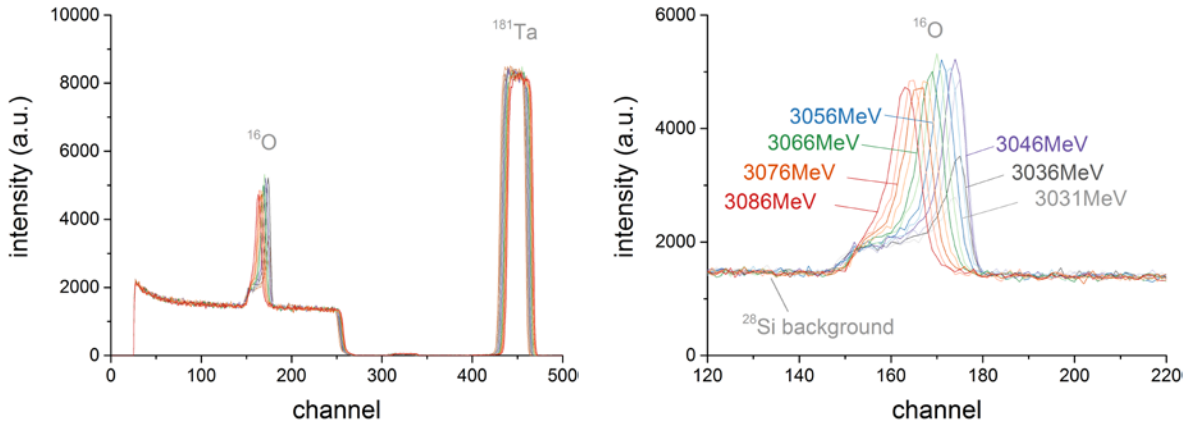

Fig. 52: Result of an oxygen profiling experiment using the resonance of the $^{16}_{8}O(^{4}_{2}\alpha,^{4}_{2}\alpha)^{16}_{8}O$ *reaction around 3.0MeV. Left: Full spectra. Right: Zoom onto the oxygen peaks at various α energies. (Deposition parameters: HiPIMS -1100V, 80W av. power,* p_w*=0.5Pa,* ϕ_{O2}*=0.5sccm,* ϕ_{N2}*=5sccm,* ϕ_{N2}*=44.5sccm.)*

It is important to note that also nitrogen and carbon have a non-flat cross section around 3.0MeV (Fig. 51). Unlike for the oxygen cross-section, however, theory and experiment match quite well. For consistency, also for those elements, the SigmaCalc cross section is used for fitting the spectra.

The fitting was done using the software SIMNRA [160] with the following assumptions:

1) *Use of Bragg's law*
   The simplifying Bragg's law is used. It states that the stopping power of a particle in a compound is the average of the stopping power of the individual elemental stopping powers weighted by their at.% in the compound.

$$\sigma_{compound} = \sum_i n_i \sigma_i, \qquad \text{Eq. 38}$$

   where n_i is the number of atoms of the ith element and σ_i its stopping power cross-section [162]. This rule actually introduces inaccuracies as the stopping power by electrons depends on the orbitals of those electrons. As this is influenced by the bonding, the exact stopping power is material-dependent. The simplification applied here is still considered to be justified as the stopping power of real materials deviates less than 20% from Bragg's law [163].

2) *Linear detector response*
   The pulse height defect in a Si detector describes the difference between the energy of the incoming particle and the observed energy by the detector. It is due to energy losses in the detector's dead layer and by losses due to nuclear interaction rather than electronic interaction [164]. As both effects depend on the incident particle's energy, this induces a non-linear response of the detector with energy. However, these effects are neglected and the detector response considered to be linear.

3.3.3 Nuclear reaction analysis (NRA)

Nuclear reaction analysis is a method to identify light elements that have a small RBS cross-section and are thus difficult to detect. It is based on a nuclear reaction which means, that the nucleus is irreversibly transformed in the reaction. The two reactions used in this thesis are $^{14}N(d,\alpha)^{12}C$ at 1400keV to detect nitrogen and $^{16}O(d,p)^{17}O$ at 850keV to detect oxygen (Table 12).

Similar to RBS, also for the NRA, references with a known content of nitrogen and oxygen are used to calibrate the number of counts measured on the samples. Fig. 53 shows the spectra from the two references. The oxygen reference (left) is a Ta_2O_5/Si sample with an areal density of ^{16}O of $340.9 \cdot 10^{15}$ cm^{-2}, the nitrogen reference (right) is a TaN/Si sample with and areal density of ^{14}N of 10^{18} cm^{-2}.

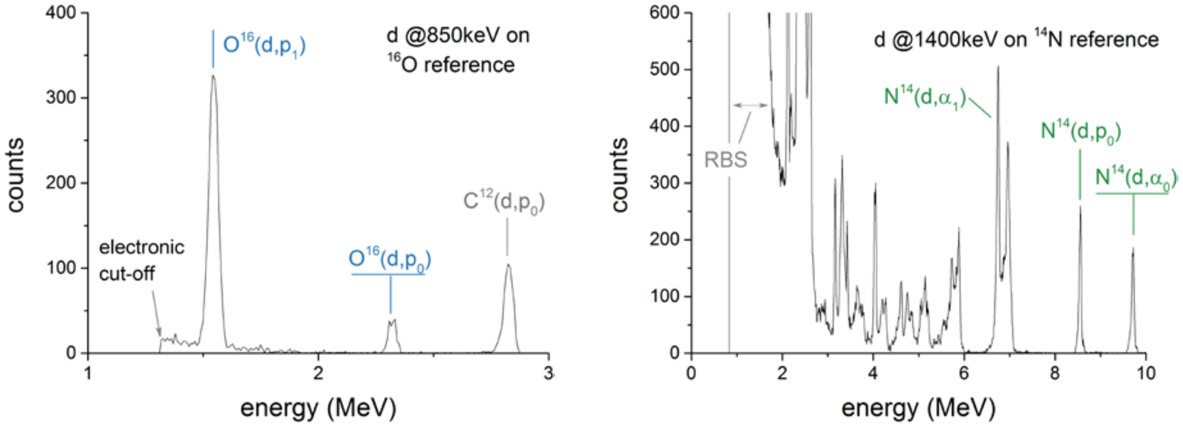

Fig. 53: Spectrum of reference samples for nitrogen (left) and oxygen (right). The reaction used to determine the oxygen and nitrogen areal densities are underlined.

Table 12: Projectiles, energies and reactions used to determine the total areal densities of ^{181}Ta, ^{14}N and ^{16}O, and to determine the O profile using ^{16}O resonance around 3MeV.

	projectile	**energy**	**reaction**	**type**
^{181}Ta	α	1800keV	${}^{181}_{73}Ta({}^{4}_{2}\alpha,{}^{4}_{2}\alpha){}^{181}_{73}Ta$	RBS
^{14}N	d	1400keV	${}^{14}_{7}N({}^{2}_{1}d,{}^{4}_{2}\alpha){}^{12}_{6}C$	NRA
^{16}O	d	850keV	${}^{16}_{8}O({}^{2}_{1}d,{}^{1}_{1}p){}^{17}_{8}O$	NRA
^{16}O,profiling	α	2.9 to 3.1 MeV	${}^{16}_{8}O({}^{4}_{2}\alpha,{}^{4}_{2}\alpha){}^{16}_{8}O$	RBS

Experimental setup

Three accelerators are used to study films for this thesis. Films from Chapter 4 were analyzed using ALTAÏS (Accélérateur linéaire tandetron pour l'analyse et l'implantation des solides) at the Université of Namur in Belgium. The oxygen profile in the film is determined using the microbeam facility at CEA Saclay in France. The analysis in Chapter 6 is done at SAFIR (Système d'analyse par faisceaux d'ions rapides) at the Université Pierre et Marie Curie. The three accelerators are based on the same principle.

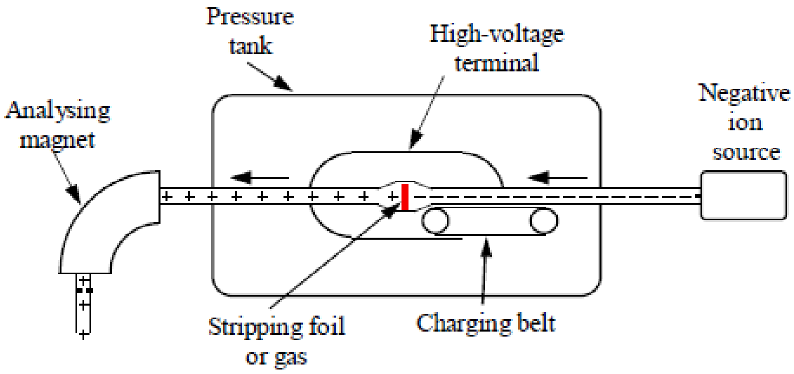

Fig. 54: Principle of an ion beam accelerator. See text for explanation. From [165].

The principal of a tandem ion beam accelerator is sketched in Fig. 54. A source supplies negative ions that are accelerated from ground to a positive MeV potential provided by a van de Graaf generator. A thin foil is then used to strip the ions of some of their electrons which leaves them with a positive charge. The same potential pushes the now positively charged ions back towards ground where they have a kinetic energy of two times the terminal voltage potential in addition to the energy at the output of the ion source. An electromagnet filters out the ions with the requested energy and further focusing optics can be used to reduce the beam size before striking the target.

The detector is placed close to the target at a fixed scattering angle of typically 150° to 170° (Fig. 48). It is a Si detector with a p-n junction in which, during the passage of a high-energy particle, free electrons are created. The charge is collected on biased electrodes and the resulting pulse is directly proportional to the incident particle energy [166].

3.4 Total transmission/reflection spectroscopy

The optics of a thin film can be described by its complex dielectric function. This parameter is not directly accessible by experiments, though, but its effects can indirectly be seen in transmission and reflection spectra of a sample. Thus, it is a typical inversion problem to determine the parameters of an underlying dielectric function model from these spectra. An automated routine is developed in this thesis to do so and a detailed description on the method is given in the following.

3.4.1 Fundamental equations and the matrix representation

The transmission/reflectance spectra are typically recorded over the ultraviolet (uv), visible (vis) and infrared (ir) wavelength range. For semiconductors with band gaps between 1 to 4eV, this range contains the band gap, an absorbing region at higher energies, and a transmission region at lower energies.

The spectral transmission T and spectral reflectance R of a material are defined in the following way as can be found in many text books on optics (cf. e.g. [87]):

$$\frac{I_t(\lambda)}{I_0(\lambda)} = T(\lambda)$$

$$\frac{I_r(\lambda)}{I_0(\lambda)} = R(\lambda) \qquad \textit{Eq. 39}$$

I_t and I_r are the transmitted and reflected intensities and I_0 the incident intensity. T and R are therefore unitless and are usually expressed in percentage.

The overall transmission and reflectance spectra T and R of a thin film sample are composed of contributions from all interfaces and layers including in particular the substrate. Generally speaking, the equations governing reflection and transmission at each interface and the absorption of each layer are the Fresnel equations, the Lambert-Beer law and Snell's law described in the following.

The Fresnel equations give the ratios of the electric field amplitudes between the incident and reflected beam r and the incident and transmitted beam t. These coefficients are distinct between the two polarization directions s and p and are thus composed of four equations with the complex refractive indices $N_0 = n_0 + j\kappa_0$ and $N_1 = n_1 + j\kappa_1$ for the two materials at each side of the interface and the angle of incidence and departure θ_0 and θ_1 at the interface [87].

$$r_s = \frac{N_0 \cos\theta_0 - N_1 \cos\theta_1}{N_0 \cos\theta_0 + N_1 \cos\theta_1}$$

$$r_p = \frac{N_1 \cos\theta_0 - N_0 \cos\theta_1}{N_1 \cos\theta_0 + N_0 \cos\theta_1} \qquad \textit{Eq. 40}$$

$$t_s = \frac{2N_0 \cos\theta_0}{N_0 \cos\theta_0 + N_1 \cos\theta_1}$$

$$t_p = \frac{2N_0 \cos\theta_0}{N_1 \cos\theta_0 + N_0 \cos\theta_1}$$

The Beer-Lambert law describes the exponential decay of intensity of a beam propagating through an absorbing medium [87].

$$I(d) = I_0 \mathrm{e}^{-\alpha(\lambda)\mathrm{d}}, \qquad \text{Eq. 41}$$

where I_0 denotes the incident beam intensity at a point d = 0, I(d) is the beam intensity at a distance d from d=0 and α(λ) is the wavelength-dependent absorption coefficient of the film and is related to the complex refractive index by Eq. 41.

$$\alpha(\lambda) = 2k(\lambda)k_0 \qquad \text{Eq. 42}$$

K_0 is the wavenumber and $k_0 = 2\pi/\lambda$.

Snell’s law describes the refraction of a beam at an interface with two different refractive indices [87]:

$$\frac{\sin(\theta_0)}{\sin(\theta_1)} = \frac{N_1}{N_0} \qquad \text{Eq. 43}$$

As multiple reflections arise, infinite but converging series in the computation of T and R occur. An elegant method uses matrices and is described in detail in many publications and text books and is outlined in the following (cf. e.g. [167] or [168]).

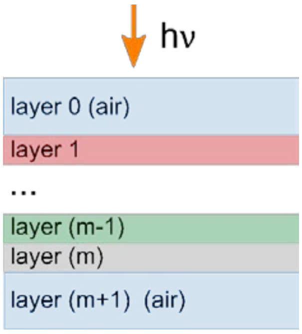

Fig. 55: Sketch of the generic multi-layered optical system.

A system of m optical layers (Fig. 55) each with a refractive index $N_i = n_i + jk_i$ can be described as a multiplication of Fresnel matrices $\mathbf{I_{ij}}$ for each interface between i and j and propagation matrices L_i for each layer as in the following equation:

$$\boldsymbol{M} = \begin{bmatrix} M_{11} & M_{12} \\ M_{21} & M_{22} \end{bmatrix} = \boldsymbol{L_0 I_{01} L_1} \dots \boldsymbol{I_{i,i+1} L_{i+1}} \dots \boldsymbol{I_{m,m+1} L_{m+1}} \qquad \text{Eq. 44}$$

The propagation matrices read:

$$\boldsymbol{L_i} = \begin{bmatrix} e^{j\beta_i} & 0 \\ 0 & e^{-j\beta_i} \end{bmatrix}, \qquad \text{Eq. 45}$$

where j is the imaginary unit ($j^2 = -1$) and β is the phase shift induced by the propagation through the layer between the two interfaces. It is a function of the thickness d_i of the i^th^ layer and its complex refractive index N_i:

$$\beta = \frac{2\pi d_i N_i}{\lambda} cos\theta \approx \frac{2\pi d_i N_i}{\lambda}, \qquad \text{Eq. 46}$$

where the last approximately equal sign is valid for θ ≈ 0° (see below).

The Fresnel matrices read:

$$\boldsymbol{I}_{\boldsymbol{i},\boldsymbol{i}+\mathbf{1}} = \frac{1}{t_{i,i+1}} \begin{bmatrix} 1 & r_{i,i+1} \\ r_{i,i+1} & 1 \end{bmatrix} \qquad \text{Eq. 47}$$

L_0 and L_{m+1} describe the first and last layer, which, in the case of this thesis, is the air layer between the film and the detector. Its refractive index can be approximated by $N_0 = N_{m+1} = N_{air} \approx 1$ which yields $\mathbf{L_0} = \mathbf{L_{m+1}} = \begin{bmatrix} \mathbf{1} & \mathbf{0} \\ \mathbf{0} & \mathbf{1} \end{bmatrix}$.

Following an algebraic proof [168], the transmission and reflection can then be calculated by:

$$T = \frac{1}{M_{11}}$$

$$R = \frac{M_{21}}{M_{11}} \qquad \text{Eq. 48}$$

All transmission spectra for this thesis where taken at $\theta = 0°$ which cancels all $\cos(\theta)$ terms and renders Snell's law irrelevant. The reflection spectra are taken at 8° which yields $\cos(8°) = 0.990\ldots \approx 1$, hence justifying the simplification in Eq. 46.

3.4.2 Dielectric function

The dielectric function of a material describes its response of a material when subjected to a static or variable electric field **E** such as incident photons. As a result to such an excitation, local electric dipoles change their orientation forming a polarization field **P** which superposes with the external electric field **E** to form a displacement field:

$$\boldsymbol{D} = \varepsilon_0 \boldsymbol{E} + \boldsymbol{P} \qquad \text{Eq. 49}$$

The parameter relating the resulting field **D** with the incident field **E** is called the permittivity ε which can be separated in a free space permittivity ε_0 and a relative permittivity ε_r describing relative changes with respect to free space.

$$\boldsymbol{D} = \varepsilon \boldsymbol{E} = \varepsilon_0 \varepsilon_r \boldsymbol{E} \qquad \text{Eq. 50}$$

The materials do not react instantaneously. The response rather depends on the frequency of the incident electric field which is why ε_r is in general complex, describing a change in magnitude and phase difference at the same time between the displacement field and the electric field.

$$\varepsilon_r = \varepsilon_r' + i\varepsilon_r'' \qquad \text{Eq. 51}$$

It is important to note that the two components are *not* independent but are related by the Kramers-Kronig relation [168].

$$\begin{aligned} \varepsilon_r'(\omega) &= 1 + \frac{1}{\pi} P \int_0^\infty \frac{\omega^* \varepsilon_r''(\omega^*)}{\omega'^2 - \omega^2} d\omega^* \\ \varepsilon_r''(\omega) &= -\frac{2\omega}{\pi} P \int_0^\infty \frac{\varepsilon_r'(\omega^*)}{\omega'^2 - \omega^2} d\omega^*, \end{aligned} \tag*{Eq. 52}$$

where P ∫ ... indicates the Cauchy principal integral to avoid the singularity at ω = ω', ω is the angular frequency and ω = 2πf.

Thus, for any model describing the optical properties of a material, it is sufficient to parameterize either the real part $\varepsilon_r'(\omega)$ or the imaginary part $\varepsilon_r''(\omega)$ of the dielectric function and to calculate the other part by Eq. 52. The integral, however, is computationally very expensive due to a slow convergence, which is why a model for ε_r'' that can be integrated analytically to yield ε_r' is necessary for an efficient fitting routine.

The relation between the dielectric function and the complex refractive index is given by [169]:

$$\begin{aligned} \varepsilon_r' &= n^2 - \kappa^2 \\ \varepsilon_r'' &= -2n\kappa \end{aligned} \tag*{Eq. 53}$$

3.4.3 Dielectric function models

3.4.3.1 Tauc-Lorentz single oscillator

A simple parameterization of the imaginary part of the dielectric function is the Tauc-Lorentz oscillator model which is a combination of two models: The Tauc joint density of states [170] describes the imaginary dielectric function close to the band extrema (Eq. 54) and the above-band gap region is modelled using a linear oscillator model for an electron bound to an atom by electrostatic forces and excited by an oscillating electric field (Eq. 55). [169].

$$\varepsilon_r''(E) \propto \left(E - E_g\right)^2 / E^2 \tag*{Eq. 54}$$

$$\varepsilon_r''(E) \propto \frac{E\Gamma}{(E_0^2 - E^2)^2 + E^2\Gamma^2} \tag*{Eq. 55}$$

The combination yields the single Tauc-Lorentz oscillator model for the imaginary dielectric function for above band gap absorption [171].

$$\varepsilon_r''(E) = \begin{cases} 0 & , E_g \leq 0 \\ \frac{A E_0 \Gamma \left(E - E_g\right)^2}{\left(E^2 - E_0^2\right)^2 + \Gamma^2 E^3}, & E_g > 0 \end{cases} \tag*{Eq. 56}$$

where A describes the oscillator amplitude, E_0 describes the resonance energy and Γ the oscillator width. This function can be integrated analytically to yield an expression for ε_r' which is omitted here but can be found in [172].

3.4.3.2 Tauc-Lorentz single oscillator with an absorption tail

Many materials are not fully transparent below the band gap but exhibit an exponentially decreasing absorption coefficient with decreasing energy, the so-called Urbach tail [173] [174].

$$\alpha = \alpha_0 \exp\left(\frac{E}{E_u}\right), \qquad \textit{Eq. 57}$$

where E_u is the Urbach energy which determines the steepness of the exponentially decaying absorption coefficient. A value close to zero means a sharp transition around the band gap (no or little effect of the Urbach tail) while for increasing values of E_u the transition becomes more and more shallow and a considerable absorption occurs within the band gap.

Including this into Eq. 56 yields [171]:

$$\varepsilon_r''(E) = \begin{cases} \dfrac{E_1}{E}\exp\left(\dfrac{E-E_t}{E_u}\right) & , E \leq E_t \\ \dfrac{AE_0\Gamma\left(E-E_g\right)^2}{E(E^2-E_0^2)^2+\Gamma^2E^3}, & E > E_t \end{cases} \qquad \textit{Eq. 58}$$

where now the TL model is separated from the UT model by an demarcation energy E_t. It takes values between the onset of absorption and the band gap E_g and adds an absorption tail that exponentially decreases with decreasing energy (Fig. 56). To obtain the special case with no Urbach tail by this model (cf. Section 3.4.3.1), set $E_1 = 0$ and $E_t = E_g$ [171]. The analytically solved integral for ε_r' is published in [171].

The effect of the Urbach tail on transmission spectra is demonstrated in Fig. 56 on a fictional sample with parameters summarized in Table 13. The model without Urbach tail is shown in red. As the Urbach energy rises, the transition region between below and above the band gap becomes smoother. For an Urbach tail energy of 500meV, a considerable absorption exists below the band gap.

Table 13: Parameters for fictional samples with transmission curves shown in Fig. 56. Case 1 corresponds to a sample showing no Urbach tail (Tauc-Lorentz single oscillator) while case 2 and 3 shows the influence of the Urbach tail model with varying demaracation energy E_t and Urbach energy E_u. t denotes the sample thickness, all other parameters are fitting parameters (see Eq. 58).

	t (nm)	A (eV)	E_0 (eV)	Γ (eV)	E_g (eV)	E_t (eV)	E_u (meV)	ε_∞
no UT	500	150	4	1	2.1	$= Eg$	not applicable	1
with UT	500	150	4	1	2.1	3.0	300, 500	1

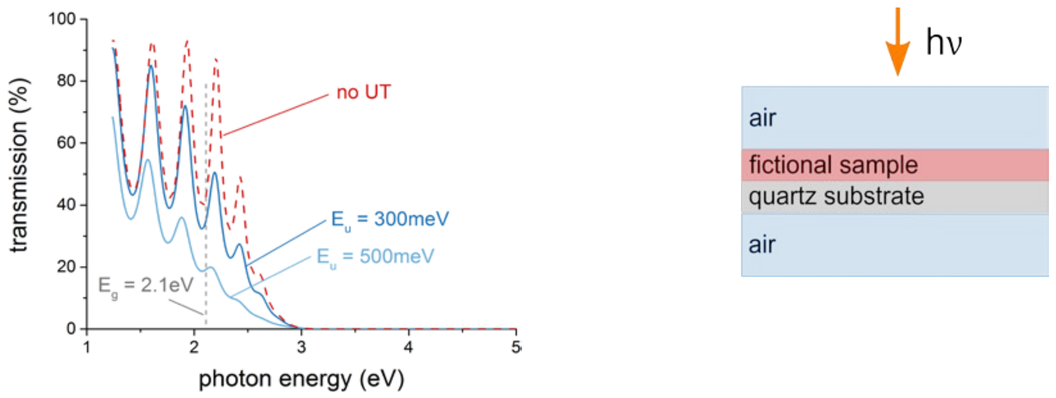

Fig. 56 : Influence on the two parameters introduced by the Urbach tail model, the Urbach energy E_u (left) and the demarcation energy E_t. For the parameters of these fictional samples, see Table 13. The sketch on the lower right illustrates the optical system configuration.

3.4.3.3 Tauc-Lorentz with multiple oscillators

More complex dielectric functions can be built by adding several Tauc-Lorentz oscillators. This keeps the advantage of the Tauc-Lorentz model, that it can be integrated analytically, because the overall dielectric function is simply the sum of the individual contributions from each oscillator.

$$\varepsilon'_{tot} = \sum_{i}^{N} \varepsilon'_i - (N-1)\varepsilon_\infty$$

$$\varepsilon''_{tot} = \sum_{i}^{N} \varepsilon''_i \qquad \text{Eq. 59}$$

An example of this is published by Morbec et al. [18] who fitted 4 TL oscillators to experimental TTRS curves and by that obtained the dielectric function for Ta_3N_5. (Section 2.2.2.2, Fig. 16).

3.4.4 Model inversion

Once a model is selected, it can be inverted to fit the underlying data. A code was developed to do this automatically based on a global optimization algorithm [175] that is found to be well suited to the inversion of transmission and reflection curves [176]. It is based on a stochastic approach in which the dielectric function is guessed by randomly choosing values for the parameterization. The dielectric function is then used to calculated the fictive transmission and reflection curves which are compared with the experimental spectra. The dielectric function having the best match with the experimental data is then selected to be the true one. The comparison is done using the following objective function [176]:

$$f_{obj} = \frac{1}{2}\sqrt{\frac{1}{N}\sum_{i}^{N}\left(\frac{R_{exp}(\lambda_i) - R_{calc}(\lambda_i)}{\Delta R}\right)} + \frac{1}{2}\sqrt{\frac{1}{N}\sum_{i}^{N}\left(\frac{T_{exp}(\lambda_i) - T_{calc}(\lambda_i)}{\Delta T}\right)}, \qquad \text{Eq. 60}$$

where R_{exp}, R_{calc}, T_{exp} , T_{calc} are the measured and calculated reflection and transmission at a certain wavelength λ_i, respectively, ΔR and ΔT are the allowed uncertainties for the reflection and transmission, respectively and N is the number of data points for each spectrum. The uncertainties are typically chosen to be 3%. In the case, that the difference between the measured and the calculated spectrum lie within the uncertainty for all data points i the objective function $f_{obj} < 1$. The smaller it is, the better is the fit.

3.4.5 The photospectrometric measurements

The photospectrometer provides an incoherent beam of monochromatic (2nm resolution) light from the combination of a halogen and a uv light bulb. The beam is split up into a sampling beam, that is directed towards an integrating sphere and a reference beam, the intensity of which is monitored by a separate CCD. In this way, possible fluctuations in intensity, e.g. due to fluctuations of the mains supply, can be compensated for in the sampling beam.

The samples are measured using an integrating sphere that is to direct all photons, including those that are diffusively transmitted or reflected, towards the detector. The term ‘total transmission’ thus refers to the sum of the regular and diffuse transmission and the term ‘total reflection’ to the sum of the specular and diffuse reflection component

For the transmission measurement (Fig. 57, center) the total intensity passing through the sample is determined by closing off the reflection port of the integrating sphere with a reflection standard. A correction to compensate for non-ideality of the spectralon, in particular in the ultraviolet region, is compensated for automatically by the photospectrometer software. In reflection mode (Fig. 57, right hand side), the transmission port is left open and the sample clamped onto the reflection port. The slight inclination of the sample with respect to the incident beam from the monochromator serves to keep the specular component of the reflected beam inside the integrating sphere rather than directing it out through the transmission port. For both types of measurements; the monochromator scans throught the spectrum of the light source from 200nm to 1000nm and records the transmitted or reflected intensity as a function of wavelength.

Before any measurments, a calibration is done (Fig. 57, left hand side). For that, the integrating sphere is closed on the reflection port by a reflection standard. For the measurements in this thesis, it is a Spectralon®. The monochromater scans the wavelengths from 200nm to 1000nm and the maximum intensity of the light incident on the detector is recorded. In this way, the spectrum of the light bulbs and the specific detector response can be taken into account and this baseline be subtracted from the sample spectra.

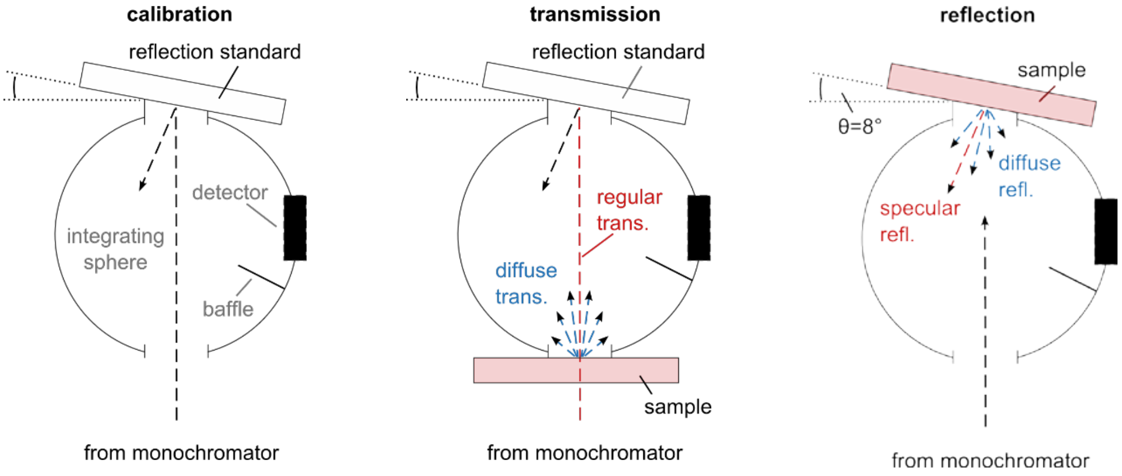

Fig. 57: Configuration of the integrating sphere for the calibration (left), the transmission (center) and reflection (right) measurements by the photospectrometer.

3.5 X-ray photoelectron spectroscopy (XPS)

X-ray photoelectron spectroscopy (XPS) serves to determine binding energies of core electrons. For that purpose, a sample is irradiated by monochromatic X-rays at a sufficient energy to eject electrons. From a measurement of their kinetic energies when leaving the sample, the initial binding energy can be calculated by the energy conservation principle:

$$E_{e,binding} = h\nu_{X-ray} - E_{e,ejected} \qquad \textit{Eq. 61}$$

The principle of an XPS measurement is sketched in Fig. 58. XPS measurements are done in ultra-high vacuum (UHV) to avoid contamination, absorption of the incident X-ray beam or collisions of ejected electrons before they reach the detector. It principally consists of the X-ray source and a detector to collect electrons leaving the sample at a certain angle θ. To compensate the positive charge left on the sample, an electron beam constantly replaces the charges ejected towards the detector. This requires also to insulate the sample from the ground to block any other compensation path which could result in different samples having differing surface potentials.

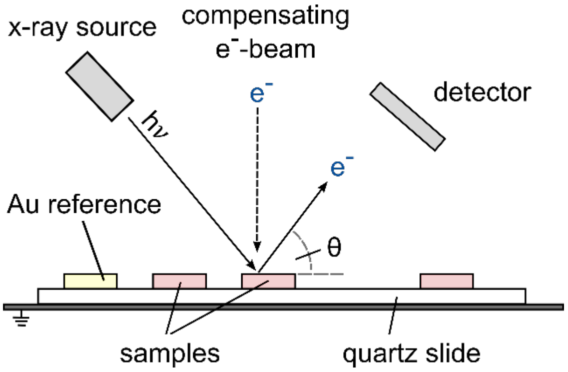

Fig. 58: Principle of X-ray photoelectron spectroscopy (XPS, left) and the instrument setup (right).

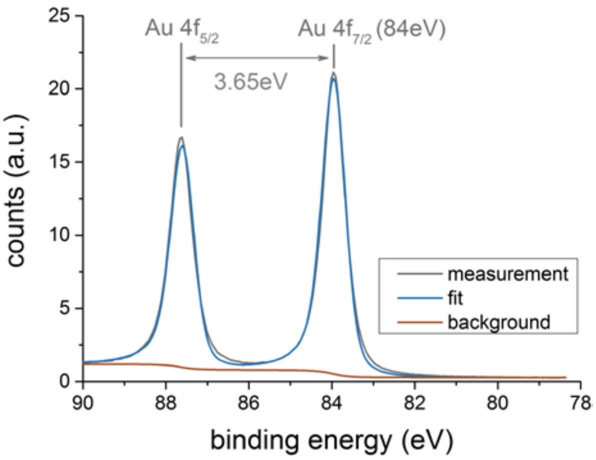

Fig. 59 : Au 4f doublet of a gold reference at $E_{binding}$ of 84eV and 87.65eV (left). On the right, fitting parameters from CasaXPS [177] are summarized.

Energy calibration is done using the 4f doublet of a gold reference that at binding energies of 84.00eV and 87.65eV *[178]*. The advantage of using gold over carbon on the surface from contaminations is, that it does not oxidize and thus has a stable peak position.

A measurement of a sample results in a spectrum (Fig. 60) that directly reflects the chemical order of an atom and the peaks are labelled accordingly, using the nomenclature from atomic physics. Electrons bound to an atom are characterized by their principal, angular and spin quantum number n (= 1,2,…), l (= s,p,d,…) and s = ±1/2 respectively. The latter two quantum numbers couple (spin-orbit coupling) to form the total angular momentum quantum number j = l + s and as the spin can take values of ±1/2 , electrons from all orbitals with l > 0 form doublets. Only s orbitals (l = 0) form singlets, as electrons have no angular momentum and thus also no spin-orbit coupling occurs.

Table 14: Possible reference peaks used for calibrating XPS spectra.

element	orbital, j	chemical	peak (eV)	reference
Au	$4f_{5/2}$ $4f_{7/2}$	Au – Au	87.65 84.0	[178]
C	C1s	C – C	284.8	[178]
		C – O – C	~ 286	[178]
		O – C = O	~ 288.5	[178]

The position of a doublet is influenced by the bonding partners of an atom. So can the presence of nitride bonds shift a metallic peak to higher binding energies and bonding to oxygen can shift it even more. Usually, due to the averaging over many atoms more than one type of bonding occurs and the resulting spectrum shows the envelop of several doublets, that need to be decomposed to see the different contributions.

This is done in this thesis using the software CasaXPS [177]. Three a priori constraints are used for this decomposition procedure for all XPS spectra shown in this thesis: 1) The surface areas of the peaks of a doublet have fixed ratios according to Table 15 which is deduced from the degeneracy of j states. 2) The FWHM of two peaks from the same doublet are equal. 3) The peaks of a doublet are 1.6 to 2.1eV apart.

Table 15: Surface area ratios between the two peaks of a doublet belonging to a certain angular quantum number.

angular quantum number l	j	surface area ratios
s	1/2	singlet
p	1/2; 3/2	1:2
d	3/2; 5/2	2:3
f	5/2; 7/2	3:4

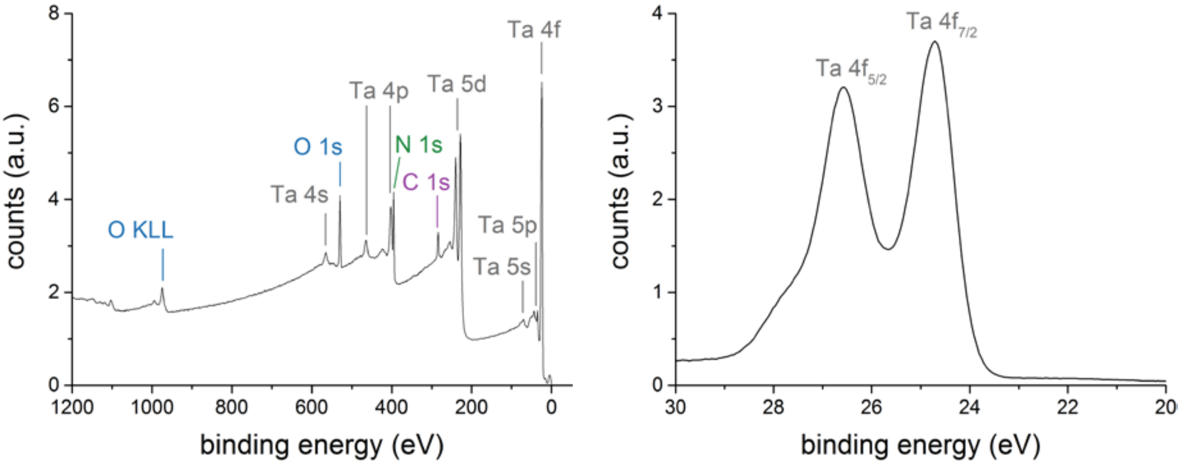

Fig. 60: Left: Survey spectrum (left) and zoom on the Ta 4f binding energies. O KLL indicates a peak arising from the ejection of an electron from the L shell during the filling of a K shell by an electron from the L shell (Auger electron). Right: Zoom on the Ta 4f doublets. The sample was deposited at a substrate temperature of 600° by DCMS at 80W in Ar/N_2/O_2 (29.5/20/0.5sccm).

3.6 Optical emission spectroscopy (OES)

Optical emission spectroscopy is a way to observe radiative deexcitation of atomic, molecular and ionic states. The spectrometer used for this thesis is Czerny-Turner monochromator with a focal length of 0.5m that has an intensified charge-coupled device (ICCD) at its exit port.

Emitted photons from the plasma discharge are collected by a collimator that focusses the light onto a fiber connected to the spectrometer. At its entrance, the fiber projects its light onto a slit from where it traverses into the monochromator. A collimating mirror projects the slit onto a grating which diffracts the light into its different colors. Further down, the collimated beam is again focused on the ICCD onto which the entrance slit is imaged, only that it is decomposed into the different colors now. Vertical binning of the pixels along the slit height, then yields a spectrum of intensity versus wavelength.

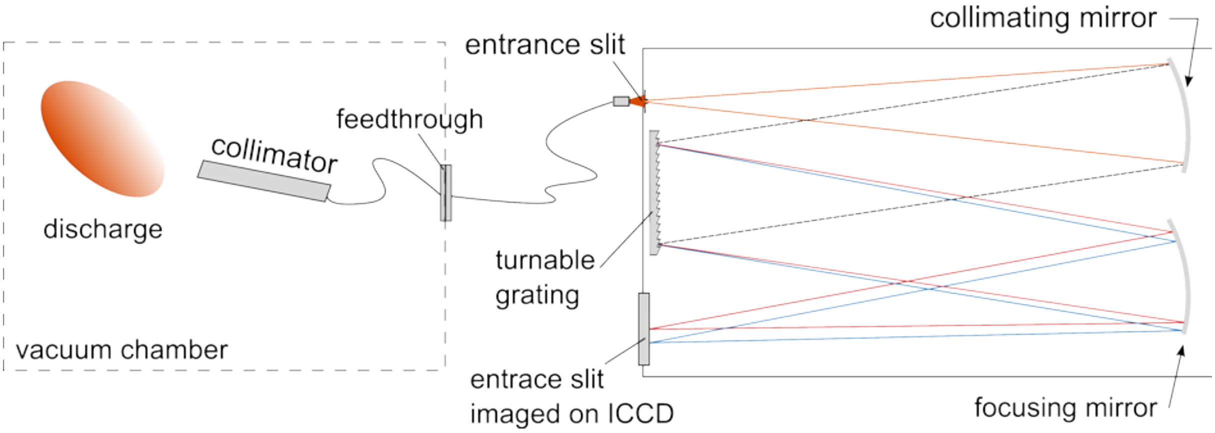

Fig. 61: Setup of the optical emissions spectroscopy and working principle of the spectrometer. See text for explanations.

3.7 Mass spectrometry (MS)

A mass spectrometer samples the atomic flux through a small orifice from a discharge and separates different charge states, masses and energies. These are counted in the mass spectrometer on a detector at the end of a filtering process. Hence, different distributions such as the ion energy distribution function can be recorded.

Its experimental setup is schematically illustrated in Fig. 62. Behind a sampling orifice is an electron injector to collisionally ionize the incoming flux. This unit was not used in the measurements presented in Chapter 4 as the focus was on measuring the *ions* that did not need further ionization. Further down the flight tube, a 45° sector analyzer selects atoms with certain velocities ratios according to the Lorentz force. This selection is further narrowed down by an electric quadrupole that consists of four electrodes positioned along the ion beam axis. The application of an alternating electric field with phase shifts between the electrodes, lets the ion beam oscillate transversely to the direction of propagation. By adopting the frequency of the bias to a resonance frequency of a certain mass, an atom of this mass can traverse the quadrupole while ions with differing masses are moved out of the axis and are thus lost. The combination of a magnetic sector analyzer and an electric quadrupole thus allows to filter for mass and energy.

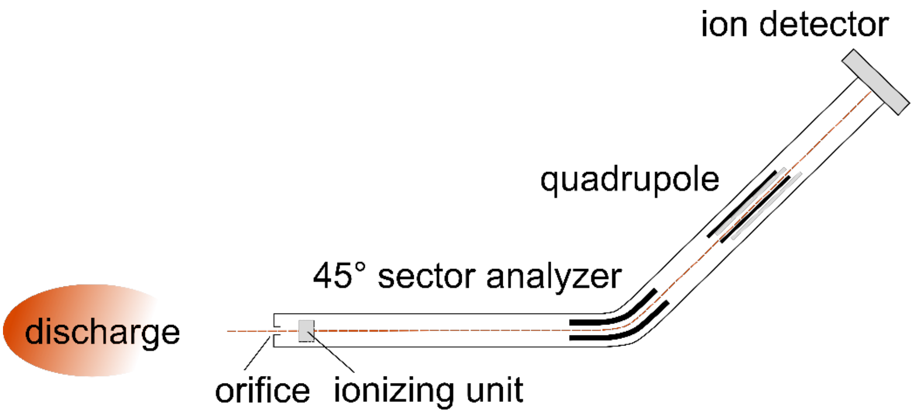

Fig. 62: Schematics of a mass spectrometer.

The adjustment of the many parameters of the mass spectrometer, in particular the potential of electromagnetic lenses, is done automatically using a tuning procedure provided by the spectrometer manufacturer. The objective of this procedure is to adopt the parameters in a way to maximize the ion signal at the detector. This, however, does not necessarily keep the shape of ion energy distribution function, as exemplified in Fig. 63. Here, the extraction voltage V_{extr}, which is the potential of the acceleration lens right behind the entrance orifice, is varied and the change of the ion energy distribution function as a function of this potential is recorded.

As observed, the apparent ion distribution function varies strongly as a function of V_{extr} in particular in the low energy region close to 0eV. The reason for this is that low energy ions are more easily deviated by the lens potential which increases the transfer function for low energy ions. For higher energies, this deviation becomes less and less effective so that the transfer function for higher energy ions decreases steadily. To still make ion energy distribution functions comparable, the same tuning was used for all experiments done for this thesis.

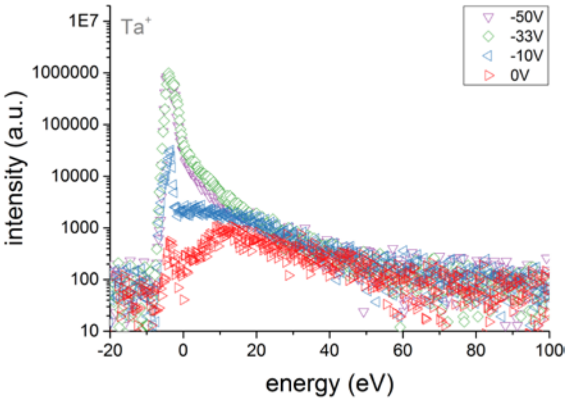

Fig. 63: Ta$^+$ *signal from a HiPIMS discharge in pure Ar as a function of extraction voltage* V_{extr}. *(Discharge parameters: HiPIMS at 80W average power, 10µs pulse length, 0.5Pa working pressure.)*

3.8 Photoelectrochemical measurements

The principal application of the samples prepared for this thesis is the photoelectrolysis of water. Its measurements are outlined here. A more detailed description of the specific device and methods used can be found in [97].

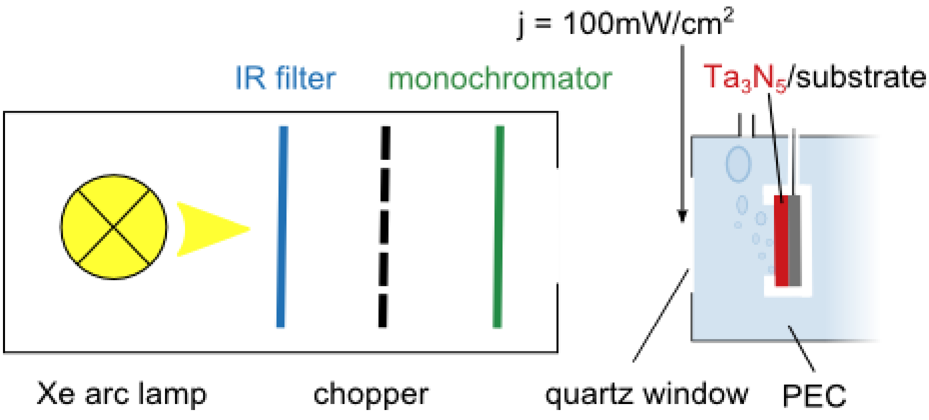

Fig. 64: Experimental setup of the photoelectrochemical measurements.

The general setup consists of a light source and the photoelectrochemical cell (PEC). The light source (Fig. 64) is a Xenon arc lamp that is filtered for infrared radiation to avoid the heat-up of the PEC. A mechanical chopper provides the continuous alternating illumination and shadowing of the sample to see the effect of the light and to determine the photocurrent. Finally, a monochromator can be used to calculate the photocurrent as a function of wavelengths, which is a measure necessary to calculate the IPCE (Eq. 14).

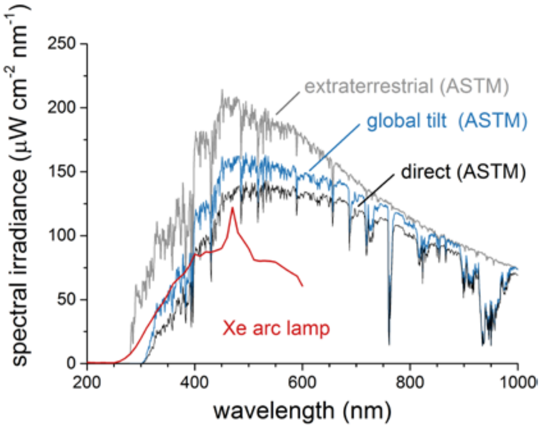

Fig. 65: Xenon arc lamp spectrum at the sample position compared to three irradiance models defined by the ASTM-G173-03 standard [179].

The irradiance just at the sample/substrate position is at 100mW/cm^2 integrated over all wavelengths which is slightly lower than the solar constant of 137 mW/cm^2 [180]. Fig. 65 presents its spectrum in comparison with three irradiance models, the irradiance just outside the Earth's atmosphere (extraterrestrial), the irradiance on the Earth onto a surface that is tilted by 37° (global tilt) and the irradiance coming directly from the sun and excluding the diffusive component (direct).

The PEC is a glass beaker filled with an electrolyte (0.1M K_2SO_4 and KOH at pH=11 or pH=13). Towards the light source, it has a quartz window that transmits wavelengths down to the ultraviolet range.

The performance of a sample is evaluated using a setup of three electrodes. The working electrode contains the material to be tested, which is a Ta_3N_5 photoanode in the case of this thesis. It can be biased with respect to a reference electrode that provides a constant reference potential. In order to remain constant, the reference electrode cannot have any currents passing through it. To close the circuit, a counter-electrode is therefore used, providing the current equal to that flowing through the working electrode [36]. The function of the potentiostat is to ensure the proper functioning of this setup, i.e. to apply the desired bias between the working and the reference electrode while having the current flow between the counter and the working electrode.

The reference electrode used in this thesis is an Ag/AgCl/sat. KCl electrode with a potential of 0.198V vs. SHE [39]. It is a silver metal electrode immersed into a saturated KCl electrolyte. The electrode is connected to the electrolyte of the photoelectrochemical cell by a membrane allowing to exchange charges, but neither ions nor neutral atoms. The potential of the semiconductor electrode vs. Ag/Cl can be converted to the SHE by [39]:

$$\phi_{vs.\ SHE} = \phi_{vs.\ Ag/AgCl} - 0.198V \qquad \textit{Eq. 62}$$

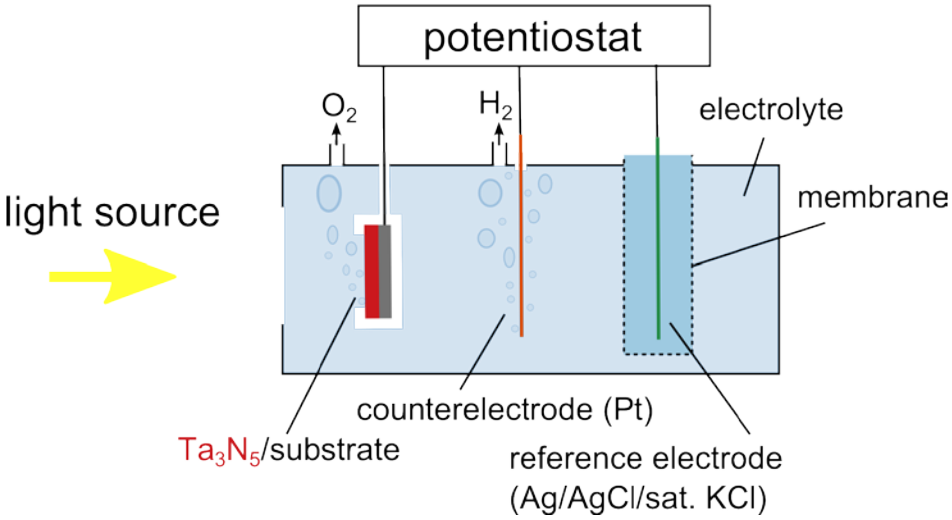

Fig. 66: Setup of the photoelectrochemical cell.

Cyclic voltammetry is a standard experiment also conducted in this thesis to judge the performance of prepared photoanodes. It consists of scanning a potential range from a negative few hundreds of mV to a positive few hundreds of mV while illuminating the sample under chopped light to observe the difference between the current in the dark and the current under illumination. A typical result is shown in Fig. 67. The difference between the current under illumination and the dark current is the photocurrent.

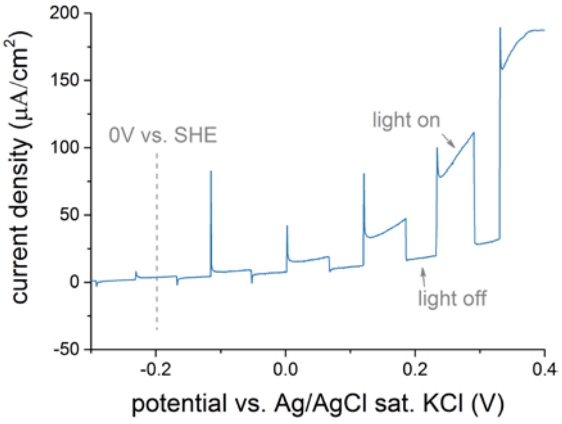

Fig. 67: Cyclic voltammetry between -0.3V and 0.4V under chopped light illumination from a Xenon arc lamp.

4 Properties of magnetron-sputtered TaN thin films

The objective of this chapter is to determine optimum conditions for the sputter-deposition of crystalline thin films from a Ta cathode in an Ar/N_2 atmosphere. The first subsection is dedicated to experiments using the abundantly found δ-TaN phase as a study system. The goal is to determine the influence of the N_2 flowrate and the magnetron operating mode on the structure and the elemental composition of the films (Section 4.1). The results of these experiments are then correlated with the results from a mass spectrometer study to determine the influence of low-energy ion bombardment onto the growing film as a function of sputter mode (Section 4.2). This is followed by a subsection to determine the effect of backscattered neutrals from the cathode (Section 4.3). Lastly, the findings are summarized and a conclusion is drawn with respect to the optimum deposition conditions of crystalline Ta_3N_5 films (Section 4.4).

4.1 Synthesis and characterization of films by DC and HiPIMS

This subsection covers the preparation of δ-TaN thin films (Chapter 4.1.1) and their structural characterization as a function of N_2 flowrate (Chapter 4.1.2.1) and deposition mode (Chapter 4.1.2.2). Interesting from the structural characterization is in particular the question under which conditions the largest grains are obtained. This becomes important for growing the semiconducting Ta_3N_5 phase as the grain size correlates with key performance parameter such as carrier mobility and carrier lifetime [181]. This first section is followed by analyzing the elemental composition and possible contaminants (Chapter 4.1.3).

4.1.1 Film preparation

Thin films were deposited on a piece of monocrystalline Si(100), without any cleaning pretreatment apart from dusting them off under a stream of N_2. The samples were clamped onto a sample holder and inserted into the deposition chamber via a load lock. Ar and N_2 were then injected into the deposition chamber with a total flowrate of 50sccm. The partial flowrates for Ar and N_2 varied from sample to sample. The pressure was controlled to 0.5Pa or 5.0Pa by adjusting the position of a throttle valve between the deposition chamber and the turbomolecular pump. The target was then sputter-etched for 5min with a closed shutter to sputter off a possibly oxidized target surface. Subsequently, the shutter was removed, and the substrate holder set to rotate at 20 rotations/min around the reactor axis. As the magnetron is placed between the axis and the reactor side wall, the substrate passed over the magnetron 20 times per minute. The purpose of having the substrate rotate was to keep the substrate temperature down and increase the homogeneity of the film thickness.

Two different magnetron sputtering modes were employed for this chapter, direct current magnetron sputtering (DCMS) and high-power impulse magnetron sputtering (HiPIMS). Both were kept at 80W average power for comparison reasons.

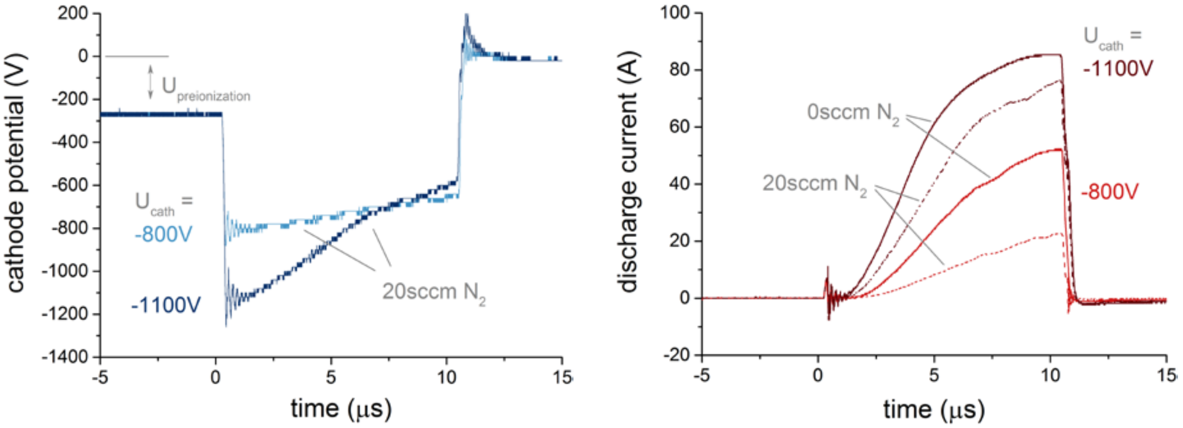

Fig. 68: Left: Cathode potential during a HiPIMS pulse in 20sccm N_2 at a cathode bias of U_{cath}=-800V and -1100V. Right: Discharge current during a pulse at the same cathode biases in a non-reactive (0sccm N_2) and reactive atmosphere (20sccm N_2).

DCMS conditions

The 80W average power for the DC discharge resulted in a voltage of approximately 240V and a current of 330mA. The exact numbers varied with N_2 flowrate as well as with the target utilization (cf. Section 3.1.2).

HiPIMS conditions

For the HiPIMS mode, a pulsing unit was used in between the DC power supply and the cathode. It had a pre-ionization feature, that biased the target to -200V prior to triggering a pulse [182]. Due to its small capacitance, the pulse length needed to be kept short and was chosen to be τ_{pulse} = 10µs. The period T was adopted for the average power to equal 80W. The cathode biases tested were essentially -800V and -1100V which gave typical discharge current and cathode potential curves presented in Fig. 68.

The majority of the films were deposited at a pressure of 0.5Pa and some additional films in HiPIMS mode were deposited at a higher pressure of 5Pa to see any effects from stopping energetic neutrals backscattered from the cathode (cf. Section 4.3).

4.1.2 Structural characterization

4.1.2.1 The influence of the N_2 flowrate

The purpose of this section is to determine the influence of the N_2 flowrate on the film structure. For that, thin film samples were deposited by HiPIMS at a cathode bias of -800V for 40min. The thickness for these films was measured to be (70 ± 10)nm without any observable change in thickness with varying the N_2 flowrate.

The resulting diffractograms are shown in Fig. 69. It is important to note, that the bump marked with ‘diffusion from aperture’ does not stem from the sample, as it can also be found on an uncoated monocrystalline Si substrate (see purple dashed diffractogram in Fig. 69). The bump evidences stray radiation from the aperture of the X-ray source. It can be seen in Fig. 69 and Fig. 70 only. For all other experiments, the aperture is replaced so that stray radiation is avoided.

In general, the films can be divided into two groups. The films deposited at low N_2 flowrates exhibit a crystalline structure in their diffractograms (Fig. 69). It is identified to be the δ-TaN phase. A representative example of these films is the one deposited at ϕ_{N2} = 3sccm (black curve). At higher N_2 flowrates, the crystalline peaks disappear and a halo appears at 23.5nm^{-1}. A representative example for this is the diffractogram of the sample deposited at ϕ_{N2} = 7sccm in Fig. 69 (blue curve).

To investigate the origin for this halo, films under the same conditions but varying deposition times were prepared. This resulted in thicknesses between 40nm and 280nm. Their diffractograms are shown in Fig. 70. It can be seen that at a thickness of 150nm, i.e. twice as thick as the samples from Fig. 69, light features appear. Increasing the thickness even more to 280nm, a clear δ-TaN signature is again observed.

It is possible, that this thickness dependence is the effect of an increased final temperature of the substrate. This could be due to the fact that the deposition process is four times longer for the thickest sample compared to the $70nm$ thick samples. However, the explanation is unlikely as the temperature is verified to remain low (< 100°C).

It is more likely that this is a direct effect of the sample thickness, showing the limits of the diffractometer. One could assume a decreasing grain size with increasing the N_2 flowrate. As this would decrease the crystalline volume in favor of grain boundaries, the diffracted intensity would decrease. Below a certain grain size, the diffracted intensity could be covered by the noise in which case a sample appears to be amorphous. As the diffracted intensity can be increased by increasing the thickness, the δ-TaN signature reappears for the thickest samples measured.

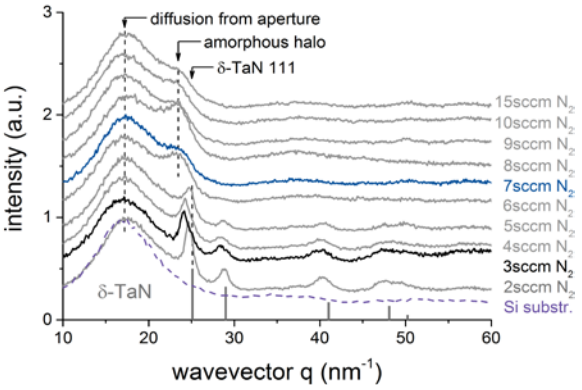

Fig. 69: Diffractograms for films by HiPIMS at a cathode bias of -800V as a function of N_2 flowrate. The Si ref. (purple dashed curve) refers to the diffractogram of a blank monocrystalline Si(100) substrate without film which proves that the bump around $q \approx 17nm^{-1}$ stems from the experimental setup. The grey bars indicate the reference peak positions from the powder diffraction file (PDF) for δ-TaN (PDF 01-089-5196).

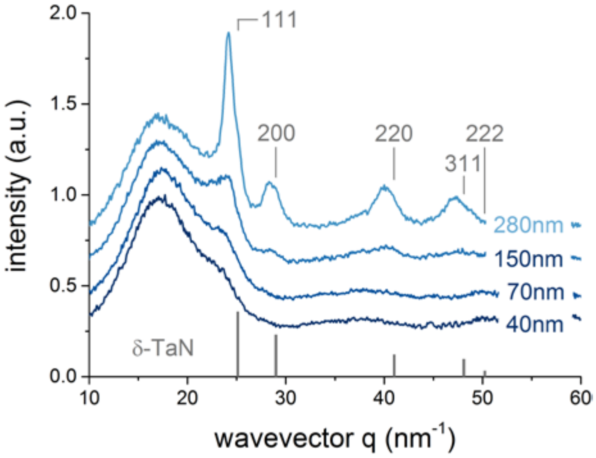

Fig. 70: Diffractograms for films deposited at an N_2 flowrate of 7sccm with varying deposition times. Only the last two samples exhibit the crystalline δ-TaN signature, while all other samples are allegedly amorphous.

A decreasing grain size with increasing the N_2 flowrate can indeed be observed. Grain sizes typically correlate with the full width at half maximum (FWHM) of diffraction peaks [183]. To see the effect, the FWHM of all crystalline samples presented in Fig. 69 and the thickest sample from Fig. 70 are measured and plotted against the corresponding N_2 flowrate (Fig. 71). A peak broadening with an increasing N_2 flowrate can be evidenced. At low N_2 flowrates, the FWHM increases strongly and flattens out at higher flowrates. The last data point from the sample with a thickness of 280nm integrates seamlessly into the trend formed by the 70nm thick samples. It suggests that there is no correlation between grain size and thickness. This supports the hypothesis from above, that the disappearing diffraction features in Fig. 69 are actually a limit of the diffractometer rather than a feature of the films.

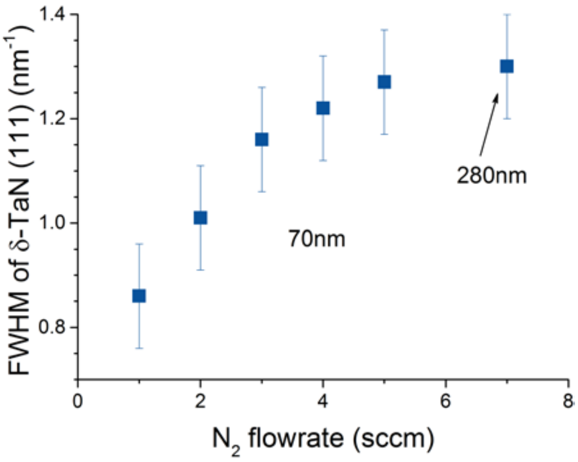

Fig. 71: FWHM of the δ-TaN (111) peak of the δ-TaN-crystalline samples from Fig. 69 (labelled by '70nm') and the thickest sample from Fig. 70 (labelled by '280nm').

The amorphous halo from Fig. 69 is thus a remainder of the (111) peak of the δ-TaN phase. Its position is slightly shifted to smaller wavevectors q which can be made plausible by the following argument. As the incorporation of nitrogen into the material creates Ta vacancies [29], the unit cell shrinks and with it the lattice parameter a. This is accompanied by a shift of the peak to lower wavevector q according to Eq. 63.

$$q_{hkl} = \frac{2\pi\sqrt{h^2+k^2+l^2}}{a}, \qquad \text{Eq. 63}$$

where h, k, l are the Miller indices. Taking the smallest and the largest experimentally determined lattice constants for δ-TaN summarized in Table 2, yields peak position of q = 25.1nm^{-1} for a = 0.4337nm and q = 21.7nm^{-1} for a = 0.502nm which indicates a large range of possible positions for the (111) peak. As the amorphous halo can be found at q ≈ 23.5nm^{-1}, it lies well in the range of possible positions for the (111) peak of the δ-TaN phase.

At the same time it is still save to use the term 'amorphous halo' as the grain size is already very small. The Scherrer equation can yield an order-of-magnitude estimate of the grain size and is given by [183]:

$$D_{Scherrer} = \frac{4\pi k_{Scherrer}}{\Delta q}, \qquad \text{Eq. 64}$$

where the equation is transformed for the use in q space. k_{Scherrer} is typically around 0.9 [183].

The broadest peak from Fig. 71 has Δq = 1.3nm^{-1} which yields a Scherrer grain size $D_{\text{Scherrer}} \approx$ 9nm at the border between a nanocrystalline and amorphous material. In fact, even the narrowest FWHMs from Fig. 71 already shows a nanocrystalline material with $D_{\text{Scherrer}} \approx$ 13nm. In this thesis, the term amorphous refers to absence of pronounced crystalline peaks in the diffractogram.

The peak broadening witnessed in Fig. 71 indicates a decreasing grain size with N$_2$ flowrate. There are several explanations for this. One hypothesis is that nitrogen is limiting the adatom mobility on the surface and in this way hindering the growth of crystallites.

This can be made plausible by comparison with other phases, for which a more comprehensive understanding of the atomic processes is available. TiN is such a phase which allows comparison to the δ-TaN phase due to its chemical and structural similarity. Both are transition metal nitrides with the metals from group 4 and group 5, respectively, that crystallize in the NaCl type [184].

In a computational study on TiN, Gall et al. [185] calculate the activation energy required for an adatom to hop on a surface from a site A to a site B of equal symmetry. The investigation is made for a Ti and N adatom and a TiN surface cluster on a TiN(001) and an N-terminated TiN(111) surface. While the metallic Ti adatom on a TiN(001) surface is rather mobile with a activation energy of 0.35eV, all other activation energies involving nitrogen bonds are more than a factor of two higher. So is the N activation energy on a TiN(001) surface at 0.95eV, the TiN-cluster diffusion activation energy is ≥ 0.88eV and the Ti diffusion energy on an N-terminated TiN(111) surface is $1.74eV$. If the same tendency is found in δ-TaN, the decreasing grain size found as a function of N_2 flowrate could be due to a decreased mobility of Ta adatoms in the presence of nitrogen.

A different explanation could hold the N_2 vibrational excitation cross-section responsible. It peaks between 1eV and 10eV (Fig. 72) and thus overlaps largely with the electron energy distribution function (EEDF) in both DCMS [186] and HiPIMS [187]. A decrease in the EEDF in that region can therefore be expected with an increasing N_2 flowrate. The consequence is a decrease in the number of ionizations of the sputtered Ta, which has an ionization energy of 7.54eV. As ions are known to promote adatom mobility, the inverse can be expected in the case of a decreasing ion flux. A reduction in grain size could thus be due to a reduction in ion flux onto the film.

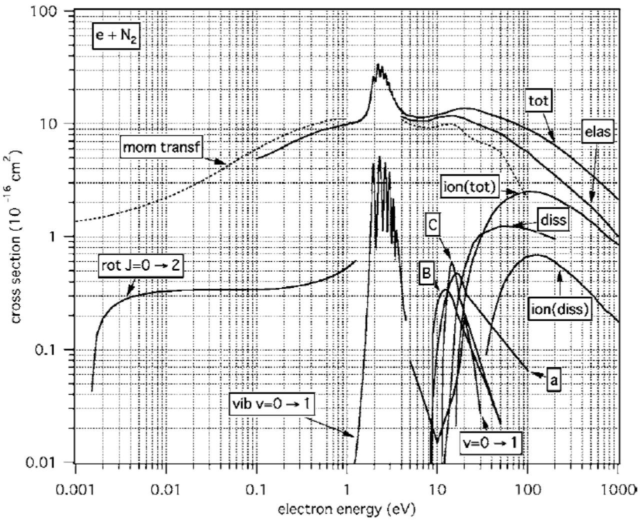

Fig. 72: Various N_2 cross-section as a function of incident electron energy. In particular, the vibrational excitation cross-section (the cross-section for v=0->1 is shown), overlaps with the average energy of the electron energy distribution function (EEDF) of several eV. From [188].

Finally, a higher nitrogen incorporation into the films (cf. Fig. 77 in Section 4.1.3) with increasing N_2 flowrate could also held responsible. Non-stoichiometries must naturally be accompanied by stress that can be released by the incorporation of defects. An over-stoichiometric nitrogen incorporation into the films could therefore be accompanied by peak broadening.

In conclusion, for the deposition of δ-TaN thin films, the N_2 flowrate should be kept to a minimum for obtaining large grains. However, as calculated above, the range of grain sizes is in any case very small, so that a limited improvement can be expected from tuning the N_2 flowrate.

4.1.2.2 The influence of the magnetron operating mode

This paragraph serves to determine the optimum magnetron operating mode. Two modes are to be compared, the conventional DC sputtering mode and the HiPIMS mode. Latter is of interest here, as it has been shown to result in many favorable film properties for different materials systems in the past (cf. Section 2.3.3). The interest for this thesis is to deposit films with large grains, a property for which little comparative studies exist between HiPIMS and DC. Furthermore, mechanisms that lead to larger or smaller grains in one operating mode or the other are yet unclear (cf. Section 2.3.3).

Films were deposited in DCMS, and HiPIMS at a cathode bias of -800V and -1100V. The deposition time was 40min resulting in thicknesses of (150 ±10)nm for the DCMS case, (70 ±10)nm for the HiPIMS case with a bias of -800V and (50 ±10)nm for the HiPIMS case with a bias of -1100V.

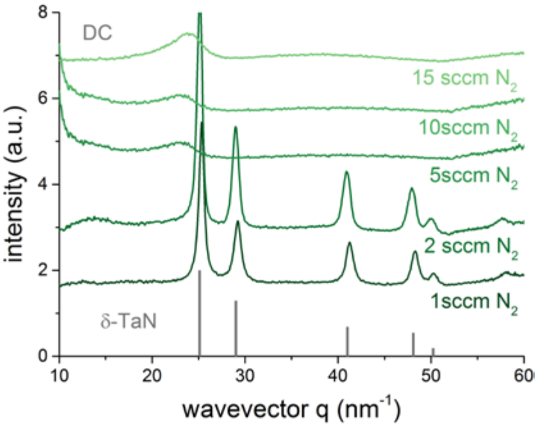

Fig. 73: Diffractograms of DC-sputtered films at varying N_2 flowrate as a function of N_2 flowrate.

The diffractograms of the samples are shown in Fig. 73 for the DCMS case and Fig. 74 for the HiPIMS case[1]. In general, all three process conditions show the same transition from a δ-TaN crystalline film to an amorphous diffractogram with increasing the N_2 flowrate as seen in the previous section (Section 4.1.2.1). A big difference, however, lies in the width of the diffraction peaks. The DC-sputtered films exhibit the narrowest peaks, while the peaks for the HiPIMS samples are broader. Among the two HiPIMS modes, the films sputtered at a bias of -1100V exhibit the broadest peaks corresponding to the smallest grain size.

---

[1] All diffractograms shown from Fig. 73 on, do not exhibit the diffusion bump any more as a different aperture of the X-ray tube was used compared to the diffractograms in Fig. 69 and Fig. 70. This is believed to also have changed the FWHM of the peaks so that samples measured with one aperture cannot be readily compared to the samples measured using other.

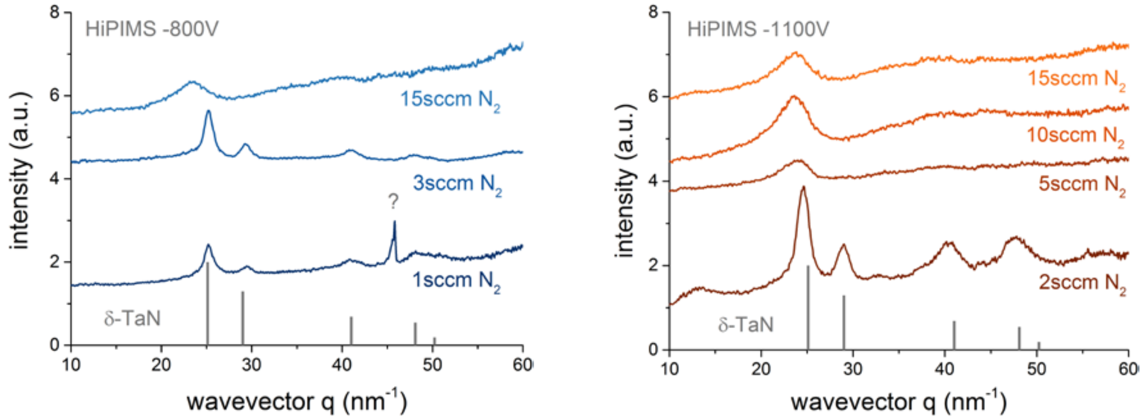

Fig. 74: Diffractograms of HiPIMS films at varying N_2 flowrate and a substrate bias of -800V (left) and -1100V (right).

The FWHM of the samples is plotted as a function of cathode bias in Fig. 75. For this, an additional sample was deposited by HiPIMS at a cathode bias of -600V. For the HiPIMS film (between -600V and -1100V), an almost linear trend can be imagined, while the DC films around -300V have a similar FWHM to the HiPIMS films at a bias of -600V. However, as mentioned in Chapter 3.2, the instrumental broadening needs to be considered which lies around 0.3nm^{-1}. Thus, the films with the lowest FWHM already lie close to the instrumental limit and are likely be influenced by this.

The peak broadening due to the incorporation of N_2 is not considered in this analysis, but error bars are added to the FWHM values that correspond to the range of FWHM values obtained by varying the N_2 flowrate (Fig. 71). With these bars it becomes obvious, that even considering possible uncertainties due to varying N_2 incorporations, the diffraction peak broadens and the grain size decreases with cathode bias.

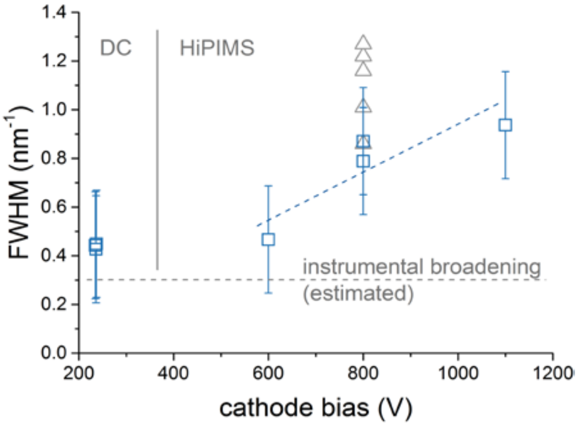

Fig. 75: FWHM of the 111-peak of the δ-TaN phase for various bias potentials (blue squares). For DC-sputtered films, rather than keeping the bias voltage constant, the power was regulated to 80W, which leads to a cathode potential of around -240V. The grey triangles indicate the FWHM of samples from Fig. 71 where the shift to higher FWHM values comes from a higher contribution from instrumental broadening. The range of these values is added as an error bar to the data points from this chapter.

The reason for this broadening could be energetic neutrals that are backscattered at the cathode and incorporate defects into the samples. The energy range of backscattered neutrals scale with the mass ratio of the impinging ions and the cathode atoms [112]. This becomes thus an issue for the heavy atoms such as Ta, sputtered in an Ar atmosphere. This hypothesis is more thoroughly analyzed in Section 4.3. For now, a low cathode potential seems to be beneficial for the deposition of Ta_3N_5 thin films.

4.1.3 Elemental composition

The elemental composition of the films analyzed above is deduced from IBA experiments. Fig. 76 shows a typical spectrum in which not only ^{181}Ta and ^{14}N is found, but also ^{40}Ar and ^{101}Ru (Fig. 76). Latter is due to experiments conducted in the reactor before this thesis. Its areal density gradually decreased with time and is not observable any more in the last samples measured by IBA for this chapter. Other contaminants are not observed. However, as the RBS cross-section rapidly decreases with decreasing atomic number (cf. Section 3.3.1), the detection of light elements becomes increasingly difficult. In addition, all elements with a smaller atomic number than Si have signals on top of a large Si background and need to be present in large quantities to be detectable (such as e.g. ^{14}N). For that reason, to determine the ^{14}N and ^{16}O areal densities, NRA has been used rather than RBS.

In the following, the Ta-to-N ratio of the films is discussed and explanations presented for the incorporation of contaminations and impurities. The error bars on the results from IBA analysis take into account a 3σ statistical uncertainty and, if applicable, the uncertainty of ±10nm from the thickness measurements.

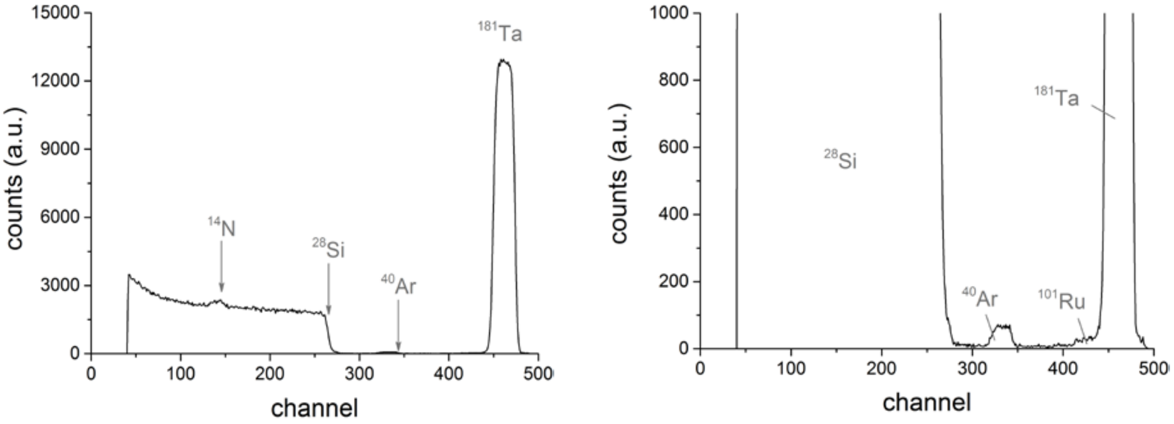

Fig. 76: Typical RBS spectra of a film deposited by HiPIMS at -800V in an Ar/N_2 atmosphere. The arrows point to the ^{181}Ta, ^{28}Si, ^{14}N and ^{40}Ar peak (left). A zoom reveals additional contamination by ^{101}Ru (right).

4.1.3.1 Tantalum and nitrogen

One condition to prepare the δ-TaN or the Ta_3N_5 phase, is that the films contain sufficient nitrogen. To quantify the nitrogen in the films, two sets of samples are prepared by DCMS and HiPIMS at a cathode voltage of -800V. The areal densities of ^{181}Ta, ^{14}N and ^{16}O are measured and the absolute densities are then calculated using the sample thickness.

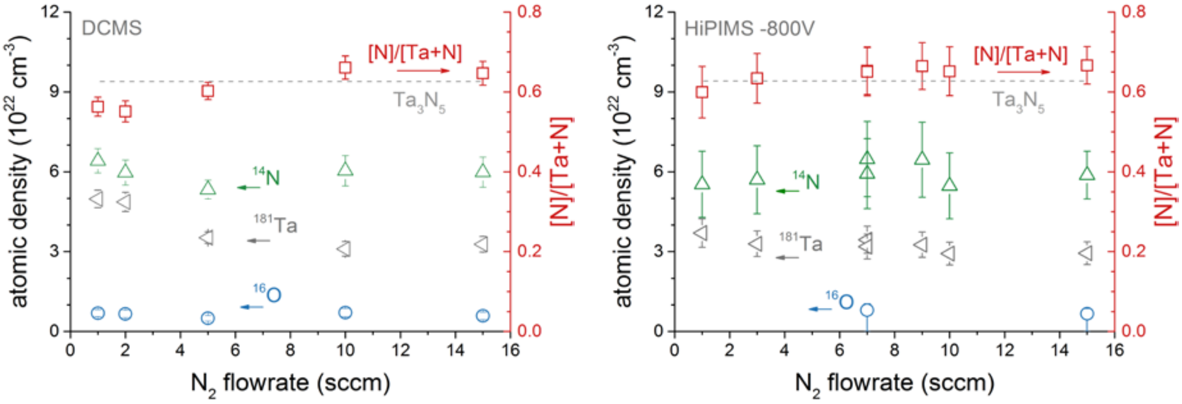

Fig. 77: ^{181}Ta, ^{14}N and ^{16}O atomic densities in films prepared by DCMS (left) and HiPIMS at a cathode voltage of -800V (right).

The result of the elemental analysis is shown in Fig. 77. For both deposition modes, the N densities are similar and remain constant at around $6{\cdot}10^{22}$cm^{-3} for the N_2 flowrates tested. The Ta densities, on the other hand, differ slightly. In the DCMS case, they start at around $5{\cdot}10^{22}$cm^{-3} at low N_2 flowrates before they drop to around $3{\cdot}10^{22}$cm^{-3}. In the HiPIMS case, the Ta density is around $3{\cdot}10^{22}$cm^{-3} and no decrease can be observed within the uncertainties.

The similar densities for ^{181}Ta and ^{14}N in both magnetron operating modes for high N_2 flowrates is likely due to a nitrogen incorporation limit set by the rate of N desorption from the film. Two processes could be imagined here that have been proven to be relevant for the desorption of an N adatom from a TiN surface [185] and could be imagined also for the δ-TaN phase: a) the recombination of two N adatoms on the film surface (Eq. 65) or, b) an atomic N in the gas phase, that attaches to an N adatom to form gas phase N_2 (Eq. 66). The rate of both processes would depend on the N adatom density, and the second process in addition on the gas phase N density. As both are likely to increase with N_2 flowrate, this is a valuable hypothesis for a limiting incorporation of N into the film.

$$2N^{ad} \rightarrow N_2^{gas} \qquad \textit{Eq. 65}$$

$$N^{gas} + N^{ad} \rightarrow N_2^{gas} \qquad \textit{Eq. 66}$$

The reason for the higher Ta density in the DCMS films compared to the HiPIMS films, at least for low N_2 flowrates, is due to the different deposition rates between DCMS and HiPIMS [189] as can be seen here in the differences in thickness of the two sets of samples ($150nm$ in DCMS vs. $70nm$ in HiPIMS). Thus, as the metal atoms arrival rate in DCMS is higher, the stoichiometry shifts in favor of Ta.

The important parameter to determine whether a process incorporates sufficient nitrogen into the films, is the ratio between N and Ta. The at.% is indicated for the DCMS and HiPIMS films in Fig. 77 by the red squares. The ideal Ta_3N_5 stoichiometry (grey line) is reached between 6 and 10sccm in the DCMS case and between 2 and 4sccm for the case of HiPIMS. Despite the stoichiometry, the films do not show the Ta_3N_5 crystalline phase by X-ray diffraction (Fig. 73 and Fig. 74).

4.1.3.2 Contaminations and impurities

IBA also allows to evaluate possible impurities, in particular ^{16}O, ^{40}Ar and ^{101}Ru, which are discussed in the following.

Oxygen

An oxygen at.% of around 10% in the DCMS and HiPIMS films is deduced in the previous section (cf. Fig. 77). The origin of the oxygen, however, cannot be resolved from those experiments and are therefore separately analyzed here. Possible sources include (1) reactor leaks that result in an unintentional non-zero O_2 flowrate, (2) an oxide layer on the substrate before deposition and, (3) the oxidation of the sample after deposition. The first case would result in a continuous oxygen incorporation during the process, while in the latter two cases, a localized oxygen concentration would be expected. To determine which of the two cases is present in the films deposited for this thesis, the oxygen areal density in the films as a function of their thickness is analyzed. A localized oxygen concentration in the film is expected to yield a constant oxygen areal density as a function of thickness, while a homogeneously distributed oxygen distribution throughout the film thickness would yield a linearly increasing oxygen areal density with thickness.

For this, thin films were prepared by HiPIMS at a cathode bias of -800V. To see the effect of the different oxygen distributions, two sets of films were deposited at 0.5Pa and 5.0Pa, both sets having films with thicknesses ranging from below 50nm to above 250nm. The Ar and N_2 flowrate were fixed to 43sccm N_2 and 7sccm, respectively.

The areal density of the elements in each film are shown in Fig. 78 for the low pressure case (0.5Pa) and the high pressure case (5.0Pa). For the low pressure case, the ^{181}Ta and ^{14}N areal densities increase linearly with thickness. The ^{16}O areal density, however, deviates from this behavior and remains almost constant for all samples.

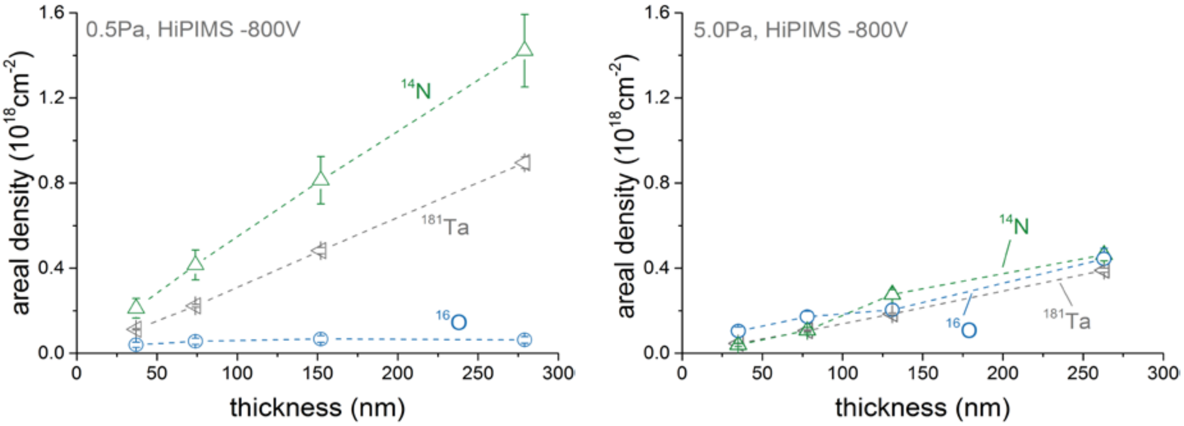

Fig. 78: O, Ta and N areal densities as a function of thickness at a working pressure of 0.5Pa (left) and 5.0Pa (right).

In the high pressure case, the ^{181}Ta and ^{14}N areal densities show a similar trend to the low pressure case, i.e. they increase linearly with thickness. Only their magnitude is slightly reduced compared to the low pressure case. This can be attributed to a lower film density at higher pressures from the deceleration of species by collisions with mainly the background gas. The ^{16}O, on the other hand, follows a completely different trend compared to the low pressure case. It has a similar areal density compared to ^{181}Ta and ^{14}N and, in addition, increases in parallel with the ^{181}Ta and ^{14}N areal densities.

Hence, following the reasoning from above, in the low pressure case, most of the oxygen is localized, thus is either on the substrate before deposition or is in a layer on the surface oxidized after the deposition. In the high pressure case, a homogeneously distributed oxygen incorporation is seen, that stems from leaks in the reactor. As all sources are present independent of the pressure during deposition, a combination of a localized and a distributed oxygen population should actually be present in both sets of samples, with one or the other dominating.

Oxygen is seen in these films as an unwanted contamination. It is thus clear, that the high pressure case, in which films are constituted by one third of oxygen (cf. Fig. 78), is not a valid choice for the deposition of Ta_3N_5. For the low pressure case, the oxygen is likely to be concentrated at the surface or at the interface between film and substrate. Both locations cannot tolerate a deviation from the oxygen at.% from the bulk as an insulating layer could inhibit charge transfer either to the electrolyte or to the conducting substrate.

Oxygen profiling

In order to evaluate the precise distribution of oxygen within the film, an oxygen profiling experiment is conducted using the procedure described in Section 3.3.2.

Two samples were prepared by HiPIMS with a cathode bias of -1100V. One was deposited with no oxygen flowrate (Sample B in Table 16), the other one served as a reference and was deposited with a small O_2 flowrate of 0.5sccm. The total flowrate (Ar, N_2 and O_2) and the pressure was equal in both cases to 50sccm and 0.5Pa, respectively. Both samples had a thickness of 70nm.

The RBS spectra for the reference (Sample B) are shown in Fig. 52. The oxygen is determined to be homogeneously distributed throughout the film thickness and the sample contains 71at.% of oxygen (Table 16). This high at.% of incorporated oxygen leads to the conclusion, that oxygen is easily incorporated, in particular when considering the small O_2 flowrate of only 0.5sccm.

Nitrogen, on the other hand, despite its comparably high flowrate of 5sccm, is little incorporated with only $2at.\%$ of nitrogen found in the films. Contrary to these findings, a sample from Fig. 77, deposited under similar conditions but without any intentional oxygen flowrate, has a nitrogen incorporation of $\geq$ 60at.%. This comparison suggests that oxygen is preferentially incorporated in the film compared to nitrogen.

Table 16: Deposition conditions of the two samples for the oxygen profiling experiments

	sample A	**sample B**
deposition conditions	HiPIMS 1100V cathode bias, 0.5Pa working pressure	
flowrates Ar/N_2/O_2	40sccm/10sccm/0sccm	44.5sccm/5sccm/0.5sccm
spectrum	Fig. 79	Fig. 52
film elemental densities	Non-homogeneously distributed, see text	$Ta_{0.25}O_{0.71}N_{0.02}Ar_{0.02}$, homogeneous
detector resolution	25keV	25keV

Sample A is deposited without any intentional oxygen flowrate. Its RBS spectra as a function of α particle energy are presented in Fig. 79 together with the SIMNRA simulations that allow to derive the elemental profile.

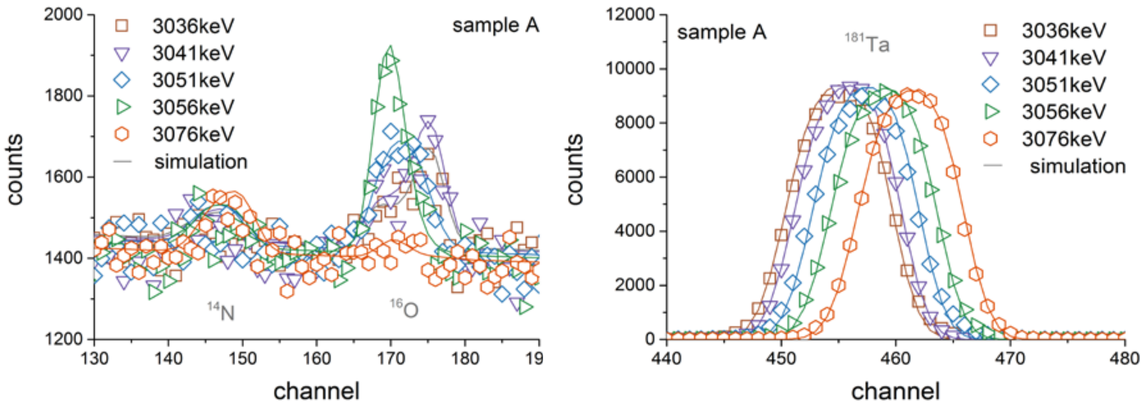

Fig. 79: Experimental (symbols) and simulated (continuous curve) RBS spectra of sample A from Table 16 at different α energies to determine the oxygen distribution.

Fig. 80 summarizes the elemental composition as a function of thickness for sample A. Two locations of concentrated oxygen can be observed. One can be found at the interface between the Si substrate and the film. This is extremely detrimental for the application in view as this large quantity of oxygen at a thickness between 5nm and 10nm certainly presents an insulating layer for charge carriers. A procedure to reduce the oxygen at the substrate/film interface is thus necessary to enable electron transfer onto the metallic substrate in a photoanode (cf. Section 5.2).

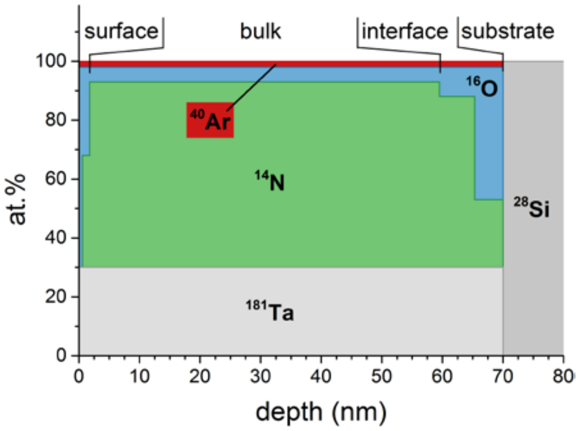

Fig. 80: Elemental composition profile of sample A from Table 16 as determined by RBS.

A second oxygen concentration is found on the surface of the film. Also this is detrimental at first sight for the application in view as, similarly to the interface, charges need to be transferred through that layer. The oxidation of the surface maybe reduced for the deposition of crystalline Ta_3N_5 as it is thermodynamically stable (cf. Section 2.2.1.3). Furthermore, the sample can be stored under N_2 to avoid any oxidation. But at latest when the sample is to be used as a photoanode, the surface is subjected to pure O_2 so that an oxidation may not be avoided. The formation of thin oxide layers in photoelectrolysis experiments is indeed known for nitride semiconductors. And although they reduce the performance of the photoanode, they also protect the anode from further oxidation [21] [39]. The surface layer is thus not considered an issue for the application.

5at.% of oxygen is incorporated into the bulk. This is not necessarily detrimental as oxygen is a critical ingredient to form the Ta_3N_5 phase [49]. However, the precise control of the oxygen incorporated into the film is lost. Furthermore, other impurities may be incorporated into the film without noticing them, as they are not detectable with the method applied here. The reduction of the oxygen incorporation and possible further unwanted species is achieved by having the substrate remain above the cathode instead of having it rotating during the deposition which effectively increases the deposition rate.

Argon

The gas phase of the reactor during the process is dominated by Ar. It is thus no surprise that Ar is also incorporated into the films as an impurity. The incorporation is quantified using the samples deposited to determine the elemental composition (cf. Fig. 77) in the DCMS and HiPIMS case at a bias of -800V.

Fig. 81 presents the Ar density as a function of N_2 flowrate for both sputtering modes investigated. The Ar density in the HiPIMS case is by a factor of 3 to 4 larger compared to the DCMS case. This is in line with the findings from the XRD experiments in which the samples prepared by HiPIMS have a smaller grain size compared to the DCMS films. This is explained by energetic Ar bombardement (Section 4.1.2.2). The energy of these Ar atoms depend on the cathode bias as explained above (Section 2.3.2.2). The higher incorporation of Ar into HiPIMS films can thus be explained by a deeper implantation compared to the DCMS case. In terms of Ar incorporation, films prepared by DCMS in this thesis therefore compare favorably to HiPIMS films.

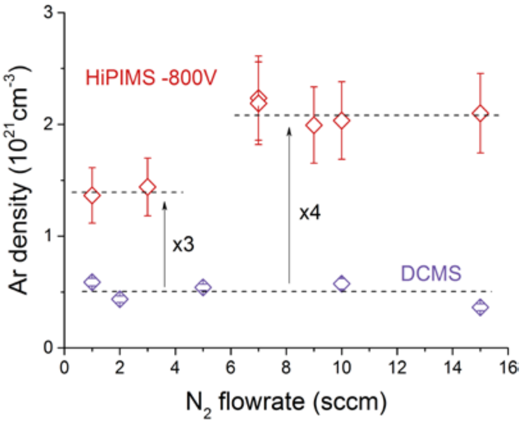

Fig. 81: Ar incorporation in films prepared by HiPIMS at a cathode voltage of -800V and by DCMS. The DCMS level corresponds to ≈ 0.5at.%, the upper HiPIMS level to ≈ 2.0at.%.

The effect of Ar on TaN films has never been studied, but again, one can resort to experiments on TiN-crystalline films studied by Petrov et al. [129]. The authors come to the conclusion that Ar trapping can be the cause for lattice strain even at a few at.% in the film. The reason for that is that they are incorporated into interstitial sites where they hinder the lattice relaxation.

Similar results on the detrimental effect of incorporation of Ar into films of $Ti_{1-x}Al_xN$ are obtained by Grecynski et al. [190]. They employed HiPIMS and synchronized the DC substrate bias to change the ratio of Al^+/Ar^+ ions. By increasing this ratio, but keeping the total number of ions incident on the growing film constant, they observed a higher quality film, i.e. lower films stress and larger grains.

4.2 Mass spectrometry

The GI-XRD results from DCMS and HiPIMS films discussed above (Section 4.1) show larger grains for DCMS samples compared to HiPIMS samples. This is partially in line with other authors but the opposite observation can also be found in literature (cf. Section 2.3.3). The principal difference between both deposition conditions are the ion flux and the flux of backscattered neutrals. Latter is evaluated below (Section 4.3) while this chapter serves to evaluate the ion flux.

In order to do so, a mass spectrometry study is conducted to observe changes in the ion energy distribution function as a function (1) the cathode bias and (2) the reactive gas flowrate. To draw a comprehensive picture, the HiPIMS mode is compared to the DCMS mode for each of these two parts.

The mass spectrometer study is conducted in a different reactor to that used for the thin film deposition. For the mass spectra to be applicable to the deposited films, the same magnetron and the same HiPIMS pulsing unit used for the film depositions were used. Fig. 82 shows the installed magnetron together with the head of the mass spectrometer. It is placed at a distance of around 10cm, which corresponds to the cathode-substrate distance in the deposition chamber. The orifice is a circular entrance with the smallest possible diameter (100µm) to reduce the noise from HiPIMS discharges.

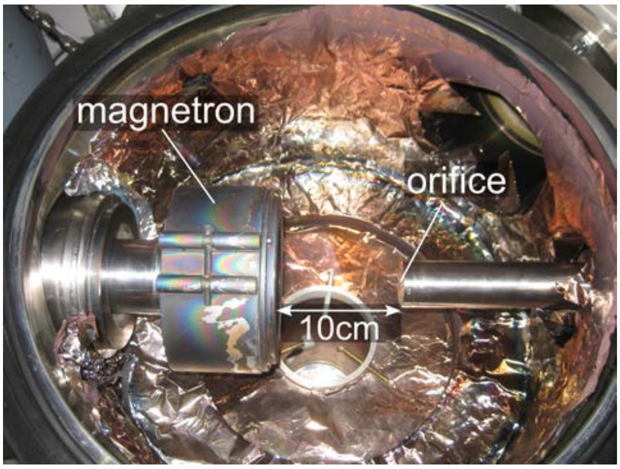

Fig. 82: Setup of the mass spectrometer at IPARC.

A typical ion energy distribution function (IEDF) is shown in Fig. 83. In this particular case, it is a HiPIMS discharge at a -1100V cathode bias, a 10µs pulse width and 80W average power in 100% Ar at 0.5Pa working pressure. The shape of the peak matches with other authors' measurements on HiPIMS discharges [191] [192] [193]. It is composed of a peak at a few eV and a long tail of energetic ions up to several 10s of eV.

Three points should be mentioned here before discussing the results. The first is that the IEDF peak is situated at negative energies. This is likely the result of a reduced conductivity of the electrostatic lenses inside the spectrometer from the deposition of insulating material during measurements prior to this study. This leads to a difference in applied potential and actual potential on the insulating surface. The energy scale of the measurements is therefore not to be taken as an absolute scale as it is likely to be shifted. Normally, the peak of the distribution lies at the plasma potential as thermalized ions are accelerated towards the grounded spectrometer from the (positive) plasma potential V_p. V_p has been measured to lie at a few eV in both, DC *[186]* and HiPIMS mode *[194]*.

Thus, the peak should be shifted by a few eV to the right. As the exact shift is unknown, the raw spectra are presented in this thesis.

Below the distribution maximum, the ion count should be zero. This is not the case in Fig. 83. In particular for the high currents of up to 90A in HiPIMS mode, the mass spectrometer shows significant levels of noise, which is believed to cause a background signal of about 100counts. As it is still difficult to determine the exact noise level for each measurement, no noise subtraction is performed on the measurements. This applies also to the integrated distributions shown later on. This is justified by the following consideration: The noise level from the HiPIMS discharge at an applied cathode bias of -1100V lies at 100counts. Multiplying this by the number of energy bins gives an uncertainty of 10^4 counts. As the integrated signal gives a value of 10^6 counts, the overall uncertainty on the integrated counts lies thus at about 1%. This is an acceptable uncertainty.

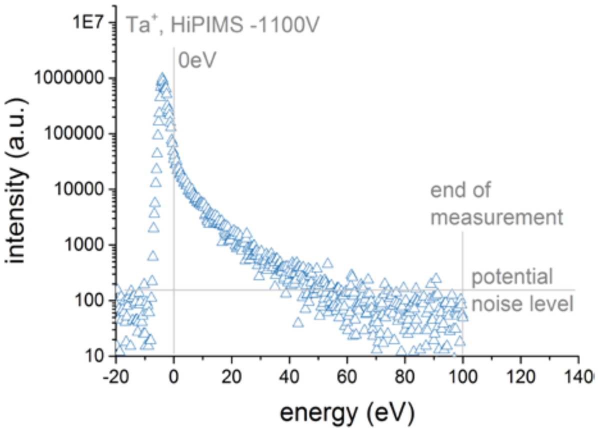

Fig. 83: Measured ion energy distribution function of a HiPIMS discharge in pure Ar.

Finally, the ion energy distribution spectra are measured on a grounded mass spectrometer. The substrate for the deposition of films is left floating, and acquires a floating potential of -15V in the DCMS case. Taking in addition of plasma potential of a few positive V, a total potential difference of 20V results. The ion energy distribution function is thus additionally shifted to higher energies in the case of depositing on an electrically floating substrate.

4.2.1 Non-reactive discharges in HiPIMS and DC mode

4.2.1.1 The influence of the cathode bias

The measurements in this chapter were conducted for pure Ar discharges in DC and HiPIMS mode. For both sputtering modes, the free variable was the cathode bias, which implied that the power in the DC case was not kept constant.

DCMS conditions
The DC discharges were conducted at cathode potentials of -257V, -276V and -285V which corresponds to currents of 312mA, 540m and 700mA and a supplied power of 80W, 140W and 200W, respectively. For convenience, the supplied power is used to distinguish the three cases in DC mode.

HiPIMS conditions
The IEDF from a HiPIMS discharge was measured at varying cathode biases with pulse widths of 10µs. The average power, contrary to the DC case, was kept constant at 80W. This was done by

reducing the period from 4.2ms in the case of a cathode bias of -1100V to 45µs in the case of a cathode bias of -400V.

Current and cathode potential during the pulse are shown in Fig. 84. In the case of the highest cathode bias, i.e. -1100V, currents of up to 80A are reached, which normalized to the surface area of the target ($\pi r^2 \approx 79cm^2$) translates to a current density of $1.1Acm^{-2}$ or a power density of $0.7kWcm^{-2}$. This is low compared to the maximum current densities stated in literature that can be reached by HiPIMS of $4Acm^{-2}$ [192] [138] or to the power density range between $0.5kWcm^{-2}$ to $10kWcm^{-2}$ [138]. Higher values, however, cannot be reached due to the small size of the capacitance in the pulsing unit.

For the highest cathode biases of -800V and -1100V, the cathode potential during the pulse does not remain flat. Also this can be explained by the small capacitance in the pulsing unit, that is discharged quickly by the high currents at those biases. When lowering the cathode bias to -600V, an almost flat potential during the pulse can be observed as less current is drawn from the capacitance during the pulse.

The effect of the pre-ionization feature is seen in Fig. 84 as a drop in potential to -200V before the actual pulse. This bias of the cathode is applied as soon as the current drops below a threshold to keep it at around 4mA. Therefore, for short periods as in the case for a bias voltage of -400V and -500V, the pre-ionization potential is not applied.

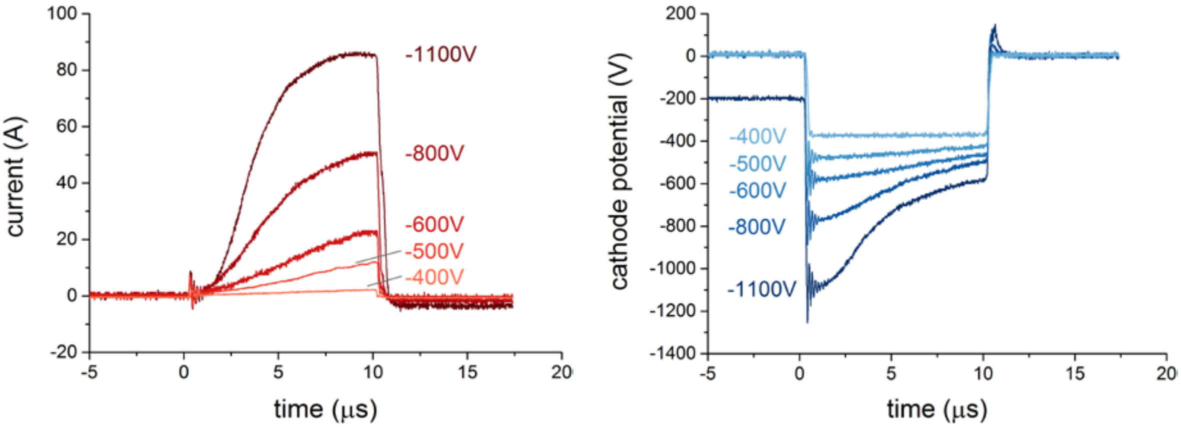

Fig. 84: Current and potential waveforms for the HiPIMS discharges in this section. (Conditions: 0.5Pa, 100% Ar). The labels on the curves indicate the cathode bias at which the capacitor of the pulsing unit is charged.

Measurements and discussion

In a pure Ar discharge, the Ta^+ species are the only film-forming ions present. Their IEDFs can be seen in Fig. 85 for the DC and the HiPIMS case. As expected and known from literature, the DC mode results in considerable less ions compared to the HiPIMS mode.

In HiPIMS mode, the IEDF at the highest applied potential of -1100V reaches its maximum height. For the lower biases of -800V and -600V, approximately the same height is reached. Only when reducing the cathode bias further to -500V and -400V, the peak maximum of the IEDF decreases. At the same time, when going from -1100V to -400V, the tail of the distribution is being cut off. While at the highest cathode bias, the tail reaches energies of up to 100eV, for the lowest cathode bias of 400V, hardly any ions can be found above 20eV.

Integrating over the Ta^+ distribution yields approximately the relative ion flux onto the substrate as a function of discharge parameters. The result is presented in Fig. 86 as a function of cathode bias for the DC and the HiPIMS case. At a low cathode bias, the integral over the Ta^+ surface area is almost linear and increases by a factor of 100 from the lowest DC case (80W) up to the HiPIMS case with a cathode bias of -600V. Beyond that, a plateau is reached for the two highest cathode biases of -800V and -1100V. The appearance of this plateau correlates with the non-flat cathode potential (cf. Fig. 84). This suggests that the cause for the deviation from the initially linear increase in relative ion flux is the inability of the pulsing unit to keep the potential constant during the pulse.

It is thus confirmed that for the specific discharge parameters and magnetron used in this thesis, a significantly higher ion flux onto the substrate is observed for the HiPIMS case compared to the DC case. This is true despite the low current densities reached during the pulse compared to the maximum values stated in literature (see above). The relative flux of ions scales with the cathode bias up to a point in which the potential during the pulse is not kept constant any more.

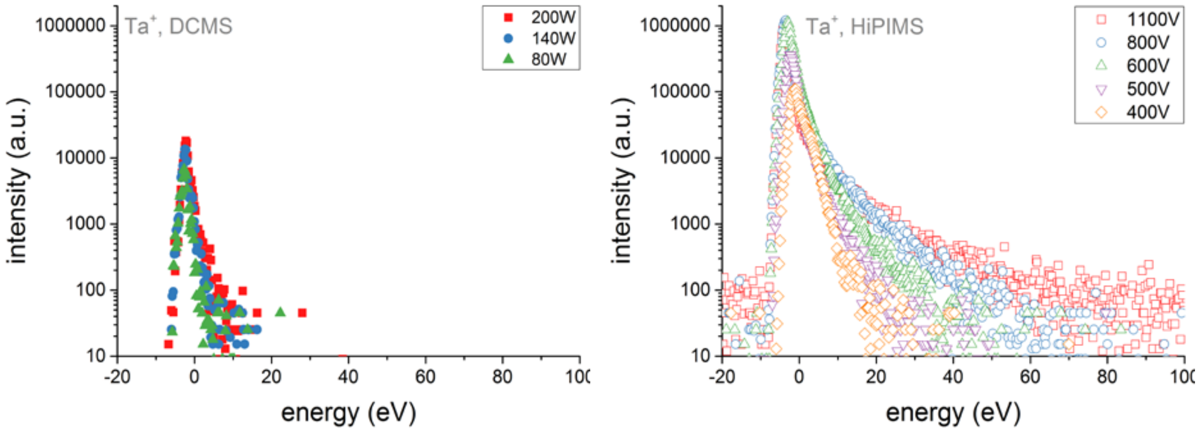

Fig. 85: Ion energy distribution function (IEDF) of Ta^+ in a DCMS discharge (left) and a HiPIMS discharge (right) at various cathode biases.

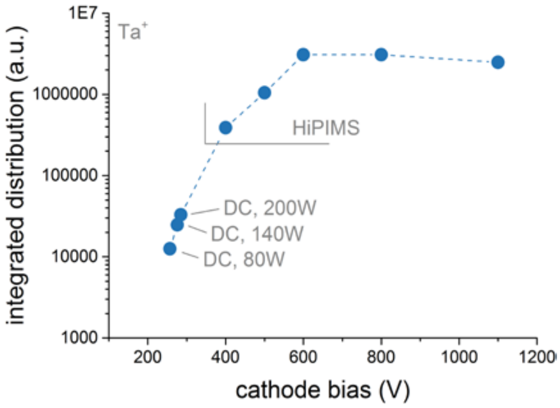

Fig. 86: Integrated distributions of the Ta^+ distribution IEDF for DCMS and HiPIMS mode.

4.2.1.2 The influence of the pulse length in HiPIMS

A second set of experiments was conducted with varying pulse widths between 1.5µs and 15µs (Fig. 87). A bias potential of -1100V was chosen for all films. Again, in order to keep the average power to 80W, the period was adjusted accordingly. This resulted in a period of 6.8ms for the longest pulses of 15µs to a period of 140µs for the shortest pulse widths of 1.5µs.

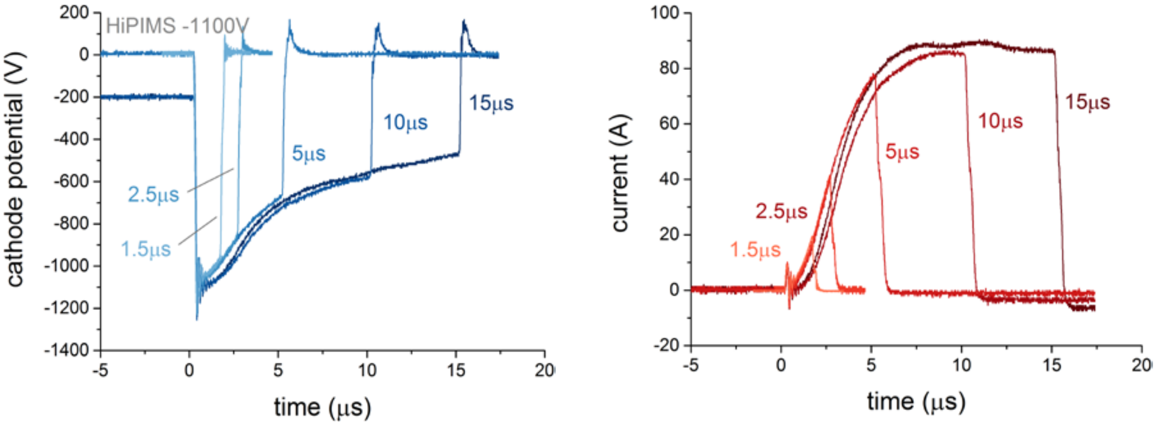

Fig. 87: Cathode potential and current waveforms for a cathode bias of -1100V as a function of pulse width.

Measurements and discussion

The result of this experiment is shown in Fig. 88. On the right hand side of the figure, the integrated distributions as a function of pulse width is presented. The tendency is clearly almost constant, potentially with a slight increase in the number of ions for longer pulse widths. This is in line with other measurements by optical emission spectroscopy done by other authors, that determined an only slight increase in metal ion density with increasing pulse width [195].

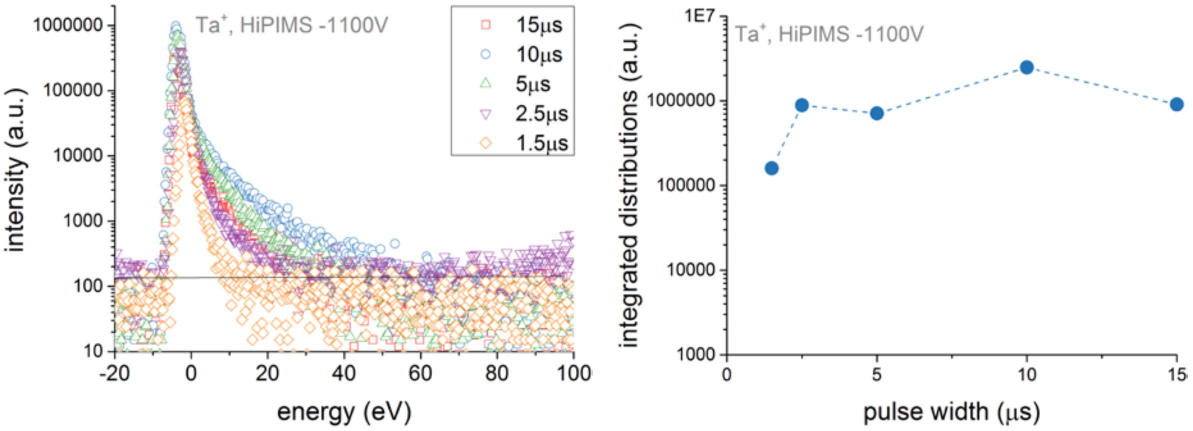

Fig. 88: Ta$^+$ energy distribution function as a function of pulse widths (left) and surface area of the Ta$^+$ peak (right).

A conclusion can naturally only be drawn for the range of pulse widths tested together with the specific pulsing unit used here. It is important to note, though, that literature knows many reports on much longer pulses of up to several 100µs, for which the change of the ion flux may be considerably different. Within the ranges tested here, though, the pulse width has little influence for the ion flux onto the substrate.

4.2.2 Ar/N_2 discharges in DCMS and HiPIMS mode

The effect on the ion energy distributions from injecting N_2 into the reactor was investigated, again using DCMS and HiPIMS discharges. For this, the DCMS discharge was fixed at a power of 80W and compared to a HiPIMS discharge at a cathode bias of -1100V and an average power of 80W. Four different N_2 flowrates were investigated, 0sccm, 1.0sccm, 3.5sccm and 7.5sccm. Ar was added to reach a total flowrate of 25scccm.

DCMS conditions

The current and voltage characteristics were recorded as a function of N_2 flowrate for the DCMS case (Fig. 89). With increasing the N_2 flowrate, the DC cathode potential increased (Fig. 89). At the same time, the current dropped in order to keep the average power at 80W. For both curves, the rate of change was fast at the beginning between the pure Ar discharge at 0sccm N_2 flowrate and the 1.5sccm N_2 flowrate, while its rate of change slowed down at higher flowrates.

HiPIMS conditions

For the HiPIMS discharge, the peak current decreased with increasing the N_2 flowrate, an effect of the delayed gas breakdown due to the energy loss of accelerated electrons by vibrational and rotational excitation on N_2 [196] (Fig. 89). Again, in order to keep the supplied power to the cathode constant at 80W, the period was decreased from 4.2ms for the discharge in pure Ar to 3.6ms for the discharge with a flowrate of 7.5sccm N_2.

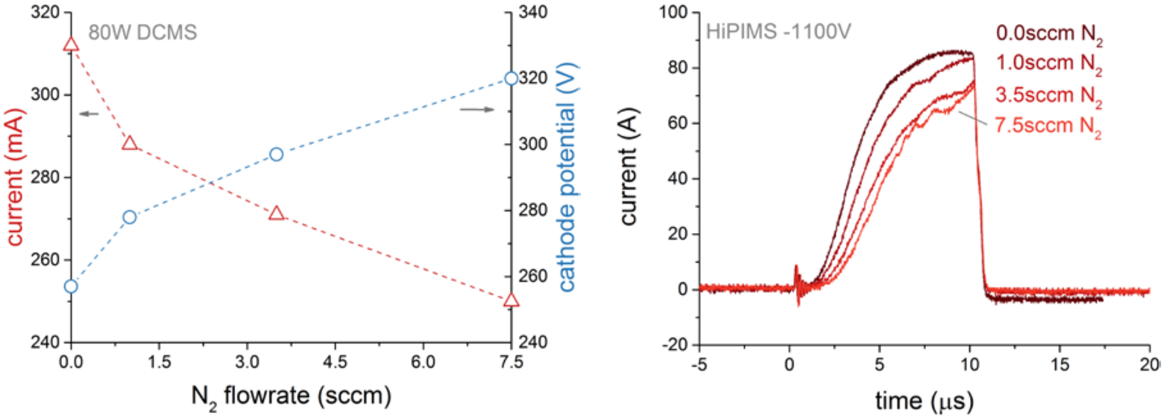

Fig. 89: Discharge curves for a DCMS (left) and a HiPIMS discharges at a cathode bias of 1100V (right) as a function of N_2 flowrate.

Measurements and discussion

The spectrum of film-forming ionic species is now much richer with N_2 injected into the reactor compared to the pure Ar cases above. The energy distributions of the principle ionic species, Ta^+, N^{2+}, N^+, are shown in Fig. 90.

The addition of N_2 to the discharge, reduces the metallic ion flux (Ta^+) in both, the DCMS and the HiPIMS case. The general shape of the two energy distributions, remain similar to the case of the pure Ar discharge, though. The DC distribution remains a peak-like distribution at low energy and the HiPIMS distribution has a similar low-energy peak but with an additional high energy tail. Latter is cut back to lower energies with increasing the N_2 flowrate.

The most abundant film-forming ion in Ar/N_2 magnetron discharges is known to be the N_2^+ ion [197]. Its energy distributions in the DCMS and the HiPIMS case resemble a lot and even the intensities between both sputter modes are of the same order of magnitude.

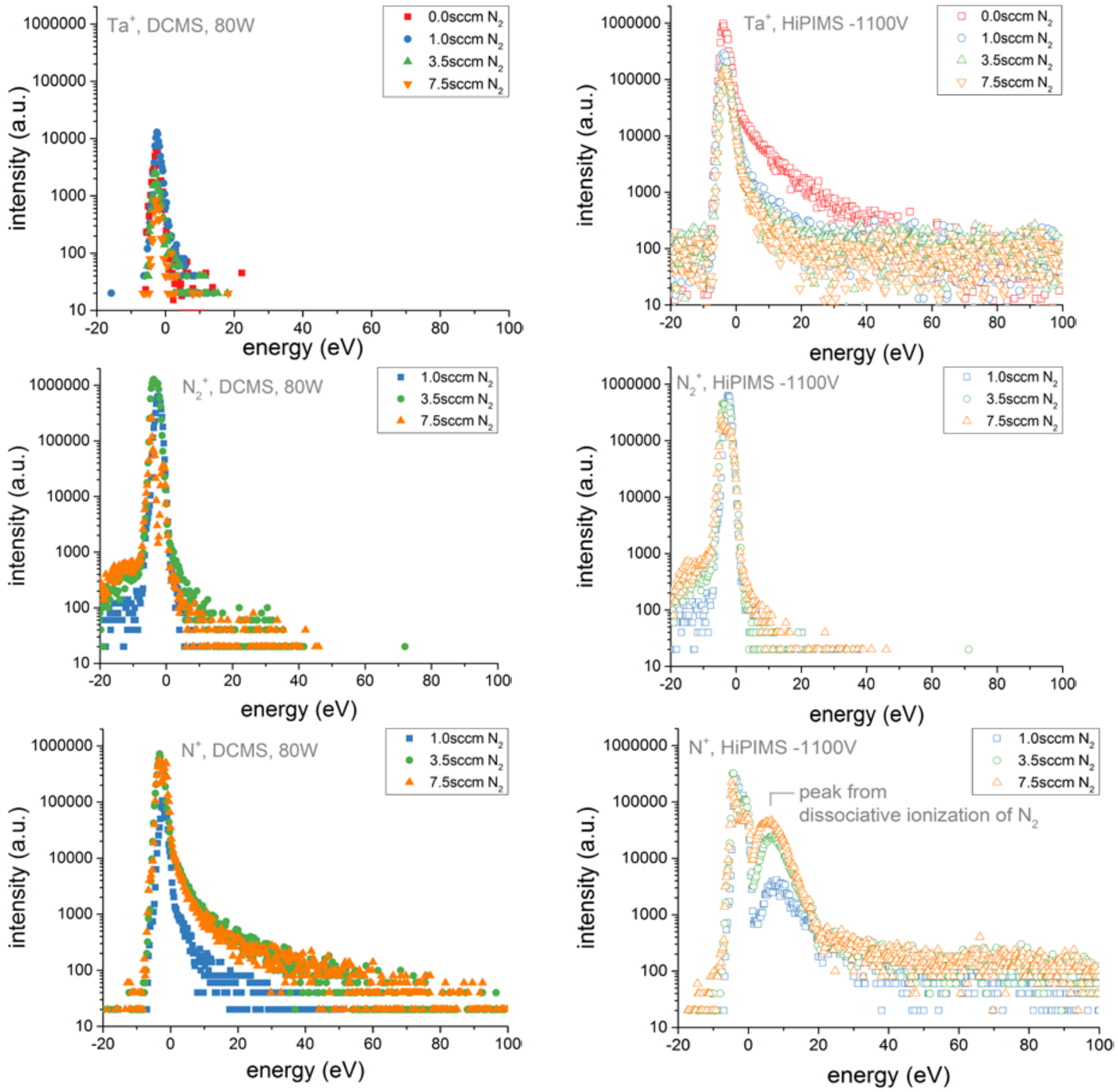

Fig. 90: Energy distribution of principal ionic species Ta^+, N_2^+ and N^+ as a function of N_2 flowrate adding for DCMS (left) and HiPIMS (right) discharges.

The N^+ energy distributions between DCMS and HiPIMS are again quite similar to each other while very distinct from the N_2^+ distributions. The N^+ distribution has a long tail towards high energies of up to 100eV similar to the Ta^+ distribution in HiPIMS mode. The common explanation for this is that the N^+ is sputtered off the target surface while the N_2^+ is produced by electron impact above the target [198].

The only difference between the DCMS and the HiPIMS case on the N^+ distribution is an additional bump in the distribution between 0 and 20eV recorded for the HiPIMS case. This has been found in literature before but is sometimes more [145] or less pronounced [199] as in Fig. 90. Jouan et al. [145] explains this double peak feature by the two origins of N^+ in a HiPIMS discharge. The first peak at low energy stems from sputtered N that is ionized in the negative glow while the peak at higher energy stems from the direct impact ionization of N_2 in the negative glow. Similar observations were made by Anderson et al. for O_2 in an Al/Ar/O_2 discharge [200].

The integrated intensities for the principal ions are presented in Fig. 91. It is important to note that the relative intensities of one species compared to another do not reflect their relative fluxes at the virtual substrate position. As the transfer function of the spectrometer is unknown, these cannot be calculated. The only knowledge that can be obtained from the plots, is the relative trends within one species as a function of discharge mode and N_2 flowrate.

The Ta^+ flux in the HiPIMS mode decreases strongly from the pure Ar discharge to the discharge with a flowrate of 1sccm N_2 by 70% and by another 40% from 1.0sccm N_2 flowrate to 7.5sccm N_2 flowrate. This is mainly due to a reduced metal sputter rate. In addition, it is likely that the electron energy distribution function is reduced due to vibrational excitation of the N_2 molecule (cf. Chapter 4.1.2.1). In the DC case, the Ta^+ distribution reduces with increasing N_2 flowrate similar to the HiPIMS case. The rise from 0.0sccm to 1.0sccm may actually be due to a measurement error (Fig. 91). When going from 1.0sccm N_2 flowrate to 7.5sccm flowrate, a 90% decline in Ta^+ flux can be observed.

For the N_2^+ and N^+ ions, the differences between the DCMS and the HiPIMS mode is much less obvious. A real trend as a function of N_2 flowrate cannot be concluded from the measurements. An important observation, however, is the similar levels of both, the N_2^+ and N^+ integrated intensities in the DCMS and the HiPIMS case.

For the Ar^+ and Ar^{++} in the DCMS case, no clear trend with N_2 flowrate can be established, either. In the HiPIMS case, it seems that the addition of N_2 into the discharge results in a strong drop in the number of the ions of both charge states, while its intensities do not change a lot with further increasing the N_2 flowrate. For Ar^+, levels are comparable between the DCMS and the HiPIMS case, while for the HiPIMS case, a smaller number of Ar^{++} is present.

As any types of ions contribute to the momentum transfer onto the film, the sum of all ions needed to be calculated and compared to the film structure. Due to the unavailability of the mass spectrometer transfer function, this is not possible. However, all species, but the Ta^+ and Ar^{++}, have similar integrated intensities in DCMS and HiPIMS. Ar^{++} is likely to be negligible for the sum of ionic species arriving on the substrate due to its low production rate. The Ta^+ is thus the determining factor for the total sum. This is clearly higher in the HiPIMS case.

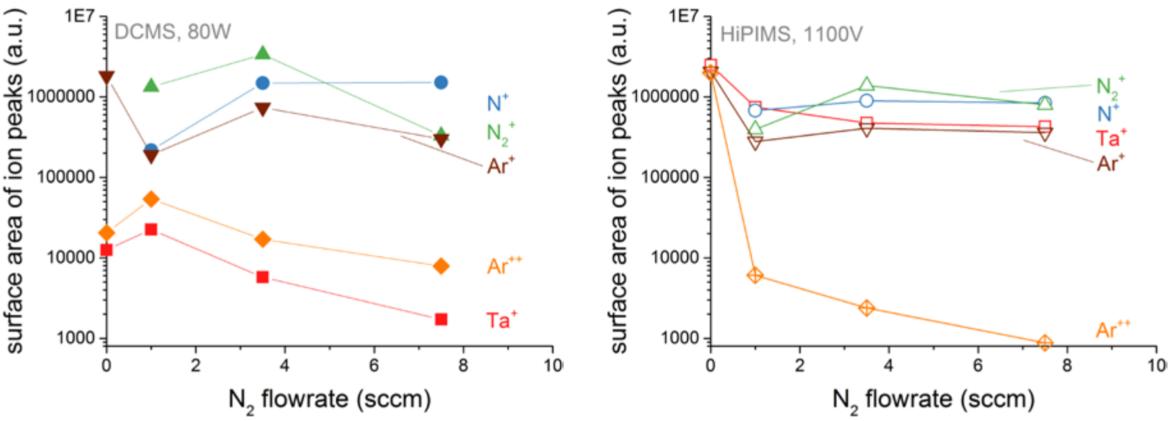

Fig. 91: Integrated intensity of principal ionic species as a function of N_2.

The principal difference between the DCMS and the HiPIMS case, regarding the ionic flux onto the substrate, thus lies in the flux of the metallic ions. Whether this changes the total number of ions arriving on the substrate cannot be resolved within this study but the comparable fluxes of N_2^+ and N^+ onto the substrate in the DCMS and HiPIMS case suggests that the difference in between the two modes of deposition could be smaller than expected. Possibly, this changes with higher current densities because, as mentioned before, the current densities for this study are low compared to the current densities for HiPIMS conditions stated in literature (cf. 4.2.1).

4.3 Evaluation of backscattered neutrals

Besides the ionic species discussed in the previous chapter, high energy neutrals that are backscattered from the cathode deliver a flux of energetic atoms onto the substrate. The purpose of this chapter is to evaluate their impact on the films by means of computer simulations. In particular shall this chapter give an answer to the question whether these high-energy backscattered neutrals could be responsible for the decreasing grain size in thin films deposited at increasingly higher cathode voltages as seen in Section 4.1.

The strategy is to determine the percentage and energy spectrum of the backscattered ions by using the Transport of ions in matter (TRIM) simulation software [201]. This can then directly be compared to the sputter coefficient that gives the number of sputtered Ta atoms per incident Ar ion. Furthermore, the backscattered particles can be transported through the Ar background gas filling the space between the cathode and the substrate to see the effect of stopping the backscattered neutrals.

4.3.1 Calculation of the backscattered energy spectrum

The TRIM software simulates the impact of energetic ions hitting a target of specific composition and density. It outputs the velocity vectors for each simulated backscattered neutral which, taking a sufficiently large number of particles into account, can be converted into an energy spectrum. In a magnetron discharge, all positive ions are accelerated towards the cathode, but the predominant ones in an Ar/N_2 discharge in DCMS and HiPIMS, are Ar^+ and N_2^+ [197] [192] which is why this evaluation is restricted to those two ions.

In a discharge, the ions traverse the presheath and sheath in front of the cathode and can thus acquire a maximum energy of the cathode potential plus the plasma potential. For simplicity, the ions hitting the target are taken to be monoenergetic at an energy equal to the cathode potential. Hence, the plasma potential, which is small compared to the cathode fall, is neglected as well as the fact that ions may be produced within the sheath region and thus acquire only a fraction of the maximum possible energy.

The impact of N_2^+ onto metallic targets at energies >100eV causes dissociation into two N atoms with each having half the energy of the molecule [202]. This is why, for the simulation, the N_2^+ are replaced by N atoms impacting at half the energy of the Ar^+ ions. This treatment is done similarly by Sarakinos et al. [203] and Petrov et al. [197].

Finally, the target composition in nitride mode is unknown. To complicate things, it also varies as a function of N_2 flowrate and likely has a nitrogen depth profile. To account for all these possibilities, two extreme cases of target composition are chosen, one being a pure Ta target, the other one being a Ta-N target with a composition of $Ta_{0.375}N_{0.625}$ which corresponds to the ideal Ta_3N_5 composition and roughly to the maximum nitrogen that can be incorporated into Ta-N films as presented in Section 4.1.3.1.

Preliminary considerations

Overall, 5 simulations were run for each of the two projectiles Ar and N and each of the two target modes, elemental and reactive. For these, the ion energies incident on the cathode were varied between 200eV and 1100eV for Ar and, correspondingly, 100eV and 550eV for N. For each simulation, the number of incident ions was kept constant at 100,000.

The share of backscattered neutrals from 100,000 incident ions is presented in Table 17 for Ar and Table 18 for N. For the pure Ta target, the share of backscattered neutrals is high and lies around 25% for the Ar^+ projectile and close to 40% for the N^+ projectile. This can be understood from the lower mass of the N compared to the Ar with an increased mass ration m_N/m_{Ta} compared to m_{Ar}/m_{Ta}. For the fully nitrided target, the share of backscattered atoms drops significantly as expected from the smaller effective target atom mass. The share of backscattered Ar drops to around 12% and that of backscattered N to 17%. All shares are almost independent of incident energy for the energy range between 200eV and 1100eV investigated here.

Table 17: Summary of the TRIM simulations to evaluate the energy spectra of backscattered Ar^+ at various Ar^+ incident energies.

Ar^+ incident energy	**200eV**	**300eV**	**500eV**	**800eV**	**1100eV**
number of incident Ar^+	100,000	100,000	100,000	100,000	100,000
share of backscattered Ar from metallic Ta (elemental mode)	26.1%	26.0 %	25.7%	25.1%	24.8%
share of backscattered Ar on $Ta_{0.375}N_{0.625}$ (reactive mode)	12.8%	12.8%	12.6 %	12.3%	12.1%

Table 18: Summary of the TRIM simulations to evaluate the energy spectra of backscattered N at various N^+ incident energies.

N^+ incident energy	**100eV**	**150eV**	**250eV**	**400eV**	**550eV**
number of incident N^+	100,000	100,000	100,000	100,000	100,000
share of backscattered N from metallic Ta (elemental mode)	39.6%	39.6%	39.5%	38.3%	37.7%
share of backscattered N from $Ta_{0.375}N_{0.625}$ (reactive mode)	16.5%	16.9%	17.2%	17.3%	17.4%

The drop in the share of backscattered neutrals can be compared to mass spectrometer measurements conducted by Petrov et al. [197]. They measured the intensity of Ar neutrals backscattered from a Ti-N target incident at the virtual substrate position as a function of N_2 injected into the reactor. Contrary to the drop in the share of backscattered Ar seen in the simulations above, they observed a flat Ar signal when going from the elemental mode to the reactive mode. And although the fully nitrided target was reached at a nitrogen fraction $p_{N2}/(p_{N2} + p_{Ar})$ of 0.06, only at very high nitrogen fractions of 0.5, the Ar signal drops (Fig. 92).

With regard to the simulation in this section, these results suggest that the target in reactive mode may contain much less N than the assumed stoichiometry of $Ta_{0.375}N_{0.625.}$ Although latter corresponds approximately to the maximum nitrogen incorporation of Ta-N films, this does not necessarily mean that the cathode contains similar amounts of nitrogen. An explanation for a smaller at.% of nitrogen in the cathode compared to that in the target could be preferential sputtering. Preferential sputtering is observed for compound targets consisting of atoms with a mass difference [204] and would lead to a preferential knock-out of N compared to Ta. This mechanism would naturally be in competition with the target nitridation and the final composition would depend on the rate constants for the two processes that are unknown. But it is at least possible, that the extreme case of a fully nitrided target with a composition of $Ta_{0.325}N_{0.675}$ may be strongly overestimated. As it represents one of the two extreme cases, it is still considered in the analysis as an upper boundary.

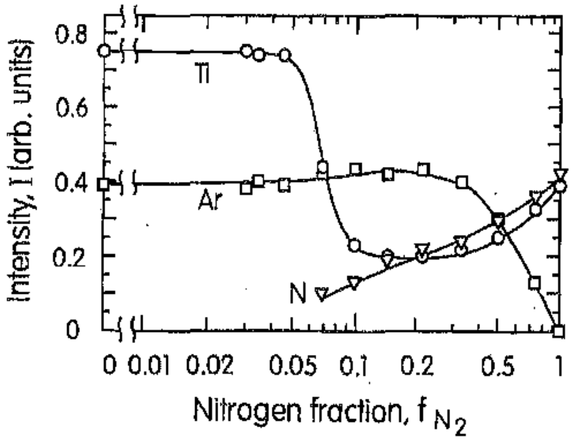

Fig. 92: Neutrals from an Ti/Ar/N₂ magnetron discharge as a function of nitrogen fraction $(p_{N_2}/(p_{N_2}+p_{Ar}))$ *arriving on the substrate as measured by mass spectrometry. From* [197].

The energy spectra of backscattered neutrals

The backscattered energy spectra for a cathode bias of -1100V is presented in Fig. 93 for backscattered Ar and N. The red bars in both plots indicate the backscattered spectrum obtained by averaging the results from a pure Ta and a fully nitrided $Ta_{0.325}N_{0.675}$ target. The uncertainty bars indicate the results if the composition varies between the two extremes. The height of the bars shows the percentage of backscattered neutrals in that energy bin from all incident ions.

In the case of Ar projectiles, a large share of around 10% of all incident ions are backscattered in an energy interval between 0eV and 10eV. The remaining backscattered neutrals, roughly 8% of all incident ions, have energies greater than 10eV with the energy spectrum going up to very high values. For Ar, 10 neutrals out of 100,000 incident ions leave the target with energies of 650eV. In the case of N projectiles, the result is similar with around 10% of all incident ions being backscattered at energies <10eV and 18% of all incident ions being backscattered at energies >10eV. For N, 10 backscattered neutrals out of 100,000 incident ions have energies of 450eV.

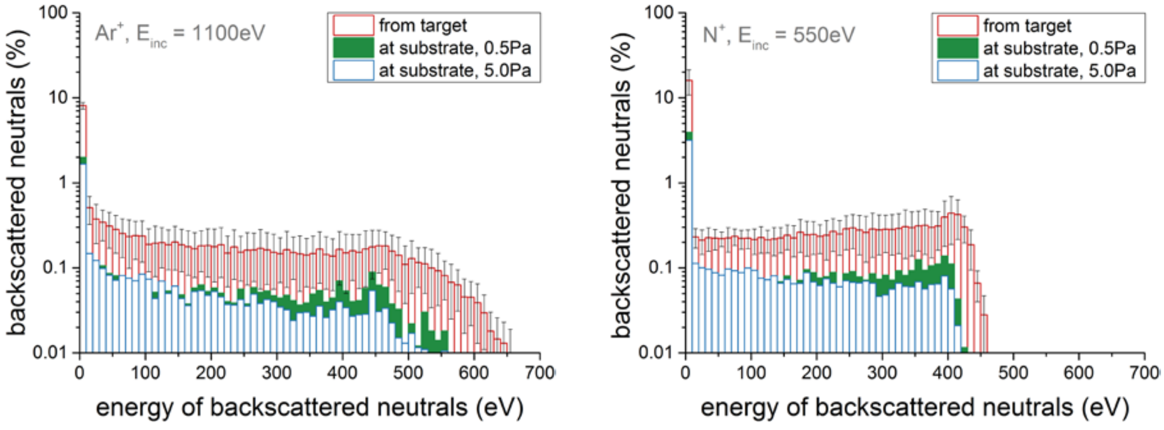

Fig. 93: Energy spectra of backscattered Ar (left) and N (right) for a cathode bias of 1100V.

These energy distributions are the distributions just above the cathode surface. As such, they may not represent the distributions of backscattered neutrals at the substrate. To simulate the energy transfer of the backscattered neutrals with the Ar background gas between the cathode and the substrate, the TRIM energy spectra are fed into a second code for simulating binary collisions using a Monte-Carlo approach.

For that purpose, the code OMEGA (Orsay Metal Transport in Gases) by Lundin et al. [120] is adopted that was originally developed for a slightly different purpose. The code injects particles at randomly chosen locations on the three-dimensional cathode surface. Their initial velocity vector is taken from the TRIM output. They are then propagated through the cathode-target space treating collisions between backscattered neutrals and the background gas using the formalism from Section 2.3.2. The backscattered neutrals passing the substrate plane are recorded (Fig. 94) and their velocities are reconverted to an energy spectrum for which all three velocity components are taken into account. Taking only the velocity component perpendicular to the substrate plane, however, results in similar spectra as most neutrals reaching the plane do so on an almost straight line. The dimensions of this virtual sputter chamber are illustrated in Fig. 94.

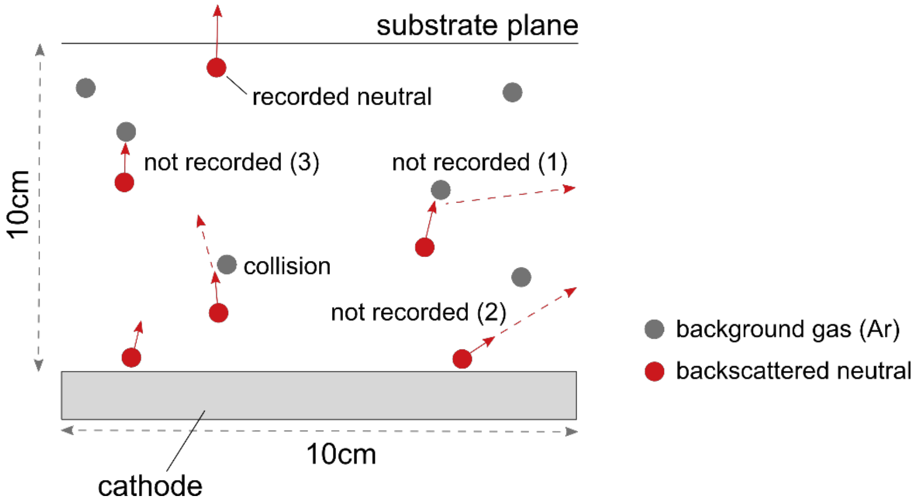

Fig. 94: Sketch illustrating the events in a Monte-Carlo simulation used to calculate the spectrum of backscattered neutrals at the substrate plane.

Collisions are treated using the Ar-Ar cross-section from Robinson [119] that is also presented in Fig. 23. For the Ar-N momentum cross-section, no such reference is available in literature. Somekh [114] proposes an interpolation scheme using the rare gas cross-sections for Ar, Kr and Xe from [119]. However, as N is even lighter than Ar, this scheme cannot be used. In addition, some doubts exists on the validity of this interpolation approach [104], so that an extrapolation is not dared here either. Therefore, the same cross-section used to treat the momentum transfer of backscattered Ar in an Ar background gas from Robinson is used to treat the momentum transfer of N in an Ar background gas. As N is lighter than Ar, this approach certainly yields an overestimation of the stopping power of the background gas for the N backscattered neutrals.

The result of the Monte-Carlo simulation is shown by the green and the blue bars in Fig. 93 for pressures of 0.5Pa and 5.0Pa, respectively. In both cases, the share of backscattered neutrals that hit the substrate is strongly reduced compared to the energy spectrum at the cathode surface. The reduction is by a factor of 5 to 10 for Ar and a factor of 2 to 3 for N. This is due to, (1) neutrals that are subjected to collisions and are scattered out of the substrate-cathode region, (2) neutrals undergoing no collisions but having an initial velocity vector that is directed out of the cathode-substrate region and finally, (3) neutrals that have come to rest after a number of collisions (Fig. 94). Little difference is observed between the low-pressure case and the high-pressure case, which suggests that particle stopping is not a dominating mechanism here for reducing the number of neutrals incident on the substrate. Only at the highest energies for Ar and N, a small difference in the maximum energy incident on the target can be observed.

Most important for this analysis is, however, that in both cases, the energy distributions are far from being thermalized. In fact, the energy spectrum for the most part retains its shape including its high energy tail. 10 out of 100,000 Ar^+ incident onto the cathode, reach the substrate with at least 500eV and 10 out of 100,000 incident N^+ reach the substrate with energies of at least 400eV.

4.3.2 Effect of the backscattered neutrals on the film

Whether the backscattered neutrals can have a measurable effect on the film depends on how many backscattered neutrals in a certain energy interval impact on the film per number of deposited atoms. To omit the uncertainties that are associated with propagating the backscattered neutrals and in particular the sputter vapor through the transport region, collisions in this region are neglected. This simplification is justified, as the shape of the energy distribution of the backscattered neutrals does not change considerably.

With this simplification, the number of backscattered neutrals per incident ion can directly be compared to the sputter yield, which is the ratio of the sputtered atoms per incident ion. The analysis is done for different incident ion energies to simulate varying cathode potentials.

Definition of energy intervals

Three intervals can be distinguished according to their expected influence on the film. At low energies, an interval without any effect can be defined to lie <10eV. At high energies, the backscattered neutrals induce defects and can even cause sputtering. To select a boundary for these detrimental energies, Table 8 can be consulted. It shows that, at least for TiN, a strong increase in the defect density is observed for atoms at energies >100eV. This boundary is in particular dependent on the mass of the atoms in the film because heavy atoms are more tolerant to bombardment due to a greater interaction cross-section [127]. The boundary for Ta-containing films could thus be slightly higher. To be on the conservative side, though, the boundary is chosen to be equal to 100eV. Finally, in the range between 10eV and 100eV, atoms have sufficient energy for displacing surface atoms but too little energy to displace bulk atoms. This energy range is thus beneficial for the growth of defect-reduced films as discussed in Section 2.3.2.2.

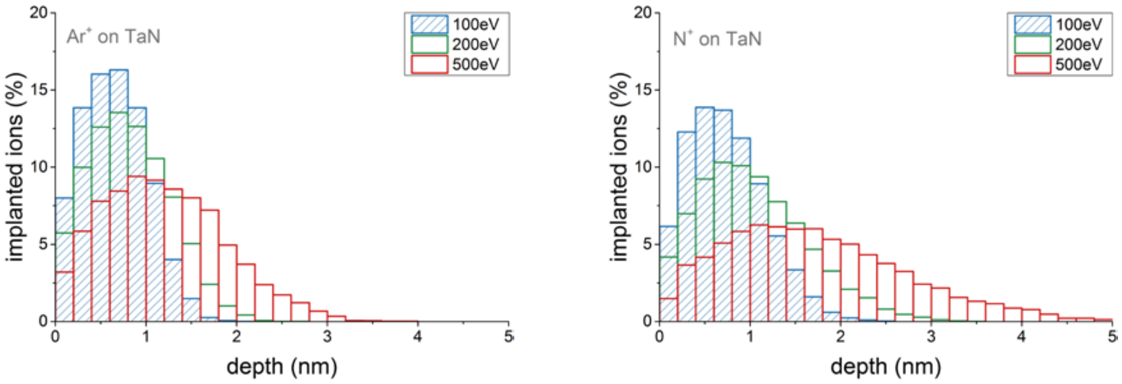

Fig. 95 : Histogram showing the distribution of settlement depths of Ar and N incident on an amorphous TaN phase.

The border of 100eV between the beneficial energy range and the detrimental energy range is made plausible by simulating the penetration depth of Ar and N atoms incident on a TaN film. The simulation is done for an amorphous film with a density of 13.5gcm^{-2} corresponding to the ideal δ-TaN density [94]. The crucial parameter whether an atom inside the bulk can induce damage to a lattice is the bulk displacement parameter [127]. In the absence of data on the δ-TaN phase, the TRIM standard value of 25eV is taken, which can also be found in other publications for different materials such as Cu films [205] and TiNi alloy [206]. It is at least well in the range between 12eV and 33eV for typical bulk displacement energies [126]. The result of this simulation is presented in Fig. 95 which shows a histogram of the settlement depth of the projectile atom. It can be seen that atoms with an initial energy of 100eV are stopped within 1nm of depth which seems already deep as this corresponds to roughly 2 to 3 times the unit cell of the δ-TaN phase (see Table 2). Atoms at higher energy have a considerable tail and thus can penetrate even further.

The backscatter spectrum as a function of ion incident energy

The backscattered energy spectra as a function of incident ion energy are presented in Fig. 96. Again, like in Fig. 93 a large percentage of the incident Ar^+ and N^+ are backscattered at very low energies, followed by a wide plateau that falls off close to the maximum energy. While the general shape is the same for all incident energies, the maximum energy of backscattered neutrals and the height of the plateau depend strongly on the incident energy. Lower incident ion energies have a smaller maximum energy while it augments the probability that an ion is backscattered in one of the remaining energy bins.

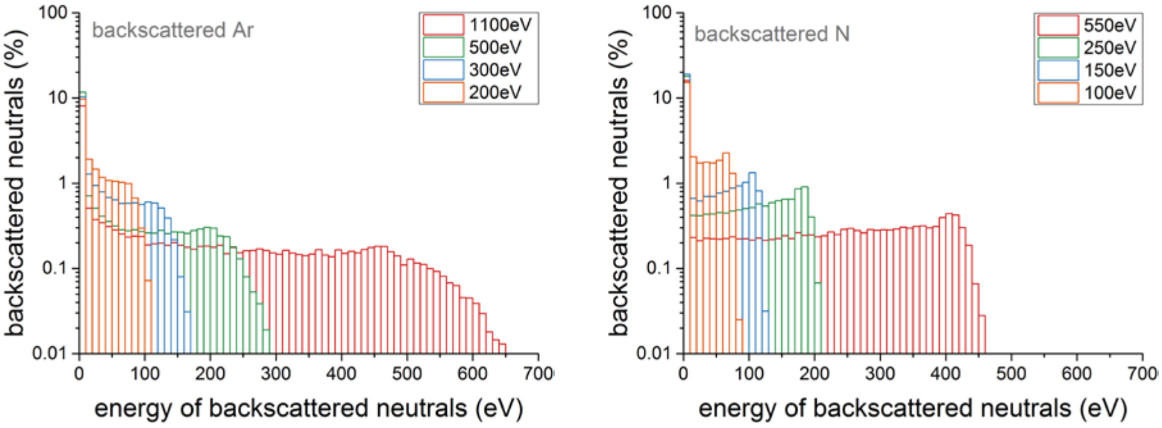

Fig. 96: Energy spectra of the backscattered neutrals for various incident ion energies for Ar (left) and N (right) at the target.

The spectra can now be divided according to the above-defined energy intervals to determine the number of backscattered neutrals in the beneficial and the detrimental energy range as a function of incident ion energy on the cathode. The curves are presented on the left hand-side of Fig. 97, and can directly be compared to the sputter yield.

The sputter yield

To calculate the sputter yield as a function of incident ion energy and as a function of the target composition, again, TRIM is used. Two parameters are to be known in order to conduct a precise calculation, the lattice binding energy and the surface binding energy. The lattice binding energy represents the energy lost on the interaction with target atoms and takes values from 1 to 3eV [207]. As this value is unknown, the average value of 1.5eV is taken but values from 1 to 3 eV do not influence the results much.

The second value is the surface binding energy that determines whether a bulk atom recoiled towards the surface has sufficient energy to leave the bulk. For pure metals, this is taken to be the heat of sublimation H_S [110]. For compound targets, expressions for removing a metal or a reactive species from a surface is provided using the Pauling formalism [204]. It takes into account the weighted arithmetic means of the bond energies between two reactive species and between a metal and a reactive species. In addition, to account for the polarity of the bond, the difference in electronegativities of the metal and the reactive species is taken into account. This yields the following expression for the surface binding energy of one N atom on a Ta_xN_y surface:

$$U_N = \frac{x}{x+y} D_{Ta-N} + \frac{y}{x+y} D_{N-N} + \frac{1}{2}(\varepsilon_{Ta} - \varepsilon_N)^2 \qquad \textit{Eq. 67}$$

where D is the bond strength and ε_{Ta} and ε_N are the electronegativities of Ta and N respectively. The Ta-N bond strength $D_{Ta\text{-}N}$ is taken to be 6.3eV [208], the N_2 bond strength to be 9.7eV [107] and the electronegativities are taken to be $\varepsilon_N = 3.04$ [209] and $\varepsilon_{Ta} = 1.5$ [210]. The resulting surface binding energy U_N for a single N then ranges between 7.4eV on a purely metallic target and 9.6eV for a fully nitrided target ($Ta_{0.375}N_{0.625}$). Taking the average yields a surface binding energy of 8.5eV that is used for the calculating the sputter yield in TRIM. Calculating the sputter yield instead with values of 7.4eV or 9.6eV does influence the result significantly. The uncertainty introduced by taking the average binding energy remains <10%.

For metals on a nitrided surface, after some simplifications, a similar expression is derived [204]:

$$U_{Ta} = H_s + \frac{1}{2}(\varepsilon_{Ta} - \varepsilon_N)^2 \qquad \textit{Eq. 68}$$

The calculated sputter yield is shown in Fig. 97 on the right hand-side. It shows that the addition of nitrogen compared to a pure Ar discharge reduces the sputter yield, an effect of the effective stronger bonding of the compound Ta-N compared to the metallic target.

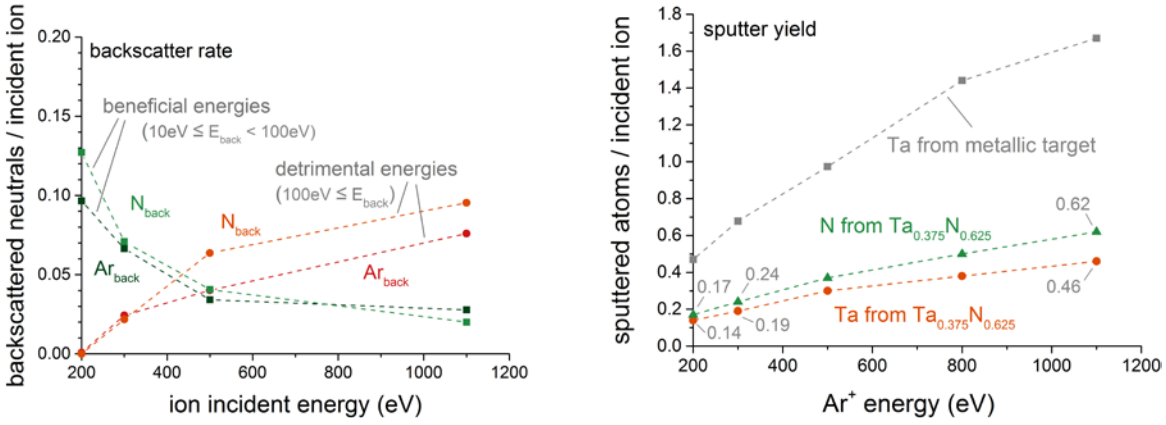

Fig. 97: Backscattered neutrals (left) and sputter yield from a metallic Ta and a compound Ta-N target (right).

Comparing the backscatter rate with the sputter yield

The results for the backscatter rate and the sputter yield allow to determine how many atoms in the beneficial energy range and the detrimental energy leave the cathode in comparison with the number of sputtered atoms. This backscatter-to-sputter ratio can then be directly compared to the ion-to-neutral ratio, a parameter that has been extensively investigated in the past to evaluate effects of energetic bombardment. This gives an idea whether a film grown at a certain cathode potential is prone to exhibit defects, or, on the other hand, can be expected to benefit from a low energy bombardment.

At a very low target bias of -200V, the sputter yield ranges between $\gamma_{Ta,nitrided} + \gamma_{N,nitrided} = 0.31$ for the fully nitrided target and $\gamma_{Ta,metallic} = 0.47$ for the metallic target. The backscatter rate in the beneficial energy range, on the other hand, lies between 0.1 for a purely Ar discharge and 0.13 for a purely nitrogen discharge. Hence, on three sputtered atoms there is one backscattered atom in the benefical energy range giving a backscatter-to-sputter rate of 0.3. A comparison can be done with the study by Shin et al. [130] that investigate effects of low energy ion bombardment (20eV) as a function of the ion-to-neutral ratio incident on the substrate. As they determine no significant effects for ratios below 5.9, a backscatter-to-sputter rate of 0.3 is likely too little to have any considerable effect on the films of Ta-N either.

On the other side, at high cathode potentials, the sputter yield lies between 1.08 for the fully nitrided cathode and 1.67 for the metallic cathode. The backscatter rate in the detrimental energy range at the highest cathode potential lies between 0.08 and 0.1, meaning that roughly one high-energy atom per 10 to 20 sputtered atoms is leaving towards the target giving a backscatter-to-sputter ratio of 0.05 to 0.1. Again, this can be compared to a study by Petrov et al. [129] who determines the onset of defect incorporation into TiN films to lie around 100eV for an ion-to-neutral flux ratio of 0.3 to 0.4. The backscatter-to-neutral ratio lies below that value, but defects incorporated from high-energy bombardment should be independent of the ion flux, at least at low substrate temperatures, where defects cannot be annealed out. In addition, it has to be taken into account that the detrimental energy range covers a large spectrum from 100eV to several 100s of eV and that higher energies, naturally, induce more defects, a fact that has not been further analyzed in this section.

From this analysis, the conclusion can be drawn that the decreasing grain size in the HiPIMS-sputtered films compared to the DCMS films is caused by the considerable amount of backscattered neutrals at energies >100eV.

4.4 Conclusion

Experiments and simulations are conducted in this chapter to evaluate conditions under which Ta_3N_5 should be grown. The parameter of primary interest in the Ta_3N_5 material is the grain size as it is known from other semiconductors that both, the mobility and lifetime of charge carriers increase with grain size. As the electrical behavior of Ta_3N_5 is important for the performance of a photoanode, the chapter focusses on mechanisms influencing the grain size in Ta/Ar/N_2 magentron discharges.

The first section reveals larger grains for DC-sputtered films compared to HiPIMS films. More precisely, the grain size scales with the cathode potential. The primary differences between the two modes are the presence of ions and backscattered neutrals in the case of HiPIMS. The effect of both is elucidated in the second and third section of this chapter.

A higher ion flux onto the substrate in HiPIMS mode compared to DCMS is proven by means of a mass spectrometry study. The ion energy distribution function lies well below 100eV for all cathode biases in reactive mode. Most of the ions present have energies of a few eV only and can be expected to be accelerated to a few 10s of eV in the sheath in front of the substrate. These ions should thus have a beneficial influence on the grain size of the films. The fact that the grain size still shrinks with cathode potential, leads to the conclusion that ions do not have a dominiating effect on the grain size of δ-TaN films with cathode bias.

The third section calculates backscatter spectra of Ar and N from a Ta(-N) cathode. In particular due to the high mass of Ta in the cathode, these can reach considerable energies of a few 100eV. At the highest cathode potential investigated, the ratio between backscatter atoms with energies >100eV and sputtered atoms lies between 0.05 and 0.1. This means that each small cluster of 10 to 20 atoms is hit by a backscattered neutral at high energies inducing defects that can cause recrystallization. Thus it is made plausible that the backscattered neutrals cause the smaller grains in HiPIMS mode compared to DCMS mode.

To minimize the energy of the backscattered neutrals, the cathode potential needs to be kept to a minimum. Therefore, the DC mode with the lowest cathode bias is the best option for the synthesis for Ta_3N_5. This comes with the additional advantage that the percentage of backscattered Ar at beneficial energies rises steeply with decreasing the cathode bias.

Some oxygen is present in the films prepared here. Although some oxygen is necessary for the growth of the Ta_3N_5 phase, the unintentional incorporation impairs the precise control of the oxygen incorporation. The oxygen present in the bulk phase can be reduced by increasing the deposition rate. This can be done by having the substrate kept at a fixed position instead of having it rotate. This goes at the expense of film homogeneity, which is affordable as only small surface samples are necessary for the film characterization.

Furthermore, a large oxygen concentration is found in the samples at the interface. This interface is of particular importance in a photoanode as it serves to transfer electrons via the conducting substrate to the counter-electrode. This oxide layer, with a thickness of 5nm to 10nm, can be expected to be insulating. Concerning the application of the Ta_3N_5 phase as a photoanode, therefore, a cleaning procedure needs to be established in order to reduce the oxide layer between the film and the surface.

5 The role of oxygen in Ta_3N_5 thin films

This chapter presents the results of the synthesis and characterization of Ta_3N_5 thin films by conventional DC magnetron sputtering as a function of oxygen incorporation. It starts with a discussion on the role of oxygen in Ta_3N_5-crystalline material (Section 5.1). This is followed by devising a cleaning procedure to remove the surface oxygen on the substrate (Section 5.2) before the recipe for the sample preparation of this chapter is presented (Section 5.3). Finally, the films are characterized as a function of their oxygen incorporation (Section 5.4). This is followed by a discussion on the optimum oxygen flowrate (Section 5.5) before finally, conclusions are drawn on the applicability of the conventional DC magnetron sputtering process with respect to the electrochemical performance of the samples (Section 5.6).

The results of this chapter are published in Rudolph et al., *Surf. Coat. Techn.*, 2016 (in press) [49].

5.1 Preamble: The necessity for oxygen and its effects

The conventional syntheses of Ta_3N_5 by ammonolysis and the preparation of Ta_3N_5 anodes by magnetron sputtering have in common, that oxygen plays a crucial role in the crystallization process as the oxygen-free synthesis has not been achieved up to date [30] [91]. The ammonolysis is typically done on pre-oxidized Ta foils (see Chapter 2.2.3) while the magnetron-sputtered films are sputtered in an $Ar/N_2/O_2$ atmosphere [21] [20]. Because the chemical formula Ta_3N_5 does not contain any oxygen and the phase stability of an ideal oxygen-free Ta_3N_5-crystalline material has been proven by DFT studies [75], the question arises why oxygen is necessary.

The answers lies in the high oxidation state of the metal atom in the Ta_3N_5 crystal. It has an oxidation number of +5 which requires a large charge transfer. To promote the oxidation of the Ta, the inductive effect can be used, in which an anion from the original formula is replaced by an anion having a greater electronegativity [211]. In the case of Ta_3N_5, the partial replacement of nitrogen by oxygen stabilizes the compound with the Ta in a +5 oxidation state [49].

The precise amount of oxygen in synthesized Ta_3N_5 material is not clear as the few values available vary largely. Ishihara et al. [20] measure by XPS an oxygen at.% of 38% (29at.% Ta, 34at.% N) for their most crystalline sample. On the other hand, Henderson et al. [95] employ thermogravimetric analysis and powder neutron diffraction and determined an oxygen content of a few at.% depending on the temperature and time of ammonolysis.

Even if the oxygen content is lower than found by Ishihara et al. [20], the oxygen can be expected to influence the properties of experimentally synthesized films. The question arises therefore, whether a certain amount of oxygen is beneficial or detrimental for the application in view. This chapter is therefore to quantify variations in properties, and to determine an optimum oxygen flowrate for the films in this study.

5.2 Sample cleaning

Before sample deposition, a cleaning method needs to be devised to free the interface between the film and the substrate from any incorporated oxygen. Experiments to evaluate the effectiveness of different cleaning steps were conducted with Ta-N samples deposited on a piece of monocrystalline Si wafer. The oxygen profile was the determined using RBS measurements. For the Ta_3N_5 samples prepared further down in this chapter, a metallic Ta substrate was used instead as a conductive substrate is necessary for the photoelectrolysis experiments. The substrate ultimately used is thus different from the Si substrate used here. The use of monocrystalline Si, however, was necessary due to the degree of purity; in particular the absence of oxygen in the Si wafer, makes it suitable for this measurement.

Moreover, Si is advantageous as it has a low atomic number Z. A metallic substrate with a higher Z would contribute to strong backscattering in the RBS measurements and possibly shadow the backscattering from oxygen in the film. By using Si substrates for these experiments, the assumption is made, that the oxygen removal from a metallic surface works similarly well compared to the oxygen removal from a Si substrate.

5.2.1 Sample preparation

Three samples were prepared for this experiment. Before each deposition, the chamber was intentionally oxygen-contaminated by running a HiPIMS discharge in Ar/O_2 for 30min with the magnetron shutter open. The cathode bias was set to -1100V, the pulse length, average power and working pressure to 10µs, 80W and 0.5Pa, respectively. The Ar and O_2 flowrates were constant at 49.5sccm and 0.5sccm, respectively.

Table 19: Cleaning and deposition procedure.

	cleaning procedure before deposition	**deposition**
Sample 1	None	DC 80W in Ar/N_2 at 30sccm/20sccm respectively for 7 min
Sample 2	Sputter-etching of target in DC mode at 80W with a closed shutter for 20min in pure Ar, and further 10min in Ar/N_2 at 30sccm/20sccm	DC 80W in Ar/N_2 at 30sccm/20sccm respectively for 7 min
Sample 3	Like sample 2 but with RF-sputtering the substrate at an effective DC bias of 100V for 10 min	DC 80W in Ar/N_2 at 30sccm/20sccm respectively for 7 min

After this intentional contamination of the chamber, the cathode and substrates underwent different cleaning processes before the deposition of the thin film took place (Table 19). The first sample served as a reference and was thus introduced right after the contamination procedure and deposited without any cleaning steps. For the second sample, the cathode was sputter-etched for 20min in DC mode in pure Ar, and then for further 10min in Ar/N_2 at flowrates of 30sccm and 20sccm, respectively. The third sample, in addition to the procedure for sample 2, was softly sputter-etched by radio-frequency biasing the substrate to an effective DC bias of 100V for 10min in pure Ar.

After the cleaning treatment, films were deposited by DC magnetron sputtering at 80W for 7min at 0.5Pa with Ar and N2 flowrates of 30sccm and 20sccm, respectively. The substrate was kept fixed above the cathode during the deposition.

5.2.2 Oxygen profiling experiments

Fig. 98 presents typical spectra from this experiments for one of the samples. Clearly visible are the backscatter peaks from oxygen that vary in position and height as a function of the energy of the alphas. The Si plateau is also visible, but its height varies strongly and in an allegedly arbitrary fashion with projectile energy. This stems from the so-called channeling in which the monocrystalline Si wafers are unintentionally oriented in way that the projectile particles can penetrate deeply into the substrate through the open channels in the crystal. This is an unwanted effect, which can, however be corrected for. The ideal method involves fitting a power law curve from the top to the bottom of the O peak. This fit is then used as the baseline and subtracted from the spectra around the O peak.

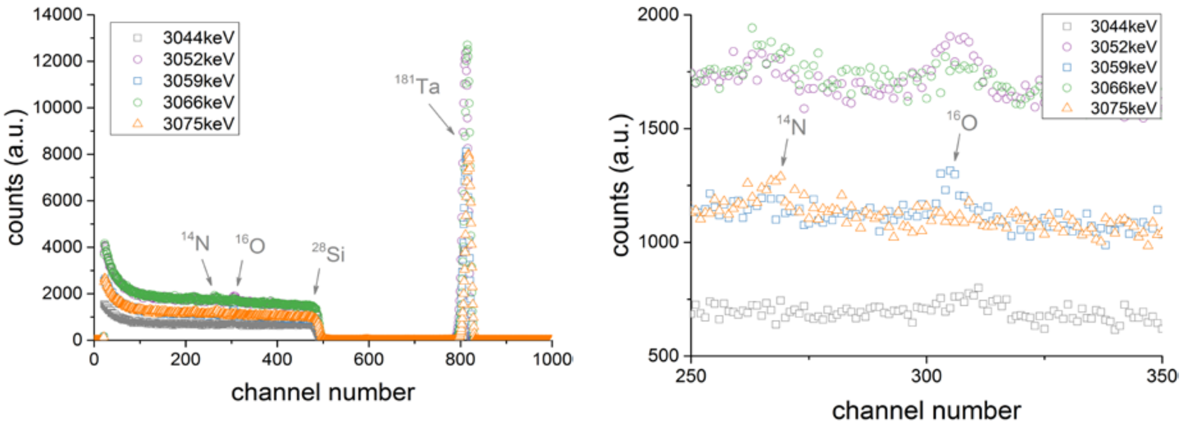

Fig. 98: RBS spectra from ^{16}O profiling experiments illustrating the channeling effect in the Si substrate. The left plot shows a zoom onto the ^{14}N and ^{16}O peaks.

The corrected spectra are shown in Fig. 99 for the three samples together with their fits from SIMNRA. As before (see Section 4.1.3.2), the SigmaCalc cross-sections were used to simulate the backscatter from O and the N. For the experiments here, the detector resolution was 31keV and lies thus slightly above the resolution of the detector used for the oxygen profiling experiments described in Section 4.1.3.2.

The depth profiles for the three samples are shown in Fig. 99. The first sample, i.e. the sample that serves as a reference, shows an oxide layer at the interface as expected. The second sample, for which the cathode was sputter etched before deposition, reveals a slightly reduced oxygen incorporation. Still, a considerable amount of oxygen can be found at the interface. Sputter-etching of the substrate, as done for the third sample, is shown to be very efficient, though. Apparently, most of the oxygen in the films is already on the substrate before transferring it into the deposition chamber.

The bulk of all samples, however, still contains a non-negligible oxygen incorporation of around 3at.%. HiPIMS films from Section 4.1.3.2 under similar conditions had an oxygen content of 5at.%. A clear reduction of the oxygen incorporated into the bulk is thus seen here. This is due to the higher deposition rate in DCMS mode instead of HiPIMS mode and due to the fact that the substrate is fixed above the substrate position and not kept rotating around the chamber axis.

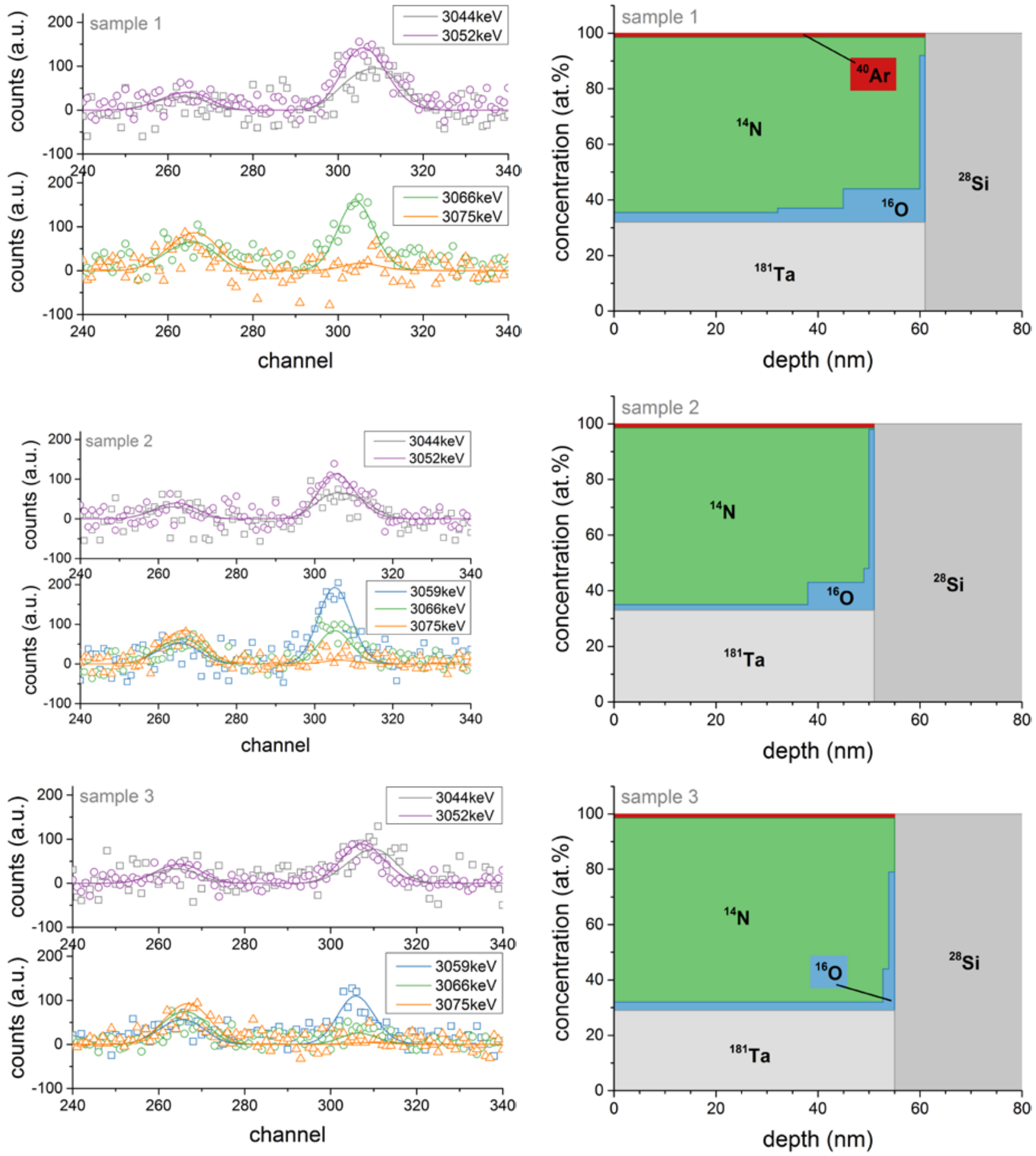

Fig. 99: ^{16}O profiling experiments for the samples 1, 2 and 3, described in Table 19. Left: Experimental and fitted RBS spectra; Right: Derived elemental composition as a function of sample depth.

Apart from oxygen, also the Ar incorporation of 1.5at.% is visible in the spectra in Fig. 90. The DCMS films analyzed in the same section (Section 4.1.3.2), however, had an Ar content of only 0.5at.% which is three times lower than for the films determined in Fig. 99. This may be due to the fact that the substrate holder is now fixed above the cathode and thus receives a higher flux of backscattered Ar.

The cathode and substrate cleaning procedure is successful in removing a large amount of oxygen. Some uncertainty exists in these measurements, notably from the small signal intensity of the O peak, the Si background subtraction to deal with the channeling, and finally due to the energy-resolution of the detector. Due to the fact, that a certain amount of oxygen is necessary in the films, however, the accuracy of these measurements is satisfying and the cleaning procedure is used on all samples from here on.

5.3 Ta_3N_5 thin film deposition

To comply with different measurement techniques, different substrates are required that are coated simultaneously. Electrochemical measurements require the use of a conducting substrate. Therefore, metallic Ta foils are used for the preparation of photoanodes in this chapter. Ta has the advantage that its work function of -4.25eV [212] closely matches the position of the conduction band of Ta_3N_5, which reduces any Schottky barrier at the interface [91]. The conduction band is believed to be positioned at -4.0eV as measured experimentally [19] although large deviations are possible as a function of oxygen content and the presence of defects [78] [89]. The electrical and optical characterization techniques employed require insulating and transparent substrate. A piece of quartz is therefore chosen as a substrate. Finally, SEM measurements require a flat substrate, for which a piece of monocrystalline Si (100) is selected.

Samples were prepared after the cleaning procedure devised in Section 5.2. During the cleaning, the substrate holder was heated up to 600°, a temperature that was determined to be necessary for magnetron-sputtered Ta_3N_5 thin films [20]. This temperature was kept constant during the deposition.

Deposition was done in conventional DC mode at an automatically controlled power supplied to the cathode of 80W. Two sets of samples were prepared, one at an N_2 flowrate of 20sccm at a total flowrate of 50sccm (corresponding to an N_2 concentration in the injected gas mixture of $c_{N2} = 40\%$), the other at 15sccm at a total flowrate of 25sccm in the injected gas mixture (corresponding to $c_{N2} = 60\%$). The different total flowrates were necessary for technical reasons.

The reason for the high N_2 flowrates employed here, despite the fact that films with Ta_3N_5 stoichiometry were deposited in the previous chapter with N_2 flowrates <10sccm (DCMS case), is the substrate temperature. Higher temperatures promote the desorption of N from the surface. Shin et al. determined a 10% lower [N]/[Ta] ratio in the films when going from 100°C substrate temperature to 600°C for close-to stoichiometric δ-TaN films [130].

The injected O_2 was varied in small quantities from one sample to another between 0sccm to a maximum of 0.9sccm. Ar was added to reach a total flowrate of 50sccm. The working pressure was controlled by a throttle valve between the turbomolecular pump and the deposition chamber and kept at 0.5Pa.

Optical emission spectroscopy of the oxygen triplet around 777nm gave only a very small signal even for the highest flowrates [213]. It was therefore expected that the low oxygen flowrates used here were not sufficient to saturate the target and that the target stayed in non-poisoned mode with respect to the oxygen. This means that the oxygen injected into the reactor was immediately gettered by the freshly deposited Ta and as a consequence, a linear incorporation of oxygen into the film with flowrate was assumed.

To reduce the amount of oxygen incorporated from the background gas pressure (see Chapter 7) the substrate holder was kept fixed above the cathode which effectively increased the deposition rate. After a deposition time of 30min kept constant for all samples, their thicknesses were between 330nm to 380nm at $\phi_{N2} = 20$sccm and between 200nm to 250nm at ϕ_{N2}=15sccm.

5.4 Sample characterization

The samples were characterized by grazing incidence X-ray diffraction (Gi-XRD) to proof the presence of the Ta_3N_5 phase. In a second step, transmission and reflection spectra were taken between 350nm and 1000nm to which a dielectric function was fitted to determine the band gap and its absorption curve. Latter was used to calculate the charge carrier mobility. Finally, XPS measurements are performed on the same samples before and after the photoelectrolysis, to see possible effects of degradation of the samples.

5.4.1 Structure

The structural characterization is done by GI-XRD. Fig. 100 shows the results for the two different N_2 flowrates of ϕ_{N2} = 20sccm and 15sccm. In general, both series show the same evolution. At very high oxygen flowrates, the samples are featureless and therefore amorphous. By lowering the oxygen concentration from this highest level, the Ta_3N_5 phase appears. The phase remains visible down to the samples deposited at a minimum, but non-zero, oxygen flowrate. For the ϕ_{N2} = 20sccm series, in addition, a sample deposited without any oxygen flowrate is deposited which shows a δ-TaN signature and no sign of the Ta_3N_5 signature any more. Obviously, also for the samples of this thesis, a minimum oxygen flowrate is necessary to promote crystallization of the Ta_3N_5 structure.

All diffractograms show low signals compared to the background noise, which could indicate a dominating amorphous phase and a small degree of crystallinity.

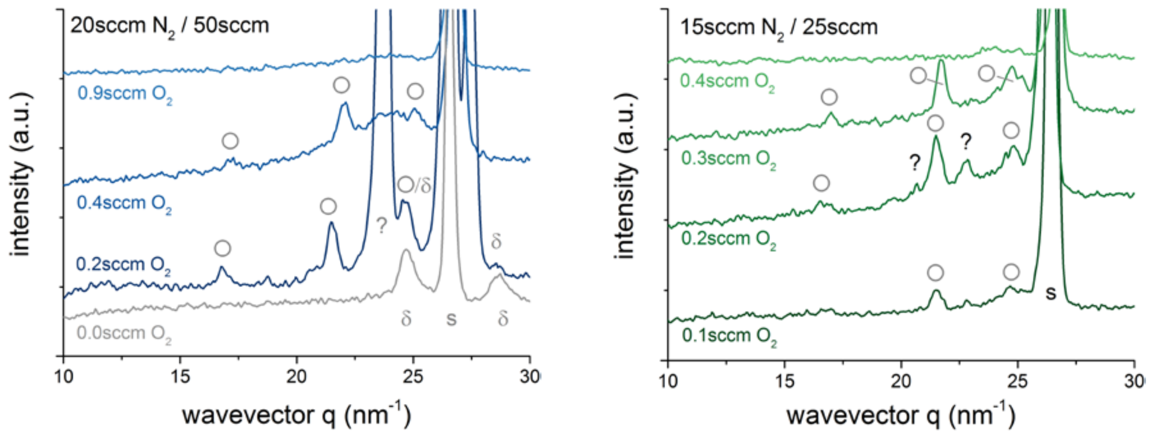

Fig. 100: GI-XRD of samples deposited at ϕ_{N2} = 20sccm (left) and 15sccm (right). The grey circles mark peaks corresponding to the Ta_3N_5 phase, the 's' marks peaks from the underlying Ta substrate and the δ marks peaks belonging to the δ-TaN phase.

5.4.2 Transmission and reflection spectra, band gap and absorption

The uv.-vis. transmission and reflection spectra were measured following the procedure in Section 3.4 using the samples deposited on a transparent piece of quartz. The spectra were subsequently fitted to a Tauc-Lorentz model with or without an Urbach tail depending on the quality of the fit judging from f_{obj} from Eq. 60 (see 3.4.3.2).

The measured and fitted transmission curves are presented in Fig. 101 for ϕ_{N2} = 20sccm and ϕ_{N2} = 15sccm. Both sets of samples behave similarly. At high oxygen flowrates, the samples are transparent down to the near ultraviolet spectrum (< 400nm). Lowering the oxygen flowrate moves this absorption edge towards longer wavelengths into the visible range.

At the same time, these spectra have a lower intensity on average in the long wavelength range of the spectra which indicates in-gap states and requires the Urbach tail model to represent this behavior. Fig. 102 shows a plot of Urbach energy as a function of the oxygen flowrate and proofs the steep rise in Urbach energy E_u with decreasing the oxygen flowrate for both series of samples.

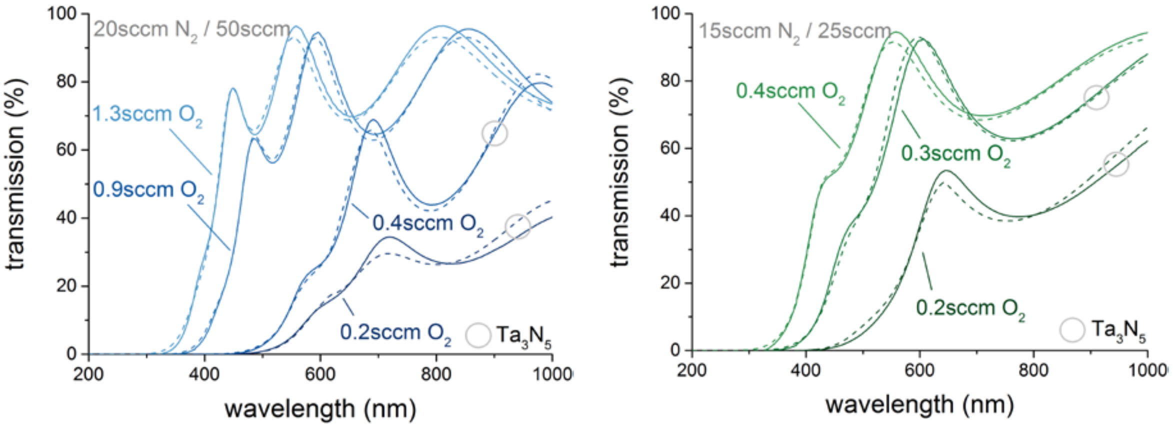

Fig. 101: Transmission curves for samples deposited at ϕ_{N2} = 20sccm (left) and ϕ_{N2} = 15sccm (right) and various O_2 flowrates. The plots show the measured curves (continuous lines) and the fitted curves (dashed lines). Ta_3N_5-crystalline samples are marked by a grey circle.

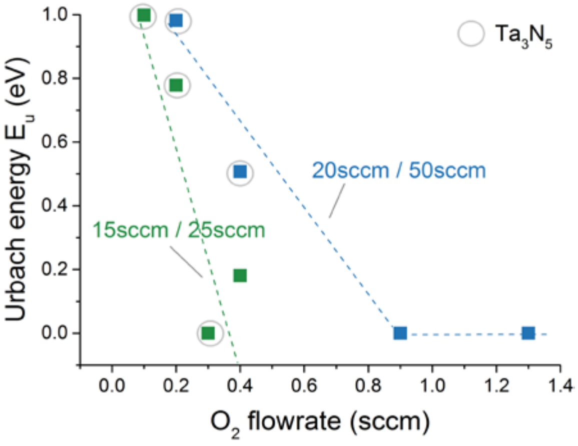

Fig. 102: Urbach tail energy E_u for the two sets of samples. Ta_3N_5-crystalline samples are marked by a grey circle.

These in-gap states have been observed before experimentally in samples prepared by ammonolysis and they are attributed to reduced Ta species in the lattice [96] [214]. DFT simulations show that the appearance of in-gap states is actually an abundant phenomenon for any deviations from the ideal Ta_3N_5 stoichiometry in which the Ta remains in a reduced state [215] while in DFT calculations with balanced charges these are absent [85]. The results obtained here thus confirm the argument from section 5.1, that oxygen is a critical ingredient for the Ta to reach its +5 oxidation state.

The physical parameter obtained by fitting the transmission and reflectance spectra is the dielectric function. Its real component ε_r' is shown in Fig. 103 together with the measured dielectric function of Morbec et al. [18] (cf. Fig. 16). The samples deposited at the highest O_2 flowrate show much too low values of ε_r' compared to the reference in the visible range. But as the O_2 flowrate is decreased, the imaginary component grows until it is close to the range of the reference value. The features of the reference between 350nm and 600nm can naturally not be represented by only a single Tauc-Lorentz oscillator. The use of more than one oscillator in the fitting procedure, however, results in arbitrary results that are not reproducible. A single oscillator is therefore considered the best choice here.

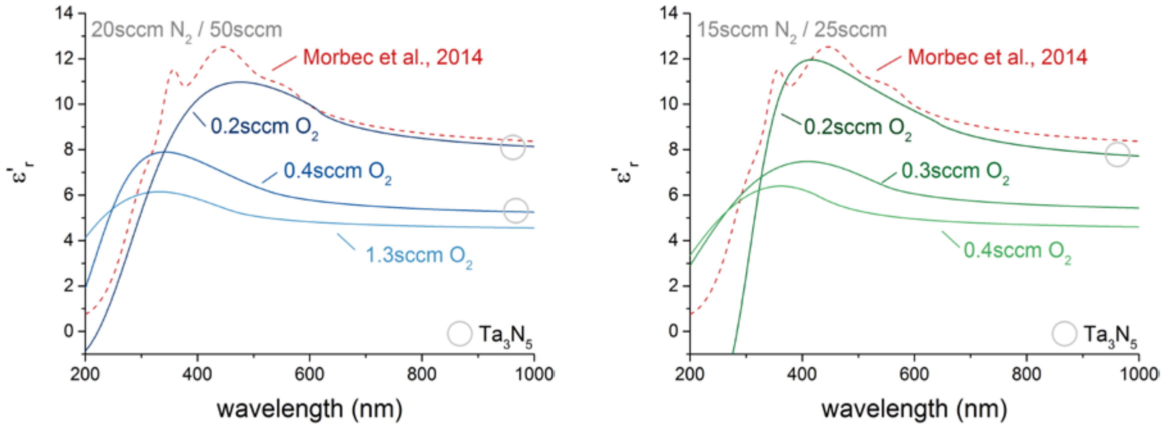

Fig. 103: Dielectric function ε_r' derived by fitting a Tauc-Lorentz with an Urbach tail model simultaneously to the transmission and reflectance spectra. As a reference, the Ta3N5 dielectric function derived by Morbec et al. [18] is shown (in red). Ta_3N_5-crystalline samples are marked by a grey circle.

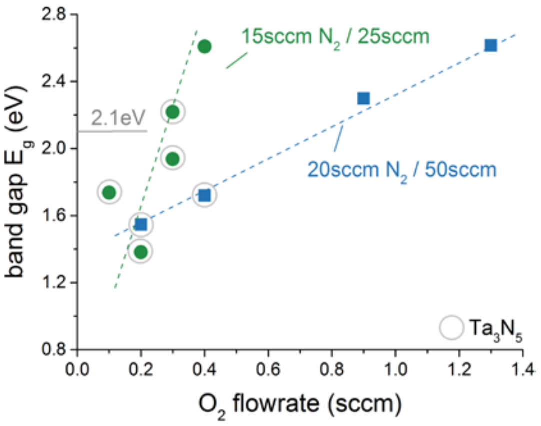

Fig. 104: Band gap as a function of c_{O2} for both c_{N2} = 40% and c_{N2}=60% samples. Ta_3N_5-crystalline samples are marked by a grey circle.

The band gap is a parameter of the Tauc-Lorentz model and thus directly accessible. It is presented in Fig. 104 for the two nitrogen flowrates. Both sets of samples show a linearly increasing band gap with O_2 flowrate. This is an effect of the lower energy level of the O 2p orbital compared to the more shallow N 2p orbital that contribute to the semiconductor valence band (see Section 2.2.1.2). The fact that both curves do not lie on top of each other is due to different deposition rates that result in a higher oxygen incorporation for the films deposited with ϕ_{N2} = 15sccm compared to those deposited at ϕ_{N2} = 20sccm for the same O_2 flowrate.

The sample exhibiting the Ta_3N_5 phase from the GI-XRD measurements, are marked by a grey circle in Fig. 104. Apparently some correlation exists between the band gap and the structure of the films, as for both N_2 flowrates, all films with a bandgap ≨2.1eV, exhibt the Ta_3N_5 phase.

Finally, from the dielectric function, the absorption length can be calculated which gives an idea of how thick a film needs to be at least, in order to absorb close to 100% of all incident photons. Fig. 105 shows the absorption length for samples deposited at varying O_2 flowrates. In general, the absorption length is lowest, i.e. most favorable for the application in view, for the low O_2 flowrates. But only for the lowest O_2 flowrates tested, acceptable absorption lengths around the band gap exist. For the sample deposited at ϕ_{N2} = 20sccm and ϕ_{O2} = 0.2sccm, the absorption length at 590nm, corresponding to 2.1eV, is 220nm. On the other hand the best sample deposited is the one at ϕ_{N2} = 15sccm and ϕ_{O2} = 0.3sccm as it does not contain any in-gap states and still exhibits the Ta_3N_5 phase. For this sample, the absorption length is 4.6μm. This is very thick when considering that the space charge layer thickness at the semiconductor-electrolyte interface (cf. Section 2.1.3) is typically ≤1μm.

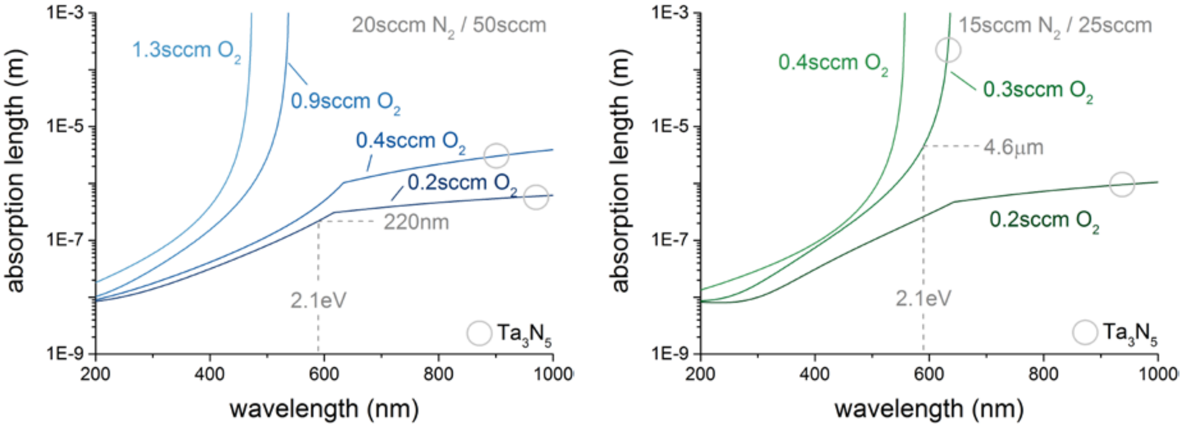

Fig. 105: Absorption length for the samples deposited at ϕ_{N2} = 20sccm (left) and ϕ_{N2} = 15sccm (right). The ideal band gap of Ta_3N_5 (2.1eV) is indicated together with the absorption length at that value for two samples.

The fact that a single Tauc-Lorentz model is sufficient to represent the transmission and reflection spectra quite well hints towards a dominating amorphous phase as this model is developed for amorphous materials [168]. The fact that the diffractograms show a clear Ta_3N_5 signature seems contradicting at first. However, as X-ray diffraction is not necessarily sensitive to any amorphous content [216], this does not show up in the diffractograms. Thus a crystalline/amorphous phase mixture with a dominating amorphous content with some crystallites could explain these allegedly contradicting results. An alternative explanation could be that the nucleation and growth of Ta_3N_5 strongly differs on metal substrates such as Ta and quartz substrates. This latter hypothesis is verified in the following chapter (Chapter 6). The optical parameters obtained from the measurements done here are therefore those of a purely amorphous Ta-O-N film.

Hence, the retrieved dielectric function, the determined band gap and the absorption do not necessarily correspond to those of the crystalline phase. However, due to the low degree of crystallinity of the films deposited on metals (cf. Fig. 100 and Fig. 110), it is believed that they as well, are dominated by an amorphous phase. The general trends of the optical parameters retrieved for the amorphous films deposited on quartz can therefore be assumed to be equally valid for the films deposited on the Ta foil.

5.4.3 Conductivity and efficiency-mobiliy-lifetime product

The mobility-lifetime product is another important property of the films as it is directly related to the diffusion length of the charge carriers. Therefore, it needs to be sufficiently high for the holes and electrons to reach the surface and the conducting substrate, respectively, from the point of their creation.

Experimental setup

The measurements were done again on films deposited on a quartz substrate as a non-conductive substrate was necessary. To apply a voltage and measure a current, two coplanar electrodes of silver were deposited onto the film surface. That means, that the measurements yield properties parallel to the surface of the film.

As the films deposited on quartz are amorphous, no preferred orientation is expected. Therefore, the films can be assumed to be isotropic and under this assumption, the properties parallel to the surface and that perpendicular to it are similar.

The conductivity of the samples was measured by applying a potential difference between the electrodes in the dark. The current-voltage characteristics showed an Ohmic behavior between -5V and +5V [49]. The conductivity could in this case simply be measured using Ohm’s law.

The current under illumination was measured using an LED light source with a photon flux of 10^{15} photons·cm^{-2}s^{-1} emitting at 450nm. This current was naturally higher than the dark current due to the increased charge carrier density from the creation of electron-hole pairs. The photocurrent I_{photo} was then determined by subtracting the dark current from the current under illumination.

From this, the combined efficiency-lifetime-mobility product $\eta\mu\tau$ for holes and electrons could be determined from Eq. 69 [217]:

$$I_{photo} = [(\eta\mu\tau)_e + (\eta\mu\tau)_h] \frac{qF(1-R)(1-\exp(-\alpha t))}{t} \frac{Vwt}{L} \qquad \textit{Eq. 69}$$

where the sum $[(\eta\mu\tau)_e + (\eta\mu\tau)_h]$ is the combined efficiency-mobility-lifetime product $\eta\mu\tau$, q is the elementary charge, F is the photon flux (here: 10^{15} photons·cm^{2} s^{-1}), the term F(1-R)(1-exp(-αt)) yields the photon flux absorbed by the sample [218], V is the applied voltage and t, w and L correspond to the film thickness, the width of the electrodes and the spacing between the electrodes, respectively.

Results

The evolution of sample conductivity with O_2 flowrate is shown in Fig. 106. The samples show a strong dependence on the O_2 flowrate with samples from the highest to the lowest conductivity covering almost 12 orders of magnitude. The conductivity of the sample deposited witout any O_2 flowrate and exhiting the metallic δ-TaN structure is similarly plotted. It lies perfectly on the trend formed by all other samples deposited at ϕ_{N2} = 40sccm. Apparently, the increasing conductivity is the result of a changing chemical order in the films towards the metallic δ-TaN phase. This is in line with the optical measurements that, with decreasing the O_2 flowrate, show a shrinking band gap and the appearance of in-gap states.

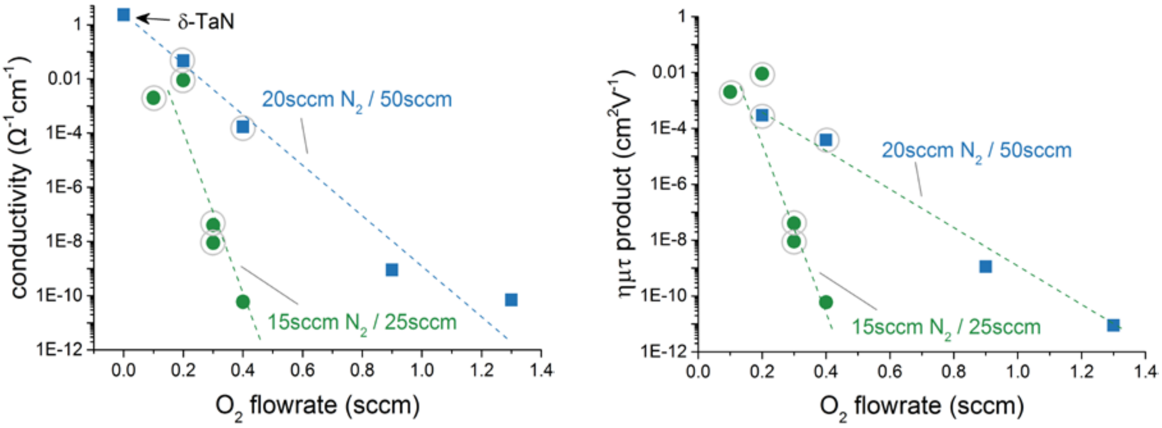

Fig. 106: Conductivity as a function of O_2 flowrate for the samples at ϕ_{N2}=20sccm (blue symbols) and ϕ_{N2}=15sccm (green symbols). The dashed curves indicate the trends for the two sets of data. The Ta_3N_5-crystalline samples are marked with a grey circle.

Table 20 : Charge carrier mobilities and $\mu\tau$-products from other studies to compare with the results of this thesis. †In the case of this thesis, the $\eta\mu\tau$-product is deduced which translates into the $\mu\tau$-product by assuming a quantum effici[ncy of η=1.

author	**phase and preparation method**	**lifetime τ**	**mobility μ ($cm^2V^{-1}s^{-1}$)**	**μτ product† (cm^2V^{-1})**	**ref.**
Ziani et al., 2015	Ta_3N_5 thin films from sputtering and post-deposition ammonolysis	3.1ps to 8.7ps	1.9 to 4.4	$4x10^{-12}$ to $32x10^{-12}$	[40]
de Respinis et al., 2015	By ammonolysis:				[47]
	Ta_2O_5	5ns	$2.2x10^{-5}$	$1.1x10^{-13}$	
	β-TaON	2.3ms	0.01	$2.3x10^{-5}$	
	Ta_3N_5	1.6ms	0.08	$1.3x10^{-4}$	
results from this chapter				$1x10^{-12}$ to 0.01	

The ημτ-product follows the conductivity in its linear decrease with O_2 flowrate (Fig. 106, right hand-side). It covers a large range of nine orders of magnitude, with the highest values having a ημτ-product of $>10^{-4}cm^2V^{-1}$. This cannot be readily converted into a minority carrier diffusion length as it is the combined ημτ-product for electrons and holes (cf. Eq. 69). The lowest ημτ-values are around $10^{-11}cm^2V^{-1}$ for samples deposited at high O_2 flowrates.

These values can be compared to two other studies which determined charge carrier mobilities and lifetimes in Ta_3N_5 thin films. They are summarized in Table 20. The first study is the one by Ziani et al. [40] who sputtered films of Ta onto a substrates and crystallized them by post-annealing at 500°C, followed by ammonolysis at 900°C. They measure a very low μτ-products between $4\cdot10^{-12}$ to $32\cdot10^{-12}cm^2V^{-1}$.

A second study is that of de Respinis et al. [47] who prepared samples similarly to above but sputtered Ta onto a quartz as a starting material. They obtain three different phases from the Ta-O-N system and determine a strong increase in the μτ-product by going from Ta_2O_5 ($\mu\tau=1.1\cdot10^{-13}$) via

TaON ($\mu\tau = 2.3\cdot10^{-5}$) to Ta_3N_5 ($\mu\tau = 1.3\cdot10^{-4}$) which they ascribe to the influence of oxygen. This supports the results obtained in this thesis that the $\eta\mu\tau$-product is strongly dependent on the incorporation of oxygen into the lattice.

The detrimental effect of the incorporated oxygen on the charge carrier mobility could be due to the stronger covalency of the Ta-O bond compared to the Ta-N bond. This induces a stronger localization of charge carriers in the lattice, decreasing their mobility [47]. A second mechanism are deep level traps that are proposed to be present in Ta_3N_5-crystalline films containing oxygen. The lower energy level of the O 2p orbitals compared to the N 2p orbitals form traps in the valence band to which holes are attracted. These promote the recombination of charge carriers and thus reduce their lifetime [53].

The detrimental effect of oxygen incorporated into the films is evident. However, the measurements are conducted on an amorphous phase, which raises the question in how far the measurements are relevant also for the crystalline Ta_3N_5 phase. As both mechanisms for the reduced mobility and the reduced lifetime are general mechanisms in solid state physics, they are believed to be equally valid for the crystalline phase. So, although the absolute value for the $\eta\mu\tau$-product may differ in Ta_3N_5 crystals, the same trend can be expected. Therefore, judging by the electronic properties, photoanodes prepared by magnetron sputtering should be deposited at an oxygen flowrate as small as possible.

5.4.4 X-ray photoelectron spectroscopy

The objective of the XPS measurements was to determine whether the chemical order of the surface of the sample changed during the photoelectrolysis experiment. For that, XPS spectra were taken before and after conducting the photoelectrolysis experiments. Before the second XPS measurement, the samples were rinsed under distilled water.

A typical survey spectra from before and after are shown in Fig. 107. While the sample before the photoelectrolysis measurements does not indicate any contamination apart from carbon (see C 1s peak around 284eV), the spectra afterwards shows strong signals from metals present as impurities in the KOH electrolyte.

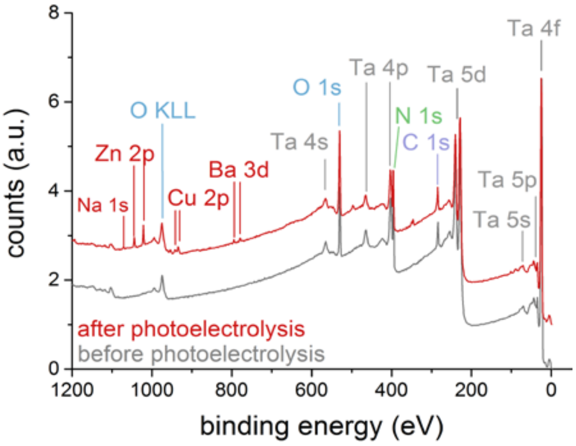

Fig. 107: XPS survey spectra of a sample before (grey) and after (red) photoelectrolysis. Clearly visible are the depositions of Ba, Zn and Cu likely from impurities from the electrolyte precursor. The red curves (after photoelectrolysis) is shifted upwards by 1 for readability.

The spectra interesting for the purpose of this study are the Ta 4f regions between 30eV and 23eV that shift according to the ratio of oxygen or nitrogen present in the film surface as discussed in section 3.5.

The resulting spectra taken before and after photoelectrolysis are shown in Fig. 108 for the samples deposited at ϕ_{N2} = 20sccm. They have been fitted with an appropriate number of components that are named according to their closest reference value. The reference values are mostly taken from Ritala et al. [219] for reasons of consistency. Only for the case of TaN, the publication by Ritala et al. did not contain any value so that the value published by Zhang et al. [220] is chosen. The reference values are summarized in Table 21.

Table 21: XPS reference value used for identifying the components in this thesis.

chemical bonding	Ta $4f_{5/2}$	Ta $4f_{7/2}$	ref.
Ta	23.7eV	21.8eV	[219]
TaN	24.8eV	23.5eV	[220]
Ta_3N_5	26.7eV	24.8eV	[219]
TaON	27.7eV	25.8eV	[219]
Ta_2O_5	28.5eV	26.6eV	[219]

The two principal components that are present in every sample are the oxynitride and the nitride component. Before photoelectrolysis, the Ta $4f_{7/2}$ oxynitride component peaks between 26.1eV and 26.4eV and is close to the reference value of TaON at 25.8eV [219]. The nitride component, is situated between 25.1eV and 25.4eV which is close to the reference value of Ta_3N_5 at 24.8eV [219]. Both nitride and oxynitride peaks are slightly shifted to higher energies by approximately 0.5eV compared to their references, which will be discussed further down.

Compared to the two samples deposited at higher oxygen concentration, the first sample with ϕ_{O2} = 0.2sccm has an additional peak at an even lower binding energy of 24.3eV which is termed metallic component. The metallic TaN reference value is only 23.5eV [220] but considering the same shift of 0.5eV as found for the nitride and oxynitride component, the two values come close. The presence of this metallic peak confirms the hypothesis from Section 5.4.2, in which reduced Ta states are proposed to being responsible for the Urbach tail that appears at small oxygen flowrates.

The two samples at ϕ_{O2} = 0.4sccm and ϕ_{O2} = 1.3sccm have very similar spectra despite the fact that the first one exhibits the crystalline Ta_3N_5 phase while the latter one is amorphous. Both have similar peak positions for their oxynitride (26.1eV compared to 26.2eV) and nitride (25.1eV compared to 25.4eV) component. The only difference is, that the oxynitride component has a larger area compared to the oxide component in the sample deposited at ϕ_{O2} = 1.3sccm. This is apparently an effect of the increased oxygen flowrate.

After the photoelectrolysis, all three spectra are slightly shifted to lower energies. However, as oxygen is produced on the samples during the measurements, a reduction of Ta in this environment is unlikely. As the peak positions fit better with the corresponding references mentioned above, a possible error in the calibration of the spectra may have occurred during the measurements before photoelectrolysis.

Strikingly are differences between before and after the photoelectrolysis for the last sample (ϕ_{O2} = 1.3sccm). It gains an additional doublet which is in the vicinity of a Ta_2O_5 reference (26.6eV [219]) and therefore termed oxide component. At the same time the surface area of the nitride doublet is drastically reduced, which hints towards an unstable surface under photoelectrolysis conditions. The amorphous nature of this sample could be the explanation for this sample to change the chemical environment of its surface.

The sample deposited at the lowest oxygen flowrate, at ϕ_{O2} = 0.2sccm has its metallic component disappear during the photoelectrolysis. This can be explained by surface oxidation, but is of minor importance, as this metallic component is an artefact not wanted in the first place, that can be avoided by a sufficiently high oxygen flowrate during deposition. Finally, the sample deposited at a flowrate between the two samples discussed above, shows very little change in the Ta 4f spectra.

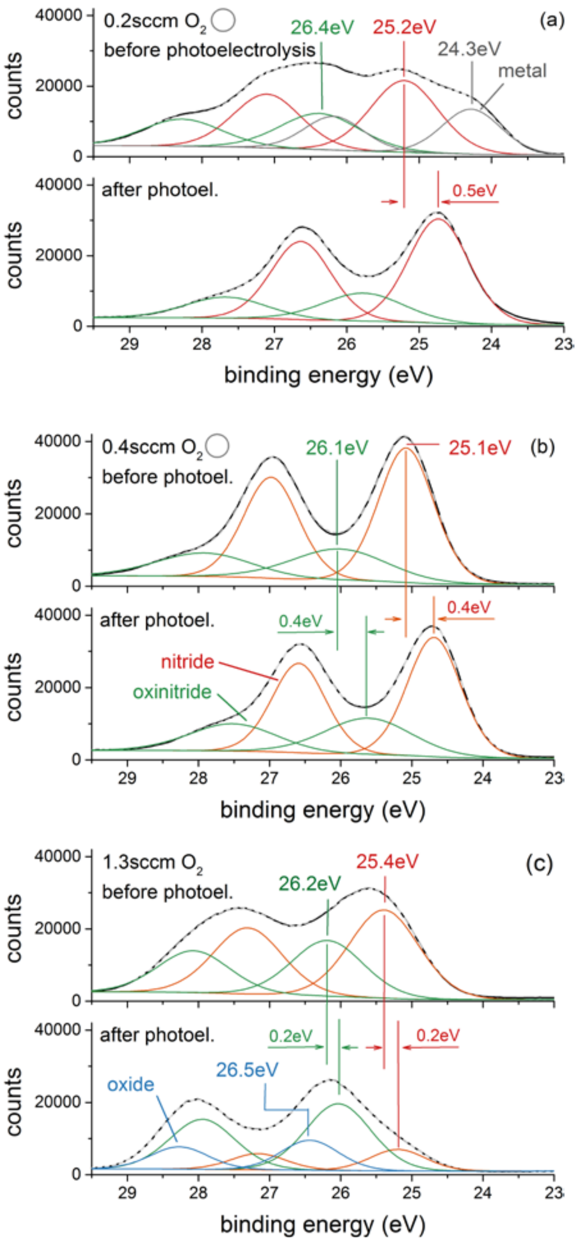

Fig. 108 : Spectra before (top) and after (bottom) photoelectrolysis. The dashed black line and continuous grey line show the measured and the fitted envelop respectively. The individual components are colored in grey (metallic), red (nitride), green (oxinitride) and blue (oxide). The Ta_3N_5-crystalline samples are marked with a grey circle.

Further insight can be gained by looking at the peak areas of fitted components. For this, all samples deposited at ϕ_{N2} = 20sccm and ϕ_{N2} = 15sccm are taken into account to increase the data set. The ratio r is defined as the nitride surface area S_N to the oxinitride surface are S_{ON} and, if present, oxide surface area S_O according to Eq. 70.

$$r = \frac{S_N}{S_{ON} + S_O} \qquad \textit{Eq. 70}$$

The values for the samples and their percentaged change can be found in Table 22 and for all samples a decrease in the so-defined r-value is observed. This is in line with other authors [21] [90] that observe a surface oxidation on their samples, which is believed to cause a reduction in photocurrent [16].

It is obvious from Table 22 that samples deposited at a higher O_2 flowrate show a stronger decrease in r during the photoelectrolysis. This applies in particular to the amorphous samples (ϕ_{N2} = 20sccm, ϕ_{O2} = 1.3sccm and ϕ_{N2} = 15sccm, ϕ_{O2} = 0.4sccm) so that the conclusion is, that oxygen in the as-deposited films promotes further oxidation during the photoelectrolysis. It is important to note though, that despite the reduction in photocurrent, the surface oxidation does not necessarily inhibit the functioning of the device as the oxidized surface serves as a protection layer which stops further growth of this layer into the film [90].

Table 22 : Ratios of peak areas of fitted components before and after photoelectrolysis. The Ta_3N_5-crystalline samples are marked with a grey circle.

ϕ_{N2}, ϕ_{O2}	r_{before}	r_{after}	$(r_{after} - r_{before}) / r_{before}$, (%)
20sccm, 0.4sccm ○	2.6	2.1	-19%
20sccm, 0.9sccm ○	1.6	0.8	-46%
20sccm, 1.3sccm	1.5	0.7	-55%
15sccm, 0.2sccm ○	2.0	1.9	-5%
15sccm, 0.3sccm ○	2.6	0.5	-79%
15sccm, 0.4sccm	2.1	0.4	-82%

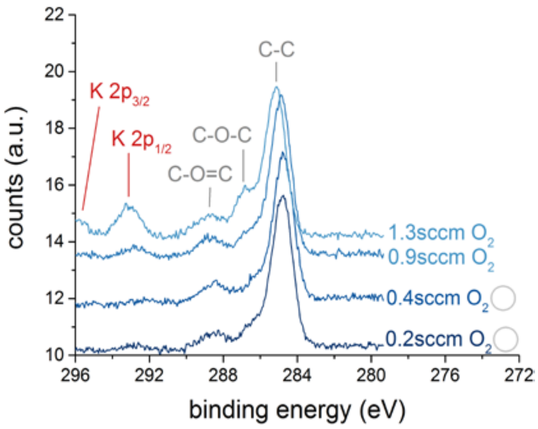

Fig. 109: Appearance of a K signature for samples deposited at higher oxygen flowrates. The Ta_3N_5-crystalline samples are marked with a grey circle.

The very strong oxidation of the two amorphous samples, though, can be a sign for the decomposition of the film. This is evidenced on the C 1s spectra in Fig. 109 by a strong peak of K that appears only at higher oxygen flowrates on amorphous samples. This hints towards a chemical reaction of the surface with the electrolyte. This change in chemistry shows the instability of the sample under photoelectrolysis. It is thus not suitable for the application.

The findings from the XPS measurements before and after photoelectrolysis allow to say that samples should be deposited at the lowest oxygen concentration possible. This is concluded from the fact that a stable surface such as that for the sample deposited at low oxygen is preferred for the application in view.

5.4.5 Surface morphology

Scanning electron microscopy images show the surface morphology of films deposited on Si wafers at two different oxygen flowrates (Fig. 110). The films are rather thick, as thinner films did not show any crystalline structure when deposited on monocrystalline Si(100) substrates (cf. Section 6.2.1). The films deposited for the measurements here therefore have a thickness of around 800nm. Although it is believed that they show the general trend concerning the surface morphology on films deposited on a sheet of Ta, they cannot directly be compared to those films due to the large difference in thickness.

At the high O_2 flowrate (0.9sccm), a cauliflower-shaped surface appears without obvious crystallites. This observation is in line with the diffraction results that proves the amorphous nature of this sample.

The lower O_2 flowrate (0.4sccm) lies within the range of flowrates for which the diffractograms show the presence of Ta_3N_5. Indeed, large crystallites can be seen on the sample that are embedded into a featureless matrix, which could be interpreted as amorphous. This would be in line with the diffractograms that indicate a dominant amorphous content due to the small intensity of diffraction peaks (Section 5.4.1).

Remarkable for the latter sample is the Ta_3N_5 crystallite sizes of up to 300nm. Typical grain sizes in magnetron-sputtered films range from close to 0nm (i.e. amorphous) over a few nanometer (i.e. nanocrystalline) up to ~100nm for metals (e.g. [221] [222]) and largely below 100nm for compounds (e.g. [223] [224]). The grain sizes observed here are therefore very large compared to other studies. This is likely to be induced by the high substrate temperature of 600°C. Striking, however, is the presence of the coexisting amorphous phase and the questions arises why this material does not crystallize. Apparently, the nucleation of Ta_3N_5 is hampered while the growth is not.

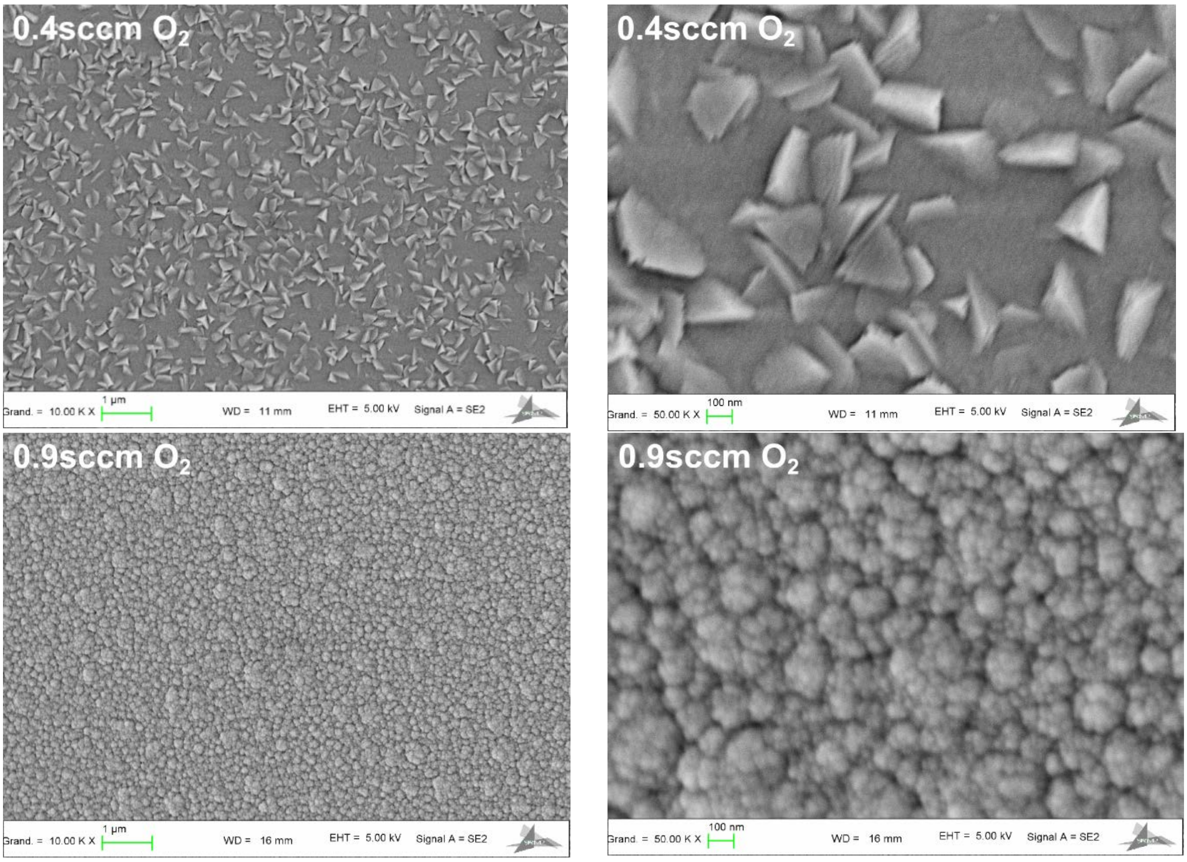

Fig. 110: Scanning electron microscopy of films deposited at $\phi_{N_2} = 20sccm$ *and at a low and a high* O_2 *flowrates. The samples are deposited on monocrystalline Si substrates and have a thickness of 800nm.*

5.4.6 Solar water-splitting performance

The solar water-splitting performance of the samples was tested by taking voltammetry curves measured under chopped light illumination. For that, the samples were immersed into an electrolyte made of a 0.1M K_2SO_4 aqueous solution into which KOH was added to reach a pH of 11. Its conductivity was determined to be 20.0mS. As the samples were observed to change between successive scans, in particular for the first scans, each sample was scanned several times until a reproducible current density curve was obtained. This required up to five scans.

Fig. 111 presents the voltammetry curves for the samples deposited at an N_2 flowrate of 20sccm N_2. For all samples, the effect of the light is visible as a rectangular-shaped step function. For the two samples deposited at a lower O_2 flowrate (ϕ_{O2} = 0.2sccm and ϕ_{O2} = 0.4sccm) this effect is barely observable. Obvious on those samples is also that the dark current (the parts of the curve in which the light is off) shows a upward bend towards a higher bias suggesting the flow of current through the electrolyte which is possible due to the conductive nature of those samples deposited at low O_2 flowrates (cf. Fig. 106).

The two samples deposited at a higher O_2 flowrate, show a more pronounced effect of the illumination (right hand-side in Fig. 111). Moreover, their dark current remains constant, which is in line with the fact that those two samples have a much higher resistivity, decreasing the current that can pass through the semiconductor electrode. These samples, however, correspond to those showing the strong signature of the K peak evidenced by XPS after the photoelectrolysis (cf. Fig. 109). These are therefore likely to be unstable, and it is unclear whether the photocurrent observed on those is indeed due to the evolution of oxygen on the semiconductor surface.

All four samples show transients at the beginning of each illumination interval. This effect is caused by a higher rate of charge carrier production compared to the transfer of charge carriers onto the solution [225]. The result is a drastic decrease in the photocurrent density from after the beginning of the pulse. They show, however, that the potential of the films is much higher than the current density actually measured at the plateau of each illumination interval. A higher surface area or the use of a co-catalyst could help to reduce these transients and to exploit to a maximum the holes produced during illumination.

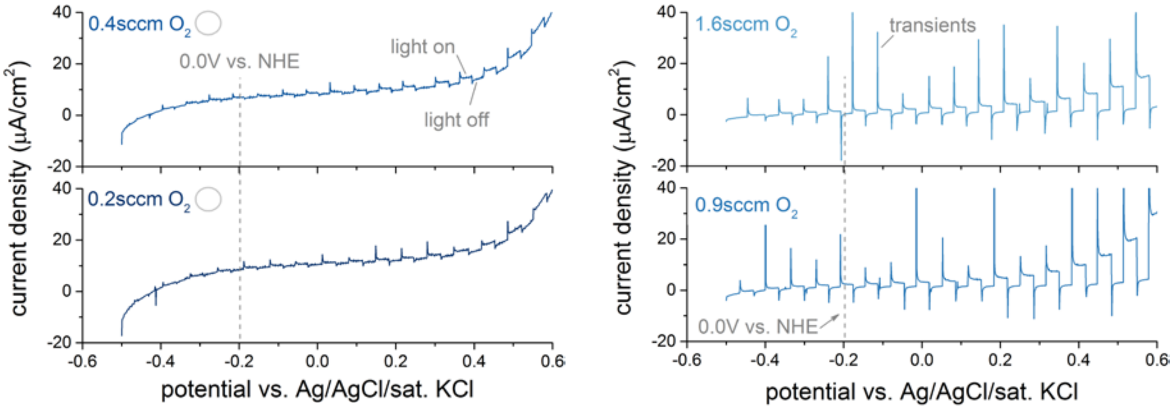

Fig. 111: Voltammetry curves for the samples deposited at ϕ_{N2} = 20sccm. The samples on the left are the crystalline samples (indicated by a grey circle).

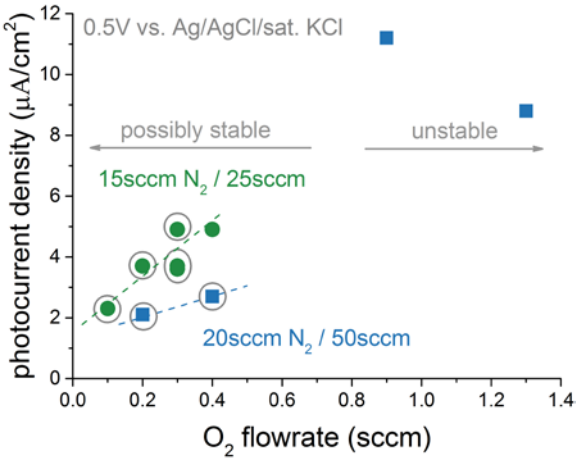

Fig. 112: Summary of photocurrent at 0.5V vs. Ag/AgCl/sat. KCl.

The performance of all samples is summarized in Fig. 112 as the photocurrent density at 0.5V vs. Ag/AgCl/sat. KCl. The samples exhibit a slight increase in current density with O_2 flowrate, which is steeper for the samples deposited at a 15sccm N_2 flowrate. These observations, however, do not proof a causal relationship as also the thickness varies with the flowrates of the reactive gases. This is a crucial parameter because it determines the compromise between a thick film that absorbs up to 100% of the photons above the band gap, and a thin film that reduces the distance travelled by charge carriers and with that, the probability of recombination. It appears unlikely that the small differences in thicknesses influence the performance of the photoanodes, but cannot be ruled out. No conclusive statement on the performance of the photoanodes as a function of oxygen incorporation is thus drawn. It is important to note, though, that all samples show a photocurrent density that is extremely low with respect to the theoretically possible. The reason for the low performance likely lies elsewhere but have little to do with the amount of oxygen incorporated into the films.

5.5 Discussion

The compilation of measurements above need to be discussed in order to determine optimum process conditions for the deposition of a Ta_3N_5 crystalline photoanodes. Apparently, a minimum amount of oxygen is necessary to avoid the metallic δ-TaN phase. At high oxygen flowrates, the material is amorphous and not stable under photoelectrolysis conditions, which restraints the oxygen flowrates to somewhere between 0.2sccm to <0.9sccm for ϕ_{N2} = 20sccm and 0.1sccm to 0.3sccm O_2 for ϕ_{N2} = 15sccm.

Little difference can be observed between the two nitrogen flowrates at ϕ_{N2} = 20sccm and ϕ_{N2} = 15sccm. The change of parameters, in particular the band gap and the ημτ-product is steeper for films deposited at ϕ_{N2} = 15sccm which is a result of the lower deposition rate. Therefore, films should be deposited at ϕ_{N2} = 20sccm to allow for small uncertainties in setting the discharge power, reactive and Ar gas flowrates, the control of the process pressure and also the background pressure including the desorption of H_2O from the deposition chamber walls due to the heating of the substrate. The process at ϕ_{N2} = 20sccm is thus expected to be more reliable.

The ημτ-product reaches its most favorable values at low O_2 flowrates. The measurement is done on an amorphous Ta-O-N phase. However, the mechanisms leading to a decreasing ημτ-product are believed to be applicable for the crystalline phase as well. Therefore, concerning the electronic properties, Ta_3N_5 thin films should be deposited at the lowest possible O_2 flowrate.

The evolution of the band gap, on the other hand suggests the opposite. Although a smaller band gap allows to absorb a larger portion of the solar spectrum, there is a limit. Overpotentials for solar water splitting are estimated to lie around 0.8V, so that a minimum band gap for water splitting of 2.03eV is necessary. This would mean, to increase the O_2 flowrate to the highest flowrate at which a Ta_3N_5 crystallinity is still observable in the diffractograms.

Judging from the poor performance of the samples in the photoelectrolysis experiments, it seems that the O_2 flowrate is not a decisive parameter, though. Over the whole range of O_2 flowrates investigated, the photocurrent remains very small with respect to the theoretically possible. Therefore, the precise tuning of the O_2 flowrate is less of an obstacle to reach a high photocurrent density.

The small intensities in the X-ray diffractograms just peaking out of the noise suggest, that the deposited material lacks crystallinity. Even if large grains are observed on thick films deposited on monocrystalline Si(100), the thin samples deposited on sheets of Ta show a low degree of crystallinity. This parameter is shown by other authors before, to play an important role in the efficiency of solar water splitting. Yokohama et al. change the crystallinity of their magnetron-sputtered samples by annealing them in NH_3. On those samples, they observe an increase in photocurrent by a factor of 10 compared to the as-deposited samples without annealing [21]. Ishihara et al. reports a similar effect of the crystallinity of Ta_3N_5 in other electrochemical processes [20]. The deposition process should therefore be optimized in order to obtain higher crystallinity samples.

5.6 Conclusion

This chapter describes the preparation of Ta_3N_5-crystalline films by conventional DC magnetron sputtering without the necessity for post-annealing them in NH_3. The films contain a single crystalline phase and do not show any signs of a TaON or Ta_4N_5 signatures as seen by other authors [21] [22]. Varying the oxygen flowrate while keeping the N_2 flowrate and the total flowrate constant, thus appears to be a good strategy for the deposition of single phase Ta_3N_5 films.

The experiments in this chapter confirm, that oxygen plays a crucial role in the crystallization process, as films deposited at no oxygen flowrate crystallize in the metallic δ-TaN phase. Films deposited with flowrates above a critical point, on the other hand, are amorphous. Thus, a small window exists for obtaining the Ta_3N_5 phase that demands a precise control of the discharge power, pressure and reactive gas flowrates to keep the deposition and gas incorporation rates stable.

The film parameters vary strongly as a function of O_2 flowrate. For the samples that show a Ta_3N_5 signature in their diffractograms the following parameter were measured: The band gap varies between 1.4eV and 2.2eV. The conductivity varies by seven orders of magnitude and similarly, the $\eta\mu\tau$-product varies by six orders of magnitude. As different substrates are used to comply with different measurement techniques, a correlation between the needs to be done carefully as the degree of crystallinity of a film may be different on different substrates.

The photocurrent density measured on the samples remains very low. An explanation for this may be the small degree of crystallinity of the films as discussed in the previous chapter. Therefore, the optimization of the deposition process should be focused on improving the degree of crystallinity.

6 Improving the crystallinity of Ta_3N_5 thin films

The objective of this chapter is to test a deposition method based on a conventional DC magnetron sputtering process, but with two additional magnetic poles, one behind the cathode and one behind the substrate. This is to increase the ion-to-neutral flux ratio arriving onto the substrate. Other authors have used this technique to investigate morphological changes that go along ion-assisted film growth [226] and changes of HiPIMS discharge parameters with varying magnetic fields [227]. The goal of this technique here is to improve the sample crystallinity compared to those deposited in the previous chapter.

The chapter starts with a description of the experimental setup and optical emission spectroscopy is used to proof the increased ion flux onto the substrate (Section 6.1). This is followed by a proof-of-concept for which films are deposited using this guided-ion DC magnetron sputter process (Section 6.2). Their increased crystallinity is evidenced by GI-XRD and AFM measurements. A third section serves to determine the stability range of Ta_3N_5 with respect to the oxygen incorporated into the films. For that, AFM measurements, that reveal the presence of the Ta_3N_5 structure from large grains on the sample surface, are correlated with the elemental composition of the films. Latter is determined from RBS and NRA experiments (Section 6.3). A final section is dedicated to determine the photoelectrochemical performance of selected films by voltammetry measurements (Section 6.4). The chapter ends with a conclusion (Section 6.5).

The results of this chapter are partially published in Rudolph et al., *Thin Solid Films*, vol. 636, pp. 48-53, 2017 [228].

6.1 Guided-ion DC magnetron sputtering

Ions incident on a growing film carry energy and momentum that increase the mobility of adatoms on the surface of that film. As a high adatom mobility increases the probability of an atom to attach to a yet unoccupied lattice site of a growing crystallite, it is expected to have a strong influence on the degree of crystallinity of films. In DC magnetron sputtering, however, the ion flux onto the substrate is small compared to other techniques such as HiPIMS. This is mainly due to the small flux of ionized metals; which is the result of the low electron density in the negative glow.

The N_2^+ ions are the most abundant film-forming species in magnetron discharges in an Ar/N_2 atmosphere. They are, however, mostly trapped in the negative glow. This is due to the fact that electrons are confined by a strong magnetic field to the cathode vicinity. And although the ions are typically too heavy to be confined, they are indirectly retained by the electric field that would appear if they left the magnetized region.

Techniques to increase the ion flux onto the substrate are the use of unbalanced magnetrons to release the trapped ions from the negative glow, or the use of a different sputtering mode such as HiPIMS to increase the flux of metallic ions. The disadvantage in both cases is, however, the increased cathode potential [229], which is unwanted considering the detrimental effect of the high-energy backscattered neutrals as discussed in Section 4.3.

Here, the idea is to superimpose an addition magnetic field with a direction parallel to the cathode axis. It is to release some of the electrons from the confined region and to steer them towards the substrate. By ambipolar diffusion, they drag the ions along with them which leads to an increased ion-to-neutral flux ratio onto the substrate. This technique resembles that of unbalancing a magnetron. The advantage, however, is that that the magnitude of the magnetic field can be adjusted for achieving optimum deposition conditions.

6.1.1 Experimental setup

To apply this technique to the inherently balanced magnetron used in this thesis, two magnetic poles are necessary. One is placed below the cathode and a second is placed above the substrate (Fig. 113). The magnets are electromagnetic coils rather than permanent magnets in order to conveniently tune the magntitude of the magnetic field. Both are positioned outside the reactor to avoid contamination by unwanted species.

The two coils are termed cathode coil and substrate coil for the coils below the cathode and above the substrate, respectively. Their corresponding currents are denoted I_{cath} and I_{sub} and their operating ranges are 0 .. 12A for the cathode coil and 0 .. 6A for the substrate coil (Fig. 113). The operating ranges are chosen to not disturb the discharge. At higher currents, a discharge at a constant power would require a higher cathode potential similar to the case of a conventional unbalanced magnetron.

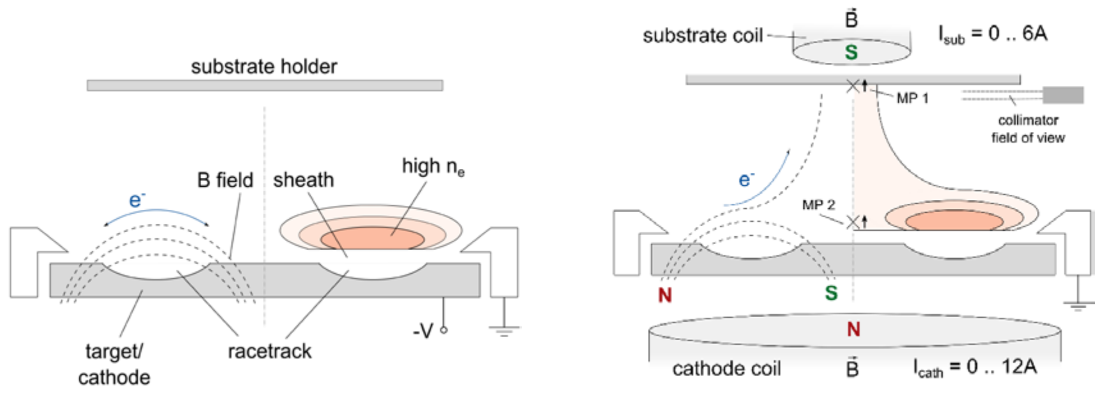

Fig. 113: Schematics of the balanced magnetron used for the thin film preparation in this thesis without electromagnetic coils (left) and the effect of the added magnetic field from two electromagnetic coils. MP1 and MP2 indicate the position and direction of the magnetic flux density measurement in Fig. 114.

A measurement of the change of magnetic flux density on the magnetron axis at two points (indicated in Fig. 113 by MP1 and MP2) is shown in Fig. 114 as a function of coil currents. The component of the magnetic flux density vector measured here is parallel to the cathode axis. A first measurement point (MP1) is located 10cm above the target surface close to the virtual substrate position. It shows a slight variation of magnetic flux density with the current through the substrate coil. A further decrease in magnetic flux density is achieved by having a current of 6A run through the substrate coil.

A second measurement point (MP2) is located approximately 5mm above the target surface. Here, a strong change of up to 15% between I_{cath} = 0A and 12A is observable, while the application of the substrate coil has no influence on the magnetic flux density at MP2.

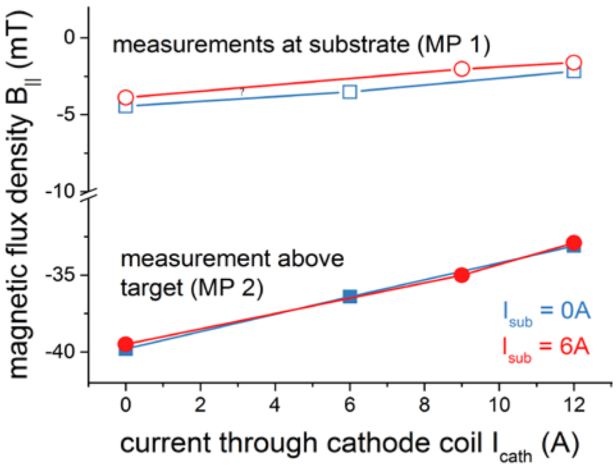

Fig. 114: Change of magnetic flux density as a function of coil currents at the two measurement points (MP1 and MP2) indicated in Fig. 113.

6.1.2 Plasma observations

The application of the magnetic field has a strong influence on the appearance of the discharge as suggested by Fig. 113 and proven by the images taken from inside the deposition chamber (Fig. 115). The photographs show a discharge of 80W in DC mode in 100% Ar at working pressure of 0.5Pa. The undisturbed discharge without the effect of any external coils can be seen in Fig. 23. Its balanced nature can be perceived by the fact that the luminous part of the discharge is confined to the cathode vicinity.

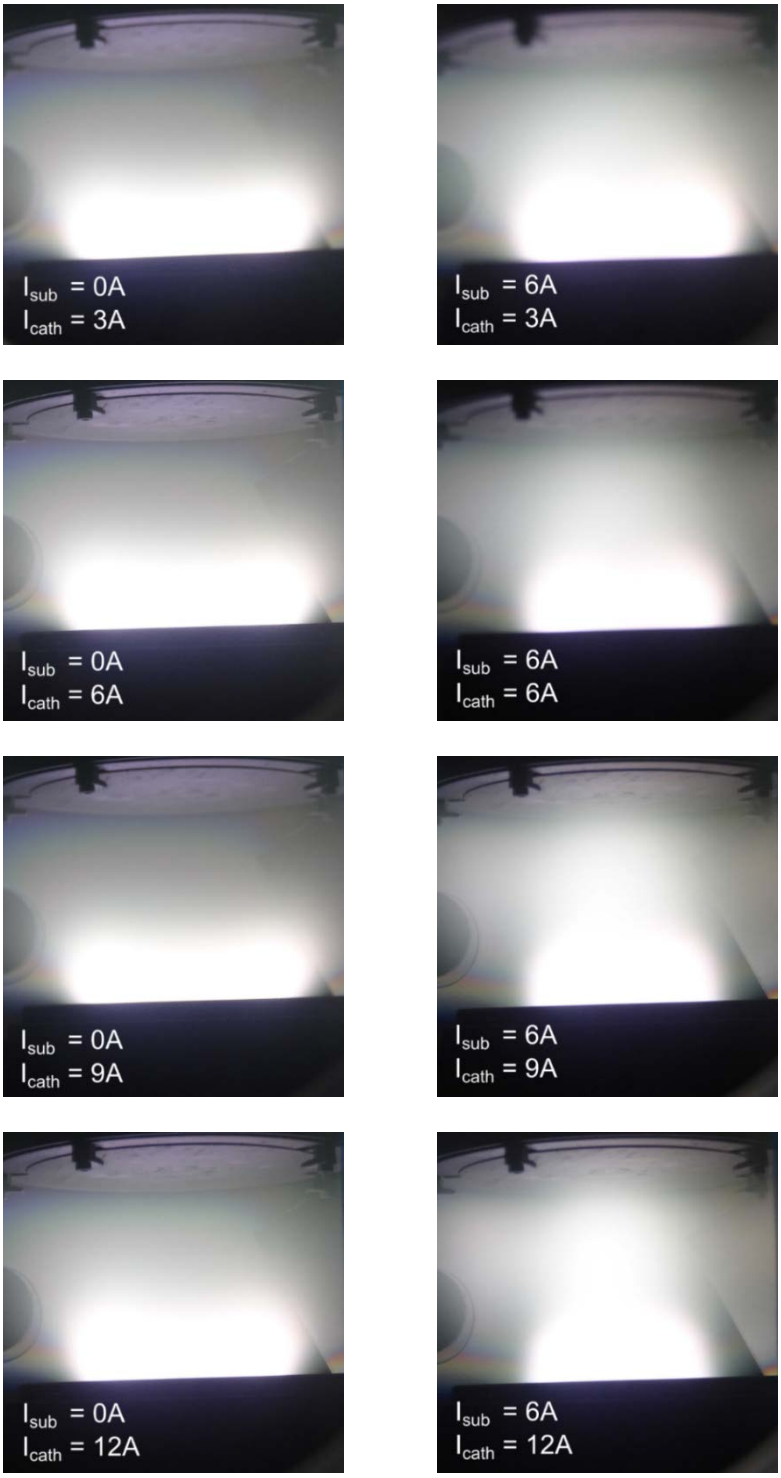

Fig. 115: Evolution of the discharge appearance with increasing the coil currents through the cathode (bottom) and the substrate (top) coil. The photograph without any currents through the coils is shown in Fig. 23.

The effect of the cathode coil only is shown in the left column of Fig. 115. A slight lateral compression of the negative glow region is perceivable between I_{cath} = 3A and I_{cath} = 12A. This is accompanied by a slight growth in height. This geometric deformation is due to the fact that the cathode coil increases the the magnetic flux density above the outer pole of the magnetron while it reduces the magnetic flux density above the inner pole of the magnetron.

The images in the right column in Fig. 115 show the effect of the substrate coil (I_{sub} = 6A), again, with increasing the cathode coil current. As before, the discharge is laterally compressed while it grows in height with increasing I_{cath}. Compared to the left column of Fig. 115, the deformation of the luminous part of the discharge, is now, however, much more pronounced. When both coils reach their maximum operating currents (I_{sub} = 6A, I_{cath} = 12A) a luminous column can be observed that extends from the negative glow and reaches up to the substrate position.

The luminous glow indicates the presence of electrons that excite species in the cathode-substrate space. They gyrate around the magnetic field lines according to Eq. 18. The connection between the cathode and the substrate by the luminous column of the discharge thus suggests, that field lines originate the cathode region and pass through the substrate as suggested by Fig. 113. Ambipolar diffusion ensures that ions are dragged along with the flux of electrons.

The higher emission intensity is verified by optical emission spectroscopy. For that, a collimator is positioned just below the substrate height, looking towards the luminous column as sketched in Fig. 113 on the right hand-side. Fig. 116 shows selected spectra from conventional DC magnetron sputtering (I_{sub} = 0A, I_{cath} = 0A) and using guided-ion DC magnetron sputtering at the maximum coil currents (I_{sub} = 6A, I_{cath} = 12A). The intensity of all lines rises strongly with the coil currents switched on.

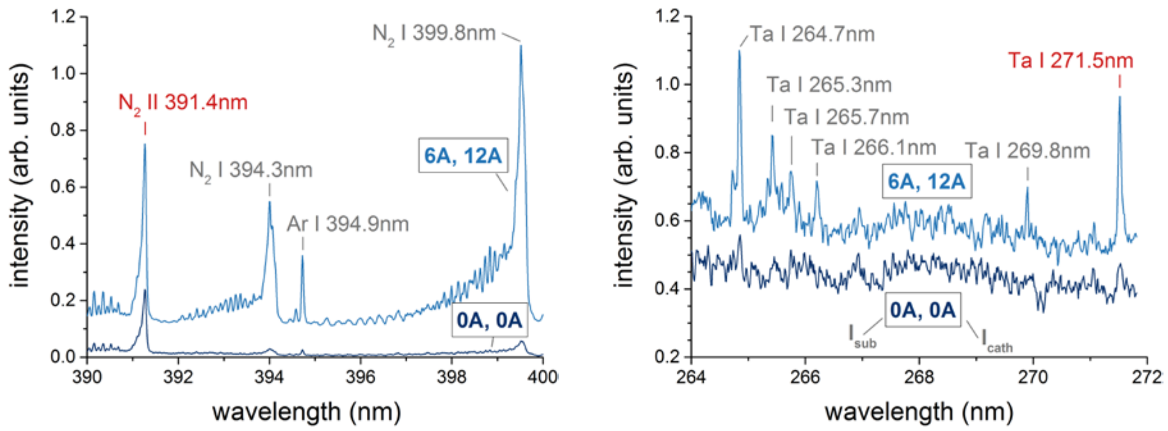

Fig. 116: Selected OES spectra showing lines of N_2 (left) and Ta (right).

To proof the higher ion flux onto the substrate, a neutral Ta line (271.5nm to the ground state) and an ionic N_2^+ line (391.4nm, $B^2\Sigma_u^+ \rightarrow X^2\Sigma_g^+$, v'=0→v''=0 [230]) are compared. Both lines are expected to rise in intensity with the additional magnetic field. This is due to the excitation from an increased electron density in the cathode-substrate space. In addition to that, the ionic N_2^+ line rises due to an increased release of ions from the negative glow. A change in ratio between the neutral Ta I and the ionic N_2 II line therefore indicates a changed ion-to-neutral flux ratio arriving on the substrate.

The individual evolution of both lines is shown on the left hand-side of Fig. 117. Their ratio is on the right hand-side of Fig. 117. Without the substrate coil (I_{sub} = 0A), the ion-to-neutral intensity ratio increases by 55%. By adding the substrate coil (I_{sub} = 6A), the ion-to-neutral ratio almost doubles with an increase of 92% compared to conventional DCMS discharge. The use of an additional magnetic pole above the substrate thus aids significantly in increasing the ion flux onto the substrate. The increased ion-to-neutral flux ratio onto the substrate is therefore proven and the technique is termed guided-ion DC magnetron sputtering from here on to distinguish it from conventional DC magnetron sputtering.

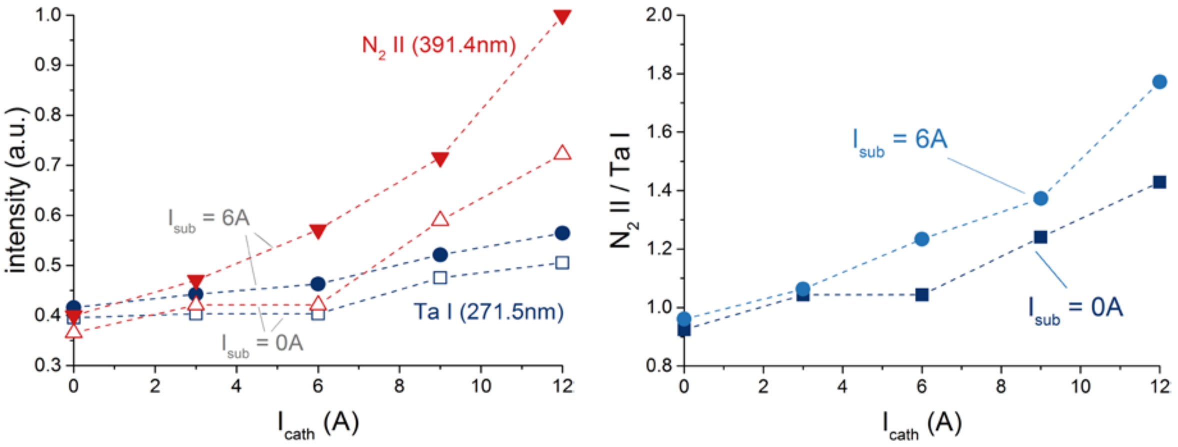

Fig. 117: Left: Evolution of N2 II and Ta I intensities as a function of coil currents. Right: Ratio of intensities for I_{sub} = 0A and I_{sub} = 6A as a function of cathode coil current.

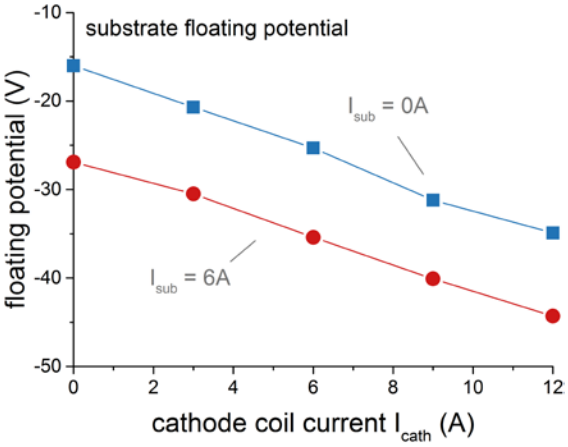

Fig. 118: Floating potential of the substrate holder at varying currents I_{cath} and I_{sub}.

With increasing the currents through the coil, a drop in floating potential of the substrate holder can be observed as seen in Fig. 118. It is important to note, that the drop in floating potential does not translate directly into an ion acceleration potential as it is likely that the plasma potential in front of the substrate holder does not retain its value during the application of the external magnetic field. On a comparable setup, Petrov et al. measure the drop in plasma potential by electric probes. They determine a decreasing plasma potential of about -10V to -20V just in front of the floating substrate [226] between the case with both coils switched off and the case with both coils running at their maximum operating currents. Probe measurements for the setup described in this thesis are not conducted but the same drop in plasma potential is expected. It should be noted, that the maximum magnetic flux density added from the external coils in the setup by Petrov et al. is significantly stronger with 60mT (=600G in the original publication) compared to 7mT in the case of this thesis (Fig. 114).

Finally, to assure that effects of the applied magnetic field are not due to a stronger substrate heating, the temperature of the substrate is measured during two depositions at a DC power of 80W, one using conventional DC magnetron sputtering (I_{cath} = 0A, I_{sub} = 0A) and one using guided-ion DC magnetron sputtering at the maximum coil currents (I_{cath} = 12A, I_{sub} = 6A). Fig. 119 shows the substrate temperature of a thermally floating substrate as a function of time. Both curves lie on top of each other while the temperature stays below 100°C, which is considered too low to cause any morphological changes on films containing the refractive metal Ta and the low diffusivity reactive gas nitrogen.

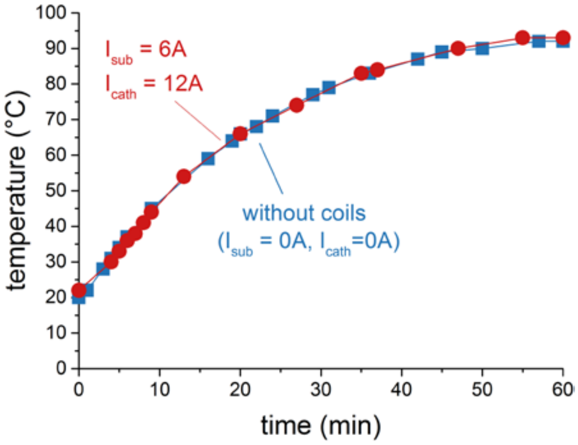

Fig. 119: Substrate temperature as a function of time during deposition of a Ta-N film in DC mode at 80W average power, 0.5Pa pressure in an Ar/N_2 gas mixture with flowrates of 30sccm and 20sccm, respectively.

6.2 Proof of concept

To show that guided-ion DC magnetron sputtering increases the crystallinity of the Ta_3N_5 films, samples are deposited at varying coil currents. Their structure is characterized by GI-XRD and their surface morphology by atomic force microscopy (AFM).

6.2.1 Explanatory note: the growth of Ta_3N_5 on monocrystalline Si(100)

The aim of this chapter is to increase the degree of crystallinity of the films. As X-ray diffraction is not sensitive to ideal amorphous material, atomic force microscopy (AFM) is used. This technique requires the use of flat substrates in order to measure the film surface topology and not any underlying substrate topology.

In the previous chapter of this thesis (Chapter 5), metallic substrates are used for the deposition of Ta_3N_5 photoanodes. These substrates have a roughness in the µm-range and are thus not usable for AFM measurements. Monocrystalline Si(100) substrates are atomically flat and thus well suited for AFM measurements. However, it is found that under conditions investigated in this thesis, Ta_3N_5 does not grow on Si. Exceptions are the samples deposited for SEM measurements presented in Fig. 110. These, are, however, exceptionally thick (≈ 800nm), which explains why the effect of the substrate is reduced. In order to grow Ta_3N_5 on Si substrate it is found that they need to be covered by a seeding layer of Ta before the deposition of the Ta_3N_5 film.

To illustrate the effect of the seeding layer on the growth of Ta_3N_5, four films were deposited by DC magnetron sputtering in $Ar/N_2/O_2$ with flowrates of 29.7sccm, 20.0sccm and 0.3sccm, respectively. Before deposition, the substrates were coated with different thicknesses of metallic Ta. These were 0nm, i.e. no Ta layer, 3nm, 10nm and 30nm.

The diffractograms are shown in Fig. 120. Clearly, only for a Ta seeding layer thickness of 30nm, the Ta_3N_5 phase grows. For all other thicknesses, amorphous diffractograms appear, without any feature.

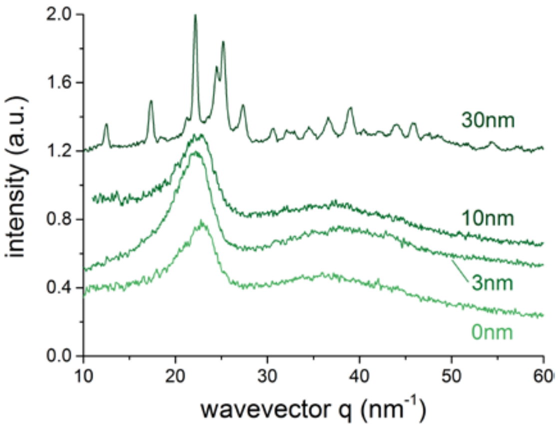

Fig. 120: Diffractograms of Ta-O-N films deposited on monocrystalline Si(100) coated with varying thicknesses of metallic Ta.

A possible explanation could be the high substrate temperatures that promotes diffusion of substrate species into the film. On quartz substrates, similar to Si substrates, no crystallization is observed either (see below). Therefore, it seems likely that Si could be held responsible for inhibiting the crystallization as it is present in large quantities in both Si and quartz substrates.

While the crystallization of the Ta_3N_5 phase remains unclear, it is to be noted that similar measures to grow the Ta_3N_5 phase on glass and quartz substrates can be found in literature. Lin et al. deposited rather thick layers of 2µm in order to obtain a Ta_4N_5/Ta_3N_5 phase mixture on a glass substrate by magnetron sputtering [22]. De Respinis et al. deposited a 5nm thick layer of Ti onto a quartz substrate before depositing Ta to be subsequently oxidized and nitrided. They call it adhesion layer but state explicitly that this layer may affect the crystallization behavior [47].

For the samples deposited in the following, a Ta seeding layer is coated on top of Si substrate in order to obtain the Ta_3N_5 phase. The steel substrats used for the voltammetry measurements at the end of this chapter, are similarly coated by such a seeding layer. This allows to directly compare the films properties despite the fact that they are deposited on different substrates.

6.2.2 Sample preparation

Overall four samples were prepared at different combinations of coil currents. The first sample was deposited by conventional DC magnetron sputtering and serves as a reference. Two samples were deposited with the substrate coil switched off (I_{sub} = 0A) and a cathode coil current of I_{cath}=6A and 12A, respectively. The last sample was deposited with both coils operating at the maximum currents (I_{sub} = 6A, I_{cath} = 12A).

Before deposition, the samples were cleaned according to the procedure described in Section 5.2. The substrate was coated by 30nm of metallic Ta (cf. Section 6.2.1) during this procedure and just before injecting the reactive gases. The coils were switched on just before opening the substrate shutter.

Samples were deposited in an $Ar/N_2/O_2$ atmosphere with flowrates of 29.7sccm, 20sccm and 0.3sccm, respectively. The O_2 flowrate corresponded to the low oxygen flowrate region from Chapter 5. Similar to previous experiments, the substrate temperature was regulated at 600° C and the power to the target was kept constant at 80W.

6.2.3 Sample crystallinity and surface morphology

The analysis of the films by GI-XRD reveals a Ta_3N_5 crystalline phase for all films. The degree of crystallinity, however, varies strongly between the films deposited by conventional DC magnetron sputtering and guided-ion magnetron sputtering at maximum currents (Fig. 121). Former shows two strong amorphous halos around $20nm^{-1}$ and $40nm^{-1}$. Similar halos are found by Stavrev et al. [148] for amorphous films of Ta-O-N. Bousquet et al. detect the first of the two halos [149], similarly in amorphous films of Ta-O-N. In both references, the authors observe these peaks at slightly higher wavevectors q (cf. Section 2.3.4) but some uncertainty exists in the determination of the peak positions from Fig. 121. Therefore, the two halos can be ascribed to a short-range ordering of the amorphous Ta-O-N phase.

On that film, deposited by conventional DC magnetron sputtering, diffraction peaks are visible that correspond to the Ta_3N_5 signature. The peaks, however, are small and in most cases almost vanish in the background noise. Many of the peaks from the references are not even visible. It is thus evident, that this film has little crystallinity, corresponding to the expectations for films deposited by conventional DC magnetron sputtering (Chapter 5).

In the same figure (Fig. 121), the diffractogram of the film deposited at maximum coil currents (I_{cath} = 12A, I_{sub} = 6A) is shown. It is immediately obvious that the amorphous halos are largely reduced in favor of the diffraction peaks of the Ta_3N_5 phase. These are much more intense than those from the sample deposited by conventional DC sputtering, and at the same many more peaks are visible.

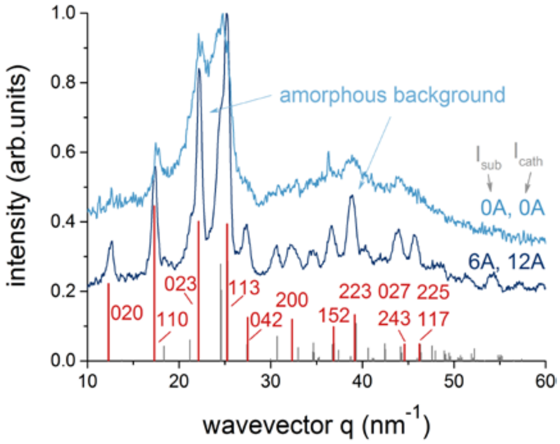

Fig. 121: GI-XRD for samples deposited with and without additional magnetic field. Red bars from the reference indicate intense peaks that can also be found in the high crystallinity sample.

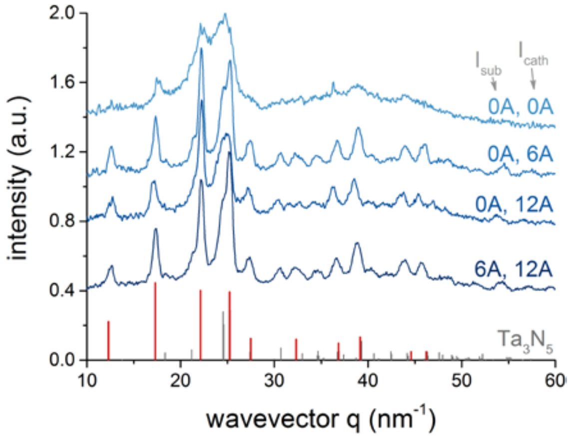

Fig. 122: Comparison of diffractograms of samples deposited at different currents running through the coils.

Fig. 122 presents the diffractograms of all samples deposited for this proof-of-concept. Little difference is observed between the three samples deposited with at least one of the coils switched on.

To actually observe the increased degree of crystallinity, AFM images are taken of the surface of each of the films (Fig. 123). The corresponding coil currents used during deposition are indicated on the images. The sample deposited by conventional DC sputtering mode shows single grains on a largely amorphous background. This corresponds to the diffractogram shown in Fig. 121. This is similar to observations made on SEM images from RF magnetron-sputtered films presented by Yokoyama et al. [21]. When increasing the coil currents, the initially sparsely populated surface, becomes densely filled with grains. The amorphous background is almost not visible any more on the last image, i.e. for the sample deposited with the coils at their maximum currents.

To determine optimum coil currents from these observations is difficult as, similarly to the diffractograms, little difference is observed between the three samples deposited with at least one of the coils switched on. From the optical emission spectroscopy measurements, the highest ion-to-neutral flux onto the substrate is reached for I_{sub} = 6A and I_{cath} = 12A. This is therefore chosen to be the optimum operating conditions for the coils and is used for the samples deposited from here on.

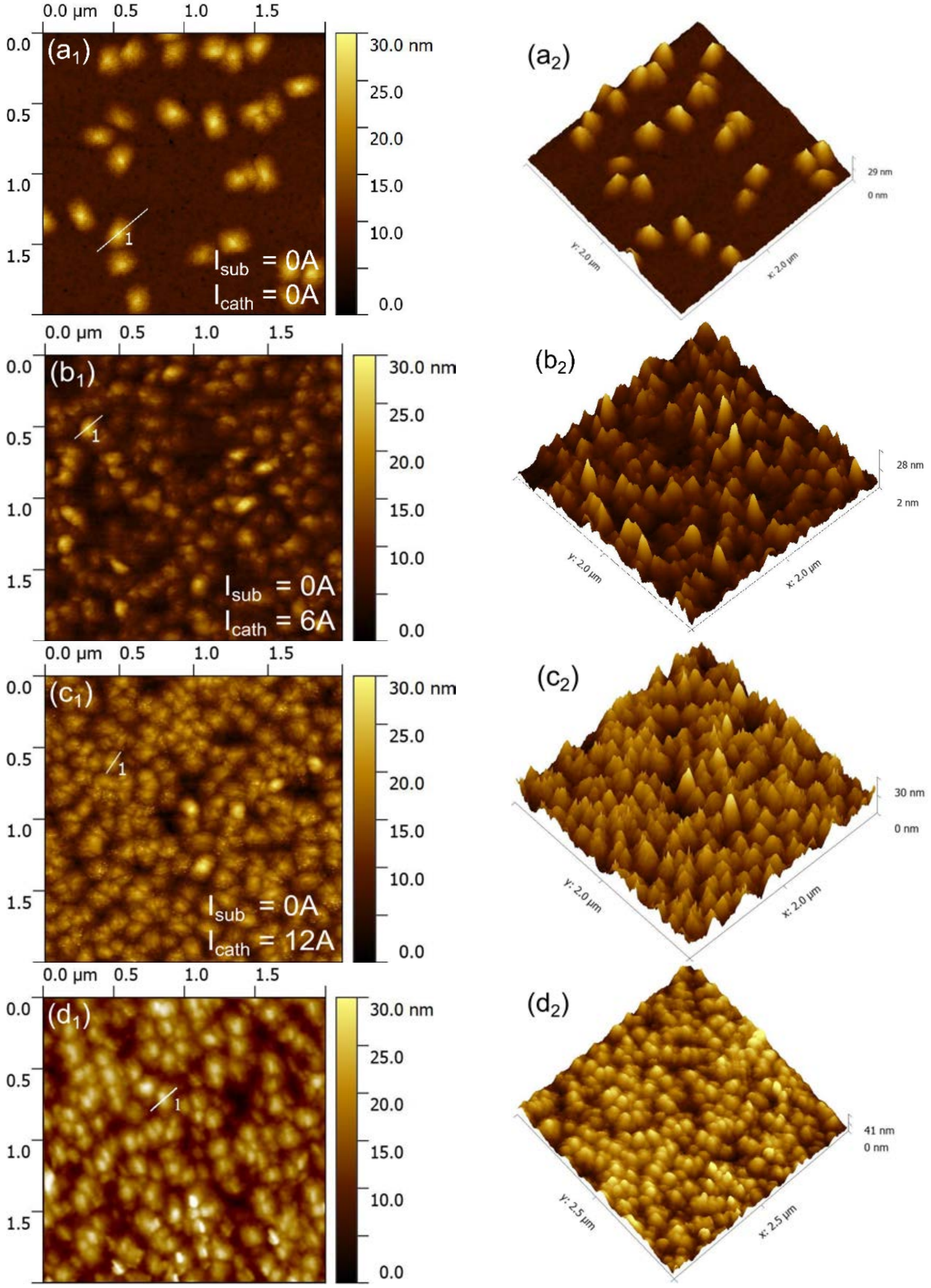

Fig. 123: AFM images of the surfaces morphology of samples deposited at varying coil currents I_{cath} and I_{sub}.

6.3 Elemental composition of magnetron-sputtered Ta_3N_5 thin films

This subchapter presents the characterization of the samples deposited at maximum coil currents as a function of O_2 flowrate. The objective is to observe the range of oxygen flowrates over which grains of Ta_3N_5 on the surface of the films can be observed. This is correlated with measurements of the elemental composition measured by RBS and NRA, which allows to determine the maximum oxygen at.% in the films that the Ta_3N_5 structure can tolerate. This is a valuable information in order to compare the samples deposited here with DFT calculations that predict the straddling of the oxygen and hydrogen evolution potential only with a certain amount of incorporated oxygen [78].

6.3.1 Deposition conditions

The samples for this subchapter were deposited as described in Section 6.2.2, only that the free variable is now chosen to be the O_2 flowrate (from 0sccm to 0.8sccm). The coils were kept at their maximum currents, i.e. $I_{sub} = 6A$, $I_{cath} = 12A$, for all samples deposited in this section. To comply with different measurement techniques different substrates are used. For the AFM and the voltammetry measurements, samples were deposited onto monocrystalline Si(100) and steel substrates, respectively. Both were covered by a 30nm thick layer of metallic Ta (cf. Section 6.2.1.). For the optical measurements, films were deposited on quartz substrates without any seeding layer.

The sample thicknesses changed slightly with O_2 flowrate, from 250nm for the sample deposited at the lowest O_2 flowrate to 300 for the sample at the highest O_2 flowrate tested. The two samples deposited for the voltammetry measurements are deposited at different deposition times in order to have the same thickness and for the results to be directly comparable.

6.3.2 Band gap

The band gap is retrieved using the same procedure as in Section 5.4.2. Measured and fitted transmission curves for selected samples are presented in Fig. 124. It can be seen that the fits match well with the curves. However, they match less well compared to those from the previous chapter (Section 5.4.2). This can also be quantified. The objective function f_{obj}, introduced in Section 3.4.4 (Eq. 59), for the samples deposited by conventional DCMS takes values between 0.34 and 0.48. For the samples deposited in this chapter, f_{obj} ranges between 0.51 and 0.79, indicating a less good fit with the single Tauc-Lorentz model. The use of additional oscillators, however, results in not reproducible results. Some changes of the material are therefore present, but they are too subtle to be quantified. Therefore, the spectra are fit by using a single Tauc-Lorentz oscillator as done for the samples in Section 5.4.2.

Fig. 125 shows the evolution of the band gap as a function of O_2 flowrate. Similar to the results before, the band gap rises with increasing the O_2 flowrate. In the same plot, the evolution of the band gap for the samples deposited by conventional DCMS in the previous chapter (cf. Fig. 104) are shown in blue. For both sets of samples, the evolution of the band gap is almost identical. A slight difference in the trend could be imagined, but this may also be due to the fact that a new target is installed for the samples in this subchapter. A similarly good match exists for the values of the Urbach energy (Fig. 125, left hand-side).

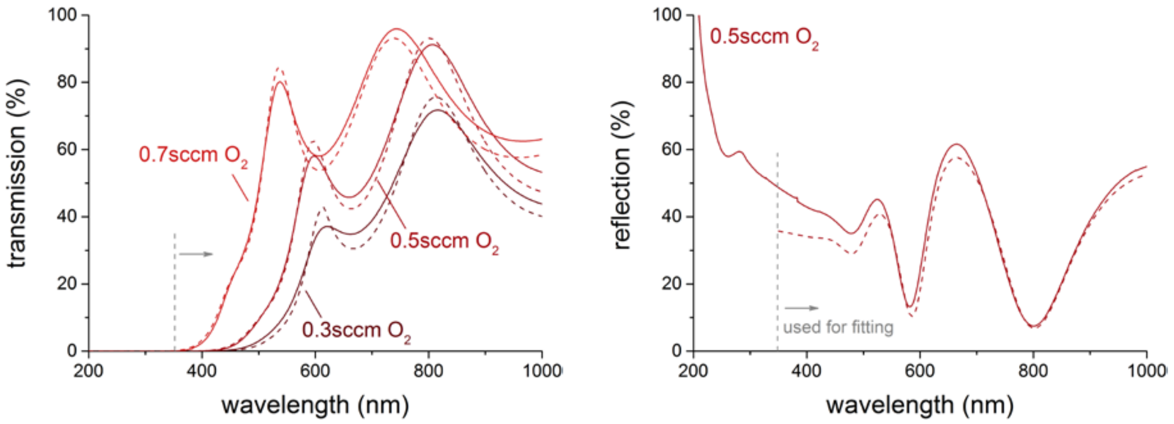

Fig. 124: Experimental (continuous) and fitted (dashed) transmission and reflection spectra for selected samples.

The large difference in crystallinity seen between samples deposited by conventional DCMS and guided-ion DCMS, is not reflected in the optical spectra measured on the samples deposited on quartz substrates. It could be, that the films on quartz do not crystallize in the Ta_3N_5 structure but form an amorphous phase, as for the case of monocrystalline Si(100) (cf. Section 6.2.1). This view would be supported by the fact that the optical spectra of all films deposited for this thesis, are well represented by a single Tauc-Lorentz oscillator.

The absolute band gap derived for these amorphous samples may therefore not necessarily correspond to those deposited on Si substrates that show a high degree of crystallinity. In the previous chapter (Section 5.4.2), the same trends were assumed in samples deposited on metal and on quartz substrates. This was justified because the films deposited on the Ta substrate were dominated by an amorphous matrix. This justification is not possible any more for the films in this section, due to the much higher crystallinity observed on samples deposited on the Ta-covered Si substrates. No statement on the value of the band gap of the highly crystalline samples deposited here can be made.

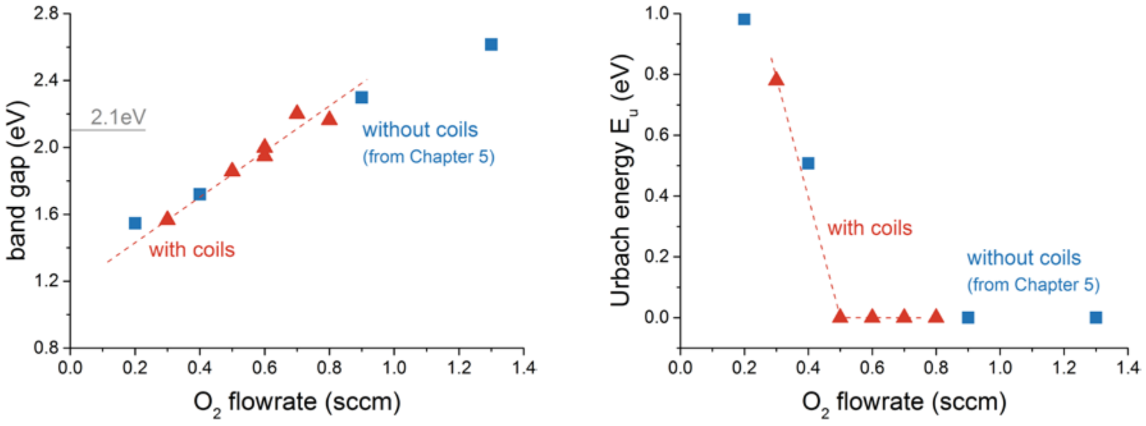

Fig. 125: Band gap E_g and Urbach energy E_u for the samples deposited at maximum coil currents (in red) in comparison to those deposited at ϕ_{N2}=20sccm N_2 flowrate for the previous chapter (cf. Fig. 102 and Fig. 104).

6.3.3 Surface topology

AFM measurements are conducted in order to see the evolution of the surfaces with O_2 flowrate. The surface topology of four samples is measured on samples deposited on Si and presented in Fig. 126. The two samples deposited at the lowest O_2 flowrates correspond well with those shown previously in Fig. 123. They both show a surface densely covered by grains. In both cases, the surface is rough with grains sticking out by several 10s of nm.

The samples deposited at an O_2 flowrate of 0.5sccm is already very different, as it has a much flatter surface. In addition, it appears that less grains are present on the surface. This trend continuous for the sample deposited at an O_2 flowrate of 0.7sccm, which has a completely flat surface.

In the previous chapter (Section 5.4.2), a correlation was revealed between the band gap and the appearance of Ta_3N_5 diffraction peaks. Samples with a band gap $\lesssim$2.1eV, showed Ta_3N_5 peaks in the GI-XRD measurements. A similar correlation can be made here. The sample deposited at 0.7sccm, has a band gap >2.1eV and, does not show any grains on its surface any more. This correlation is remarkable, in particular when considering that the optical and AFM measurements are done on samples having different structures due to the use of different substrates.

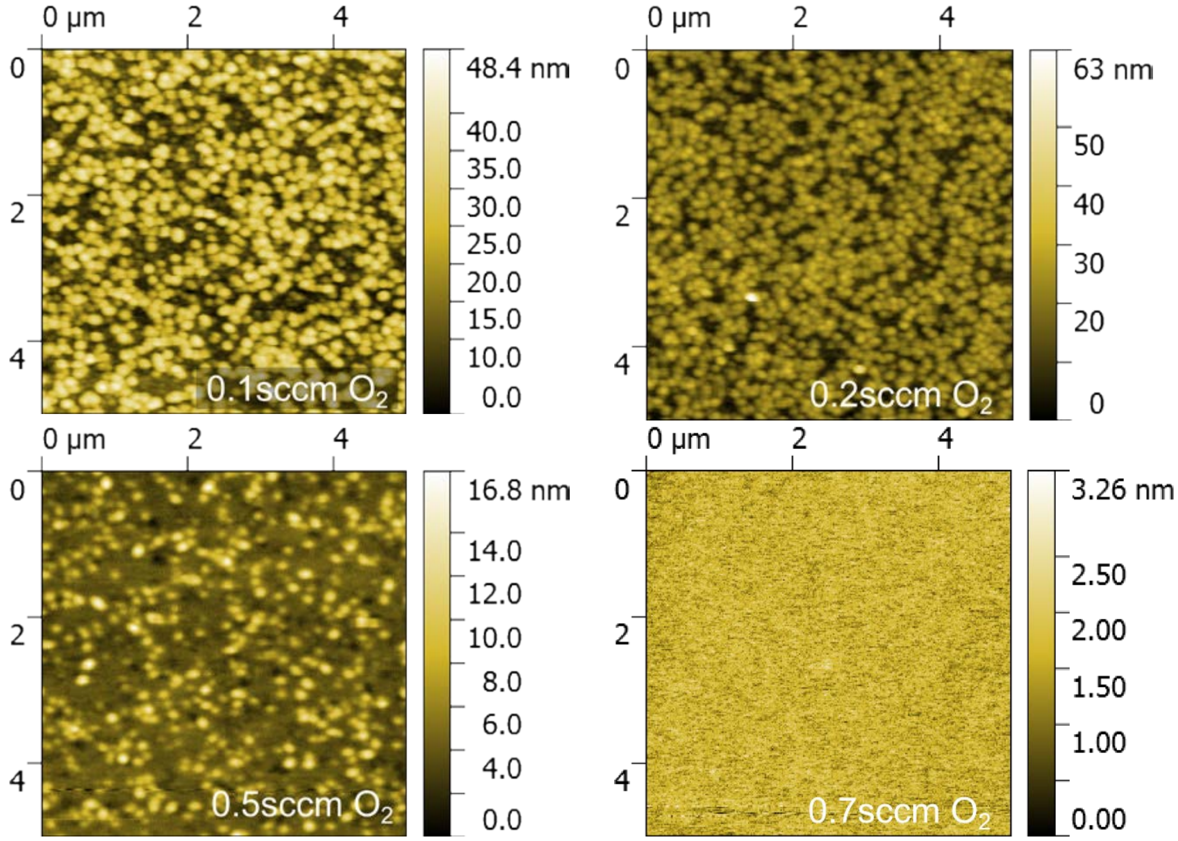

Fig. 126: Surface topology of samples for two different O_2 flowrates.

6.3.4 Elemental composition

The elemental composition of all films were measured by RBS and NRA using the typical reactions and energies to determine the areal densities of Ta, N and O (cf. Section 3.3). Only for nitrogen, a slightly different deuteron energy of 1100keV was used for technical reasons.

Rutherford backscattering

The RBS spectra are fitted using SIMNRA [160] as done in Chapter 4. Overall, 4 elements are detected in the spectra, Ta, N, O and Ar. The N and O peak are naturally found on top of the Si plateau from the underlying substrate. Similar to the experiments described in Section 5.2.2, channeling is observed. The same procedure to substract the Si background from the raw spectra is thus applied. This is done by fitting a power law curve from just below the N and O peaks to just above the peaks. This baseline is then subtracted from the spectra.

The Ta peak is presented together with the results of the simulation in Fig. 127. The seeding layer coated on top of the Si substrates clearly stands out from the Ta-O-N thin film as the Ta density is strongly increased. However, the fit to the spectrum reveals, that this layer is not a made of pure Ta but likely contains oxygen, as shown in Fig. 127 on the right hand-side. As the fitting of a pure Ta layer is not yielding satisfactory results, a $Ta_{0.7}O_{0.3}$ stoichiometry of this layer is assumed. This is likely due to the deposition procedure. Between depositing the 30nm thick seeding layer, and the start of the deposition of the thin film, the target is presputtered in an $Ar/N_2/O_2$ atmosphere while it is already heating up to 600° C. The combination of sample heating and the injection of O_2 seems likely to be responsible for the considerable oxygen found on the seeding layer. However, due to the fact that the O_2 flowmeter needed a few minutes to stabilize, a different procedure is not possible.

The Ta peak from the Ta-O-N layer on top of the seeding layer shows a decreasing height of the plateau with increasing the O_2 flowrate (Fig. 127). This is due to the increased incorporation of oxygen which decreases the Ta density in the film. The Ta at.% in this layer reduces from 39at.% in the film deposited at a flowrate of 0.1sccm down to 30% for the film deposited at 0.8sccm (Table 23).

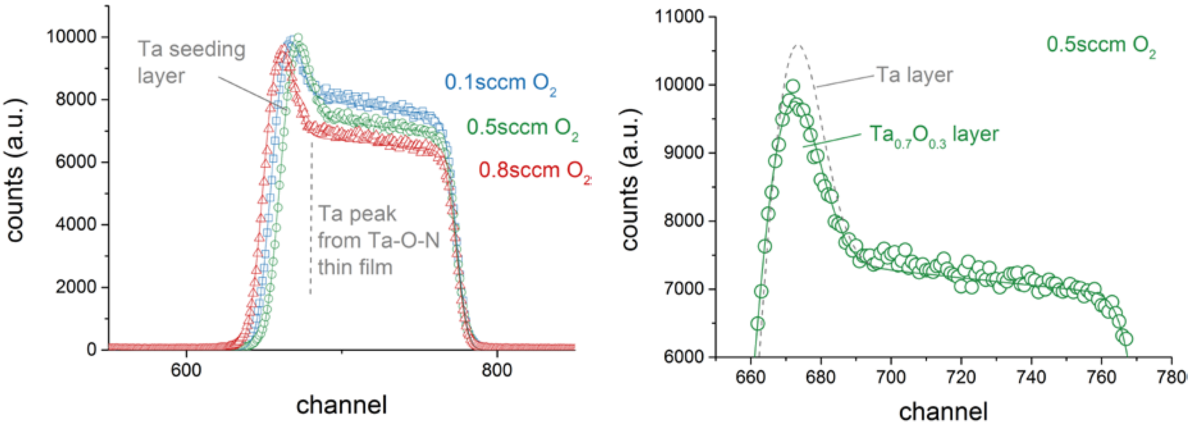

Fig. 127: Left: Zoom on the Ta peak from the RBS spectra of samples deposited at different flowrates. Right: The fitting of the seeding layer using two different layer compositions, Ta and $Ta_{0.7}O_{0.3}$.

The nitrogen and oxygen peaks from the RBS spectra are presented in Fig. 128 for the three samples. Due to the thickness of the samples, the N and the O peaks are overlapping but their individual contribution can be revealed from the SIMNRA fits. The oxygen at.% in the film is observed to increase from 5% to 32% (Table 23). At the same time, the nitrogen at.% stays constant at 55at.% when increasing the flowrate from 0.1sccm to 0.5sccm, and only drops considerably to 37at% for the highest O_2 flowrate of 0.8sccm.

Ar is found as a fourth element in the films similar to experiments conducted in Chapter 4. The Ar peak for the three spectra is shown in Fig. 128 on the right hand side. Its at.% is estimated to lie around 1%, however due to the the large background noise, this is only a rough estimate. The high level of noise stems from pulse pile-up in the detector that occurs when two particles hit the detector almost simultaneously with a temporal delay that cannot be resolved by the detector. The particles are therefore effectively detected as one particle at a higher energy. Estimating the background noise to lie at 16 counts, the simulated Ar spectra can be shifted upwards where it lies on top of the experimental spectrum.

For the samples deposited at flowrates of 0.1sccm and 0.5sccm, the normally flat level of backscattering from Ar could be imagined to be slightly inclined. This would indicate a higher Ar density at the surface of the film compare to the film at the interface with the substrate. This could be reasoned by considering that the first layers deposited are subjected to a temperature of 600°C for a longer time. Ar from these layers can therefore outdiffuse from the film while Ar found in the last layers cannot, as the sample is quickly cooled down after the deposition. Due the high level of noise, however, the Ar profile is not fitted into these spectra and the Ar at.% is assumed to lie at 1at.%.

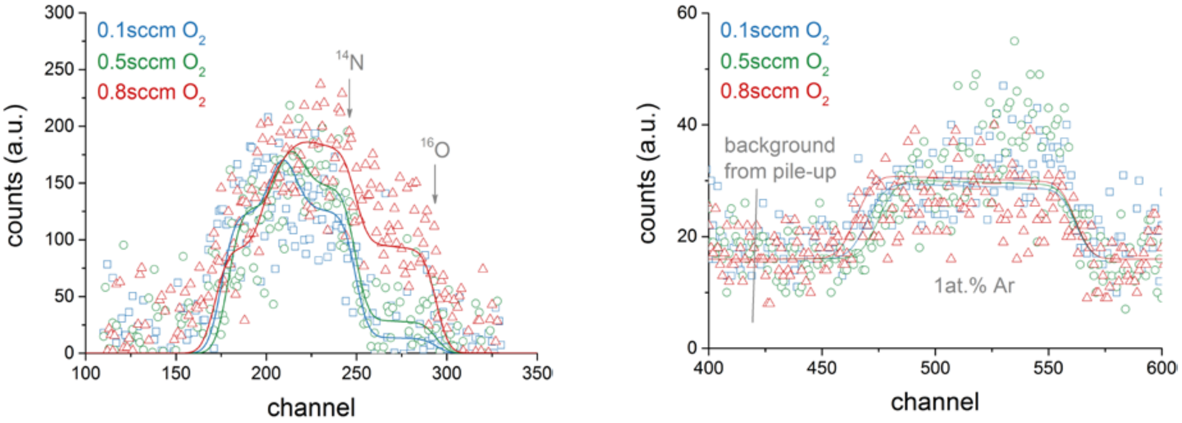

Fig. 128: Left: Zoom on the O and N peaks from the RBS spectra of samples deposited at varying O_2 flowrates. Right: Zoom on the Ar peaks. The simulated curves is shifted by 16 upwards in roder to compensate high level of background nois.

Table 23 summarizes the results obtained from fitting the RBS spectra. Uncertainties from these fits arise due to the small peak heights from the nitrogen and oxygen in the films, and in particular from the procedure implemented to subtract the Si background. However, a comparison with the combined evaluation from RBS and NRA shows, that the differences between the two is actually not large. The largest difference arises for the sample deposited at an O_2 flowrate of 0.1sccm. Here, the oxygen at.% is estimated to be at 5at.% from the RBS spectra, while the combined RBS/NRA spectra indicate only 2at.% of oxygen in the film. For the other two samples, the results from both methods match well, indicating that the uncertainty from deriving the elemental composition from RBS spectra alone, can be small.

Table 23: Elemental composition of samples from three different flowrates

O_2 flowrate	element	from RBS	from RBS/NRA	chemical formula (from RBS/NRA)
0sccm	Ta	n/a	0.38	$Ta_3N_{4.86}O_{0.12}$
	N		0.61	
	O		0.02	
	Ar			
0.1sccm	Ta	0.39	0.37	$Ta_3N_{4.99}O_{0.20}$
	N	0.55	0.60	
	O	0.05	0.02	
	Ar	0.01		
0.5sccm	Ta	0.34	0.34	$Ta_3N_{5.25}O_{0.68}$
	N	0.55	0.59	
	O	0.10	0.08	
	Ar	0.01		
0.8sccm	Ta	0.30	0.33	$Ta_3N_{4.05}O_{2.09}$
	N	0.37	0.44	
	O	0.32	0.32	
	Ar	0.01		

Nuclear reaction analysis

Nuclear reaction analysis is used to determine the areal densities of N and O with a higher level of confidence compared to the RBS measurements. The results of these experiments is summarized in Fig. 129 together with the Ta areal density found from the RBS measurements. Error bars on the N areal density indicate the 3σ statistical uncertainty. The Ta density in the Ta-O-N layer is corrected for the Ta found in the seeding layer. As a clear border cannot be drawn between these layers and some doubt exist about the stoichiometry of the seeding layer, error bars are chosen to cover the interval of ± half the Ta areal density of the seeding layer. Similarly, some oxygen may have been found by RBS in the seeding layer. As no conclusive proof exists, though, the oxygen areal density in the Ta-O-N layer is conservatively estimated to have a uncertainty of ± the oxygen density found in the seeding layer. These uncertainty estimates for Ta and O exceed those of the 3σ statistical uncertainty.

The summary of the Ta, N and O areal densities for all films is shown in Fig. 129. Clearly two regions can be separated. Below an O_2 flowrate of 0.5 or 0.6sccm, the oxygen incorporation is linear with flowrate and increases only slightly. This has limited influence on the Ta and the N areal densities as they stay approximately constant. This region coincides approximately with the region for which Ta_3N_5 grains are found on the surface of the films by AFM (cf. Section 6.3.3). Above a flowrate of 0.6sccm, the oxygen incorporation strongly increases its slope with O_2 flowrate. At the same time, the nitrogen areal density drops due to a substitution of O by N already observed in Section 4.1.3.

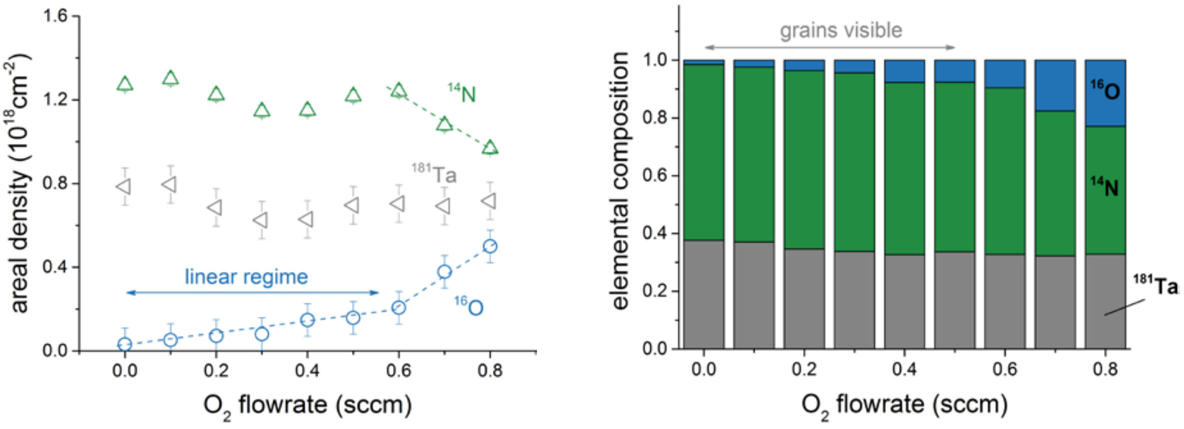

Fig. 129: Left: Evolution of areal densities for Ta, N and O as a function of O_2 flowrate. Right: Elemental composition of the films. For both plots, the contribution from the seeding layer is subtracted.

The elemental composition of the films is shown on the right hand-side of Fig. 129. The oxygen at.% increases steadily with increasing the O_2 flowrate. This is mainly at the cost of nitrogen at.% in the films, while the Ta at.% almost stays constant with increasing the O_2 flowrate.

Grains on the surface of the films are observed by AFM up to an O_2 flowrate of 0.5sccm. As revealed in Section 6.2.3, these correspond to the presence of the Ta_3N_5 structure. The correlation between the presence of the grains and the elemental compositions of the films can therefore be done and a stability range for the incorporation of oxygen in the Ta_3N_5 structure can be estimated. The at.% of the film still exhibiting grains on its surface has an oxygen at.% of 8%. The film deposited at a higher O_2 flowrate of 0.7sccm, is completely flat as observed by AFM, and therefore is believed to not have any Ta_3N_5 structure. This film contains 18at.% of oxygen. The maximum oxygen at.% that Ta_3N_5-crystalline films deposited by guided-ion DCMS can tolerate, therefore lies between 8 and 18at.%.

6.4 Voltammetry measurements

Two crystalline samples were deposited for voltammetry measurements. The first was deposited at an O_2 flowrate of 0.3sccm, which corresponds to an oxygen content of 4at.%. A second one was deposited at a flowrate of 0.5sccm which corresponds to the limit of oxygen that can be incorporated into Ta_3N_5-crystalline films. Both samples had a thickness of 250nm and could therefore be directly compared.

The samples were tested for their photocurrent in the same setup used for the previous chapter (cf. Section 5.4.6) but with an electrolyte at a higher pH. For the experiments, a 0.1M K_2SO_4 solution was used, enriched by KOH to reach a pH of 13. The conductance was ≈ 40mS and thus twice as high as the electrolyte used in Chapter 5. The potential is scanned between -0.4V and 0.4V.

The samples were initially measured by five successive scans, out of which three are presented in Fig. 126. Two observations can be made. The photocurrent for both samples rapidly decreases with the number of scan. Secondly, the photocurrent on the sample deposited at a higher O_2 flowrate (0.5sccm O_2) is considerably higher than that deposited at a lower O_2 flowrate (0.3sccm O_2).

Latter effect is already observed in the previous chapter (Fig. 112), although due to the varying thickness of the films, the effect is not further analyzed. Here, the thickness of the samples are equal while a drastic change in photocurrent is observed. Taking the first scan at a bias vs. Ag/AgCl/sat. KCl of 0.3V, a photocurrent density of 8μA/cm^2 for the sample deposited at 0.3sccm O_2 can be observed compared to a photocurrent density at the same bias of 82μA/cm^2 for the sample deposited at 0.5sccm O_2.

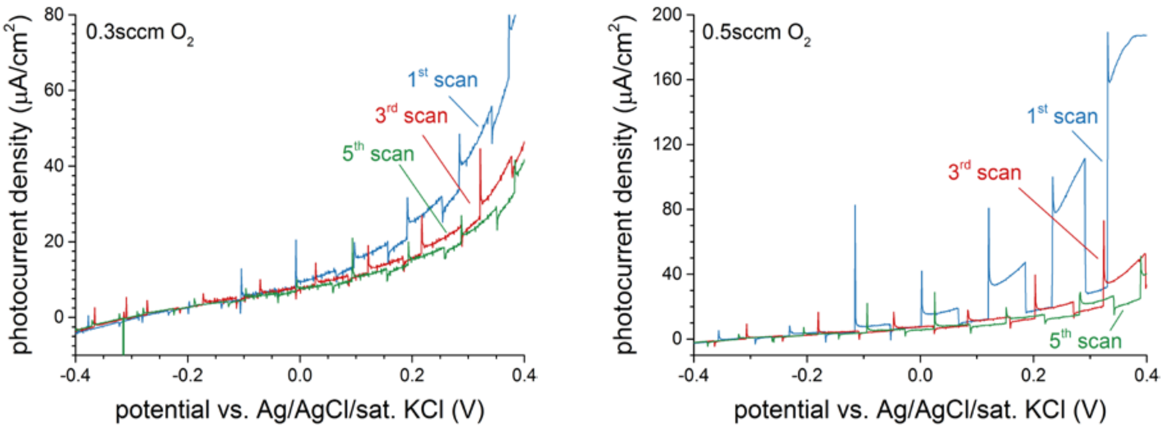

Fig. 130: Voltammetry curves at low (0.3sccm) and high (0.5sccm) O_2 flowrate for different scans. Note the different scales used on the ordinates.

This observations correlates well with theoretical predictions made by Harb et al. [78]. They show that the increase in oxygen incorporation into the lattice, decreases the position of the valence band maximum and the conduction band minimum (Fig. 131). Moreover, they claim that only by the incorporation of a minimum at.% of oxygen, starting from a stoichiometry of $Ta_{2.83}N_{4.16}O_{0.83}$, the bands straddle the hydrogen and oxygen evolution potential. This corresponds to an oxygen content of 10.6at.% compared to an oxygen content of 8at.% for the sample deposited at 0.5sccm. The results obtained from these two samples thus support the theoretical predictions.

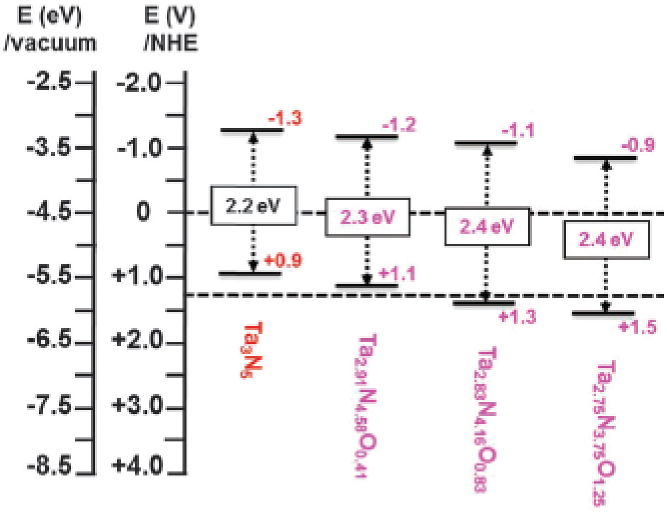

Fig. 131: Ta_3N_5 band positions with respect to the oxygen and hydrogen evolution potential from DFT calculations as a function of incorporated oxygen. From [78].

The rapid decrease of photocurrent with the number of scans on both samples in Fig. 130 is further analyzed. At first glance, this degradation suggests that the sample is not stable under photoelectrolysis conditions. The degradation could be attributed to the formation of an oxide layer which would be typical for nitride photoanodes [39] and was has already been observed for Ta_3N_5 photoanodes [21].

To analyze this degradation further, the sample deposited at an O_2 flowrate of 0.5sccm, was dried and a second series of measurements was performed. The result is summarized in Fig. 132. The plot shows the photocurrent at a bias voltage of 0.3V from voltammetry scans for both series. Striking is that the photocurrent recovers partially after having left to dry, so that, besides a possible oxidation of the sample, a second effect influences the water splitting performance.

This could be explained by the formation of O_2 bubbles on the semiconductor surface during the measurements. As small bubbles could remain attached to the surface, they prevent the direct contact between the electrolyte and the semiconductor. During the drying of the sample, the bubbles desolve into air and the surface of the sample is cleared. Thus, the large reduction in photocurrent seen in Fig. 130 is only partially an irreversible degradation.

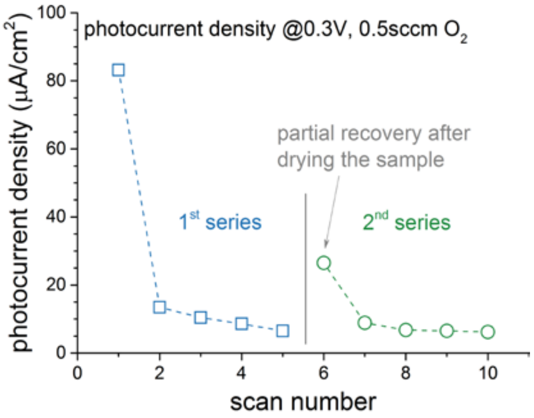

Fig. 132: Photocurrent recovery after two series of 5 scans each shown at a bias of 0.3V.

6.5 Conclusions

The samples from this chapter are deposited using a newly implemented process with an increased ion flux onto the substrate. This is achieved by installing electromagnetic coils behind the cathode and the substrate in order to guide ions from the negative glow into the substrate. The effect is proven by comparing emission lines from ions, notably N_2^+ ions with that of neutral Ta. While a large difference in crystallinity is observed between the films sputtered by conventional DC magnetron sputtering, less difference is observed in the crystallinity for films deposited with at least one of the coils switched on.

Using this guided-ion DC magnetron sputtering process, the films show a high degree of crystallinity as observed by GI-XRD and AFM. Their surface is densely covered by Ta_3N_5 grains with sizes ranging between 200nm to 300nm. The amorphous content found in DC-sputtered films in Chapter 5 is largely suppressed.

RBS and NRA measurements are used to determine the elemental composition of the films as a function of flowrate. Correlating these results with the presence of the Ta_3N_5 structure, observed indirectly by grains on the surface of the sample, allows to estimate how much oxygen Ta_3N_5-crystalline films can tolerate. The maximum oxygen content is determined to lie between 8at.% and 18.at%.

Large differences are remarked for the crystallization behavior of Ta_3N_5 thin films on different substrates. While Ta_3N_5 crystallizes on metal substrates, notably on Ta foils and steel substrates, it appears not to crystallize on Si or quartz substrates. This could be due to the high substrate temperature during the deposition process that promotes diffusion between the substrate and the film. As both contain Si, it seems likely that Si diffuses into the films were it prevents the crystallization in the Ta_3N_5 structure.

A large difference in photocurrent density is observed on two films deposited at different O_2 flowrates. The sample deposited at a higher O_2 flowrate shows an increase in photocurrent by a factor of 10 compared to that deposited at the lower O_2 flowrate. This confirms theoretical calculations done by Harb et al. [78], that predict the onset of photoelectrolysis only at a certain minimum at.% of oxygen incorporated into the films. Despite better electronic properties at low oxygen flowrates, as seen in Chapter 5, a minimum oxygen at.% is therefore necessary in order to trigger the photoelectrolysis.

7 Conclusions and future work

The objective of this thesis was to synthesize thin films of Ta_3N_5 by magnetron sputtering and optimize their properties with regards to their application in the photoelectrolysis of water. In this chapter, the principal findings from this thesis are summarized and a conclusion is drawn with respect to the use of magnetron sputtering for the deposition of Ta_3N_5 films. In a second section, perspectives are given for continuing this work.

7.1 Conclusions

Ta_3N_5 is a promising candidate for efficient solar water-splitting. This is due to the position of its valence band maximum and conduction band minimum that straddle the oxygen and hydrogen evolution potential. In addition, its small band gap allows the material to absorb a large part of the solar spectrum. Its synthesis is challenging, as it contains a high at.% of nitrogen which hampers atomic diffusion. In addition, the Ta atom in the lattice is in a high oxidation state that requires a large charge transfer towards the anions. Therefore, the crystalline phase is only obtained at high temperatures combined with the incorporation of oxygen into the lattice.

Magnetron sputtering is a technique widely used in industry to deposit thin films for a variety of applications. Its success is due to a high deposition rate combined with the possibility of creating depositions on large substrates. In addition, it uses a plasma to activate species, which typically permits depositions at low temperatures. For nitrides, such as Ta_3N_5, this allows the supply of nitrogen in the form of N_2 rather than using toxic NH_3 which is necessary in the conventional synthesis of Ta_3N_5 by ammonolysis.

Magnetrons can be operated in different modes, two of which are investigated in this thesis. These modes are direct current (DC) and high-power impulse magnetron sputtering (HiPIMS). The latter is known for providing a high ion flux onto the substrate, enhancing film density and film adhesion over DC depositions, and requiring a lower necessary substrate temperature. Experiments in this thesis, however, reveal smaller grains in films deposited by HiPIMS mode compared to DC magnetron sputtering. This is despite a higher ion flux in the HiPIMS case, as verified by mass spectrometry. Energetic backscattered neutrals are revealed to cause the smaller grains. As their maximum energy depends on the target-to-projectile mass ratio, the maximum energy is particularly high in the case of heavy metal targets such as Ta.

Oxygen is a crucial ingredient for Ta_3N_5. It is shown, that the Ta_3N_5-crystalline phase can only be obtained in a certain range of oxygen at.% in the film. Below this range, films crystallize in the δ-TaN phase, above this range, they are amorphous. The necessity for oxygen is explained by the higher electronegativity of oxygen that promotes the charge transfer from the Ta metal. It is shown that insufficiently oxidized films exhibit in-gap states due to Ta atoms in a reduced state. By increasing the O_2 incorporation, the in-gap states diminish and they disappear completely for samples with a band gap close to 2.1eV. The increased oxygen incorporation drastically reduces the mobility-lifetime of the films, though. The surface of the films deposited by conventional magnetron sputtering shows large crystallites in the range of 200 to 300nm embedded into an amorphous matrix. All Ta-O-N films deposited by conventional DC magnetron sputtering are photoactive and evolve oxygen and hydrogen in a photoelectrochemical cell. Films deposited at a high oxygen flowrate, however show a reaction with the electrolyte and are therefore considered to be not stable under photoelectrolysis conditions. In general, the samples show a small photocurrent that is explained by the low degree of crystallinity of the samples.

Ta_3N_5 films with a high degree of crystallinity are obtained by using ion-assisted growth. For that, an additional magnetic field is created in the cathode-substrate space that guides electrons towards the substrate. Ions a dragged along with them by ambipolar diffusion. This guided-ion DC magnetron sputtering is shown to promote crystallization of the samples and results in a surface densely covered by Ta_3N_5 grains. On those samples, the maximum at.% of oxygen incorporated into the films is determined to lie between 8 at.% and 18at.%. Below this maximum oxygen incorporation limit, samples are photoactive. It is shown that the oxygen in these films is the determining factor for the performance of a Ta_3N_5 photoanode as the valence and conduction bands fall into the right position at an increased oxygen content in the films only.

Magnetron sputtering is a highly suitable technique to deposit thin films of Ta_3N_5 for the photoelectrolysis of water. In addition to the advantages over ammonolysis, are in particular the possibility to precisely control the oxygen incorporated into the films. This is shown to have a strong impact on film properties and on the performance of the photoanode. The possibility to finely tune the O_2 flowrate, therefore allows to trade-off individual film properties. For example, films containing little oxygen show better charge carrier mobility. On the other hand, valence and conduction band positions are more favorable at an increased oxygen at.% in the film. A precise and reproducible tuning of the oxygen in the lattice therefore allows to find optimimum deposition conditions for the preparation of Ta_3N_5-based photoanodes.

7.2 Future work

The perspectives that this thesis opens up are multifaceted and can be grouped into three main subjects, the nucleation and growth of Ta_3N_5, the process characterization and optimization, and the configuration of the photoanode for the solar water-splitting application.

Nucleation and growth of Ta_3N_5

On the material side, the most pressing question is how the material nucleates and grows. Two factors are found to be influential to the growth of Ta_3N_5 thin films, the underlying substrate on which the material is grown and the oxygen incorporated into the film.

It is shown that Ta_3N_5-crystalline material can be deposited on metal substrates, notably on Ta and steel sheets. On the other hand, quartz substrates and monocrystalline Si(100) seem to hamper the crystallization even for thick films (~ 200nm) for which the influence of the substrate is expected to be negligible. The hypothesis suggested in this thesis is that this is due to the diffusion of Si species into the film. However, this still needs to be proven experimentally.

Oxygen plays a crucial role for the crystallization of Ta_3N_5. The precise mechanism by which it influences nucleation and the growth of grains, however is not understood. The AFM images in Section 6.3.3 suggest a correlation between the O_2 flowrate and the grain density on the surface. The question of interest here is whether this is influenced by initial conditions during the nucleation of the grains or at a later stage during growth.

Efforts should be undertaken to reduce the substrate temperature. This would suppress atomic diffusion between the film and the substrate possibly increasing the crystallinity on blank Si and quartz substrates. In addition, a reduction of temperature would be interesting in view of a possible industrialization because heating up large substrates to 600°C is energy consuming. Additionally, deposition chambers, in particular the joints, need to be cooled or capable of withstanding those temperatures.

Process characterization and optimization

The use of electromagnetic coils to increase the ion-to-neutral flux ratio onto the substrate has shown to be highly efficient in increasing the degree of crystallinity of the films. The extension of the operating range of the electromagnetic coils could determine a maximum limit up to which the ion flux increases. This should be coupled with probe measurements to determine the ion-to-neutral flux ratio and to correlate this parameter independently of the configuration of the deposition chamber used.

A high ion-to-neutral flux ratio was shown in the past to induce a preferred orientation of the crystals. Due to the high anisotropy concerning the mobility of holes and electrons, an updated version of the external coils should be used to force such an orientation, which could allow the studying of the effect of different crystal orientations on the photoanode performance.

Photoanode modifications

In order for the deposited material to be used as a photoactive material in a photoanode, a co-catalyst needs to be used. This enhances the kinetics of the charge transfer from the electrode to the electrolyte and makes sure that electron-hole pairs created in Ta_3N_5 actually contribute to a photocurrent. This would also allow a fairer comparison of performances between magnetron-sputtered photoanodes and those deposited by other processes.

In addition to this, nanostructuring the surface or the underlying substrate in order to increase the surface area should be done. This has been shown in the past to enhance the kinetics of films grown by ammonolysis. It has, however, never been shown on magnetron-sputtered photoanodes.

8 Appendix: Abbreviations

AD	Areal density
AFM	Atomic force microscopy
ALD	Atomic layer deposition
ALTAÏS	Accélérateur linéaire tandetron pour l'analyse et l'implantation des solides
ASTM	American Society for testing and materials
c-AFM	Conductive AFM
bcc	Body-centered cubic
CB	Conduction band
CBM	Conduction band minimum
CEA	Commissariat à l'énergie atomique et aux énergies alternatives
CT	Charge transfer
DC	Direct current
DCMS	Direct current magnetron sputtering
DFT	Density functional theory
DOS	Density of states
EC	electrochemical
EDS	Energy-dispersive X-ray spectroscopy
fcc	Face-centered cubic
FWHM	Full width at half maximum
GeePs	Laboratoire de génie électrique et électronique de Paris
GI-XRD	Grazing incidence XRD
IBA	Ion beam analysis
IBANDL	Ion beam analysis nuclear data library
ICCD	Intensified charge-coupled device
ICSD	Inorganic crystal structure database
INSP	Institut de NanoSciences de Paris
IPARC	Iași Plasma Advanced Research Center
ir	infrared
IUPAC	International Union of Pure and Applied Chemistry
JCPDS	Joint committee on powder diffraction standards
LEEL	Laboratoire d'Etude des Eléments Légers
LPGP	Laboratoire de Physique des Gaz et des Plasmas
MT	Momentum transfer
n/a	Not available
NHE	Normal hydrogen electrode
NRA	Nuclear reaction analysis
OMEGA	Orsay Metal Transport in Gases
PDF	Powder diffraction file
PEC	Photoelectrochemical cell
RF	Radio frequency
RBS	Rutherford backscattering spectrometry
RHE	Reversible hydrogen electrode
SAFIR	Système d'Analyse par Faisceaux d'Ions Rapides
sccm	Standard cubic centimeter per minute
SHE	Standard hydrogen electrode

SPEC	Service de l’état condense, CEA Saclay
SRIM	Stopping and range of ions in matter
SRMP	Service de recherches de métallurgie physique
TL	Tauc-Lorentz
TRIM	Transport of ions in matter
UHV	Ultra-high vacuum
UPS	Ultraviolet photoelectron spectroscopy
UT	Urbach tail
uv	ultraviolet
VB	Valence band
VBM	Valence band maximum
vis	visible
XRD	X-ray diffraction

9 Appendix: Résumé

Introduction

La transition énergétique nous impose à moyen terme de remplacer nos combustibles fossiles, qui représentent aujourd'hui la majorité des sources d'énergie dans les pays industrialisés, par des énergies renouvelables. Ces dernières années nous avons assisté à une croissance significative de la génération d'électricité par les éoliennes ou bien les panneaux photovoltaïques, mais il y a encore des challenges à résoudre pour continuer à remplacer les énergies fossiles par des énergies propres. Un des challenges est la fluctuation de la production d'électricité et l'absence de technologie pour la stocker. C'est un vrai problème pour les panneaux photovoltaïques qui ont des pics de production autour de midi tous les jours alors qu'ils ne produisent rien pendant la nuit [4]. Un autre challenge est l'absence d'une technologie pour décarboner le secteur du transport, qui dépend encore aujourd'hui presque exclusivement des énergies fossiles [6].

Une solution pour ces deux problèmes serait de produire de l'hydrogène d'une façon propre. L'hydrogène présente une densité énergétique hors concours par rapport aux batteries actuelles et son utilisation permettrait de stocker l'énergie en grande quantité. En plus, l'hydrogène est facilement transformable en électricité en utilisant des piles à combustible. Il est donc utilisable dans le secteur du transport pour les voitures électriques qui sont en train de faire leur entrée sur le marché [12] [13]. Mais la production verte d'hydrogène ne servirait pas seulement à la décarbonation du secteur du transport, mais serait aussi une solution pour stocker l'énergie dans le cas où ni le soleil, ni le vent serait disponible.

La production verte d'hydrogène est basée aujourd'hui sur l'électrolyse de l'eau et l'utilisation de l'électricité produite par les éoliennes ou bien les panneaux photovoltaïques. C'est un processus à deux étapes avec des pertes associées. Sachant qu'un panneau photovoltaïque a une efficacité de 20% et un électrolyseur de 50%, le rendement théorique maximum est ~10%. Une façon directe et peut-être plus efficace, serait d'utiliser directement l'énergie des photons solaires pour scinder les molécules d'eau en hydrogène et oxygène. Ce processus s'appelle la photo-électrolyse.

La photo-électrolyse

La photo-électrolyse de l'eau consiste à séparer les molécules H_2O en H_2 et O_2 en utilisant directement l'énergie des photons incidents. Elle a lieu dans des cellules électrochimiques avec deux électrodes, dont l'une au moins est un semi-conducteur qui peut absorber les photons.

L'absorption des photons par le semi-conducteur crée des pairs électron-trou, qui grâce à la présence d'une charge d'espace à l'interface entre le semi-conducteur et l'électrolyte, se séparent. Les électrons migrent vers l'électrode métallique de la cellule électrochimique et peuvent, sous certaines conditions, réagir avec les molécules d'eau et produire de l'hydrogène. Les trous se déplacent vers l'électrolyte où ils se combinent avec les hydroxydes (HO^-) pour produire de l'oxygène (Fig. A).

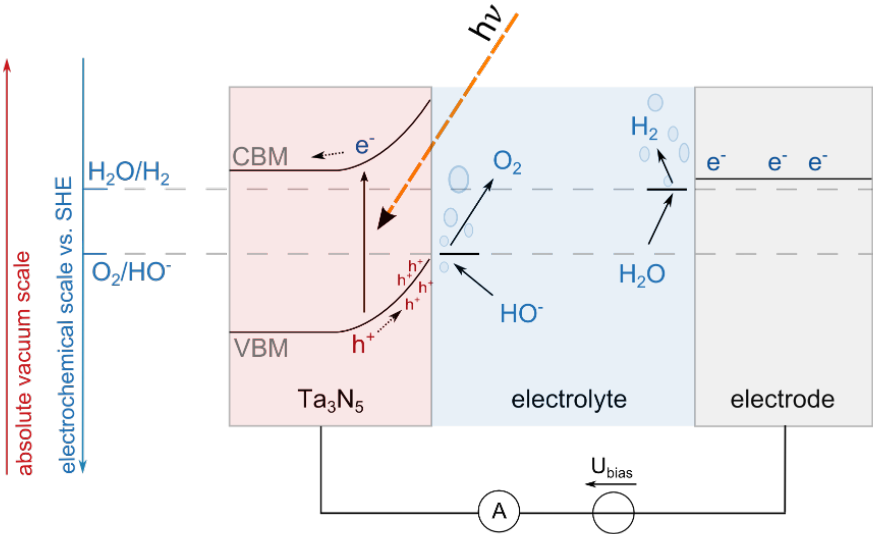

Fig. A : Schéma de la photo-électrolyse de l’eau.

Pour que la photo-électrolyse de l’eau fonctionne, les matériaux doivent présenter certaines propriétés spécifiques. La bande de valence du semi-conducteur doit être située plus bas que le potentiel chimique de l’oxygène et la bande de conduction doit être située plus haut que le potentiel chimique de l’hydrogène. Cela implique une largeur minimum de bande interdite de 1.23eV, qui correspond à l’énergie théorique nécessaire pour scinder la molécule d’eau. Pour compenser les pertes, un potentiel supplémentaire de 0.8eV doit être ajouté. Un band-gap minimum d’environ 2eV est donc optimal [38]. L’utilisation des matériaux avec des gaps plus grands est possible, mais une partie du spectre solaire n’est pas absorbé.

D’après deux études de modélisation, peu de matériaux satisfaisant ces conditions sont connus à ce jour. En utilisant des lois empiriques pour estimer le positionnement des bandes et le band gap, des phases existantes et fictives ont été analysées. Castello et al. ont analysé 5400 phases de type pérovskite et leurs dérivés, parmi elles seulement 15 satisfont les deux conditions citées ci-dessus [50]. Wu et al. ont analysé 2948 nitrures et oxynitrures et parmi eux, 27 satisfont les conditions [51]. Ces études ont été basées sur le positionnement des bandes seulement. D’autres paramètres importants pour l’efficacité de la photo-électrolyse comme les propriétés optiques et électroniques, mais aussi la stabilité dans une solution basique n’ont pas été étudiés. Parmi les matériaux identifiés, certains ne seront pas utilisables ce qui diminue encore leur nombre.

La phase Ta_3N_5

Ta_3N_5 est parmi les matériaux les plus prometteurs. Sa phase a un band gap de 2.1eV et les études expérimentales confirment le bon positionnement des bandes par rapport au potentiel chimique de l’hydrogène et l’oxygène [19]. Des études théoriques montrent toutefois que cela est le cas, juste pour des films de Ta_3N_5 avec de l’oxygène incorporé ou présentant des défauts [78].

Les autres propriétés sont moins étudiées. Les propriétés électroniques sont connues principalement par des études théoriques. Elles montrent que la mobilité des porteurs minoritaires (les trous) de charge dépend fortement des directions cristallographiques et certaines directions peuvent être très défavorables [18] [88]. Par contre, d’autres auteurs montrent que la durée de vie de ces porteurs est élevée et peut attendre des valeurs proches de celles trouvées pour le Si [47].

La fonction diélectrique de Ta_3N_5 montre une faible absorbance autour du band gap. Cela implique qu’il faut une épaisseur élevée pour absorber les photons de la gamme visible du spectre solaire.

Les calculs réalisés dans la thèse montrent qu'une épaisseur d'environ 1µm est nécessaire pour absorber pratiquement 100% des photons incidents dont l'énergie est supérieure à 2.1eV (Fig. B).

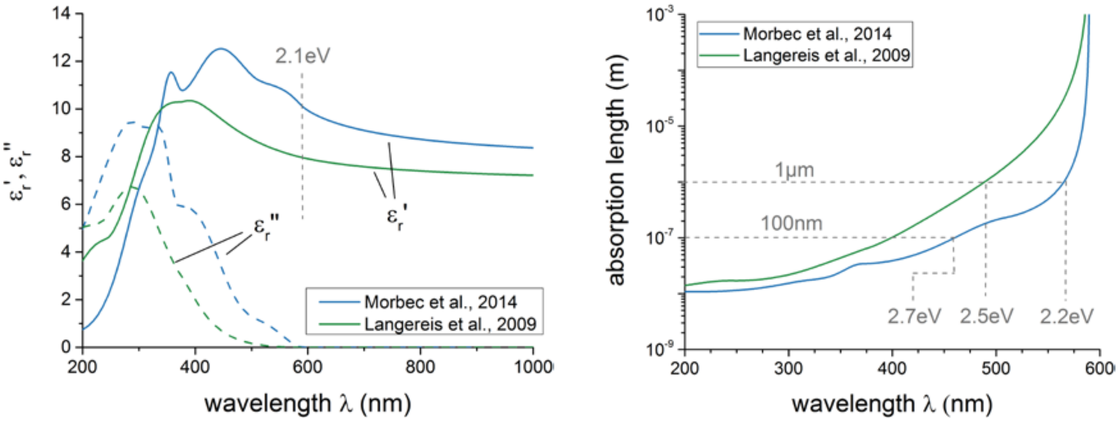

Fig. B: Gauche: fonction diélectrique de Ta_3N_5 *mesurée sur des échantillons préparés par « Atomic layer deposition » (Langereis et al.* [86]*) et par nitruration de couches de Ta-O (Morbec et al.* [18]*). Droite: Longueur d'absorption en fonction de la longueur d'onde calculée en utilisant la fonction diélectrique.*

Une photoanode n'est pas exclusivement composée du matériau photo-actif (Ta_3N_5 dans le cas de cette thèse), les interfaces jouent un rôle important au niveau de l'efficacité vu que les porteurs de charges doivent les traverser. Les électrons sont collectés à l'arrière de la couche Ta_3N_5. Pour faciliter ce processus, un contact ohmique est nécessaire. Il faut donc déposer la couche de Ta_3N_5 sur un substrat, ayant un travail de sortie assez proche de la bande de conduction de Ta_3N_5 [91] qui se trouve autour de –4.0eV par rapport au niveau du vide [19]. Différents substrats ont été utilisés dans des études passées, notamment des feuilles de Ti ($W_{f,\,Ti}$ = 4.33eV [212]) ou de Ta ($W_{f,Ta} \approx$ 4.25eV [212]). A la surface du semi-conducteur ou bien à l'interface entre le semi-conducteur et l'électrolyte, normalement, un co-catalysateur est utilisé pour augmenter le rendement. Le co-catalysateur est également indispensable pour éviter la dégradation des couches par l'oxydation de la surface, ce mécanisme de dégradation est connu pour la plupart des nitrures pour la photo-électrolyse de l'eau [39]. Malgré les efforts fournis par beaucoup d'études publiées, l'efficacité de Ta_3N_5 reste autour de 1% (η_{STH}). Cela est faible par rapport à l'efficacité théorétique de ce matériau de 15.9%.

La synthèse de Ta_3N_5

Une raison de cette faible valeur pourrait être du processus conventionnel de synthèse de Ta_3N_5. Le processus conventionnel est un processus en deux étapes. Dans un premier temps, Ta dans son état métallique est oxydé, puis dans un deuxième temps il est nitruré à haute température (> 800°C) dans une atmosphère d'ammoniac (NH_3).

Cette méthode conventionnelle présente des inconvénients. L'incorporation de l'oxygène et de l'azote dans le matériau est réalisée par diffusion. Cela implique que la quantité d'oxygène et d'azote incorporée est peu contrôlable. En plus, un gradient de concentration des espèces peut être attendu à l'interface avec le substrat métallique. Un autre effet est l'apparition de fissures et la délamination du film [30] à cause des différences de densité entre le métal (ρ = 16.65g/cm^2 [92]), la phase Ta_2O_5 (ρ = 8.2g/cm^3 [93]) et la phase Ta_3N_5 (ρ = 9.85g/cm^3 [94]).

Un processus alternatif pour la synthèse de Ta_3N_5 est la pulvérisation cathodique. Cela permet de déposer les espèces nécessaires (Ta, N, O) simultanément ce qui permet de contrôler précisément l'épaisseur et la composition du film. En plus, grâce à la présence dans la décharge d'espèces énergétiques (ions et neutres avec des énergies < 50 à 100eV) la morphologie du film peut être modifiée tout en conservant une faible température pour le substrat pendant le processus [126]. Jusqu'à présent, trois études ont montré la faisabilité de ce procédé pour réaliser des couches minces cristallines de Ta_3N_5. Deux études utilisent la pulvérisation en mode radio-fréquence (RF) [20] [21]. Une autre étude prépare les films en mode continu (DC). Les trois études ont en commun qu'il faut pulvériser la cible de Ta dans une atmosphère d'$Ar/N_2/O_2$. Le rôle de l'oxygène dans le réseau de Ta_3N_5 est discuté dans [49]. Les films sont préparés à une température du substrat élevée ($\gtrsim$ 600°C), mais qui reste quand même inférieure à celle nécessaire pour la nitruration en NH_3.

Objectifs de cette thèse

L'objectif de cette thèse est de déposer des couches minces de Ta_3N_5 par pulvérisation. Pour éviter les pertes par recombinaison électrons-trous, il faut tenter d'arriver à des tailles de grains les plus grandes possibles. Les films préparés par pulvérisation cathodique dans le passé ont donné des couches minces peu cristallisées. Un autre objectif est donc d'augmenter la cristallinité directement pendant le processus de dépôt. Une bonne cristallinité augmenter fortement les performances de ce matériau pour la photoelectrolyse de l'eau [21].

1. Les propriétés des films δ-TaN préparé par la pulvérisation cathodique

Les couches minces préparées pour cette thèse ont été élaborées dans un bâti de pulvérisation avec une pression résiduelle $<5\cdot10^{-6}$ mbar. Il est équipé d'un sas pour insérer les substrats dans la chambre de dépôt sans couper le vide. Un magnétron balancé de 10cm de diamètre a été utilisé. Pendant les dépôts, les trois gaz Ar, N_2 et O_2 peuvent être injecté dans le réacteur simultanément.

La première partie de cette thèse identifie des mécanismes relevant pour la croissance des couches minces à partir d'une cible de Ta. Pour cela, la phase δ-TaN a été sélectionnée parce que sa préparation est bien connue dans la littérature et elle se fait même à basse température. Les échantillons ont été préparés sur des substrats en Si monocristallin (100).

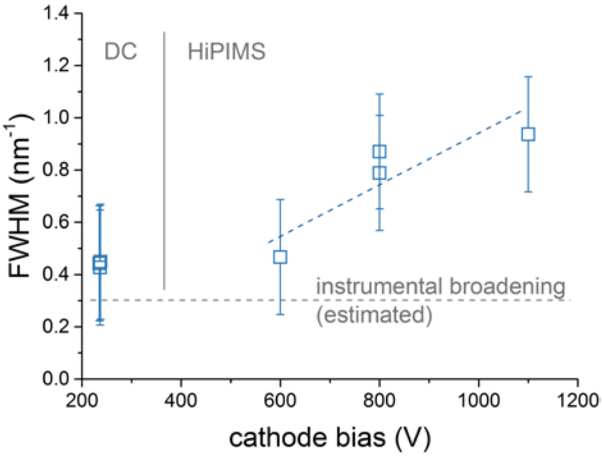

Fig. C: La FWHM du pic (111) de la phase δ-TaN en fonction de la polarisation de la cathode.

Une comparaison entre la pulvérisation en mode DC et en mode HiPIMS (high-power impulse magnetron sputtering) met en évidence la diminution de la taille des grains pour les films réalisés en HiPIMS. Plus précisément, la largeur à mi-hauteur (FWHM) des grains augmentent en fonction de la polarisation de la cible (Fig. C). Vu que les propriétés électroniques sont meilleures avec une taille de grain la plus grand possible, cela montre que les films en HiPIMS sont de qualité inférieure par rapport aux films en DC.

Cette contre-performance de la technique HiPIMS est à relier aux neutres rétrodiffusés à la cathode dont l’énergie maximum et leur nombre dépendent de la différence de masse entre les projectiles (Ar) et les atomes dans la cible (Ta). Pour une polarisation de la cible de -1100eV, par exemple, l’énergie maximale des neutres atteint une valeur entre 600eV et 700eV (Fig. D, bars rouges). Même en prenant en compte la décélération des neutres par le gaz Argon qui se trouve entre la cathode et le substrat (distance = 10cm), la distribution en énergie ne se thermalise pas, même pour une pression de gaz de 5.0Pa.

La conclusion tirée de ce chapitre est qu’il faut pulvériser la cible de Ta en mode DC au lieu d’utiliser le mode HiPIMS.

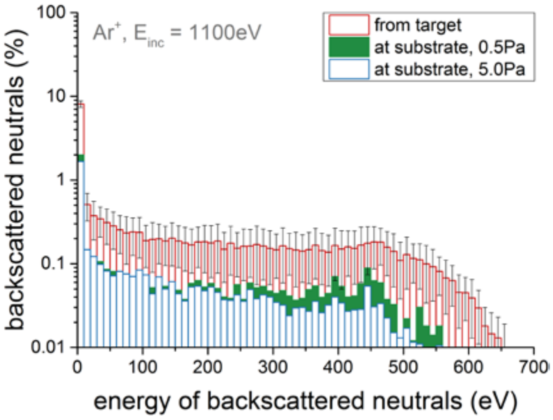

Fig. D: Distribution en énergie des neutres calculée par TRIM (distribution à la cathode, en rouge) [201], *et en utilisant OMEGA* [104], *un code Monte-Carlo qui prend en compte les collisions entre les neutes retrodiffusés et le gaz d’Ar entre la cathode et le substrat à differentes pressions.*

2. La rôle d’oxygène dans des couches minces de Ta_3N_5

La deuxième partie de cette thèse utilise la connaissance acquise dans la première partie pour déposer des films de Ta_3N_5 en pulvérisation cathodique.

Avant de déposer les films, un processus de nettoyage a été mis en place, pour diminuer la concentration d’oxygène à l’interface entre le substrat et la couche mince. Il consiste à pulvériser la cible pendant 20min en Ar pur pour enlever les oxydes à la surface, puis, 10min dans un mélange de gaz qui correspond à celui du dépôt. Pour nettoyer la surface du substrat, le porte substrat a été polarisé en radio-fréquence avec une polarisation effective de -100V. L’efficacité de ce processus a été évaluée en utilisant la rétrodiffusion de Rutherford avec des particules α autour de 3MeV. A cette énergie la section-efficace de ^{16}O avec des α a une forte résonance très étroite qui permet de doser ^{16}O en fonction d’épaisseur. Fig. E montre le profil de ^{16}O en fonction de l’épaisseur sans nettoyage (gauche) et avec nettoyage (droite).

Les couches minces de Ta_3N_5 sont déposées en pulvérisation cathodique en mode DC dans un atmosphère d’$Ar/N_2/O_2$. Pour étudier les propriétés des couches minces en fonction de l’incorporation d’oxygène, le débit d’oxygène injecté dans la chambre de dépôt a été varié entre 0sccm et 0.9sccm. La pression pendant le dépôt est restée à 0.5Pa. La température du substrat a été fixée à 600°C ce qui correspond à celle utilisé par d’autre chercheur pour la synthèse des couches minces de Ta_3N_5.

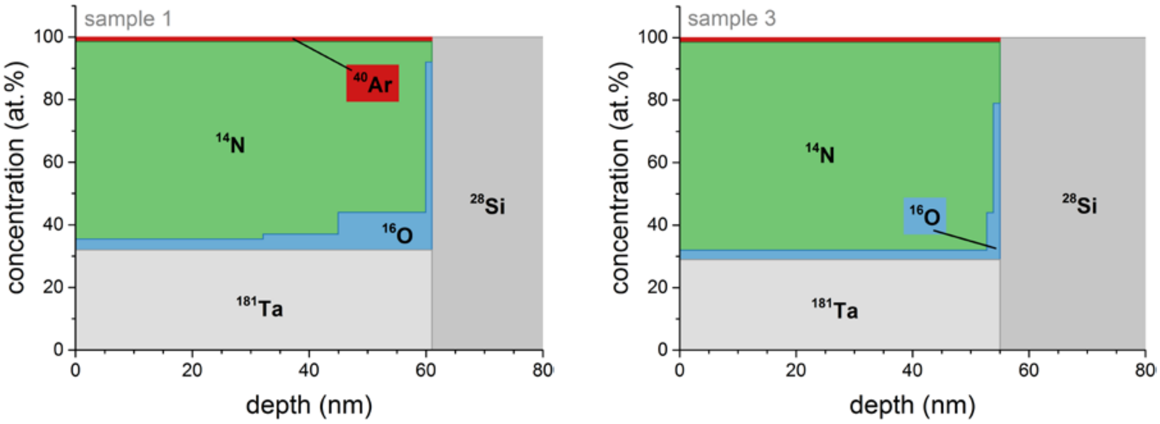

Fig. E : Profil d'oxygène dans les films de Ta-N sans processus de nettoyage (à gauche) et avec le processus mis en œuvre (à droite).

Fig. F montre des diffractogrammes d'une série de couches minces en fonction du débit d'oxygène. Sans l'injection d'oxygène dans le réacteur, les films présentent la phase δ-TaN. La phase Ta_3N_5 apparait des 0.2sccm d'O_2. Ce résultat montre la nécessité d'incorporer de l'oxygène dans les films pour obtenir la phase semiconductrice Ta_3N_5. L'image MEB faite à un débit de 0.4sccm d'O_2 montre des cristallites d'une taille de 300nm au moins (Fig. G). Elles sont incorporées dans une matrice qui semble amorphe. La coexistence d'une phase amorphe est visible aussi sur des diffractogrammes vu que les pics ne sont pas très prononcés. L'image MEB faite à un débit de 0.9sccm d'O_2 montre la surface d'un échantillon amorphe.

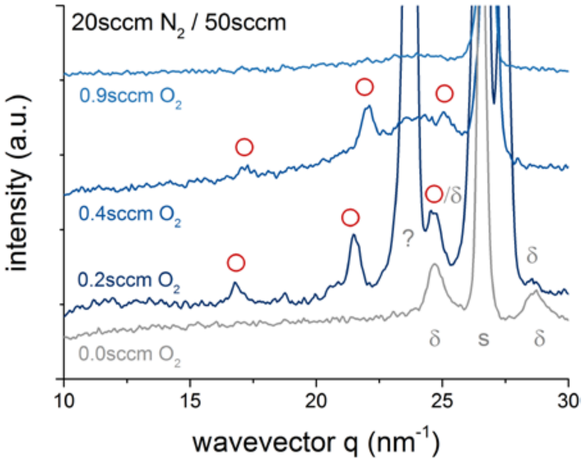

Fig. F: Diffractogrammes des couches minces en fonction du débit d'O_2. Les cercles rouges indiquent des pics correspondant à la phase Ta3N5. Les δ indiquent les pics de la phase δ-TaN et 's' indique le pics qui vient du substrat en Ta métallique.

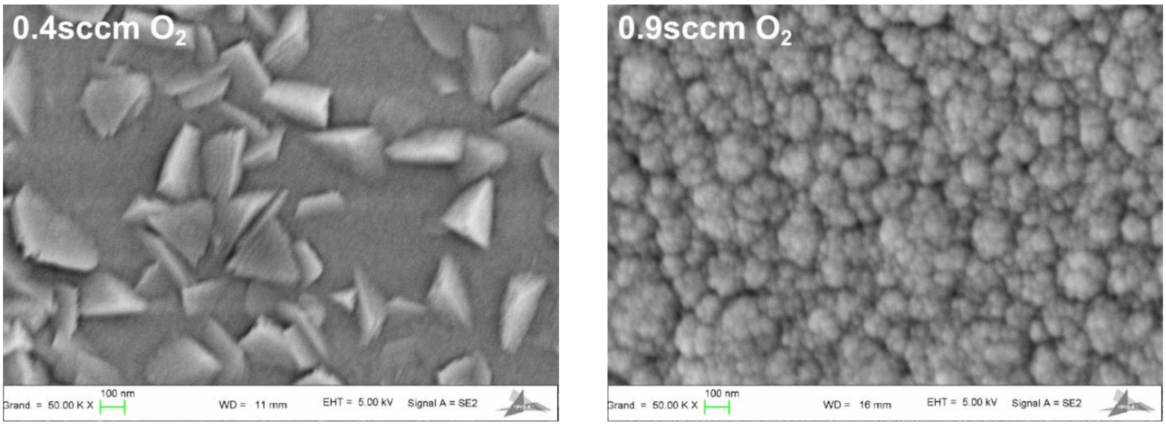

Fig. G: Images de microscopie électronique à balayage pour des films cristallins en Ta_3N_5 (gauche) et amorphe (droite).

Pour déterminer les propriétés optiques, notamment le band gap, les couches ont été déposées également sur des substrats transparents en quartz. Ceci permet de mesurer les coefficients de transmission et de réflexion des films en utilisant un photo spectromètre. Les spectres ont été ensuite modélisés avec une loi de dispersion pour la fonction diélectrique. La loi de dispersion choisie est une loi Tauc-Lorentz avec une queue Urbach. Fig. H montre les spectres expérimentaux et modélisés.

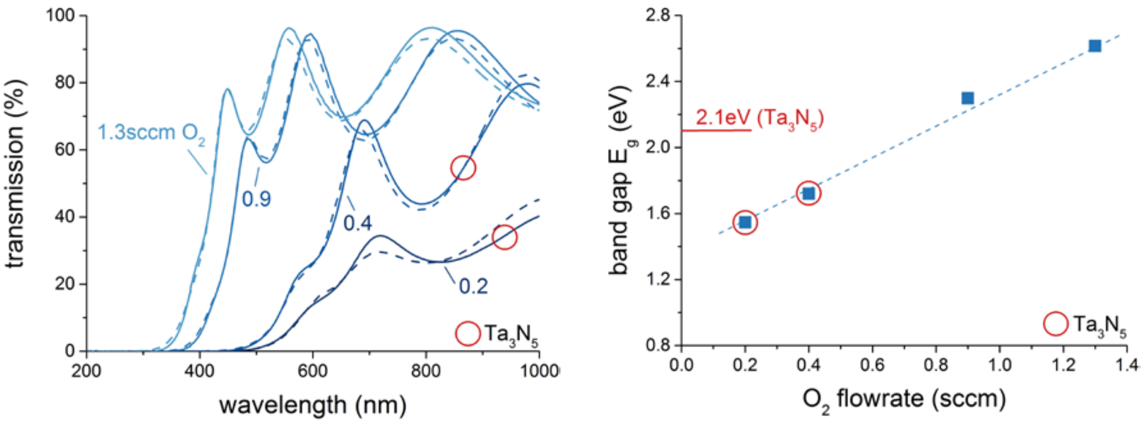

Fig. H: Gauche : Spectres de transmission (experimental et fitté). Droite : band gaps des film en fonction du débit d'O_2. Les cercles rouges indiquent la présence de la phase Ta_3N_5 (voir Fig. F).

L'évolution du band gap est linéaire avec le débit d'O_2. Le matériau Ta_3N_5 a un band gap de 2.1eV, très proche du band gap optimum (2.0eV) pour la photo-électrolyse de l'eau [38]. La Fig. H indique qu'un débit d'oxygène entre 0.6sccm et 0.8sccm est nécessaire pour arriver au band gap idéal.

En général, les films montrent la signature de Ta_3N_5, mais vu que les diffractogrammes présentent peu de pics visibles, il est probable que les films soient peu cristallisés. Cela est confirmé par des images MEB (Fig. G). L'objective du dernier chapitre est donc d'augmenter le degré de cristallinité des couches minces.

3. La croissance des couches mince de Ta_3N_5 à haut degré de cristallisation

Ce chapitre s'intéresse à la croissance assistée par des ions pour augmenter le degré de cristallinité des couches minces de Ta_3N_5. Pour cela le flux d'ions sur le substrat doit être amélioré. Dans le cas de la pulvérisation en mode DC, normalement, il n'y a que peu d'ions métalliques [138]. Par contre, dans les décharges Ar/N_2, des ions d'N_2^+ sont présents [197]. Mais à cause du confinement des électrons, ces ions sont largement piégés électrostatiquement ce qui fait que seulement peu arrivent à s'échapper de la zone magnétisée.

Pour dé-piéger les ions, un champ magnétique est superposé au champ magnétique du magnétron. Deux bobines sont installées en-dessous de la cathode et au-dessus du substrat. Cela permet de rapidement modifier l'amplitude du champ magnétique appliqué en variant les courants des bobines (I_{sub} et I_{cath}). En faisant fonctionner les bobines à courants maximums (I_{sub} = 6A et I_{cath} = 12A) l'apparence de la décharge lumineuse change drastiquement et une colonne lumineuse apparait qui monte jusqu'au substrat (Fig. I).

Cette région lumineuse indique la présence des électrons qui se font remarquer en excitant des atomes de gaz. En invoquant la notion de diffusion ambipolaire, on peut faire l'hypothèse qu'il y aura aussi des ions dans cette région. Cela est confirmé dans la thèse par la spectroscopie d'émission optique.

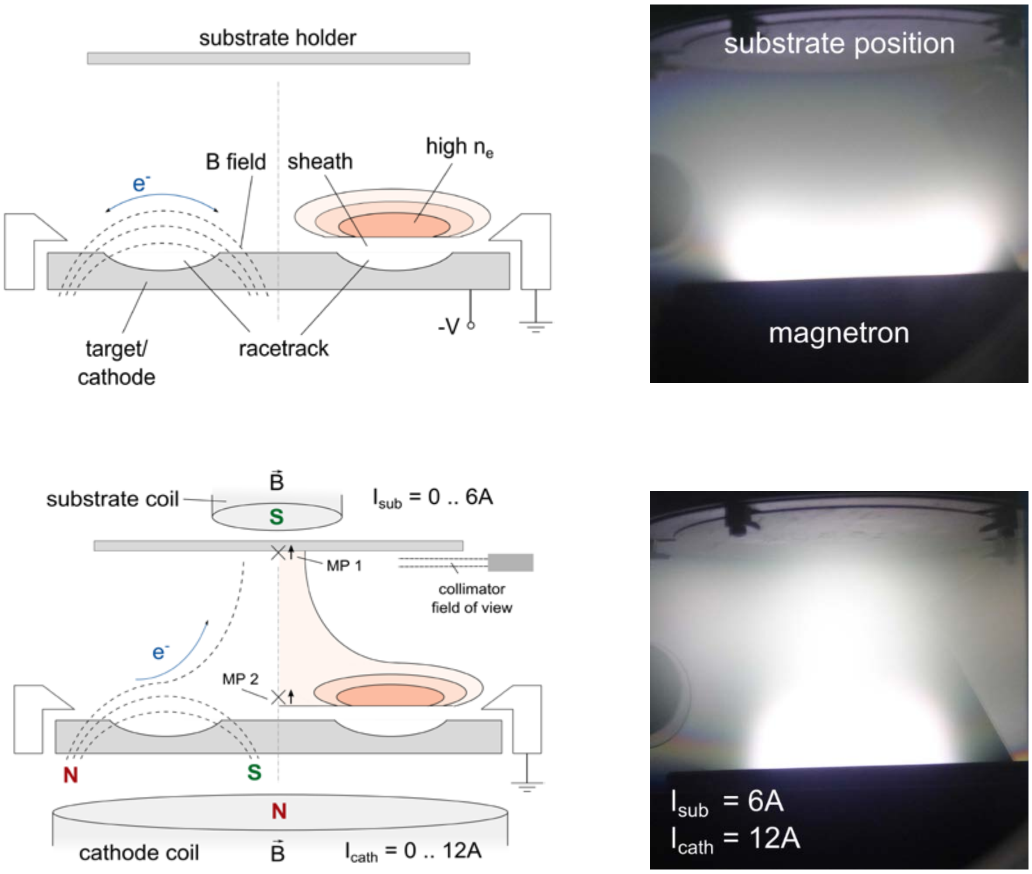

Fig. I: Magnétron équilibré (en haut) et le même magnétron avec un champ magnétique superposé sur le champ magnétique de la cathode (croissance assistée par des ions).

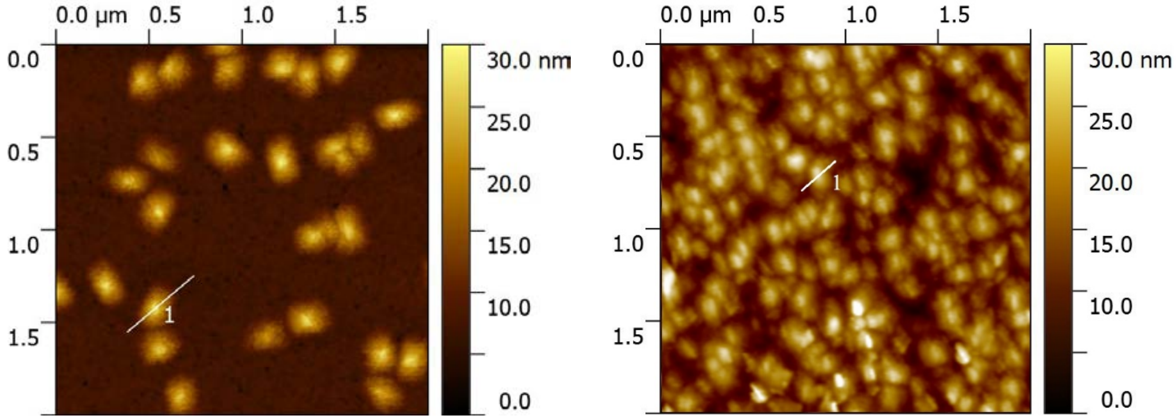

Fig. J: Image de microscopie à force atomique de couches minces déposées avec un magnétron équilibré (gauche) et un magnétron avec un champ magnétique axial supplémentaire (droite).

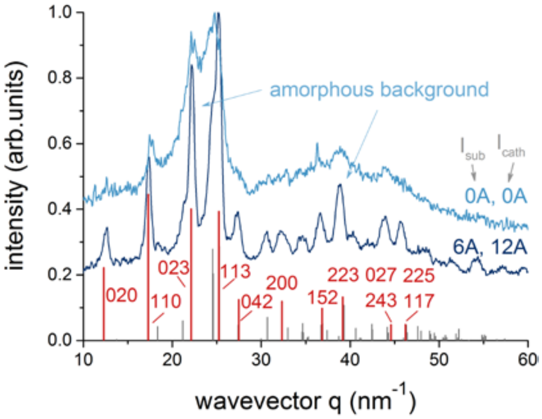

Fig. K : Diffractogrammes de couches mince de Ta_3N_5 déposées en mode conventionnel et avec un champ magnétique axial supplémentaire.

Les échantillons déposés en utilisant la croissance assistée par des ions montrent une plus forte cristallinité. Cela se voit sur des images de microscopie à force atomique. Fig. J montre peu de cristallites sur une matrice amorphe alors qu'en mode de croissance assisté par des ions, la surface est largement couverte par des cristallites. Ces résultats sont confirmés en regardant des diffractogrammes (Fig. K). L'échantillon, déposé en utilisant le champ magnétique axial supplémentaire, montre un diffractogramme avec une intensité et un nombre de pics beaucoup plus élevé.

Cette méthode a été utilisée pour déposer un film avec une band gap de 1.9eV (débit d'O_2 de 0.5sccm). Le film est composé de 34at.% de Ta, 59at.% de N et de 0.08at.% de O mesurés par la rétrodiffusion élastique de Rutherford (RBS) et réaction nucléaire (NRA). Son épaisseur est de 250nm.

Sa capacité pour produire de l'hydrogène par photo-électrolyse de l'eau est montrée dans une cellule électrochimique à trois électrodes en illuminant l'échantillon avec de la lumière pulsée. On obtient un signal de forme rectangulaire (Fig. M). Le niveau haut correspond au courant pendant l’illumination, le niveau bas correspond au courant d’obscurité. La différence est le photo-courant.

La mesure est réalisée en polarisant l’échantillon vs. une électrode de référence (Ag/AgCl sat. KCl). La mesure montre que l’échantillon est photo-actif. Par contre, en répétant les mesures, le photo-courant se dégrade. Cela est probablement du à une oxydation de la surface qui empêche le transfert des charges entre le semi-conducteur et l’électrolyte.

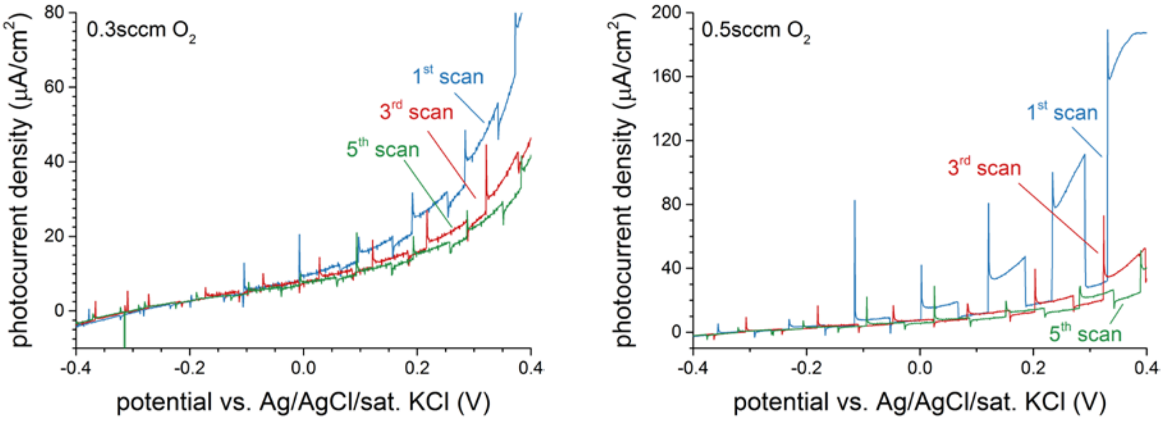

Fig. M : Voltamètrie des couches minces à basse débit d’oxygène (gauche) et haute débit d’oxygène (droite).

Conclusion

En conclusion, la thèse montre la possibilité de déposer des couches minces de Ta_3N_5 avec un haut degré de cristallinité en pulvérisation cathodique directement sans la nécessité de faire un recuit sous NH_3 après le dépôt. L’avantage de ce processus par rapport à la synthèse conventionnelle est le contrôle de l’épaisseur des couches et de l’incorporation d’oxygène, une température de synthèse plus faible et l’utilisation de N_2 par rapport au NH_3 toxique.

La thèse met en évidence l’effet des neutres rétrodiffusés sur une cathode en métal lourd sur la taille des grains dans la couche. Pour cette raison, les couches de Ta_3N_5 sont déposées en mode continue avec une polarisation de la cible la plus faible possible. Ce processus est amélioré en ajoutant des bobines pour modifier le champ magnétique de la cathode de façon que les électrons soient guidés vers le substrat. Par diffusion ambipolaire, ils entrainent les ions, qui, accélérés dans la gaine présente devant le substrat, apportent une quantité de mouvement à la surface du film en croissance, et permet par ce biais d’augmenter fortement le degré de cristallisation du film.

La thèse montre la forte influence de l’oxygène incorporé dans les couches. Non seulement elle montre que l’oxygène est indispensable pour synthétiser la phase Ta_3N_5. Mais elle montre également que des paramètres relevant pour la photo-électrolyse dépendent fortement du pourcentage atomique d’oxygène dans les couches: avec une incorporation d’oxygène croissante, le band gap augmente, le produit mobilité-durée de vie des porteurs de charge augmente, et finalement, la stabilité des couches dans une cellule électrochimique diminue.

La couche déposée montre qu’elle fonctionne pour la photo-électrolyse de l’eau. Son utilisation dans des photo-anodes avec des substrats appropriés et un co-catalyseur est la prochaine étape pour arriver à scinder efficacement la molécule d’eau en hydrogène et oxygène.

10 References

[1] A. Cho, "Energy's tricky tradeoffs," *Science,* vol. 329, no. 5993, pp. 786-787, 2010.

[2] E. E. A. Report, "Renewable energy in Europe 2016, recent growth and knock-on effects," 2016.

[3] J. Salvatore, G. Turner, H. Boyle, E. Nekhaev, A. Clerici and S. Ulreich, "World Energy Perspective - Cost of Energy Technologies," World Energy Council, 2013.

[4] E. Barbour, G. Wilson, P. Hall and J. Radcliffe, "Can negative electricity prices encourage inefficient electrical energy storage devices?," *Int. J. Env. Studies,* vol. 71, no. 6, pp. 862-876, 2014.

[5] P. Denholm, E. Ela, B. Kirby and M. Milligan, "The role of energy storage with renewable electricity generation," National renewable energy laboratory, 2010.

[6] European Commision, "State of the art on alternative fuels transport systems in the European Union," 2015.

[7] I. Gyuk, P. Kulkarni, J. H. Sayer, J. D. Boyes, G. P. Corey and G. H. Peek, "The United States of storage [electric energy storage]," *IEEE Power Energy Mag.,* vol. 3, no. 2, pp. 31-39, 2005.

[8] K. Divya and J. Østergaard, "Battery energy storage technology for power systems - an overview," *Electr. Pow. Sys. Res.,* vol. 79, pp. 511-520, 2009.

[9] M. Balat, "Potential importance of hydrogen as a future solution to environmental and transportation problems," *Int. J. Hydorgen Energy,* vol. 33, pp. 4013-4029, 2008.

[10] J. J. Romm and J. G. Moser, "Der Wasserstoff-Boom: Wunsch und Wirklichkeit beim Wettlauf um den Klimaschutz," Wiley-VCH Verlag , Weinheim, 2006.

[11] M. W. Melaina, O. Antonia and M. Penev, "Blending hydrogen into natural gas pipeline networks: a review of key issues," National renewable energy laboratory, 2013.

[12] "Toyota to begin selling hydrogen fuel cell car Mirai for first time," *The Guardian,* 18 November 2014.

[13] "Honda debuts Clarity, its first mass production hydrogen car," *The Japan Times,* 10 March 2016.

[14] A. Fujishima and K. Honda, "Electrochemical photolysis of water at a semiconductor electrode," *Nature,* vol. 238, pp. 37-38, 1972.

[15] M. M. May, H.-J. Lewerenz, D. Lackner, F. Dimroth and T. Hannappel, "Efficient direct solar-to-hydrogen conversion by in situe interface transformation of a tandem structure," *Nat. Commun.,* vol. 6:8286, 2015.

[16] Y. Li, T. Takata, C. Dongkyu, K. Takanabe, T. Minegishi, J. Kubota and K. Domen, "Vertically aligned Ta3N5 nanorod arrays for solar-driven photoelectrochemical water splitting," *Adv. Mater.*, vol. 25, pp. 125-131, 2013.

[17] Y. Li, L. Zhang, A. Torres-Pardo, J. M. González-Calbet, Y. Ma, P. Oleynikov, O. Terasaki, S. Asahina, M. Shima, D. Cha, L. Zhao, K. Takanabe, J. Kubota and K. Domen, "Cobalt phosphate-modified barium-doped tantalum nitride nanorod photoanode with 1.5% solar energy conversion efficiency," *Nat. Commun.,* vol. 4:2566, 2013.

[18] J. M. Morbec, I. Narkeviciute, T. F. Jaramillo and G. G., "Optoelectronic properties of Ta3N5: A joint theoretical and experimental study," *Phys. Rev. B,* vol. 90, p. 155204, 2014.

[19] W.-J. Chun, A. Ishikawa, H. Fujisawa, T. Takata, J. N. Kondo, H. Michikazu, M. Kawai, Y. Matsumoto and K. Domen, "Conduction and valence band positions of Ta2O5, TaON, and Ta3N5 by UPS and electrochemical methods," *J. Phys. Chem. B,* vol. 107, pp. 1798-1803, 2003.

[20] A. Ishihara, S. Doi, S. Mitsishima and K.-i. Ota, "Tantalum (oxi)nitrides prepared using reactive sputtering for new nonplatinum cathodes of polymer electrolyte fuel cell," *Electrochim. Acta,* vol. 53, pp. 5442-5450, 2008.

[21] D. Yokoyama, H. Hashiguchi, K. Maeda, T. Minegishi, T. Takata, R. Abe, J. Kubota and K. Domen, "Ta3N5 photoanodes for water splitting prepared by sputtering," *Thin Solid Films,* vol. 519, pp. 2087-2092, 2011.

[22] D.-H. Lin and K.-S. Chang, "Photocatalytic and photoelectrochemical performance of Ta3N5 microcolumn films fabricated using facile reactive sputtering," *J. Appl. Phys.,* vol. 120:075303, 2016.

[23] R. F. Pierret, Advanced semiconductor fundamentals, Modular series on solid state devices, Vol. 4, Pearson Education Inc. , 2003.

[24] C. Kittel, Introduction to solid state physics, 8th ed., John Wiley and Sons, 2004.

[25] N. W. Ashroft and N. Mermin, Festkörrperphysik, Oldenbourg: De Gruyter, 2013.

[26] H. Gerisher and W. Ekardt, "Fermi levels in electrolytes and the absolute scale of redox potentials," *Appl. Phys. Lett.,* vol. 43, no. 4, 1983.

[27] M. Marquez-Mijares, B. Lepetit and D. Lemoine, "Carbon adsorption on tungsten and electronic field emission," *Surf. Sci.,* no. 645, pp. 56-62, 2016.

[28] A. Kahn, "Fermi level, work function and vacuum level," *Mater. Horiz.,* vol. 3, pp. 7-10, 2016.

[29] C. Stampfl and A. J. Freeman, "Metallic to insulating nature of TaNx: Role of Ta and N vacancies," *Phys. Rev. B,* vol. 67:064108, 2003.

[30] A. Ishikawa, T. Takata, J. Kondo, M. Hara and K. Domen, "Electrochemical behavior of thin Ta3N5 semiconductor film," *J. Phys. Chem. B,* vol. 108, pp. 11049-11053, 2004.

[31] D. M. F. Santos, C. A. C. Sequeira and J. L. Figueiredo, "Hydrogen production by alkaline water electrolysis," *Quim. Nova*, vol. 36, no. 8, pp. 1176-1193, 2013.

[32] C. H. Hamann, A. Hamnett and W. Vielstich, Electrochemistry, Weinheim: Wiley VCH, 2007.

[33] S. Trasatti, "The absolute electrode potential: An explanatory note," *Pure & Appl. Chem.*, vol. 58, no. 7, pp. 955-966, 1986.

[34] IUPAC, "IUPAC Gold Book," [Online]. Available: https://goldbook.iupac.org/S05917.html. [Accessed 06 02 2017].

[35] A. Bard, M. Stratmann and S. Licht, Encyclopedia of electrochemistry, Semiconductor electrodes and photoelectrochemistry, Vol. 6, Wiley-VCH, 2002.

[36] R. Memming, Semiconductor electrochemistry, Weinheim: Wiley VCH, 2001.

[37] Y. Xu and M. A. A. Schoonen, "The absolute energy positions of conduction and valence bands of selected semiconductor minerals," *Am. Mineral.*, vol. 85, pp. 543-556, 2000.

[38] A. B. Murphy, P. R. F. Barnes, L. K. Randeniya, I. C. Plumb, I. E. Grey , M. D. Horne and J. A. Glasscock, "Efficiency of solar water splitting using semiconductor electrodes," *Int. J. Hydrogen Energy*, vol. 31, pp. 1999-2017, 2006.

[39] R. van de Krol and M. Grätzel, Photoelectrochemical hydrogen production, New York: Springer, 2012.

[40] A. Ziani, E. Nurlaela, D. S. Dhawale, D. A. Silva, E. Alarousu, O. F. Mohammed and K. Takanabe, "Carrier dynamics of a visible-light-responsive Ta3N5 photoanode for water oxidation," *Phys. Chem. Chem. Phys.*, vol. 17, pp. 2670-2677, 2015.

[41] M. W. Kanan and G. Nocera, "In situ formation of an oxygen-evolution catalyst in neutral water containing phophate and Co2+," *Science*, vol. 321, no. 5892, pp. 1072-1075, 2008.

[42] S. Licht, B. Wang, S. Mukerji, T. Soga, M. Umeno and H. Tributsch, "Efficient solar water splitting, exemplified by RuO2-catalyzed AlGaAs/Si photoelectrolysis," *J. Phys. Chem. B*, vol. 104, pp. 8920-8924, 2000.

[43] Z. Chen, F. Jaramillo, T. G. Deutsch, A. Kleiman-Shwarsctein, A. J. Forman, N. Gaillard, R. Garland, K. Takanabe, C. Heske, M. Sunkara, E. W. McFarland, K. Domen, E. L. Miller, J. A. Turner and H. N. DInh, "Accelerating materials development for photoelectrochemical hydrogen production: Standards for methods, definitions, and reporting protocols," *J. Mater. Res.*, vol. 25, no. 1, pp. 3-16, 2010.

[44] M. Rioult, H. Magnan, D. Stanescu and A. Barbier, "Single crystalline hematite films for solar water splitting: Ti-doping and thickness effects," *J. Phys. Chem. C*, vol. 118, no. 6, pp. 3007-3014, 2014.

[45] B. J. Trześniewskia and W. A. Smith, "Photocharged BiVO4 photanodes for improved solar water splitting," vol. 8, pp. 2919-2926, 2016.

[46] V. Cristino, S. Caramori, R. Argazzi, L. Meda, G. L. Marra and C. A. Bignozzi, "Efficient photoelectrochemical water splitting by anodically grown WO3 electrodes," *Langmuir*, vol. 27, no. 11, pp. 7276-7284, 2011.

[47] M. de Respinis, M. Fravventura, F. F. Abdi, H. Schreuders, T. J. Savenije, W. A. Smith, B. Dam and R. van de Krol, "Oxynitrogenography: Controlled synthesis of single-phase tantalum oxynitride photoabsorbers," *Chem. Mater.*, vol. 27, pp. 7091-7099, 2015.

[48] M. Higashi, K. Domen and R. Abe, "Highly stable water splitting on oxynitride TaON photoanode system under visible light irradiation," *J. Chem. Soc.*, vol. 134, no. 16, pp. 6968-6971, 2012.

[49] M. Rudolph, D. Stanescu, J. Alvarez, E. Foy, J.-P. Kleider, H. Magnan, T. Minea, N. Herlin-Boime, B. Bouchet-Fabre and M.-C. Hugon, "The role of oxygen in magnetron-sputtered Ta3N5 thin films for the photoelectrolysis of water (in press)," *Surf. Coat. Technol.*, 2016.

[50] I. E. Castelli , T. Olsen, S. Datta, D. D. Landis, S. Dahl , K. S. Thygesen and K. W. Jacobsen, "Computational screening of perovskite metal oxides for optimal solar light capture," *Energy Env. Sci.*, vol. 5, pp. 5814-5819, 2012.

[51] Y. Wu, P. Lazic, G. Hautier, K. Persson and G. Ceder, "First principles high throughput screening of oxynitrides for water-splitting photocatalysts," *Energy Environ. Sci.*, vol. 6, pp. 157-168, 2013.

[52] K. Maeda and K. Domen, "New non-oxide photocatalysts designed for overall water splitting under visible light," *J. Phys. Chem. C*, vol. 111, pp. 7851-7861, 2007.

[53] G. Fu, S. Yan, T. Yu and Z. Zou, "Oxygen related recominbation defects in Ta3N5 water splitting photoanode," *Appl. Phys. Lett.*, vol. 107:171902, 2015.

[54] D. Johnson, Some thermodynamic aspects of inorganic chemistry, Cambridge: Cambridge University Press, 1982.

[55] H. J. Coyne and R. N. Tauber, "Preparation, structure, and properties of sputtered, highly nitrided tantalum films," *J. Appl. Phys.*, vol. 39, pp. 5585-5592, 1968.

[56] N. Schönberg, "An X-ray study of the tantalum-nitrogen system," *Acta Chem. Scand.*, vol. 8, no. 2, pp. 199-203, 1954.

[57] J. Gatterer, G. Dufek, P. Ettmayer and R. Kieffer, "The cubic tantalum mononitride (B 1) and its mixability with the isotypic mononitrides and monocarbides of the 4a and 5a group metals," *Monatsh. Chem.*, vol. 106, no. 5, pp. 1137-1147, 1975.

[58] A. Ganin, Plasma-enhanced synthesis of transition metal nitrides, PhD thesis, University Stuttgart, 2005.

[59] A. Y. Ganin, L. Kienle and G. V. Vajenine, "Plasma-enhanced CVD synthesis and structural characterization of Ta2N3," *Eur. J. Inorg. Chem.*, p. 3233, 2004.

[60] G. Brauer and K. H. Zapp, "Die Nitride des Tantals," *Z. Anorg. Allg. Chemie,* vol. 277, pp. 129-139, 1954.

[61] H. Wiesenberger, W. Lengauer and P. Ettmayer, "Reactive diffusion and phase equilibria in the V-C, Nb-C, Ta-C and Ta-N systems," *Acta. Mater.,* vol. 46, no. 2, pp. 651-666, 1998.

[62] D. Li, F. Tian, D. Duan, K. Bao, B. Chu, X. Sha, B. Liu and T. Cui, "Mechanical and metallic properties of tantalum nitrides from first-principle calculations," *RSC Adv.,* vol. 4, pp. 10133-10139, 2014.

[63] A. Bousquet , F. Zoubian, J. Cellier, T. Sauvage and E. Tomasella, "Control the composition of tantalum oxynitride films by sputtering a tantalum target in Ar/O2/N2 radiofrequency magnetron plasmas," *Plasma Process. Polym.,* vol. 10, no. 11, pp. 990-998, 2013.

[64] C. S. Shin, Y. W. Kim, D. Gall, J. E. Greene and I. Petrov, "Phase composition and microstructure of polycrystalline and epitaxial TaNx layers grown on oxidiyed SI(001) and MgO(001) by reactive magnetron sputter deposition," *Thin Solid Films,* vol. 402, pp. 172-182, 2002.

[65] T. Mashimo and S. Tashiro, "Synthesis of the WC-type tantalum nitride by mechanical alloying," *J. Mater. Sci. Lett.,* vol. 13, pp. 174-176, 1994.

[66] N. Terao, "Structure of tantalum nitrides," *Jpn. J. Appl. Phys.,* vol. 10, no. 2, pp. 248-259, 1971.

[67] G. Brauer, E. Mohr, A. Neuhaus and A. Skogan, "ϑ-TaN, eine Hochdruckform von Tantalnitrid," *Monatsh. Chem.,* vol. 103, no. 3, pp. 794-798, 1972.

[68] N. E. Brese, M. O'Keefe , P. Rauch and F. J. Disalvo, "Structure of Ta3N5 at 16K by time-of-flight neutron diffraction," *Acta Cryst.,* no. C47, pp. 2291-2294, 1991.

[69] L. Yu, C. Stampfl, D. Marshall, T. Eshrich, V. Narayanan, J. M. Rowell, Newman N. and A. J. Freeman, "Mechanism and control of the metal-to-insulator transition in rocksalt tantalum nitride," *Phys. Rev. B,* vol. 65:245110 , 2002.

[70] M.-W. Lumey and R. Dronskowski, "First-principles electronic structure, chemical bonding, and high-pressure phase prediction of the oxynitrides of vanadium, niobium and tantalum," *Z. Anorg. Allg. Chem.,* vol. 631, pp. 887-893, 2005.

[71] M.-W. Lumey and R. Dronskowski, "The electronic structure of tantalum oxinitride and the falsification of α-TaON," *Z. Anorg. Allg. Chem.,* vol. 629, no. 12-13, pp. 2173-2179, 2003.

[72] A. H. Reshak, "Ab initio study of TaON, an active photocatalyst under visible light irradiation," *Phys. Chem. Chem. Phys.* , vol. 16, pp. 10558-10565, 2014.

[73] B. R. Sahu and L. Kleinman, "Theoretical study of structure and electronic properties of beta-Ta2O5 and delta-Ta2O5," *Phys. Rev.,* vol. 69:165202 , 2004.

[74] G. Hautier, A. Jain, H. Chen, C. Moore, S. P. Ong and G. Ceder, "Novel mixed polyanions lithium-ion battery cathode materials predicated by high-throughput ab initio computations," *J. Mater. Chem.,* vol. 21, pp. 17147-17153, 2011.

[75] C. Stampfl and A. J. Freemann, "Stable and metastable structures of the multiphase tantalum nitride system," *Phys. Rev. B,* vol. 71:024111, 2005.

[76] E. Orhan, F. Tessier and R. Marchand, "Synthesis and energetics of yellow TaON," *Solid State Sci.,* vol. 4, no. 8, pp. 1071-1076, 2002.

[77] J. Wang, J. Feng, L. Zhang, Z. Li and Z. Zou, "Role of oxygen impurity on the mechanical stability and atomic cohesion of Ta3N5 semiconductor photocatalyst," *Phys.Chem.Chem.Phys.,* vol. 16, pp. 15375-15380, 2014.

[78] M. Harb, P. Sautet, E. Nurlaela, P. Raybaud, L. Cavallo, K. Domen, J.-M. Basset and K. Takanabe, "Tuning the properties of visibile-light-responsive tantalum (oxy)nitride photocatalysts by non-stoichiometric compositions: a first-principles viewpoint," *Phys. Chem. Chem. Phys.,* vol. 16, pp. 20548-20560, 2014.

[79] D. D. Wagman, W. H. Evans, V. B. Parker, R. H. Schumm, I. Halow, S. M. Bailey, K. Churney and R. L. Nuttall, "The NBS tables of chemical thermodynamic properties; Selected values for inorganic and C1 and C2 organic substances in Si units," *J. Phys. Chem. Ref. Data,* vol. 11 supplement no. 2, 1982.

[80] J. M. McHale and A. Navrotsky, "Energetics of ternary nitrides: Li-Ca-Zn-N and Ca-Ta-N systems," *Chem. Mater.,* vol. 9, no. 7, pp. 1538-1546.

[81] D. Stull and H. Prophet, JANAF thermochemical tables, National Buereau of Standards, 1971.

[82] P. Violet, E. Blanquet and O. Le Bacq, "Density functional study of the stability and electronic properties of TaxNy compounds used as copper diffusion barriers," *Microelectron. Eng.,* vol. 83, no. 11-12, p. 2077–2081, 2006.

[83] U. Strähle, "Die Kristallstruktur des Tantal(V)-nitrids Ta3N5," *Z. Anorg. Allg. Chem.,* vol. 402, pp. 47-57, 1973.

[84] S. Khan, M. J. M. Zapata, M. B. Pereira, R. V. Gonçalves, L. Strizik, J. Dupont, M. J. L. Santos and S. R. Teixeira, "Structural, optical and photoelectrochemical chatacterization of monoclinic Ta3N5 thin films," *Phys. Chem. Chem. Phys.,* vol. 17, pp. 23952-23962, 2015.

[85] E. Nurlaela, S. Ould-Chikh, M. Harb, S. del Gobbo, M. Aouine, E. Puzenat, P. Sautet, K. Domen, J.-M. Basset and K. Takanabe, "Critical role of the semiconductor–electrolyte interface in photocatalytic performance for water-splitting reactions using Ta3N5 particles," *Chem. Mat.,* vol. 26, pp. 4812-4825, 2014.

[86] E. Langereis, S. B. S. Heil, H. C. M. Knoops, W. Keuning, M. C. M. van de Sanden and W. M. M. Kessels, "In situ spectroscopic ellipsometry as a versatile tool for studying atomic layer deposition," *J. Phys. D: Appl. Phys.,* vol. 42:073001, 2009.

[87] M. Bass, V. N. Mahajan and E. (. Van Stryland, Handbook of Optics, Volume II, Design, Fabrication, and Testing; Sources and Detectors; Radiometry and Photometry, New York City: McGraw Hill, 2003.

[88] E. Nurlaela, M. Harb, S. del Gobbo, M. Vashista and K. Takanabe, "Combined experimental and theoretical assessments of the lattice dynamics and optoelectronics of TaON and Ta3N5," *J. Solid State Chem.,* vol. 229, pp. 219-227, 2015.

[89] M. Harb, L. Cavallo and J.-M. Basset, "Major difference in visible-light photocatalystic features between perfect and self-defective Ta3N5 materials: A screened Coulomb hybrid DFT investigation," *J. Phys. Chem. C*, pp. 20784-20790, 2014.

[90] M. Hara, E. Chiba, A. Ishikawa, T. Takata, J. N. Kondo and K. Domen, "Ta3N5 and TaON thin films on Ta foil: surface composition and stability," *J. Phys. Chem.,* vol. 107, pp. 13441-13445, 2004.

[91] B. A. Pinaud, P. C. K. Vesborg and T. F. Jaramillo, "Effect of film morphology and thickness on charge transport in Ta3N5/Ta photoanodes for solar water splitting," *J. Phys. Chem. C,* vol. 116, pp. 15918-15924, 2012.

[92] P. Patnaik, Handbook of inorganic chemical compounds, Mcgraw-Hill Professional, 2002.

[93] S. Venkataraj, H. Kittur, R. Drese and M. Wuttig, "Multi-technique characterization of tantalum oxynitride films prepared by reactive direct current magentron sputtering," *Thin Solid Films*, vol. 514, pp. 1-9, 2006.

[94] J.-S. M. Lehn, P. van der Heide, Y. Wang, S. Suh and D. M. Hoffmann, "A new precursor for the chemical vapor deposition of tantalum nitride films," *J. Mater. Chem.,* vol. 14, pp. 3239-3245, 2004.

[95] S. J. Henderson and A. L. Hector, "Structural and compositional variations in Ta3N5 produced by high-temperature ammonolysis of tantalum oxide," *J. Solid State Chem.,* vol. 179, no. 11, pp. 3518-3524, 2006.

[96] A. Dabirian and R. van de Krol, "Resonant optical absorption and defect control in Ta3N5 photoanodes," *Appl. Phys. Lett.,* p. 033905 (4 pages), 2013.

[97] M. Rioult, "Hematite-based epitaxial thin films as photoanodes for solar water splitting," PhD thesis, Ecole Polytechnique, 2015.

[98] B. Chapman, Glow discharge processes, New York City: John Wiley & Sons, 1980.

[99] M. A. Lieberman and A. J. Lichtenberg, Principles of plasma discharges and materials processing, Hoboken, New Jersey: John Wiley & Sons, 2005.

[100] P. M. Martin, Handbook of deposition technologies for films and coatings: Science, applications and technology, William Andrew, 2009.

[101] M. J. Druyvesteyn and F. M. Penning, "The mechanism of electrical discharges in gases of low pressure," *Rev. Mod. Phys.,* vol. 12, no. 2, pp. 87-174, 1940.

[102] G. D. Magnuson and C. E. Carlston, "Electron ejection from metals due to 1- to 10-keV noble gas ion bombardment. I. Polycrystalline materials," *Phys. Rev.,* vol. 129, pp. 2403-2408, 1963.

[103] A. Bogaert, E. Neyts, R. Gijbels and J. van der Mullen, "Gas discharge plasmas and their applications," *Spectroc. Acta B,* vol. 57, no. 4, pp. 609-658, 2002.

[104] D. Lundin, P. Larsson, E. Wallin, M. Lattemann, N. Brenning and U. Helmersson, "Cross-field ion transport during high power impulse magnetron sputtering," *Plasma Sources Sci. Technol.,* vol. 17:035021, 2008.

[105] B. Window and N. Savvides, "Unbalanced dc magnetrons as sources of high ion fluxes," *J. Vac. Sci. Technol. A,* vol. 4, pp. 453-456, 1986.

[106] P. Chabert and N. Braithwaite, Physics of radio-frequency plasmas, Cambridge University Press, 2011.

[107] D. Gall, C.-S. Shin, T. Spila, M. Odén, M. J. H. Senna , J. E. Greene and I. Petrov, "Growth of single-crystal CrN on MgO(001): Effects of low-energy ion-irradiation on surface morphological evolution and physical properties," *J. Appl. Phys,* vol. 91, no. 6, pp. 3589-3597, 2002.

[108] R. Behrisch, W. Eckstein and (Eds.), Sputtering by particle bombardment,, Heidelberg: Springer, 2007.

[109] P. Sigmund, "Theory of Sputtering I: Sputtering yield of amorphous and polycrystalline targets," *Phys. Rev.,* vol. 184, no. 2, pp. 383-416, 1969.

[110] D. Depla, Magnetrons, reactive gases and sputtering, Raleigh, North Carolina: Lulu Press, 2015.

[111] M. W. Thompson, "II. The energy spectrum of ejected atoms during the high energy sputtering of gold," *Phil. Mag.,* no. 18, pp. 377-414.

[112] Y. Takagi, Y. Sakashita, H. Toyoda and H. Sugai, "Generation processes of super-high-energy atoms and ions in magnetron sputtering plasma," *Vacuum,* vol. 80, pp. 581-587, 2006.

[113] L. R. Testardi, J. H. Wrnick and W. A. Royer, "Superconductivity with onset above 23°K in Nb-Ge sputtered films," *Solid State Commun.,* vol. 15, no. 1, pp. 1-4, 1974.

[114] R. E. Somekh, "The thermalization of energetic atoms during the sputtering process," *J. Vac. Sci. Technol. A,* no. 2, pp. 1285-1291, 1984.

[115] S. Schiller, G. Beister and W. Sieber, "Reactive high rate d.c. sputtering: Depostiion rate, stoichiometry and features of TiOx and TiNx films with respect to the target mode," *Thin Solid Films,* vol. 111, pp. 259-268, 1984.

[116] J. Schulte and G. Sobe, "Magnetron sputtering of aluminum using oxygen or nitrogen as reactive gas," *Thin Solid Films,* vol. 324, pp. 19-24, 1998.

[117] S. Mahieu and D. Depla, "Reactive sputter deposition of TiN layers: modelling the growth by characterization of particle fluxes towards the substrate," *J. Phys. D: Appl. Phys.*, vol. 42:053002, 2009.

[118] W. D. Westwood, "Calculation of deposition rates in diode sputtering systems," *J. Vac. Sci. Technol.*, vol. 15, no. 1, pp. 1-9, 1978.

[119] R. S. Robinson, "Energetic binary collisions in rare gas plasmas," *J. Vac. Sci. Technol.*, vol. 26, no. 2, pp. 185-188, 1979.

[120] D. Lundin, C. Vitelaru, L. de Poucques, N. Brenning and T. Minea, "Ti-Ar scattering cross sections by direct comparison of Monte Carlo simulations and laser-induced fluorescence spectroscopy in magnetron discharges," *J. Phys. D: Appl. Phys.*, no. 46:175201, 2013.

[121] A. V. Phelps, "Cross sections and swarm coefficients for nitrogen ions and neutrals in N2 and Argon ions and neutrals in Ar for energies from 0.1 eV to 10 keV," *J. Phys. Chem. Ref. Data*, vol. 20, pp. 557-573, 1991.

[122] H. Lüth , Solid surfaces, interfaces and thin films, Springer, 2014.

[123] B. Movchan and A. V. Demchishin, "Structure and properties of thick condensates of nickel, titanium, tungsten, aluminum oxides, and zirconium dioxide in vacuum," *Fiz. Metal. Metalloved,* vol. 28, pp. 653-660, 1969.

[124] J. A. Thornton, "Influence of apparatus geometry and deposition conditions on the structure and topography of thick sputtered coatings," *J. Vac. Sci. Technol.*, vol. 11, no. 4, pp. 666-670, 1974.

[125] T. Narusawa, S. Shimizu and S. Komiya, "Simultaneous RHEED-AES-QMS study on epitaxial Si film growth on Si(111) and sapphire (1102) surfaces by partially ionized vapour deposition," *J. Vac. Sci. Technol.*, vol. 16, no. 2, pp. 366-388, 1979.

[126] A. Anders, "A structure zone diagram including plasma-based deposition and ion etching," *Thin solid films*, vol. 518, no. 15, pp. 4087-4090, 2010.

[127] D. K. Brice, J. Y. Tsao and S. T. Picraux, "Partitioning of ion-induced surface and bulk displacements," *Nucl. Instr. Meth. Phys. Res. B,* vol. 44, pp. 68-78.

[128] H. Kheyrandish, J. S. Colligon and J.-K. Kim, "Effect of deposition parameters on the microstructure of ion beam assisted deposition TiN films," *J. Vac. Sci. Technol. A,* vol. 12, pp. 2723-2727, 1994.

[129] I. Petrov, L. Hultman, U. Helmersson, J.-E. Sundgren and J. E. Greene, "Microstructure modification of tiN by ion bombardment during reactive sputter deposition," *Thin Solid Films,* vol. 169, pp. 299-314, 1989.

[130] C.-S. Shin, D. Gall, Y.-W. Kim, H. N. , I. Petrov and J. E. Greene, "Development of preferred orientation in polycrystalline NaCl-structure d-TaN layers by reactive magnetron sputtering: Role of low-energy ion surface interaction," *J. Appl. Phys.*, vol. 92, no. 9, pp. 5084-5093, 2002.

[131] L. Hultman, S. A. Barnett, J.-E. Sundgren and J. E. Greene, "Growth of epitaxial TiN films deposited on MgO(100) by reactive magnetron sputtering: the role of low-energy ion irradiation during deposition," *J. Cryst. Growth,* vol. 92, pp. 639-656, 1988.

[132] L. Wei, M. ZHong-Quan, W. Ye and W. De-Ming, "Optimization of energy scope for titanium nitride films grown by ion beam-assisted deposition," *Chin. Phys. Lett.,* vol. 23, no. 1, pp. 178-181.

[133] S. V. Jagadeesh Chandra, M. Chandrasekhar, G. Mohan Rao and S. Uthanna, "Substrate bias voltage influenced structural, electrical and optical properties of dc magnetron sputtered Ta2O5 films," *J. Mater. Sci: Mater. Electron.,* vol. 20, pp. 295-300, 2009.

[134] S. Schiller, K. Goedicke, J. Reschke, V. Kirchhoff, S. Schneider and F. Milde, "Pulsed magnetron sputter technology," *Surf. Coat. Technol.,* vol. 61, pp. 331-337, 1993.

[135] A. P. Ehiasarian, J. G. Wen and I. Petrov, "Interface microstructure engineering by high power impulse magnetron sputtering for the enhancement of adhesion," *J. Appl. Physi.,* vol. 101:054301, no. 5, 2007.

[136] K. Macák, V. Kouznetsov, J. Schneider , U. Helmersson and I. Petrov, "IOnized sputter deposition using an extremely high plasma density pulsed magnetron discharge," *J. Vac. Sci. Technol. A,* vol. 18, pp. 1533-1537, 2000.

[137] V. Kouznetsov, V. Macák, J. Schneider , U. Helmersson and I. Petrov, "A novel pulsed magnetron sputter technique utilizing very high target power densities," *Surf. Coat. Technol.* , vol. 122, no. 2-3, pp. 290-293, 1999.

[138] J. T. Gudmundsson, N. Brenning, D. Lundin and U. Helmersson, "HIgh power impulse magnetron sputtering discharge," *J. Vac. Sci. Technol. A,* vol. 30:030801, no. 3, 2012.

[139] M. Samuelsson, D. Lundin, J. Jensen, M. A. Raadu, J. T. Gudmundsson and U. Helmersson, "On the film density using high power impulse magnetron sputtering," *Surf. Coat. Tech.,* vol. 205, no. 2, pp. 591-596, 2010.

[140] E. Wallin, T. I. Selinder, M. Elfwing and U. Helmersson, "Synthesis of a-Al2O3 thin films using reactive high-power impulse magnetron sputtering," *Europhys. Lett.,* vol. 82, p. 36002, 2008.

[141] S. Konstantinidis, J. P. Dauchot and M. Hecq, "Titanium oxide thin films deposited by high-power impulse magnetron sputtering," *Thin Solid Films,* vol. 515, no. 3, pp. 1182-1186, 2006.

[142] J. Alami, P. O. Å. Persson, D. Music, J. T. Gudmundsson, J. Bohlmark and U. Helmersson, "Ion-assisted physical vapor deposition for enhanced film properties on nonflat surfaces," *J. Vac. Sci. Technol. A,* vol. 23, pp. 278-280, 2005.

[143] F. Magnus, A. S. Ingason, O. B. Sveinsson, S. Olafsson and J. T. Gudmundsson, "Morphology of TiN thin films grown on SiO2 by reactive high power impulse magnetron sputtering," *Thin Solid Films,* vol. 520, pp. 1621-1624, 2011.

[144] J. Alami, K. Sarakinos, F. Uslu and M. Wuttig, "On the relationship between the peak target current and the morphology of chromium nitride thin films deposited by reactive high power pulsed magnetron sputtering," *J. Phys. D: Appl. Phys.*, vol. 42:015404, 2009.

[145] P.-Y. Jouan, L. Le Brizoual, M. Ganciu, C. Cardinaud, S. Tricot and M.-A. Djouadi, "HiPIMS ion energy distribution measurements in reactive mode," *IEEE Trans. Plasma Sci.,* vol. 38, no. 11, pp. 3089-3094, 2010.

[146] C. S. Shin, Phase composition, microstructure, and physical properties of poly- and single-crystal TaNx layers, PhD thesis, Urbana, Illinois: University of Illinois, 2002.

[147] X. Sun, E. Kolawa, J.-S. Chen, J. S. Reid and M.-A. Nicolet, "Properties of reactively sputter-deposited Ta-N thin films," *Thin Solid Films,* vol. 236, pp. 347-351, 1993.

[148] M. Stavrev, D. Fischer, C. Wenzel, K. Drescher and N. Mattern, "Crystallographic and morphological characterization of reactively sputtered Ta, Ta-N and Ta-N-O thin films," *Thin Solid Films,* vol. 307, no. 1-2, pp. 79-88, 1997.

[149] A. Bousquet, F. Zoubian, J. Cellier, C. Taviot-Gueho, T. Sauvage and E. Tomasella, "Structural and ellipsometric study on tailored optical properties of tantalum oxynitride films deposited by reactive sputtering," *J. Phys. D: Appl. Phys.,* vol. 47:475201, 2014.

[150] H. Le Dréo, O. Banakh, H. Keppner, P.-A. Steinmann, D. Briand and N. F. de Rooij, "Optical, electrical and mechanical properties of the tantalum oxynitride thin films deposited by pulsing reactive gas sputtering," *Thin Solid FIlms,* vol. 515, pp. 952-956, 2006.

[151] M. Ohring, Material science of thin films, San Diego, California: Academic Press, 2002.

[152] A. Hammersley, "The fit2d home page," [Online]. Available: http://www.esrf.eu/computing/scientific/FIT2D/. [Accessed 15 09 2016].

[153] H. Peatz gen. Schiek, Nuclear Reactions; An introduction, New York: Springer, 2014.

[154] A. F. Gurbich, "SigmaCalc recent development and present status of the evaluated cross-sections for IBA," *Nucl. Instr. Meth. Phys. Res.,* vol. 371, pp. 27-32, 2016.

[155] R. A. Jarjis, "On the investigation of alpha-particle resonance elastic scatttering from the 16O nucleus," *Nucl. Instr. Meth. Phys. Res. B,* vol. 12, no. 3, pp. 331-333, 1985.

[156] J. Demarche and G. Terwagne, "Precise measurement of the differential cross section from the 16O(a,a)16O elastic reaction at 165° and 170° between 2.4 and 6.0 MeV," *J. Appl. Phys.,* vol. 100:124909 , 2006.

[157] J. A. Leavitt, L. C. McIntyre, M. D. Ashbaugh, J. G. Oder, Z. Lin and B. Dezfouly-Arjomandy, "Cross sections for 170.5° backscattering of 4He from oxygen for 4He energies between 1.8 and 5.0 MeV," *Nucl. Instr. Meth. Phys. Res. B,* vol. 44, no. 3, pp. 260-265, 1990.

[158] Z. Y. Zhou, Y. Y. Zhou, Y. Zhang, W. D. Xu, G. Q. Zhao, J. Y. Tang and F. J. Yang, "Simultaneous analysis of light elements using non-Rutherford helium backscattering," *Nucl. Instr. Meth. Phys. Res. B,* vol. 100, no. 4, pp. 524-528, 1995.

[159] C. Huan-sheng, S. Hao, T. Jia-yong and Y. Fu-jia, "The studies of non-Rutherford backscattering cross sections of 4He from 16O," *Acta Phys. Sin.-Ov. Ed.,* vol. 2, no. 9, 1993.

[160] M. Mayer, "SIMNRA, a simulation program for the analysis of NRA, RBS and ERDA," *AIP Conf. Proc.* , vol. 475, no. 541, 1999.

[161] IAEA, "Ion beam analysis nuclear data library," 2014. [Online]. Available: http://www-nds.iaea.org/ibandl/. [Accessed 01 02 2016].

[162] D. I. Thwaites, "Bragg's rule of stopping power additivity: a compilation and summary of results," *J. Radiat. Res.,* vol. 95, pp. 495-518, 1983.

[163] J. Ziegler, "SRIM Special - Stoppin in compounds".

[164] M. Mayer, "SIMNRA User's guide," Max-Planck-Institut für Plasmaphysik, Garching, Germany, 2002.

[165] P. J. Bryant, "A brief history and review of accelerators," in *CAS - CERN Accelerator School: 5th General Accelerator Physics Course, Jyväskylä, Finland*, 1992, pp. 1-16.

[166] Hamamatsu, "Chapter 10 Si detectors for high energy particles," in *Hamamatsu Opto-semiconductor Handbook.*

[167] C. C. Katsidis and D. I. Siapkas, "General transfer-matrix method for optical multilayer systems with coherent, partially coherent, and incorherent interference," *Appl. Opt.,* vol. 41, no. 19, pp. 3978-3987, 2002.

[168] J. Singh, Optical properties of condensed matter and applications, Chichester, West Sussex: Jon Wiley & Sons Ltd., 2006.

[169] G. Reider, Photonik, Wien: Springer, 2012.

[170] J. Tauc, R. Geigobovich and A. Vancu, "Optical properties and electronic structure of amorphous germanium," *Phys. stat. sol.,* vol. 15, pp. 627-637, 1966.

[171] A. S. Ferlauto, G. M. Ferreira, J. M. Pearce, C. R. Wronski, R. W. Collins, X. Deng and G. Ganguly, "Analytical model for the optical functions of amorphous semiconductors from the near-infrared to ultraviolet: applications in thin film photovoltaics," *J. Appl. Phys.,* vol. 92, no. 5, pp. 2424-2436, 2002.

[172] G. E. Jellison, J. Modin and F. A. Modine, "Parameterization of the optical functions of amorphous materials in the interband region," *Appl. Phys. Lett.,* vol. 69, no. 3, pp. 371-373, 1996.

[173] F. Urbach, "The long-wavelength edge of photographic sensitivity and of the electronic absorption of solids," *Phys. Rev.,* vol. 92, p. 1324, 1953.

[174] K. Boubaker, "A physical explanation to the controversial Urbach tailing universality," *Eur. Phys. J. Plus,* vol. 126, no. 1,10, 2011.

[175] T. Csendes, L. Pál, J. O. H. Sendín and J. R. Banga, "The GLOBAL optimization method revisited," *Optim. Letter,* vol. 2, pp. 445-454, 2008.

[176] L. Gao, F. Lemarchand and M. Lequime, "Reverse engineering from spectrophotometric measurements: performances and efficiency of different optimization algorithms," *Appl. Phys. A,* no. 108, pp. 877-889, 2012.

[177] CasaXPS, "CasaXPS: Processing Software for XPS, AES, SIMS and more," 2016. [Online]. Available: http://www.casaxps.com/.

[178] Thermo Scientific, "XPS Reference Table," [Online]. Available: http://xpssimplified.com/periodictable.php. [Accessed 20 09 2016].

[179] ASTM, "Terrestrial Reference Spectra for Photovoltaic Performance Evaluation," [Online]. Available: http://rredc.nrel.gov/solar/spectra/am1.5/. [Accessed 13 09 2016].

[180] G. Kopp and J. L. Lean, "A new, lower value of total solar irradiance: evidence and climate significance," *Geophys. Res. Lett.,* vol. 38, pp. 1-7, 2011.

[181] A. K. Ghosh, C. Fishman and T. Feng, "Theory of the electrical and photovoltaic properties of polycrystalline silicon," *J. Appl. Phys.,* vol. 51, no. 1, pp. 446-454, 1980.

[182] M. Ganciu-Petcu, M. Hecq, J.-P. Dauchot, S. Konstantinidis, J. Bretagne, L. Poucques and M. Touzeau, "Pulsed magentron sputtering deposition with preionization". Patent US Patent 7927466 B2, 2011.

[183] J. I. Langford and A. J. C. Wilson, "Scherrer after sixty years: A survey and some new results in the determination of crystallite size," *J. Appl. Cryst.,* vol. 11, pp. 102-113, 1978.

[184] P. Patsalas and S. Logothetidis, "Optical, electronic, and transport properties of nanocrystalline titanium nitride thin films," *J. Appl. Phys.,* vol. 90, no. 9, pp. 4725-4734, 2001.

[185] D. Gall, S. Kodambaka, M. A. Wall, I. Petrov and J. E. Greene, "Pathways of atomistic processes on TiN(001) and (111) surfaces during film growth: an ab initio study," *J. Appl. Phys.,* vol. 93, no. 11, pp. 9086-9094, 2003.

[186] J. W. Bradley, S. Thompson and Y. Aranda Gonzalvo, "Measurement of the plasma potential in a magnetron discharge and the prediction of the electron drift speed," *Plasma Sources Sci. Technol.,* vol. 10, pp. 490-501, 2001.

[187] A. D. Pajdarová, J. Vlček, P. Kudláček and J. Lukáš, "Electron energy distributions and plasma parameters in high-power pulsed magnetron sputtering discharges," *Plasma Sources Sci. Technol.,* vol. 18, p. 025008 (7pp), 2009.

[188] Y. Itikawa, "Cross sections for electron collision with nitrogen molecules," *J. Phys. Chem. Ref. Data,* vol. 35, no. 1, pp. 31-53, 2006.

[189] M. Sauelsson, D. Lundin, J. Jensen, M. A. Raadu, J. T. Gudmundsson and U. Helmersson, "On the film density using high power impulse magnetron sputtering," *Surf. Coat. Technol.*, vol. 205, pp. 591-596, 2010.

[190] G. Greczynski, J. Lu, J. Jensen, I. Petrov, J. E. Greene, S. Bolz, W. Kölker, C. Schiffers, O. Lemmer and L. Hultmann, "Metal versus rare-gas ion irradiation during Ti1−xAlxN film growth by hybrid high power pulsed magnetron/dc magnetron co-sputtering using synchronized pulsed substrate bias," *J. Vac. Sci. Technol. A,* vol. 30:061504, no. 6, 2012.

[191] J. Bohlmark, M. Lattemann, J. T. Gudmundsson, A. P. Ehiasarian, Y. Aranda Gonzalvo, N. Brenning and U. Helmersson, "The ion energy distributions and ion flux composition from a high power impulse magnetron sputtering discharge," *Thin Solid Films,* no. 515, pp. 1522-1526, 2006.

[192] A. P. Ehiasarian, Y. A. Gonzalvo and T. D. Whitmore, "Time-resolved ionisation studies of the high power impulse magnetron discharge in mixed argon and nitrogen atmosphere," *Plasma Process. Polym.,* vol. 4, pp. S309-S313, 2007.

[193] M. Palmucci, N. Britun, T. Silva, R. Snyders and S. Konstantinidis, "Mass spectrometry diagnostics of short-pulsed HiPIMS discharges," *J: Phys. D: Appl. Phys.,* vol. 46:215201, no. 21, 2013.

[194] A. Hecimovic, K. Burcalova and A. P. Ehiasarian, "Origins of ion energy distribution function (IEDF) in high power impulse magnetron sputtering (HIPIMS) plasma discharge," *J. Phys. D: Appl. Phys.,* vol. 41:095203, 2008.

[195] S. Konstantinidis, J. Dauchot, M. Ganciu, A. Ricard and M. Hecq, "Influence of pulse duration on the plasma characteristics in high-power pulsed magnetron discharges," *J. Appl. Phys.,* vol. 99:013307, no. 1, 2006.

[196] M. Hala, N. Viau, O. Zabeida, J. E. Klemberg-Sapieha and L. Martinu, "Dynamics of reactive high-power impulse magnetron sputtering discharge studied by time-and space-resolved optical emission spectroscopy and fast imaging," *J. Appl. Physics,* vol. 107:043305 , 2010.

[197] I. Petrov, A. Myers, J. E. Greene and J. R. Abelson, "Mass and energy resolved detection of ions and neutral sputtered species incident at the substrate during reactive magnetron sputtering of Ti in mixed Ar+N2 mixtures," *J. Vac. Sci. Technology,* vol. 12, no. 5, pp. 2846-2854, 1994.

[198] G. Greczynski, J. Jensen and L. Hultman, "CrNx films prepared by dc magnetron sputtering and high-power pulsed magentron sputtering: a comparative study," *IEEE T. Plasma Sci.,* vol. 38, no. 11, pp. 3046-3056, 2010.

[199] M. Lattemann, U. Helmerson and J. Greene, "Fully dense, non-faceted 111-textured high power impulse magnetron sputtering TiN films grown in the absence of substrate heating and bias," *Thin Solid Films,* vol. 518, pp. 5978-5980, 2010.

[200] J. M. Andersson, E. Wallin, E. P. Münger and U. Helmersson, "Energy distributions of positive and negative ions during magnetron sputtering of an Al target in Ar/O2 mixtures," *J. Appl. Phys.,* vol. 100:03305, no. 3, 2006.

[201] J. Ziegler, M. D. Ziegler and J. P. Biersack, "SRIM – The stopping and range of ions in matter (2010)," *Nucl. Instr. Meth. Phys. Res.,* vol. 268, p. 1818–1823, 2010.

[202] Z. Wang, S. A. Cohen, D. N. Ruzic and M. J. Goeckner, "Nitrogen atom energy distribution in a hollow-cathode planar sputtering magnetron," *Phys. Rev. E,* vol. 61, no. 2, pp. 1904-1911, 2000.

[203] K. Sarakinos, J. Alami, P. M. Karimi, D. Severin and M. Wuttig, "The role of backscattered energetic atoms in film growth in reactive magnetron sputtering of chromium nitride," *J. Phys. D: Appl. Phys.,* vol. 40, no. 3, pp. 778-785, 2007.

[204] J. B. Malherbe, S. Hofmann and J. M. Sanz, "Preferential sputtering of oxides: A comparison of model predictions with experimental data," *Appl. Surf. Sci.,* vol. 27, no. 3, pp. 355-365, 1986.

[205] T. Ishitani and R. Shimizu, "Computer simulation of knock-on effect under ion bombardment," *Phys. Lett.,* vol. 46A, pp. 487-488, 1974.

[206] A. R. Kilmametov, D. V. Gunderov, R. Z. Valiev, A. G. Balogh and H. Hahn, "Enhanced ion irradiation resistance of bulk nanocrystalline TiNi alloy," *Scr. Mater.,* vol. 59, pp. 1027-1030, 2008.

[207] D. Ziegler, TRIM Manual, 2013.

[208] Y.-R. Luo, Comprehensive handbook of chemical bond energies, CRC Press Inc. , 2007.

[209] A. L. Allred, "Electronegativity values from thermochemical data," *J. Inorg. Nucl. Chem.,* vol. 17, no. 3-4, pp. 215-221, 1961.

[210] J. E. Huheey, E. A. Keiter, R. L. Keiter and O. K. Medhi, Inorganic chemistry: principles of structure and reactivity, Addison Wesley Inc. , 1993.

[211] J. Etournea, J. Portier and F. Ménil, "The role of the inductive effect in solid state chemistry: how the chemist can use it to modify both the structural and the physical properties of the materials," *J. Alloy Compd.,* vol. 188, pp. 1-7, 1992.

[212] H. B. Michaelson, "The work function of the elements and its periodicity," *J. Appl. Phys.* , vol. 48, no. 11, pp. 4729-4733, 1977.

[213] G. S. Chen, C. C. Lee, H. Niu, W. Huang, R. Jann and T. Schütte, "Sputter deposition of titanium monoxide and dioxide thin films with controlled properties using optical emission spectroscopy," *Thin Solid Films,* vol. 516, pp. 8473-7478, 2008.

[214] K. Maeda, N. Nishimura and K. Domen, "A precursor route to prepare tantalum (V) nitride nanoparticles with enhanced photocatalytic activity for hydrogen evolution under visible light," *Appl. Catal. A,* vol. 370, no. 1-2, pp. 88-92, 2009.

[215] L. Cui, M. Wang and Y. X. Wang, "Nitrogen vacancies and oxgen substitution of Ta3N5: First-principles investigation," *J. Phys. Soc. Jpn.,* vol. 83:114707, 2014.

[216] V. K. Pecharsky and P. Y. Zavalij, Fundamentals of powder diffraction and structural characterization of materials, Springer, 2009.

[217] W. B. Jackson, R. J. Nemanich and N. M. Amer, "Energy dependenc of the carrier mobility-lifetime product in hydrogenated amorphous silicon," *Phys. Rev. B,* vol. 27, pp. 4861-4871, 1983.

[218] M. Fox, Optical properties of solids, 2 ed., Oxford: Oxford University Press, 2010.

[219] M. Ritala, P. Kalsi, D. Riihelä, K. Kukli, M. Leskelä and J. Jokinen, "Controlled growth of TaN, Ta3N5 and TaOxNy thin films by atomic layer deposition," *Chem. Mater.,* vol. 11, no. 7, pp. 1712-1718, 1999.

[220] Q. Zhang, X. Mei, D. Yang, F. Chen, T. Ma, Y. Wang and F. Teng, "Preparation, structure and properties of TaN and TaC films obtained by ion beam assisted deposition," *Nucl. Instr. Meth. Phys. Res.,* Vols. 127-128, pp. 664-668, 1997.

[221] V. Chawla, R. Jayaganthan, A. K. Chawla and R. Chandra, "Microstructural characterization of magnetron sputtered Ti films on glass substrate," *J. Mater. Process. Technol.,* vol. 209, pp. 3444-3451, 2009.

[222] F. Cemin, D. Lundin, D. Cammilleri, T. Maroutian, P. Lecoeur and T. Minea, "Low electrical resistivity in thin and ultrathin copperlayers grown by high power impulse magnetron sputtering," *J. Vac. Sci. Technol. A,* vol. 34:051506 , no. 5, 2016.

[223] P. Mayrhofer, F. Kunc, J. Musil and C. Mitterer, "A comparative study on reactive and non-reactive unbalanced magnetron sputter deposition of TiN coatings," *Thin Solid Films,* vol. 415, pp. 151-159, 2002.

[224] U. Wahlström, L. Hultmann, J.-E. Sundgren, F. Adibi, I. Petrov and J. E. Greene, "Crystal growth and microstructure of polycrystalline Ti1-xAlxN alloy films deposited by ultra-heigh-vacuum dual-target magnetron sputtering," *Thin Solid Films,* vol. 235, pp. 62-70, 1993.

[225] H. Dotan, K. Sivula, M. Grätzel, A. Rothshild and S. C. Warren, "Probing the photoelectrochemical properties of hermatite (a-Fe2O3) electrode using hydrogen peroxide as a hole scavenger," *Energy Environ. Sci.,* vol. 4, pp. 958-964, 2011.

[226] I. Petrov, F. Adibi, J. E. Greene, W. D. Sproul and W.-D. Münz, "Use of an externally applied axial magnetic field to control ion/Neutral flux ratios at the substrate during magnetron sputter deposition," *J. Vac. Sci. Technol. A,* vol. 10, no. 5, pp. 3283-3287, 1992.

[227] V. Tiron, I.-L. Velicu, F. Ghiorghiu and G. Popa, "The effect of the additional magnetic field and gas pressure on the sheath region of a high power impuilse magnetron sputtering discharge," *Rom. Rep. Phys.,* vol. 67, no. 3, pp. 1004-1017, 2015.

[228] M. Rudolph, A. Demeter, E. Foy, V. Tiron, L. Sirghi, T. Minea, B. Bouchet-Fabre and M.-C. Hugon, "Improving the degree of crystallinity of magnetron-sputtered Ta3N5 thin films by augmenting the ion-to-neutral ratio onto the substrate (in press)," *Thin Solid FIlms,* vol. 636, pp. 48-53, 2017.

[229] B. Window and N. Savvides, "Charged particle fluxes from planar magnetron sputtering sources," *J. Vac. Sci. Technol. A,* vol. 4, no. 2, pp. 196-202, 1986.

[230] Y. M. Kim, J. U. Kim and J. G. Han, "Investiagation on the pulsed DC plasma nitriding with optical emission spectroscopy," *Surf. Coat. Technol.,* Vols. 151-152, pp. 227-232, 2002.

universite PARIS-SACLAY
ÉCOLE DOCTORALE
Ondes et Matière
(EDOM)

Titre: Synthèse et caractérisation des couches minces de Ta_3N_5 élaborées par pulvérisation cathodique pour la photo-électrolyse de l'eau

Mots clés: pulvérisation cathodique, oxy-nitrure de tantale, Ta_3N_5, photo-électrolyse

Résumé: Le Ta_3N_5 fait partie des matériaux les plus prometteurs pour la photo-électrolyse de l'eau. En effet, la bande de valence et la bande de conduction sont situées autour du potentiel d'évolution de l'hydrogène et de l'oxygène et son petit gap (2.1eV) permet l'absorption d'une grande partie du spectre solaire. Par contre la synthèse de ce matériau est difficile à cause de la structure riche en azote (faible diffusion) et de l'état d'oxydation élevé du Ta (+5) dans le cristal de Ta_3N_5. Sa synthèse par pulvérisation cathodique est peu exploitée à ce jour, malgré que cette technique de dépôt permette d'augmenter le rapport ion-neutre arrivant sur le film en croissance et donc de fournir de l'énergie supplémentaire à la surface du film favorisant ainsi la cristallisation.
Lors cette thèse, des couches minces de Ta_3N_5 ont été déposées par pulvérisation cathodique dans une atmosphère réactive. Il y est montré que la pulvérisation d'une cible de Ta produit des Ar rétrodiffusés avec des énergies élevées qui augmentent l'incorporation de défauts dans la couche lorsque la polarisation de la cible est élevée. Des films de Ta_3N_5 ont été déposés en mode continu ce qui a permis de maintenir une polarisation faible. Il a été mis en évidence que l'oxygène incorporé dans le cristal joue un rôle crucial pour la déposition du film de Ta_3N_5. De plus, l'oxygène influence fortement les propriétés des couches minces, notamment les propriétés optiques et électroniques. Un nouveau système, augmentant le flux d'ions vers le substrat, a été installé dans le réacteur de dépôt ce qui a augmenté le degré de cristallisation de la phase Ta_3N_5. Les connaissances acquises lors de cette thèse ont été utilisées pour préparer des photoanodes à partir de Ta_3N_5 et leur aptitude à décomposer l'eau sous l'illumination du soleil a été démontrée.

Title: Synthesis and characterization of magnetron-sputtered Ta_3N_5 thin films for the photoelectrolysis of water

Keywords: magnetron sputtering, tantalum oxi-nitride, Ta_3N_5, photoelectrolysis

Abstract: Ta_3N_5 is one of the most promising candidates for efficient water splitting using sunlight due to its band positions with respect to the oxygen and hydrogen evolution potentials and its small band gap of 2.1eV. Its synthesis, however, is challenging given its high content of nitrogen, with its low diffusivity, and the Ta metal atom in a high oxidation state. Few investigations into its synthesis by magnetron sputtering exist to date although this technique offers the possibility of tuning the ion-to-neutral flux ratio onto the growing film. This can change the supply of energy onto its surface and therefore promote the crystallization.
In this thesis, reactive magnetron sputtering is investigated for the preparation of Ta_3N_5 thin films. It is shown that sputtering of a Ta target in an Ar atmosphere produces energetic backscattered Ar neutrals at high target potentials. To keep the potential low, Ta_3N_5 is deposited by sputtering in DC mode. The growth of the Ta_3N_5 phase requires the incorporation of oxygen into the lattice. It is shown that optical and electronic properties of these samples vary strongly with the precise amount of oxygen in the thin film. Samples with a high degree of crystallinity are obtained by increasing the N_2^+ flux onto the substrate by changing the form of the magnetic field of the magnetron. The highly crystalline samples prepared by this method are proven to work as photoanodes for the splitting of water under illumination.

Université Paris-Saclay
Espace Technologique / Immeuble Discovery
Route de l'Orme aux Merisiers RD 128 / 91190 Saint-Aubin, France